Louisiana State University
LSU Digital Commons

LSU Doctoral Dissertations | Graduate School

2013

Emergence of Delamination Fractures around Casing and Its Stability

Wei Wang
Louisiana State University and Agricultural and Mechanical College, wwang19@tigers.lsu.edu

Follow this and additional works at: https://digitalcommons.lsu.edu/gradschool_dissertations

 Part of the Petroleum Engineering Commons

Recommended Citation
Wang, Wei, "Emergence of Delamination Fractures around Casing and Its Stability" (2013). *LSU Doctoral Dissertations*. 264.
https://digitalcommons.lsu.edu/gradschool_dissertations/264

This Dissertation is brought to you for free and open access by the Graduate School at LSU Digital Commons. It has been accepted for inclusion in LSU Doctoral Dissertations by an authorized graduate school editor of LSU Digital Commons. For more information, please contactgradetd@lsu.edu.

EMERGENCE OF DELAMINATION FRACTURES AROUND CASING AND ITS STABILITY

A Dissertation

Submitted to the Graduate Faculty of the
Louisiana State University and
Agricultural and Mechanical College
in partial fulfillment of the
requirements for the degree of
Doctor of Philosophy

in

The Craft & Hawkins Department of Petroleum Engineering

by
Wei Wang
B.S., Northeast Petroleum University, 2004
M.S., Northeast Petroleum University, 2007
M.S., University of Wyoming, 2009
May 2014

ACKNOWLEDGEMENTS

I would like to express my appreciation to my major professor, Dr. Arash Dahi for his enlightenment, guidance, supervision, patience and encouragement. His insights and suggestions have always been valuable and beneficial for the research progress.

I would also like to thank my examining committee members, Dr. Andrew K. Wojtanowicz, Dr. Ted Bourgoyne, and Dr. George Wong, Dr. Sam Bentley, who were enthusiastic to serve on the examining committee and gave valuable suggestions.

I wish to express my gratitude to the funding from Shell Exploration & Production Company. Without their support, this work would not have been possible.

Many thanks are given to the LSU Craft and Hawkins Department of Petroleum Engineering and State of Louisiana for providing financial support to my graduate studies.

Thanks to my husband, my daughter, my parents, their encouragements and supports have helped me to go through my hard times during my studies.

Thanks extend to all other faculty members and students who have offered help and been kind to the author.

TABLE OF CONTENTS

ABSTRACT

The cement sheath failures and nearby wellbore failures may lead to upward flow of drilling fluid or formation fluid, which may have significantly adverse consequences like loss of reserve and environmental hazards. In order to maintain wellbore integrity in the long term, it is expedient to examine the causes of failures around the wellbore and propose suitable numerical models to predict annulus cracks around the casing.

The complex failure behavior of cement/rock interfaces observed in the laboratory experiments does not look like the behavior of linear or simple nonlinear mechanical interfaces. Cohesive zone method (CZM) with BK-form bilinear traction separation law can be a good candidate to reproduce the complicated failure behavior around the casing. Then fracture critical energy, cohesive strength, and the deformability can be derived for cohesive zone constitutive equations by reproducing the loading-displacement curves from laboratory and inverse analyses. In this work, the comprehensive analysis for microannulus formation is presented by utilizing axisymmetric or three-dimensional poroelastic finite element models with CZM.

This dissertation investigated these aspects: 1) Two and three-dimensional analysis of cement sheath integrity around wellbores due to presence of a leakage point; 2) Stimulation multi-zone fracturing and its cement sheath integrity during hydraulic fracturing. In this research, the physical mechanism of the loss of wellbore integrity is explained by the combined effects of fluid pressure, tensile and shear stresses, as well as failures. The excessive fluid pressure induced by leakage or hydraulic fracturing fluid acts as the drive for failures. The intensified tensile stress and shear stress occur at the crack tip initiate failures if they satisfy with the failure initiation criterion. Moreover, Lab and field scaled sensitivity analysis extract the influential parameters involved in failure development. Furthermore, the matching between failure patterns from numerical analysis and real field measurements using radioactive tracer-logs provides a comparison basis for model accuracy. Additionally, micro-annulus cemented systems are further analyzed by considering interface strength heterogeneity, anisotropic in situ stresses, wellbore inclination and

eccentricity. The proposed approach provides a tool for more accurate predictions of cement integrity in the subsurface conditions to quantify the risk of wellbore integrity issues.

CHAPTER 1. INTRODUCTION

The underground blowout (UGB) is in general characterized by a lack of pressure response on the annulus while pumping on the drill pipe or by a general lack of pressure response while pumping (Grace, et al, 1994). In UGBs, excessive pressure of formation fluid generates excessive stress on the wellbore, which could cause delamination along the interface of casing and cement (or cement and formation) in the weakest parts. This failure zone accommodates fluid transfer, especially for abnormal fluid with excessive pressure (Barnhill and Adams, 1979). At this stage if fluid pressure is large, the failure zone may develop further upward. This propagation will continue until the failure zone reaches to surface along the casing or the fluid finds an escape path to upper zones or the surface. Most commonly, the underground blowouts are not identified, as they do not show considerable evidence on the ground due to limited failure (Grace, 2003); but under certain circumstances, the failure could become progressive and cause catastrophic damages not only to production but to the surface facility and personnel. The catastrophic damage of UGB is especially serious when a crater develops. Large rigs and platforms have been lost in craters with no sign of the rig remaining at the surface. There is a large probability of severe environmental damage. Losses can reach hundreds of millions of dollars.

Underground blowouts can occur during drilling or production of the wells (Branhill and Adams, 1979, Flak, et al, 1995, Ing. Rudi Rubiandini, et al, 2008, Roohi, et al, 2009, and Ferrara, et al, 2011). There are some examples of UGB formed during kill procedures in regular blowouts (Leraand, et al, 1992 and Strickler, et al, 2006) or completion of adjacent wells (Flak, et al, 1995). There is a strong belief that UGB is more common in the latter case because of potential corrosion induced by casing leaks in older completions. UGBs in the production stage range from being indiscernible to catastrophic. An underground blowout can result in minor continuous transfer of fluids to shallower zones or in flow which reaches the seafloor or ground surface (Smith, et al, 1997). Compared to other kinds of blowouts, the unrecognized or unreported characteristics give underground blowouts an infrequently detected occurrence in the oil industry, which is manifested by the data set provided by SINTEF Offshore Blowout

Database (SOBD). Figure 1.1 shows blowout and well release frequencies for offshore operations in the North Sea in different operational phases. Based on Figure 1.1, underground blowout frequencies are much lower than other forms of blowouts, which could be due to the limited detection of underground blowouts. The Bureau of Ocean Energy Management, Regulation and Enforcement (BOEMRE) posted Outer Continental Shelf (OCS) in the Gulf of Mexico (GoM) and Pacific Region (PAC) Losses of Well Control from 2006 to 2010, shown in Table 1.1 and Figure 1.2. In the last five years, the number of underground flow events is 2, which accounts for 7.41% of the reported well control events. According to the data shown, the frequencies of underground blowouts are significantly lower than conventional blowouts. However, this may be due to the difficult detection of underground blowouts. Some important hidden conditions in the UGBs include but are not limited to: influx volume, fluid composition, unreliable descriptions of the conditions of the wellbore and tubular. These make it difficult to recognize and diagnose UGBs speedily and make it nearly impossible to control them in a timely fashion to avoid serious problems.

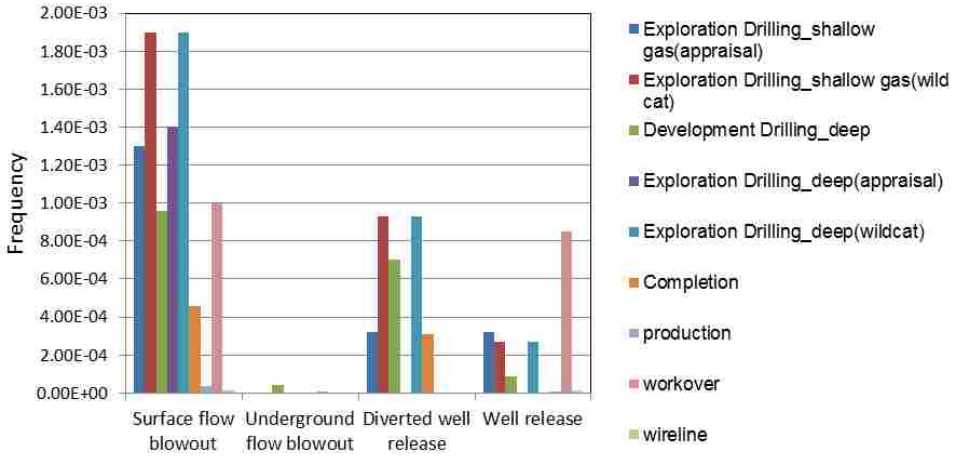

Figure 1.1 Blowout and well release frequencies for offshore operations in North Sea (SINTEF).

There are several techniques, such as temperature logging, traditional sonic logging (the combination of cement bond logs and variable density logs), and ultrasonic logging used to identify UGBs (Curtis, et al, 1979, Nagy, 1992, Ipek, et al, 1999 and 2002, and Le Guen, et al, 2009). Temperature logging is

conventionally used to detect the early leaking of UGBs by locating fluid flow in the casing or in the annulus surrounding the casing. It is used to identify entry and exit points of underground blowouts by considering the transient radial heat transfer relationship inside the well (Ipek, et al, 2002). The flow rate can be estimated using temperature logs (Curtis, et al, 1979). However in general, early detection of UGBs remains a challenging problem. Sonic logging and ultrasonic logging are used to identify fluid types based on the thresholds set for acoustic impedance boundaries between different materials. Moreover, ultrasonic logging provides advanced cement integrity evaluation by 360 ° scan of the casing-to-cement bond at a broadband frequency ranging from 250 to 700 kHz (Le Guen et al. 2009). Furthermore, ultrasonic logging is more advanced than sonic longing by extracting required parameters for cohesive models, such as the casing-to-cement bond strength, in a more reliable range due to high sensitivity of ultrasonic reflection coefficient of a material interface to imperfections (Nagy, 1992). However, new ultra sonic technology can only give post failure measurements without predictive capability.

Table 1.1 OCS and PAC Losses of Well Control: 2006-2010 (BOEMRE, 2010)
(Note: Gulf of Mexico (GOM) Region, Pacific (PAC) Region)

Loss of Well Control	2006		2007		2008		2009		2010		Sum
	GOM	PAC	GOM	PAC	GOM	PAC	GOM	PAC	GOM	PAC	
Flow Underground	0	0	1	0	1	0	0	0	0	0	2
Flow Surface	0	0	3	0	3	0	2	0	1	0	9
Diverter Flow	0	0	0	0	1	0	0	0	0	0	1
Surface Equipment Failure	2	0	3	0	3	0	4	0	3	0	15
LOSS OF WELL CONTROL (TOTALS)	2	0	7	0	8	0	6	0	4	0	27

The consequences of underground blowouts are frequently disastrous and extremely expensive. These include: pollution to the environment, reservoir depletion and hydrocarbon reserve losses, damage or abandonment of the well, water coning (in bottom-water reservoirs), safety risks due to the uncontrolled flow of dangerous (flammable and potentially toxic) formation fluids (gas, oil, salt water and /or hydrogen sulfide), large financial losses and injury and death of personnel (Nesheli, et al, 2006). Moreover, compared to other kinds of blowouts, the underground blowouts can be the most difficult, dangerous, and destructive situation in well control (Grace, 2003; Barnhill and Adams, 1979). Remedies to UGBs include relief wells (Leraand, et al, 1992 and Flak, et al, 1995), dynamic methods (Gillespie, et al, 1990), injectable pressure-activated sealant technology (Rusch, et al, 2004), and the application of novel lost-circulation material squeeze systems (Sweatman, et al, 1997).

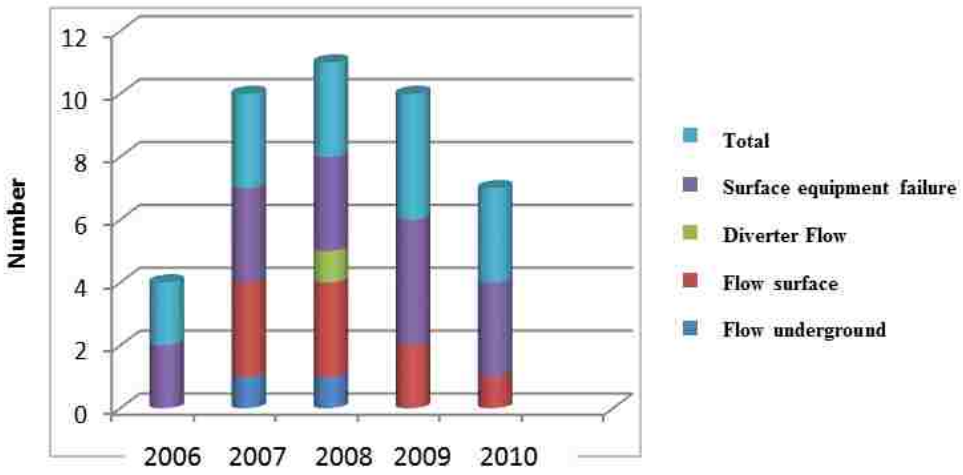

Figure 1.2 OCS Losses of Well Control: 2006-2010 (BOEMRE, 2010).

UGBs are also not limited to specific types of formations or reservoirs. They are not restricted by depth and may occur in shallow or deep reservoirs; however, shallow gas leakage is the most common manifestation of underground blowouts. Shallow gas blowouts have been notorious as one of the worst problems in the oil and gas industry. Drilling surveys for the periond between 1971 and 1991 for the outer continental shelf of the Gulf of Mexico, pointed out that one well out of every 359 drilled had experienced a shallow gas blowout. Shallow gas blowouts reached a dramatic percentile of 67% of

blowouts occuring in that area (Danenberger, et al, 1993). Sstatistics for different parts of the world show a similar fraction of events related to UGBs. The main reason for the occurance of shallow gas blowouts is generally the short casing string configurations and low formation strength, especially in unconsolidated formations (shallow GOM) existing near the well surface, which favor easy upward fluid migration through failure zones or intact high permeabilty zones. In cases occurring in depths less than 3,000 to 4,000 feet of the surface, the potential to form craters can be extremely high (Santos Rocha, 1993). Cratering happens because the excessive fluid pressure reduces the effective stress in shallow zones to a very small value, so rock behaves like a fluidin a process called "liquifaction". It can be most destructive when the crater is under a rig or platform. When a crater occurs, the consequences can be catastrophic. Large rigs and platforms have been lost in craters with no sign of the rig remaining at the surface. The chance of environmental disaster can be huge. Losses can reach hundreds of millions of dollars. Two typical extreme cases of cratering accidents occurred in the Main Pass 299 (U.S Gulf of Mexico) and in the Cabinda Field (Angola) (Santos Rocha, 1993). In both incidents, the jack up rigs sank into the huge crater that was formed on the sea floor by upward flowing gas. An example of a crater which occurred in an onshore well is shown in Figure 1.3. It shows that the rig and the related equipment sank in the huge crater. Shallow UGBs in offshore operations can be even more dangerous for several

Figure 1.3 Example of onshore underground blowout (Walter, et al, 1991)

reasons. First, there are more constraints on the quick evacuation of rig personnel. If the flow fractures to the sea floor, the only safe egress from the well site is by helicopter because when the sea is gasified,

seawater density drops and boats lose their buoyancy, as do life preservers. Second, sediments are very young, and the flow is more likely to surface immediately beneath the rig (Grace, 2003).

This dissertation examines the mechanisms of numerous actual underground blowouts. Finite element techniques are used to analyze the blowouts from the geomechanical perspective. Because cement sheath failures have been recognized as the main causes of upward fluid migration, the analyses of the effect of cement sheath integrity on underground blowout are specifically analyzed. At the first stage, an axisymmetric poroelastic finite element model with pre-inserted cohesive interfaces is utilized to predict the initiation of a failure zone and possible broaching of the failed zone along the wellbore. This model is used to check wellbore integrity by considering the parameter property sensitivity, the heterogeneity, and the interactive effects of different interfaces nearby the wellbore. However, this axisymmetric model cannot correctly predict the non-planar failure patterns caused by porous heterogeneous microstructures of cement and formation. These effects make failures around the wellbore complex. Other complicating effects include anisotropic stresses effects, inclination angle, and wellbore eccentricity. Hence, a practical three dimensional model is applied to further reflect and analyze the real situation of wellbore integrity. The spatial propagation of cement sheath failures and failure patterns and rates are further analyzed under different wellbore conditions.

Research Objectives

The proposed research aims to model the integrity between casing, cement and rock to provide a better understanding of the physical phenomena behind initiation and development of underground blowouts. Through numerical mechanistic models, different mechanisms involved in different stages of UGB developments will be introduced and compared. Followings are the outline of the objectives pursued in this dissertation:

1. Model the initiation of cement failure (disintegration) in deep parts of the wellbore
    a. Build a coupled deformation-fluid flow finite element model to simulate deep bottom-hole environment. This model incorporates overburden stress, in-situ tectonic stresses and stresses

induced due to pore pressure changes. Failure initiation is predicted based on nonlinear traction separation law.

b. Build an algorithm to consider pre- and dynamically inserted cohesive elements along the original element edges near the wellbore zone to avoid any dependency of failure development geometry on pre-defined paths and avoiding extra computational effort by removing unnecessary cohesive elements.

c. Model the cement-casing interface using cohesive elements mainly based on non-linear traction separation law. However, other models for failure initiation will also be tested and compared. The appropriate range for cohesive elements parameters will be investigated using cement bond logs data (sonic and ultrasonic). The fluid flow through the failure induced openings is incorporated in the model.

d. Investigate the role of cement flaws and heterogeneities on annular and radial fracture initiation.

e. Assess the effect of buildup pressure in the bottom-hole area due to quick shut down or top kill procedures on the wellbore integrity in highly over pressurized formations.

f. Investigate the effect of rock heterogeneity near the wellbore on the wellbore integrity.

2. Conduct field scale sensitivity tests to select the dominant factors on fracture containment

   a. Cement rigidness

   b. Normal and shear strength

   c. Critical energy

   d. Young's modulus ratio of cement to formation

3. Predict failure and explore the mechanism in various wellbore conditions

   a. Heterogeneous cement properties

   b. Anisotropic in-situ stress

   c. Wellbore Inclination

d. Wellbore eccentricity

4. Check wellbore integrity influenced by Hydraulic Channelization

   a. Build a field-scale three-dimensional poroelastic model to predict transverse fractures, longitudinal fractures, annulus failures and their competition.

   b. Predict the failure patterns shown in ultrasonic cement bond log image.

   c. Match failure patterns from numerical analysis and real field radioactive tracer-logs, which provide a benchmark for the model accuracy.

   d. Analyze the wellbore integrity under the fluid invasion.

   e. Assess wellbore isolation between perforation zones in vertical, horizontal and inclined wells.

   f. Evaluate the effect of property heterogeneity on failure patterns.

      (i) Fully random distribution of properties and effect of its statistics like variance on failure emergence. Is it easier or harder situation for failure?

      (ii) Could channelization or early time flow at the cement change failure geometry?

References

Barnhill, C. C., and Adams N. J., 1979, Underground Blowouts in Deep Well Drilling, SPE 7855, SPE Deep Drilling and Production Symposium, Amarillo, Texas, 1-3 April 1979.

Berger, A., Fleckenstein, W. W., Eustes, A. W., and Thonhauser, G., 2004, Effect of Eccentricity, Voids, Cement Channels, and Pore Pressure Decline on Collapse Resistance of Casing, SPE 90045, SPE Annual Technical Conference and Exhibition, Houston, Texas, 26-29, September 2004.

BOEMRE, 2010, The Alaska Outer Continental Shelf (OCS) Region of the Bereau of Ocean Energy management, Regulation and Enforcement, http://boemre.gov/incidents/blowouts.htm.

Curtis, M. R., and Witterholt, E. J., 1973, Use of Temperature Log for Determining Flow Rates in Producing Wells, SPE 4637, Offshore Technology Conference, Houston, Texas, 2-5 May 1983.

Ferrara, P., Molaschi, C., Oppelt, J., Buda, R., Amicosante, M., and Grimmer, H., 2011, Downhole Isolation Packers for Drilling Operations: Field Experiences, SPE 147033-MS, SPE Annual Technical Conference and Exhibition, Denver, Colorado, 30 October-2 November 2011.

Flak, P. E., Larry, H., Muhanna, G. A., and Al-Qassab, M., 1995, Case History: Relief Well Control of Underground Blowout in Bahrain. SPE 29859-MS, Middle East Oil Show, Bahrain, 11-14 March 1995.

Gillespie, J. D., Morgan, R. F., and Perkins, T. K., 1990, Study of the Potential for an Off-Bottom Dynamic Kill of a Gas Well Having an Underground Blowout, SPE 17254-PA, SPE Drilling Engineering, Vol. 5 (3), pp: 215-219.

Grace, R. D., 1994, Analyzing and Understanding the Underground Blowout, IADC/SPE 27501, SPE/IADC Drilling Conference, Dallas, Texas, 15-18 February 1994.

Grace, R. D., 2003, Blowout and Well Control Handbook, ISBN 10: 0-7506-7708-2.

Ing. Rudi Rubiandini, R. S., 2008, Dynamic Killing Parameters Design in Underground Blowout Well, SPE 115287-MS, IADC/SPE Asia Pacific Drilling Technology Conference and Exhibition, Jakarta, Indonesia, 25-27 August 2008.

Ipek, G, 1999, Estimation of Underground Blowout Using Temperature logs, M.S. Thesis, LSU, 1999.

Ipek, G., Smith, J. R., and Bassiouni, Z., 2002, Estimation of Underground Blowout Magnitude Using Temperature Logs, SPE 77476-MS, SPE Annual Technical Conference and Exhibition, San Antonio, Texas, 29 September-2 October 2002.

Le Guen, Y., Le Gouevec, J., Chammas, R., Gerard, B., and Poupard, O., Oxand S. A., Van Der Beken, A., and Jammes, L., 2009, CO2 Storage: Managing the Risk Associated With Well Leakage Over Long Time Scales, SPE 116424-PA, SPE Projects, Facilities & Construction, Vol. 3, pp: 87-96.

Leraand, F., Wright, J. W., Zachary, M. B., and Thompson, B. G., 1992, Relief-Well Planning and Drilling for a North Sea Underground Blowout, SPE 20420-PA, Journal of Petroleum Technology, Vol. 44(3), pp: 266-273.

Nagy, P. B., 1992, Ultrasonic Classification of Imperfect Interfaces, Journal of Nondestructive Evaluation, Vol. 11, Nos. ¾, 1992.

Nesheli, B. A., and Schubert, J. J., 2006, Effect of Water Depth on Bridging Tendencies in Ultradeepwater Blowouts in Gulf of Mexico, SPE 103139-MS, SPE Annual Technical Conference and Exhibition, San Antonio, Texas, 24-27 September 2006.

Roohi, A., Bahmani, H., and Makvandi, M., 2009, Case History of Successful Underground Flow Control in Persian Gulf Field, SPE 13434-MS, International Petroleum Technology Conference, Doha, Qatar, 7-9 December 2009.

Rusch, D. W, Sabins, F., and Aslakson, J., 2004, Microannulus Leaks Repaired with Pressure-Activated Sealant, SPE 91399-MS, SPE Eastern Regional Meeting, Charleston, West Virginia, 15-17 September 2004.

Santos Rocha, L. A., and Bourgoyne, A. T., 1993, Identifying Crater Potential Improves Shallow Gas Kick Control, Oil and Gas Journal, 1993, pp: 93-97.

SINTEF Offshore Blowout Database, 2010. http://www.ogp.org.uk/pubs/434-02.pdf.

Smith, J. R., and Bourgoyne, A. T., 1997, Case History-Based Training for Control and Prevention of Underground Blowouts, 38605-MS, SPE Annual Technical Conference and Exhibition, San Antonio, Texas, 5-8 October 1997.

Strickler, R. D., Moore, D., and Solano, P., 2006, Simultaneous Dynamic Killing and Cementing of a Live Well, SPE 98440-MS, IADC/SPE Drilling Conference, Miami, Florida, 21-23 February 2006.

Sweatman, R. E., Kessler, C. W., and Hillier, J. M., 1997, New Solutions to Remedy Lost Circulation, Crossflows, and Underground Blowouts, SPE 37671-MS, SPE/IADC Drilling Conference, Amsterdam, Netherlands, 4-6 March 1997.

Walters, J. V., and Mij., B. V., 1991, Internal Blowouts, Cratering, Casing Setting Depths, and the Location of Subsurface Safety Valves, SPE 20909-PA, SPE Drilling Engineering, Vol. 6(4), pp: 285-292.

Zhai, Z., Abou-Sayed, A., 2011, Fully Coupled Chemical-Thermal-Poro-Mechanical Effect on Borehole Stability, SPE140946-MS, Brasil Offshore, Macaé, Brazil, 14-17 June 2011.

CHAPTER 2. DEVELOPMENT OF DELAMINATION FRACTURES AROUND CASING AND ITS STABILITY

Abstract

Casing support and zonal isolation are principal objectives in cementing the wells; however the later objective always raises the most concern particularly when there is a potential for formation fluid migration into the cement sheath. Wellbore integrity is highly dependent upon the integrity of the interfacial bond between the cement and the formation as well as the bonding between casing and cement. A closer look at the common cement strength test data, performed routinely in the labs, reveals complicated behavior that cannot be simply modeled using a single parameter (i.e. the interfacial strength).In this work we used a cohesive interface constitutive equation to model the behavior of cement interfaces. Comprehensive analysis of microannulus formation is presented by utilizing an axisymmetric poroelastic finite element model enriched with cohesive interfaces to simulate initiation of the failure zone and possible broaching of the failure zone along the wellbore to shallower zones. Using this model, we demonstrated that it is possible to use data from routine tests, such as the push-out test, to determine not only the shear strength but also normal fracture energy and the stiffness of the cement-formation interface. Cohesive interface properties are calibrated such that simulated test results match with the measured response of the specimens. In the next step, we used these parameters to anticipate well-cement behavior for the field-scale problem. A sensitivity analysis is provided at the end of the part to show the role of each parameter in initiation and development of the failure zone. Interestingly, the shear strength, which is commonly measured from push-out tests are not the only parameter determining the size of the fracture. Other parameters derived in this approach such as normal strength show equal influence on initiation and propagation of the failure zone. The proposed approach provides a tool for a more accurate prediction of cement integrity in the subsurface conditions to quantify the risk of wellbore integrity issues.

Introduction

Cement is used to support the casing and also provide hydraulic isolation of various formations penetrated by the wellbore, accordingly preventing fluid flow from high- pressure to low pressure zones. Cement also protects casing from corrosion by chemically aggressive brines. The quality and integrity of a cement job can determine how long a well remains stable and productive without requiring repair. The cement sheath failures and nearby wellbore failures may lead to upward flow of formation fluid, which has significantly adverse consequences on wellbore integrity. Field and laboratory experiments have revealed two types of mechanisms responsible for the loss of cement sheath integrity: mechanical degradation (Goodwin and Crook, 1992) and chemical degradation (Kutchko et al., 2007). For instance wet or dissolved CO2 form a corrosive fluid to induce chemical degradation in cements. Degradation-kinetics data show that chemical degradation is controlled by fluid diffusion rate, so it may not be very fast until leakage pathways already exist due to mechanical degradation (van der Kuip et al. 2011). As a consequence, it is crucial to understand mechanisms lead to mechanical degradation before chemical degradation occur (Bois et al. 2012). In this chapter, we mainly focused on mechanical degradation mechanisms.

Nowadays, environmental protection is a greater concern than ever, especially protection of shallow aquifers during and after drilling. Therefore, understanding the formation of liquid movement paths has become an important step to achieve long-term mechanical durability of a cement sheath exposed to different conditions during the well life. It is notable that liquid movement does not usually occur around the wellbore uniformly. Due to the inherent heterogeneity of rock and cement, fluid flow around the casing tend to limit itself to a number of routes, which leads to a higher fluid flow velocity and consequently larger fluid drag forces on cement particles. Larger drag forces may move cement and rock particles easier and provide a preferential path for fluid to flow. These paths, so called channels, may further fracture the rock to form small cracks. The integrity of the cement sheath could be undermined as a result of these annular cracks development (Goodwin and Crook, 1992, and Garnier, et al., 2010). The

creation and the deteriorating impact of these fractures are controlled by several factors initiated from cement composition, the cement curing process, thermal stresses, hydraulic stress, compaction, wellbore tubular, and downhole environment (Jutten et al. 1989, Berger et al. 2004, Bour, 2005, Saidin et al. 2008).

The cement sheath failures have been recognized as the main cause responsible for upward fluid migration. Considering the very low permeability of cements, the fluid seeps around the casing mainly via cracks and micro-annulus channels in the cement (Saidin, et al. 2008). Parcevaux and Sault (1984) have listed potential factors for cement-casing and cement-rock bonding, including poor mud removal, the condition of the formation surface before slurry placement, chemical interaction at the cement-to-formation interface, and the environmental formation, each of these aspects have received special attention in the literature (for instance Jutten, et al. 1989, Ladva et al. 2005, Ma, et al. 2007, and Saidin, et al. 2008). Cement sheath failure, in general, can be classified into four major categories: a) radial cracking, b) plastic deformation in cement, c) circumferential cracking due to the loss of bonds between cement and casing interfaces, so called debonding; and d) incomplete cement sheath, all cases are illustrated in Figure 2.1. Incomplete cement sheath indicates partially cemented and no cement sheath.

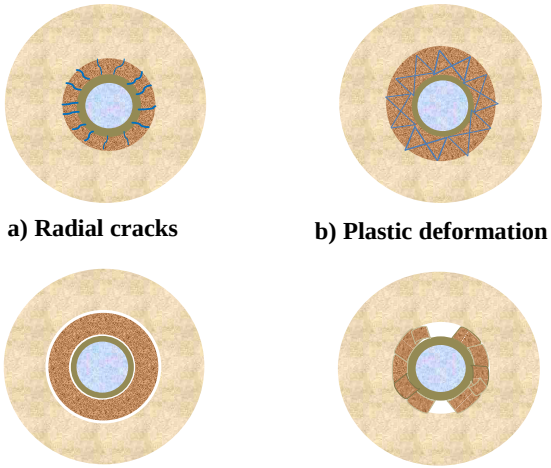

Figure 2.1 Potential mechanisms for fluid migration outside the casing are demonstrated. Casing is shown in dark beige, cement sheath in yellowish brown, formation in tan, cracks in blue, and debonding or incomplete cementing in white.

Debonding may exist in two forms: debonding at the casing-cement interface and debonding at cement and formation rock interface. Some hydraulic mechanisms may expedite the damage. For instance, high cement permeability and porosity may cause the inner shrinkage of cement, which provide a considerable amount of empty volume. Hydration and chemical shrinkage may accommodate debonding, channeling or plastic deformation of cement. The invasion of the empty space formed during shrinkage by highly mobile fluid (gas) and its upward percolation creates channels. This phenomenon is more frequent during "cement setting" (Parcevaux, 1984). High pressure and temperature cycles are other influential factors for cement sheath integrity (Jackson and Murphey, 1993, and Bour, 2005). Fortunately, the chemical and geomechanical properties of cement sheaths can be improved and optimized by suitable design to minimize fluid migration (Tahmourpour et al. 2008). Moreover, the loss of cement-sheath integrity depends not only on cement properties but also on the wellbore architecture and well history (Bois, et al. 2011).

Several testing methods have been designed in the last couple of decades to measure cement normal and shear bond strength in the lab (Ma, et al. 2007). Cement- interface bonding strengths, in general, are a function of cement slurry composition, formation properties, which are roughly measured with cement bond log (CBL) by utilizing CBL attenuation rate and acoustic impedance of the cement in combine with empirical correlations, also similar relationships exist between compressive strength and acoustic wave velocity (Jutten, et al. 1989). Temperature changes and pressure variations are recognized as the main driving forces for initiating interface delamination from impurities (Griffith et al. 2004, and Ladva et al. 2005).

Despite recent advances in inventing new variety of cements and additives to address fluid migration issues and considering tremendous economic loss and environmental hazards initiated because of the subterranean fluid migration, a comprehensive understanding of the whole process of casing–cement delamination or cement–formation-rock delamination is still missing. The complex nature of this multiphysics phenomenon on one side and the inherent indeterminacy of in-situ properties such as cement

properties including permeability, porosity, shrinkage ability, adherence, cement heterogeneity and so on make this problem very complicated. However, economic and environmental sensitivity of this issue keeps research on cement-casing and cement-rock bonding popular during the past 30 years.

Due to the complicated nature of the fluid migration problem, analyses were mainly qualitative and the models presented in the literature simply ignore stress redistribution due to presence of delamination fractures along the interfaces, and particularly disregarding the likelihood of failure propagation. Earlier models were mainly based on linear elasticity and failure analysis was based on the unconfined compressive strength of cement and its tensile strength (for instance, Thiercelin et al. 1998). These models only predict the onset of failure in plane strain geometry, and poroelastic effects of rock are also ignored. Hence, other models (Fleckenstein, et al. 2000, Ravi et al. 2007 and Gray et al. 2009) developed to utilize more sophisticated constitutive laws to model elastoplastic behavior of cement based on Mohr-type criteria. Nabipour, et al. (2010) used von Mises criterion to simulate cement failure in the downhole environment. Their model was still continuous and could not consider formations of cracks i.e. the cement is assumed to be fully bonded to the casing and formation. In continuous models, no debonding was allowed even if stresses exceed cement-casing or cement-formation bond strengths. Further experimental studies like shear tests revealed a much complicated relationship between loading force and cement interface deformation that cannot be described by a constant, so called shear or tensile strength (Lavda et al. 2005). However, the problem of failure along two materials interface is not limited to the cement casing problem, similar problem exist in different engineering disciplines from electronic chips manufacturing to aerospace industry. In this chapter, we try to utilize one of the techniques developed originally for interfacial failure in microchips and concrete for the cement sheath failure problem.

Following advances of interfacial measurement techniques for nondestructive tests, sophisticated constitutive models have been developed to predict the behavior of different materials interfaces, which have provided deeper understanding of physics behind delamination cracks in electronic chips in small scale and aeronautics in large scale (Hutchinson, et al. 1990, and He et al. 1994). Cohesive interface

models or cohesive zone models are a series of techniques developed to describe crack initiation and its growth without any presumption of the initial crack size or location (Yang and Chen, 2004) along the interface of different materials. The cohesive interface model has found a wide range of applications especially in the problems involving non-linear fracture mechanics (Petersson, 1981, and Kanninen and Popelar 1985). Over the past fifty years, the cohesive interface model has gradually drawn people's attention because it is easy to combine with other material and geometric nonlinearities and allows for efficient implementations in a finite element setting by realistically representing the energy dissipation during the fracture process. Cohesive interface model theory was developed from experimental observation results in Dugdale (1960). Cohesive interface models were developed originally for ductile materials (Dugdale, 1960, and Barenblatt, 1962). Later, the cohesive zone approach was extended by Hillerborg et al. (1976) and Needleman et al. (1990) to model an initial crack-like flaw, where a crack is not present or a crack is not associated with a non-vanishing energy release rate. Due to the nonlinear nature of these problems, numerical techniques to implement these constitutive models developed in parallel. Different cohesive element models have been utilized so far in different problems and in different scales (Needleman, 1990, and Camacho and Ortiz, 1996, and Yang, et al. 2008 and 2009). Based on these papers, an appealing feature of this approach is that it does not need to designate a particular type of constitutive response in the bulk of the material, the extent of crack growth, or the size of the plastic zone. Moreover, complex crack propagation paths have been modeled by dynamically inserting cohesive elements (Camacho and Ortiz, 1996, and Pandolfi and Ortiz, 2002). The dynamic embedding cohesive elements method has become more and more popular because of its ability to represent the different and complex geometries of the correct path, and also saving in the computational costs. In the fully cemented annulus, cement interfaces may act as a weak path for failure initiation and further propagation. To incorporate the potential facilitating role of cement sheath interfaces into the analysis of wellbore integrity, cohesive interfaces with coupled fluid flow could be a good candidate to simulate mechanical integrity and hydraulic conductivity of the cement sheath.

In the meanwhile along the line of the deterministic approach, cohesive interface models have been introduced to study heterogeneous and indeterministic aspects of local failure by randomly spreading embedded cohesive interface elements in the potential failure zone (Yang and Xu, 2008, and Yang, et al. 2009). These two papers showed that the combined application of the cohesive interface model and stochastic methods may address modeling difficulties for macroscopic discrete fractures simulation and failure prediction of complex structure fracture systems involving multiple length scale as well as uncertainties.

There are few examples of using cohesive interface method in the oil and gas literature to predict rock failure in hydraulic fracturing (Salehi and Nygaard, 2011, and Hsu et al. 2012), but no attempt has been made to use this method to model well integrity problems. Development of new measurement tools such as azimuthal sonic and ultrasonic measurements provides an opportunity to extract required parameters for cohesive models in a more reliable range. For instance, the in situ cement integrity can be assessed by ultrasonic logging tools (ULTs). ULTs provide advanced cement integrity evaluation by 360 ° scan of the casing-to-cement bond at a broadband frequency ranging from 250 to 700 kHz (Le Guen et al. 2009). Gas, liquid or cement can be identified based on the thresholds set for acoustic impedance boundaries between different materials. Additionally, imperfections and interface properties may also be assessed effectively by the ULTs due to high sensitivity of ultrasonic reflection coefficient of a material interface to imperfections (Nagy, 1992). Choosing reliable interface parameters is the first step for establishing cohesive interface models to track the wellbore integrity, which became conceivable via new azimuthal measurement tools.

Development of new measurement technologies such as CBM, ULT on one side (Boyd, et al, 2006 and Jiang, et al, 2012) and more sophisticated constitutive models to predict the behavior of different materials interfaces on the other hand, provide more opportunities to apply more a sophisticated model to gain deeper understanding of the physics behind fluid migration behind the casing. In this chapter,

initiation of the failure zone is modeled using an axisymmetric poroelastic finite element model, which is enriched with cohesive interfaces to model cement interfaces.

In the next section, we provide the list of equations governing fluid flow and rock deformation. Then, we discuss the theory of cohesive zone interfaces. This is followed with numerical examples on initiation and development of cement sheath failure in the lab scale and field scale. Some sensitivity analyses have been performed to show the role of each parameter in the cohesive zone model.

Governing Equations

The compatibility and consistency of laboratory measurements of poroelastic parameters of cements have proved that cement should be considered as a porous material (Ulm et al. 2004, Ghabezloo et al. 2008) for modeling purposes. We still assume rock as a continuum medium, but discontinuity may occur only due to failure. In continuum mechanics, we can imagine a representative elementary volume (REV) around any mathematical point considered in the domain always contains both solid and the fluid phase, and classical microscopic mass balance laws of continuum mechanics hold for each phase. In a fluid saturated medium, the pore fluid-flow and deformations are coupled. The classical Biot (1941) theory of poroelasticity considers explicit coupling between the elastic response of the solid skeleton of the rock and the pressure of diffusing viscous fluid filled the pore space (Wang, et al. 2000). The poroelastic media deformation differs from the quasi-static deformations of solids as a time dependent diffusion is introduced in time-independent elasticity equations.

At this stage, we ignore any plastic deformation of rock or cement and considered rock as a linear elastic isotropic medium. Therefore, we can use linear poroelasticity equations to relate stresses and strains (Wang, et al. 2000)

$$2G e_{ij} = S_{ij} - \nu S_{kk}\,\delta_{ij} + \alpha(1-2\nu)\delta_{ij}\,p + 2\beta\,\delta_{ij}\,T \quad , \qquad (\mathbf{2.1})$$

$$2G\zeta = \alpha(1-2\nu)\,S_{kk} + \frac{\alpha^2(1-2\nu)^2}{\nu_u - \nu}\,p - 2G\,\beta_f\,T \quad , \qquad (\mathbf{2.2})$$

where G, υ, α are shear modulus, Poisson's ratio and Biot's constant of the rock, respectively. Other parameters are explained in the nomenclature section at the end of the chapter.

A part of the migrated fluid is lost to the formation; the other part is migrating along the conduits provided by debonded cements. Mass conservation should be locally satisfied in the formation

$$\frac{\partial \varsigma}{\partial t} + q_{i,j} = 0 \ , \qquad \textbf{(2.3)}$$

where ς denotes the change of fluid content and q denotes the fluid flux. The next equation to be satisfied is force equilibrium. The three equilibrium equations are written in compact notation as

$$S_{ij,j} = 0 \ , \qquad \textbf{(2.4)}$$

where S_{xx} , S_{yy} , and S_{zz} are normal stress, which are those for which the force is parallel to the normal to the face. S_{xy} , S_{xz} , and S_{yz} are shear components of the stress tensor.

Regardless of the cement system, gas and liquid can migrate at the cement/formation or cement/casing interface if a microannulus has developed, or along paths of weakness, where the bond strength is over-passed. We assumed laminar fluid flow in the formation and also laminar flow inside induced delamination cracks, so we can use Darcy's Law

$$q_i = -\frac{k_{ij}}{\mu} \nabla p_j \ . \qquad \textbf{(2.5)}$$

Here k is the permeability tensor, μ is dynamic fluid viscosity; and ∇P is the gradient vector of fluid pressure, and q is the fluid velocity.

Migrating fluid is most of the time traveling from depths with higher temperature. The resultant heat transfer is expected to induce thermal stress along the migration paths. The equation governing thermal energy transfer,

$$\rho C_v \frac{\partial T}{\partial t} = -\left(\rho_f C_v\, q\right).\nabla T + \nabla \cdot \left(-\lambda \nabla T\right), \qquad \textbf{(2.6)}$$

where ρ, ρ_f, T and t are rock density, fluid density, temperature and time, respectively, C_v and λ are average heat capacity and average heat conductivity of the fully saturated rock, respectively. The first term in the right hand side corresponds to thermal convection and second term corresponds to heat conduction, and the third term relates to the outside heat.

Theory of Cohesive Interfaces

The criteria for fracture propagation are basically based on the energy release rate approach, which states that a fracture propagates when the stress intensity factor at the tip exceed rock toughness. For inherent nonlinear nature of interfacial cracks, the most robust criterion is described by the constitutive model of the cohesive zone (Barenblatt 1962; Hilerborg et al. 1976). In the cohesive crack approach, the fracture processing zone is modeled by a cohesive crack of zero width with traction transferring capacity. The energy dissipation with the fracture processing zone is taken into account through the traction crack opening displacement constitutive model (Xie, et al. 1995a). The cohesive interface starts to open when the tractions applied to the interface reach a critical point, which is described by traction separation law (Tvergaard and Hutchinson, 1996).

Traction separation law is the basic theory for description of damage initiation and its propagation. One of the advantages of this criterion over similar ones is its flexibility to tune the parameters to incorporate the behavior of different fracture mechanisms. For instance, different materials show different bridging properties across the fracture tips, which could be quantified from lab measurements. Some relatively simple bridging laws often used in analyses are (a)constant traction for perfect plasticity (Dugdale et al, 1960); (b) smooth nonlinear (Cox and Marshall,1991); (c) trapezoidal behavior (Sorensen, et al., 2003); (d) bilinear or triangular (Davila, et al, 2001) . In any case, the maximum stress σ_0 and the critical displacement δ_c are the two most important parameters to characterize traction-separation relations.

Different experimental studies have shown that bilinear or triangular traction separation law is suitable for fracture analysis in cementitious materials (Hillerborg, et al. 1976, Gerstle and Xie, 1992, Li, and Liang, 1994, Davila, et al. 2001). Typical bilinear softening curves for $t_n - \delta_n$ and $t_s - \delta_s$ are illustrated in Figure 2.2a and b, respectively. Damage initiation refers to the beginning of stiffness degradation of the response of a material point where tractions in the failure planes reach their peak values in the interface, represented by t_{n0} and t_{s0} in Figure 2.2. The t_{n0} and t_{s0} are traction at the inset of damage initiation when the formation is either purely normal to the interface or purely in shear direction, respectively. The general mixed mode condition will be discussed later. The initial tensile stiffness, K_{n0}, before the tensile strength t_{n0} is reached should be high as it represents the un-cracked rock. Too high initial tensile stiffness is not favorable as it may cause sudden instable failure, i.e. brittle failure. The initial shear stiffness K_{s0} is also representing the situation before the shear strength t_{s0} is reached. K_{n0} and K_{s0} can be determined by a trial and error approach. If δ_n is negative during loading increments or numerical iterations, a compressive stiffness of magnitude equal to k_{n0} is assigned in order to prevent any unrealistic penetration of crack faces. δ_{nf} and δ_{sf} are the critical relative displacements when the tractions diminish i.e. the cohesive forces between crack faces are gone at this point.

Before normal and shear traction reaches t_{n0} and t_{s0}, a linear ascending branch is added in each softening curve to model the initially un-cracked material. After normal and shear traction reaches t_{n0} and t_{s0}, the tractions decrease monotonically as functions of the corresponding relative displacements of the crack surfaces (crack opening displacement δ_n and crack sliding displacement δ_s in 2D problems), which is often termed strain softening. The areas under the traction curves in Figure 2.2a and b represent, respectively, the mode-I fracture energy G_n and twice the mode-II fracture energy, G_s. Both G_n and G_s

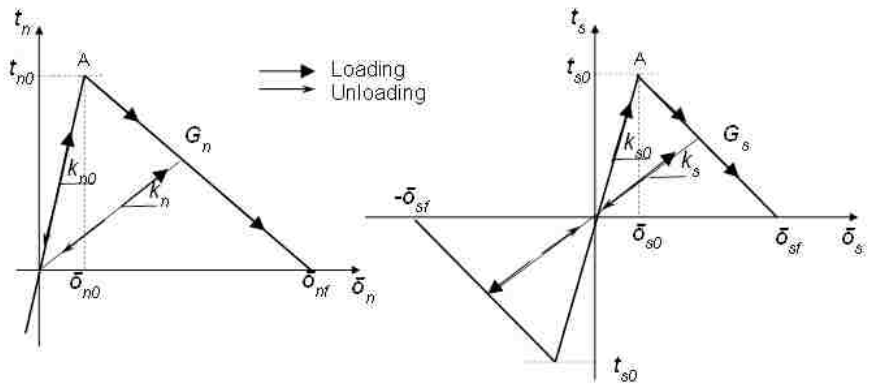

(a) t_n-δ_n curve in normal direction **(b) t_s-δ_s curve in normal direction**

Figure 2.2 Linear Softening law for a typical cohesive element.

are material properties. When fracture energy reaches G_n (or G_s) in mode-I (or mode-II), the fracture starts to propagate.

The interfacial delamination fractures between two dissimilar materials are commonly mixed modes Hutchinson, 1990, and Xie, et al. 1995b). For the mixed mode condition, quadratic nominal stress law is considered to predict damage initiation. Damage is assumed to be initiated when a quadratic interaction function involving nominal stress ratios (as defined below) reaches the value of one, i.e.

$$\left\{\frac{\langle t_n \rangle}{t_{n0}}\right\}^2 + \left\{\frac{t_s}{t_{s0}}\right\}^2 = 1 \qquad (\mathbf{2.7})$$

where t_n and t_s represent the real values of normal and tangential (shear) tractions across the interface, respectively. < > is the Macaulay bracket and

$$\langle t_n \rangle = \begin{cases} t_n, \ t_n \geq 0 & (tension) \\ 0, \ t_n < 0 & (compression) \end{cases} \qquad (\mathbf{2.8})$$

The resilient feature of this approach is that its formulation is based on the damage mechanics framework, within which the stiffness components k_s and k_n upon unloading and reloading are degraded as δ_s and δ_n increase, due to irreversibly progressive damage. The damage is characterized by

a scalar stiffness degradation index D representing the overall damage of the interface caused by all stress components. The stiffness degradation index is a function of the so-called effective relative displacements δ_m combining the effects of δ_s and δ_n i.e.

$$\delta_m = \sqrt{\langle \delta_n \rangle^2 + \delta_s{}^2} \quad , \tag{2.9}$$

where < > is again the Macaulay bracket. For the linear softening law discussed above, the damage evolves with the index

$$D = \frac{\delta_{mf}(\delta_{m,\max} - \delta_{m0})}{\delta_{m,\max}(\delta_{mf} - \delta_{m0})} \tag{2.10}$$

where $\delta_{m,\max}$ is the maximum effective relative displacement attained during the loading history. δ_{m0} and δ_{mf} are effective relative displacements corresponding to δ_{n0} and δ_{s0}, and δ_{nf} and δ_{sf} in Figure 2.2a and b, respectively.

Fracture propagation occurrence is closely related to energy. In traction separation law, the maximum stress σ_0 and the critical displacement δ_c are two important parameters to describe the traction separation relationship and energy dissipation process, which can be described by Equation 11 below (Nguyen, et al. 2011)

$$G = \int_0^{\delta_c} \sigma(\delta) d\delta \approx \sigma_0 \delta_c \tag{2.11}$$

When the energy in the fracture processing zone reaches to $\sigma_0 \delta_c$, crack starts to propagate. For different materials, σ_0 and δ_c have different values, which can be determined by lab measurements (Davila, et al. 2001).

Energy dissipation during the process of failure formation has a more complex behavior in the mixed mode condition. Benzeggagh-Kenane (BK) fracture criterion (Benzeggagh et al. 1996) is considered here to describe the mixed mode fracture propagation here. If G_T ($G_T = G_n + G_s + G_t$) defines the total energy in the mixed mode condition. G_n , G_s and G_t denote the work done by the tractions and their conjugate relative displacements in the normal, first and second shear directions, respectively. BK fracture criterion is defined as

$$G_n{}^C + (G_s{}^C - G_n{}^C)\left\{\frac{G_S}{G_T}\right\}^\eta = G^C, \qquad \textbf{(2.12)}$$

where $G_S = G_s + G_t$, $G_T = G_n + G_S$, and η are material properties can be measured in the rock mechanics lab.

Determination of Cohesive Parameters

The main challenge in using this model is measuring the cohesive model parameters in the lab or in the field. Cement to formation and pipe bonding has been a subject of discussion for a long time, but few papers have been published on this fundamental subject (Nelson, 1990). Carter and Evans (1964) presented two experimental setups to measure shear bond and hydraulic bond between casing and cement and one experimental setup to measure hydraulic bond between cement and rock formation. What they measured as the hydraulic bond is a mixed mode of shear and tensile cohesive energy. The following outlines a process for using finite element method to arrive at cohesive stiffness, strength and energy properties. Properties are calibrated such that simulated tests match the measured response of the specimens. Using pure mode test data to characterize cohesive behavior minimizes the number of cohesive properties that must be simultaneously determined. Fortunately, shear bond test is pure shear mode for the large extent of deformations, but unfortunately, no such a test has been developed to measure cement interface properties in pure normal mode.

Evan and Carter (1962) proposed the push-out test as a way to measure the shear bonding strength between cement and formation. A schematic picture of push-out tester is demonstrated in Figure 2.3. The center shale plug has a diameter of 25.4 mm and a nominal length of 20 mm. The shale core is being dragged slowly by a brass rod with a diameter of 20mm where the cell surrounding cement ring is constrained again any movement. A typical force versus displacement plot for this test is provided in this Evan and Carter's paper and is considered as the benchmark for our numerical tests.

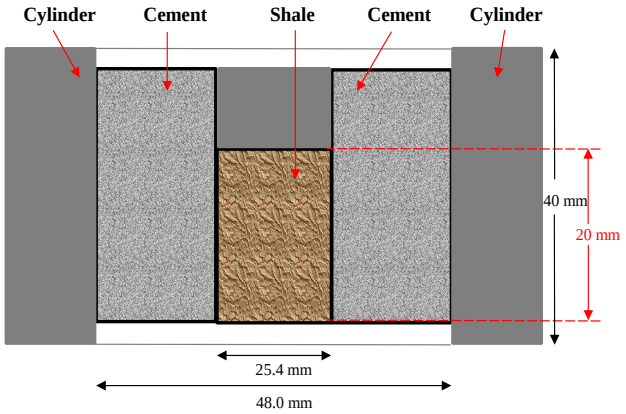

Figure 2.3 A schematic of the push-out tester.

In an attempt to characterize the failure damage mechanism between cement and formation, numerical simulation was made to estimate shear strength (peak and residual), and deformability (shear stiffness) of the interface. An axisymmetric finite element model is built in ABAQUS for this objective. The mechanical properties of cement and shale are listed in Table 2.2 and Table 2.3 of Appendix. In the process of pulling out, shear displacement was imposed by applying a constant velocity, v = 0.002 m/s, to the top part of the rock sample. The shear force applied to generate the constant velocity to the shale was monitored via a shear displacement relative to the cement. Confining pressure (normal stress) might be added at the outside of cement to simulate downhole condition.

Two types of traction separation laws were used to reproduce lab tests reported in Ladva's experiments (Figure 2.4): one is bilinear traction separation law and the other is BK form traction separation law. The interface parameters are listed in Table 2.1. The shear force vs. cement shear

displacement is shown in Figure 2.4. These two failure initiation criteria show identical linear behavior at the initial stage due to elastic deformation. The peak strength occurred at shear displacement around 2 mm, which is about 10% of the specimen's length. The observed sharp peak strength demonstrates an effective locking of the cement to the rock. Initial linear elastic response produced using bilinear and BK both agrees with the experimental results. Then peak strength is followed by a sharp softening process in

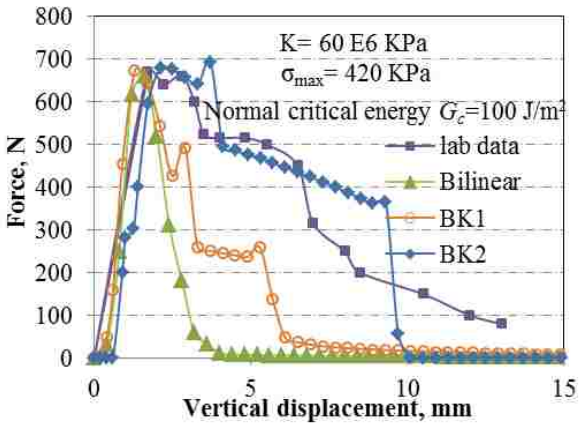

Figure 2.4 Comparison shear force with cement shear displacement in models with different traction separation law.

bilinear form, whereas, the peak stress-softening in BK form is followed by another two peaks and sharp softening processes, which is probably due to the change in loading mechanism from shear to tension cause by large deformations. The softening comes into play after reaching the peak strength. After these two softening stages, shear force decreases to zero (i.e. sample reaches to complete failure). The interface was finally sheared up to a total tangential displacement of 4 mm in the bilinear form but 7 mm in the BK form. It can be observed that compared with the bilinear model, the softening process of BK model shows better agreements with the experimental results. In the calibrated results produced by BK criterion, two softening stages are observed after reaching peak strength. The first soften strength is larger than the second one. The second softening and stabilization process is significantly wider than the first one. At the same time, more numerical investigations have also proved that the second softening plateau is not sensitive to any shale properties. Further investigations have been conducted for detecting the influential parameters on the second softening and stabilization process. Two tests are selected to clarify this

problem. These two tests are called BK1 and BK2, which have the same cement-shale interface properties but BK2 uses a very high value for energy between casing and cement. It can be observed that second softening plateau can be widened by increasing the critical energy of cement-casing interface shown in BK2. The width extension of the second softening plateau makes numerical results better match with the experiment data. However, critical energy is not the properties between cement and shale although it is very sensitive to the second softening plateau. Hence, second softening process is governed by cement-casing interface, rather than shale cement interfaces and associated parameters. In other words, the second softening plateau is not a shale property and it is expected to not be seen in the field.

Therefore we may conclude that shale properties tested from this lab test are polluted with cement-casing interface interference and the real behavior of shale-cement interface is the one simulated only by considering cement and shale interface, which is shown by BK1 in Figure 2.4.

Table 2.1 Properties of the cement interface

Models	Maximum normal strength, KPa	Maximum shear strength at 1^{st} and 2^{nd} direction, KPa	Energy, J/m^2	Cohesive stiffness, KPa
Interface properties of cement and shale				
BK1	420	420	100	60 E6
BK2				
Bilinear				
Interface properties of cement and casing				
BK1	350	350	150	60 E6
BK2	350	350	10000	

Further sensitivity analysis revealed that Lavda's experiment results are sensitive to maximum shear strength (Figure 2.5), normal fracture energy (Figure 2.6) and shear stiffness. Figure 2.5 demonstrates that the peak force required to initiate the failure process is strongly dependent on the shear strength. In other words, failure initiation is governed mainly by shear strength, while propagation is governed mainly by

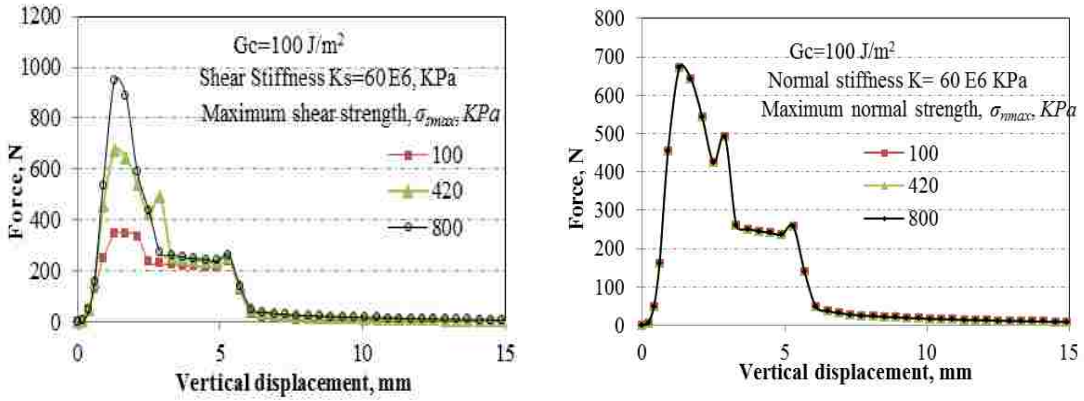

(a) Maximum shear strength **(b) Maximum shear strength**

Figure 2.5 Loading curve of push-out test for different interface shear and normal strength is shown in this graph. Higher shear strength leads to larger maximum force. Failure initiation is governed mainly by shear, while propagation is governed mainly by tension; the peak force required to initiate the failure process is strongly dependent on the shear strength, however, the force required to propagate the failure is not.

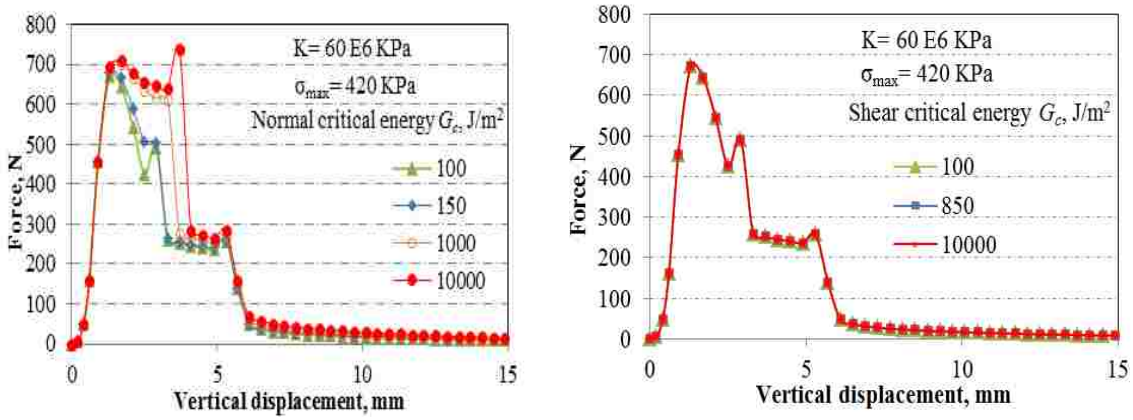

(a) Normal critical energy **(b) Shear critical energy**

Figure 2.6 Loading curve of pull-out test for different normal and shear fracture energy is shown in this graph. The effect of normal toughness on loading curve is significant but no effect of shear toughness on loading curve. The force required to propagate the failure is dependent on the normal fracture energy while the load require to initiate the failure is not.

tension. On the other hand, our simulations shown in Figure 2.6 show that the effect of normal toughness on loading curve is significant but no effect of shear toughness on loading curve in this experiment. Moreover, the force required to propagate the failure is dependent on the normal fracture energy while the load required to initiate the failure is not. Based on demonstrated results of our virtual numerical

experiment, specimen should reach maximum shear strength to start failure process; however, failure development is mainly tensile fracture propagation due to large deformation of the shale sample.

Field-scale Problems

Using cohesive parameters derived from loading samples in the lab where in this part, field scale response of the wellbore in different situations could be predicted. To illustrate an application of the proposed methodology in the field scale, we consider a well, shown in Figure 2.7, with leakage at the casing-shoe at the depth 6150 ft. Flow of fluid with pressure higher than the formation pressure at the casing shoe is considered as the main drive for failure initialization and further propagation. In situ stresses and viscous dissipation in fluid flow and fracturing are resisting against expansion of the failure

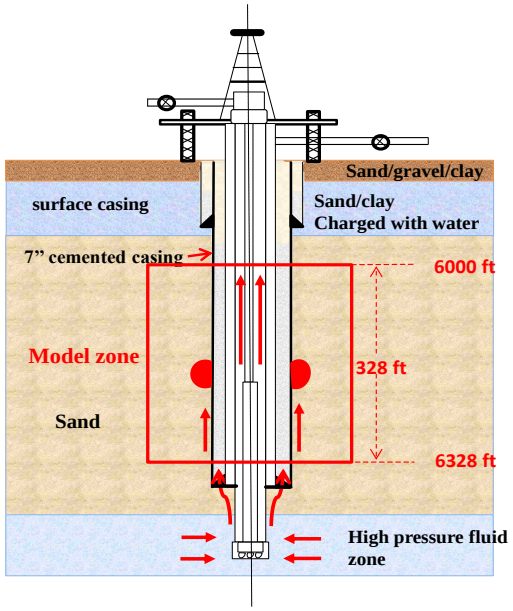

Figure 2.7 Well configuration and dimensions are not shown in scale.

zone. The wellbore consists of a 7-in cemented production casing in an 8 1/2-in hole at the depth of 6,000 ft. with the length of 131 ft. The weight of the drilling fluid (9.3 lbm/gal) provides 3,000 psi pressure at the point of our study (casing shoe). The overburden gradient and pore pressure gradient are assumed to be 1.0 psi/ft, and 0.465 psi/ft, respectively.

We assumed that delamination propagation initiates from an all-around cylindrical flaw. Hence, an axisymmetric finite element model, which is a slice of the three dimensional geometry, can be used for stress analysis (shown in Figure 2.8). This model is meshed using commercial and in-house mesh generators. The model consists of casing, cement sheath and a permeable elastic surrounding rock. The cohesive interface is introduced as a layer of elements with zero thickness to predict initiation and growth of a possible casing/cement fracture delamination. It is notable due to importance of fluid pressure in development of the failure zone, a coupled fluid-flow and deformation model has been incorporated in the cohesive elements. Moreover, the model is considered large enough to avoid any potential interference with boundaries.

Figure 2.9 shows the arrangement of cohesive elements with respect to casing and rock. From the left to the right, the model consists of the casing with 0.01 m thickness, zero thickness cohesive interface zone (connecting casing and cement), cement with 0.02 m thickness, zero thickness cohesive interface zone (connecting cement to rock), and formation rock. Rock is assumed to be homogeneous with 50 mD

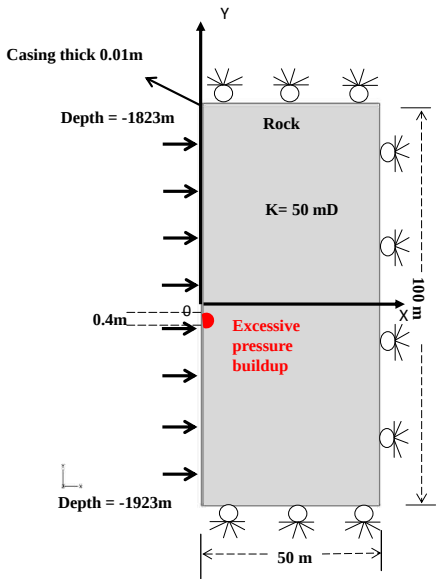

Figure 2.8 A schematic picture of the model is shown with its dimensions, boundary conditions, and loading conditions for the axisymmetric model.

permeability, which is much larger than cement permeability (0.001 md). The top and bottom of the

model is constrained in y-direction, and the right of the model is constrained in the x-direction to simulate the confinement induced by the surrounding rocks. In situ-stresses were applied as initial stress. The source of excessive pore pressure is assumed to be at a casing shoe located at the center of the model. Cement and rock properties used in the model are borrowed from available sources published in the rock physics handbooks or measurements reported in the literature. Properties of cement, casing and the interface bonding, rock mechanical parameters used for modeling purposes here are listed in the appendix.

The numerical mesh, demonstrated in Figure 2.9, consists of a layer of 3,000 four-node quadrilateral elements for casing, and 52,827 four-node quadrilateral elements with coupled displacements and pore pressure to model the formation and cements. Due to the high gradient of stress and displacement around potential failure zones, finer elements are used in the vicinity of the casing to minimize numerical

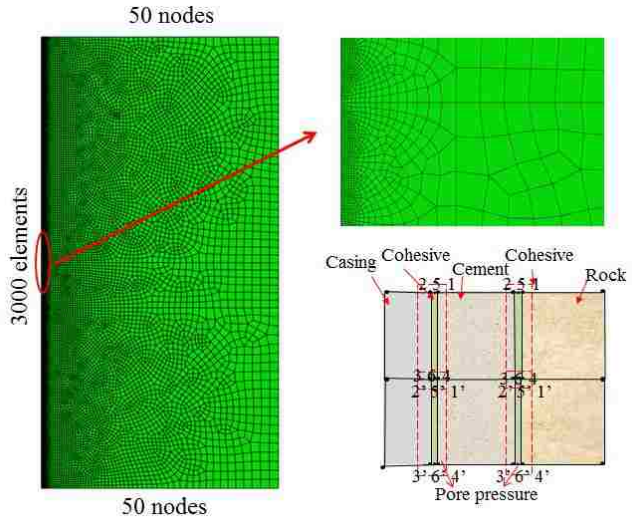

Figure 2.9 Finite element mesh for the axisymmetric geometry is demonstrated. Due to the large gradient of stresses and pressure, the elements in the vicinity of the wellbore and cement liner are adaptively refined. Moreover, interface layers between casing and cement, or cement and formation are attached by the two-dimensional cohesive elements for displacements and pore pressure.

inaccuracy. The hydraulic conductivity between the two sides of the cohesive zones is considered to be present before and after failure as cement is a low but still permeable medium. Pore pressure is coupled in

cohesive elements via two degrees of freedom in the middle of cohesive elements to catch high pressure gradient across the interface. The cohesive interface consists of 6,000 elements in this example.

The excessive fluid pressure leaking from the casing shoe, is simulated in two steps: In the first step, initial equilibrium is established under initial in situ stresses and initial pore pressure; then in the second step, pore pressure starts to buildup locally at the casing shoe. Excessive pore pressure is introduced in a very narrow zone. Cement is assumed to be free of impurities but there is a source of excessive pore pressure, which initiates failure.

The excessive pore pressure could be charged from a deeper charging zone through a leak in casing shoe or simply fluid migration from deeper sites but off the casing. The excessive pressure of 5000 KPa (725 psi) is considered in this example, which is gradually applied in the second step of modeling followed by re-equilibration at the third step. Excessive pressure then increased again by additional 5000 KPa excessive pressure.

Before discussing simulation results, it would be helpful to define dimensionless parameters which may govern the problem under general conditions. Dimensionless pressure, stress, crack length, crack opening and slippage and eventually dimensionless time are used to demonstrate delamination crack initiation and its propagation for varying mechanical and petrophysical properties. Pressurized fluid could open a cylindrical crack and fill the crack's volume or it may leak into the formation, which makes this problem similar to the hydraulic fracturing problem, although there is a fundamental difference in their drive mechanism, a hydraulic fracture is driven by a source of constant injection rate, gas migration is driven by a source with constant pressure. First, let's define the dimensionless time based on the wellbore radius and poroelastic diffusion coefficient (Detournay and Cheng, 1991, and Howison, 2003),

$$t^* = \frac{c.t}{r_w^2}. \qquad (\mathbf{2.13})$$

The constant c is the poroelastic diffusivity coefficient, which is different from usual diffusivity and given by

$$c = \frac{2KG(1-\nu)(\nu_u - \nu)}{\alpha^2(1-2\nu)^2(1-\nu_u)}. \quad \textbf{(2.14)}$$

where K is fluid mobility; ν is the drained Poisson's ratio, ν_u is undrained Poisson's ratio, ν_u; G denotes shear modulus of rock; t^* denotes dimensionless time; t real time in seconds; r_w denotes wellbore radius; Biot-Willis coefficient, α; Skempton's coefficient, B. Dimensionless fracture length is defined based on the wellbore radius

$$L^* = \frac{L_f}{r_w}, \quad \textbf{(2.15)}$$

where L^* denotes dimensionless crack length; L_f denotes the length of the failure zone. Similarly, dimensionless fracture width, Δw^*, is defined with respect to wellbore radius. Dimensionless stress, S* is defined as

$$S^* = \frac{S}{E}, \quad \textbf{(2.16)}$$

where *S* is stress, and *E* is the rock Young's modulus.

$$P_p^* = \frac{P_p}{E} \quad \textbf{(2.17)}$$

where P_p^* is dimensionless pore pressure. Hereafter, Discussions of results are based on dimensionless parameters listed above.

In the examples presented in this chapter, gravity effect is ignored for the sake of simplicity; hence failure zones look symmetric with respect to the leakage point. Failure is initiated from a short length area in the middle of the model. The failure zone starts expanding as soon as the pressure at the source goes beyond a certain threshold. The moment that the cement liner begins to fail, the stress and pore pressure distribution around the failure zone will undergo changes to satisfy equilibrium condition. The induced

effective normal and shear stresses, for the beginning stages, have been plotted in Figures 2.10 and 2.11. The effective stress is the portion of the total stress that is applied to the solid skeleton of the rock. The

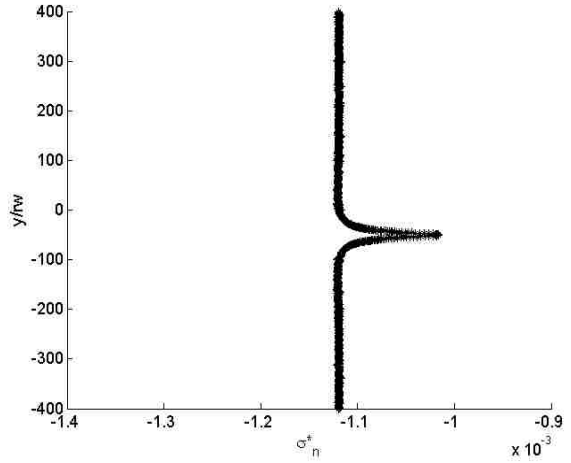

Figure 2.10 Normal tractions along the cement-rock and cement-casing are drawn. A considerable difference exists between stresses on both sides of the cement liner in the failure zone.

induced stresses are compressive (compression is negative), but at the failure cement zone due to the excessive pore pressure is less compressive.

The effective shear stress distribution along the cohesive zone reveals a complex and quite interesting

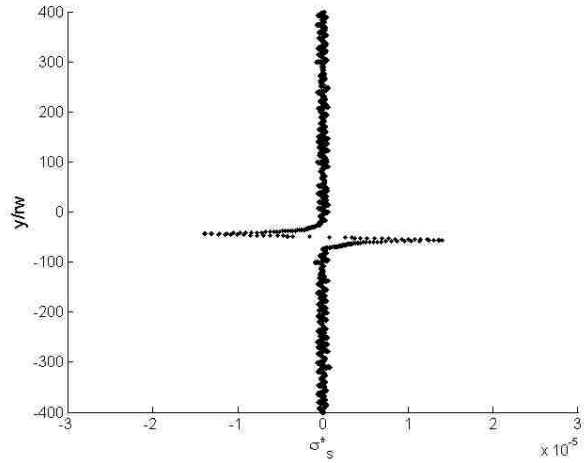

Figure 2.11 Shear traction along the cement liner at end of failure process. Large shear stress concentration observed at the end of failure zone is an indication of presence of shear failure in development of delaminating fractures.

phenomenon. Shear tractions along the cement liner is demonstrated in Figure 2.11. Induced shear stresses show a singular behavior at the tips of failure zone. Comparing shear tractions in Figure 2.11 with normal tractions in Figure 2.10, the first intriguing observation is the comparable magnitude of the shear stress with the normal stress, which implies the significant role of the shear tractions on initiation and propagation of a failure driven by excessive pressure from pre-existing damage. It is notable that onset of failure occurs where effective stress is not necessarily in tension, but less compressive. Due to the large amount of shear, stresses develop around the failure zone; cement will fail mainly due to the large shear and lack of enough compression at the leak zone. Analytical solutions show that a pressurized cylindrical crack is not like a planar pressurized crack that is represented by a pure mode I crack, but it also has a shear stress intensity factor because of the curvilinear natural of the crack surface. Therefore, a delamination crack around the casing is not a simple mode I crack. Additionally since the resultant mixed-mode fracture is confined between a stiff (i.e. steal casing) material and a softer material (rock)

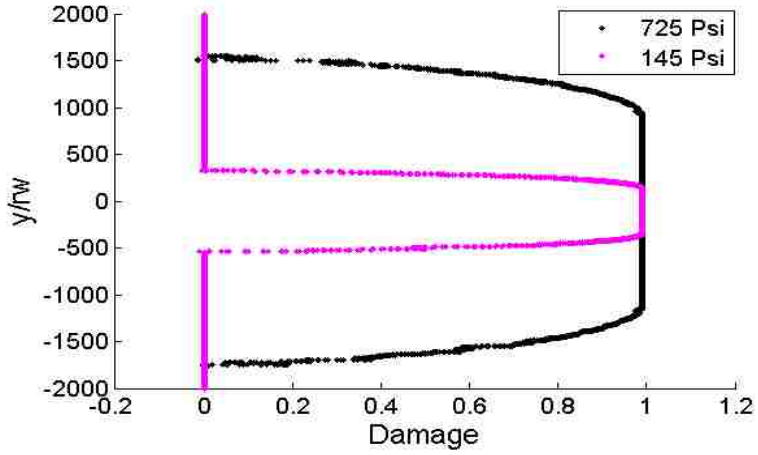

Figure 2.12 Damage index along cohesive zone at the end of the failure shows the extension of the failure zone which is in accordance with calculated shear stress distribution.

shearing is not as simple as a shear crack in a homogenous medium and slippage due to shearing is not stable slippage. Similar phenomenon has been observed in faults along dissimilar materials (He, et al,. 1989 and 1994).

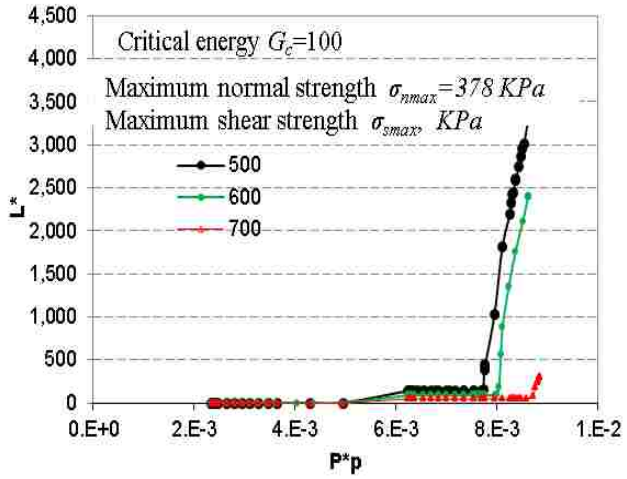

Figure 2.13 Fracture length developments due to increase of excessive pressure for cases with different shear strength but similar critical energy and normal strength is shown above.

The damage profile along the cohesive interface demonstrated in Figure 2.12 shows the propagation of a delamination fracture along the casing. Damage index (D) is characterized by scalar stiffness degradation (Equation 10). This index can vary from 0 to 1 due to the damage degree influenced by excessive energy provided. The complete damage (D=1) indicates the open part of the fracture. The zones with non-zero damage indices in Figure 2.12 shows strong correspondence with the shear traction

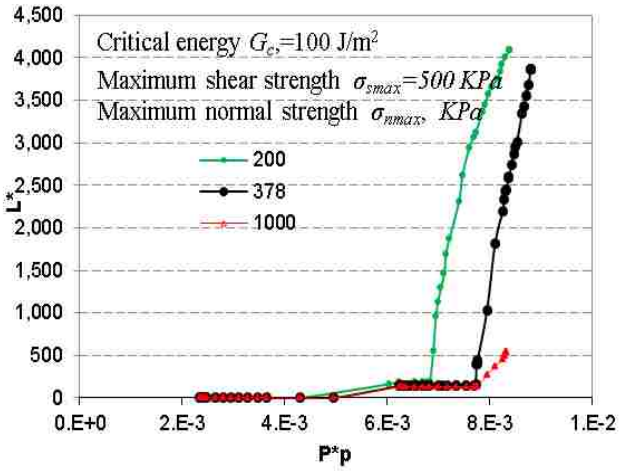

Figure 2.14 Propagation of delamination crack due to increase of excessive pressure for cases with different normal strength but similar critical energy and shear strength is shown above.

distribution shown in Figure 2.11, indicating the failure is processing with expanding large shear stress

fronts. The length of failure zone along the cement liner is another important parameter. Failure length can directly determine the severity of damage. The crack length calculated at different steps is shown in Figure 2.13, which is shown versus dimensionless time. Fracture propagation versus excessive pressure for cases with different shear strength but similar critical energy and maximum normal strength is shown in Figure 2.13. This plot shows that cements with stronger shear strengths at the interface may arrest fracture growth or in other words contain it. Figure 2.14 shows propagation for cases with different normal strength. It has been observed that increasing normal strength will improve the resistance of the system against uncontrolled fracture growth. Figure 2.15 shows propagation of delamination fracture for cases with different critical fracture energy. Despite the previous example, in this example cases with higher fracture energy leads to similar fracture growth i.e. broaching to the shallow zone. Hence, we might conclude that shear strength which is usually the only parameter determined from push out tests is not the only dominant factor on fracture containment. Additionally, the cement interface toughness

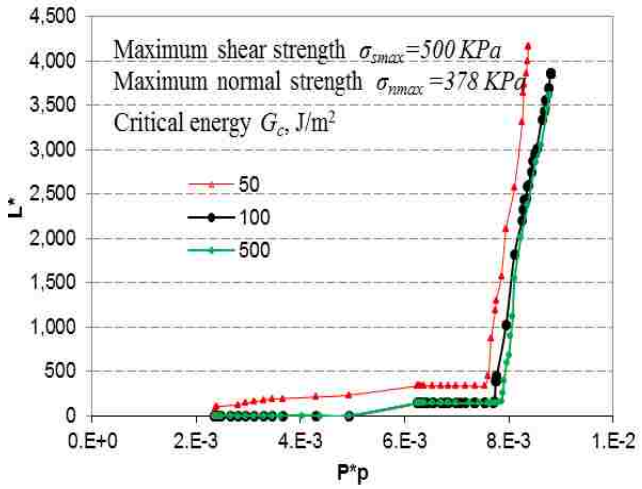

Figure 2.15 Propagation of delamination crack due to increase of excessive pressure for cases with different normal critical energy with similar tensile and shear strength are shown in this figure.

(critical fracture energy) which can also de deduced from the test results indirectly, has no significant effect to stop fractures from broaching to surface or shallow aquifers.

Conclusions

Protection of shallow aquifers is an increasing concern, so regulatory requirements for cement performance in well abandonments and drilling become stricter; however at the same time more sophisticated techniques are required for assessment and simulation of long-term integrity in the oil and gas wells. Advent of new ultra sonic technology which gives azimuthal measurements provides a reliable assessment tool but these tools have no predictive capability. Additionally, appearance of new cement additives in the market requires more sophisticated techniques to predict cement integrity under severe conditions in the surface based on the common lab test data. To address these needs, more sophisticated models are required to predict mechanical behavior of cement interfaces. Here, we used cohesive interface constitutive equation to describe mechanical characteristics of cement interface during failure. Potential delamination paths can be predefined by cohesive elements without any presumption of the initial crack size or location.

The main challenge in using a cohesive model is in measuring, cohesive model parameters in the lab. A process for using the finite element method to arrive at cohesive stiffness, strength and energy properties is explained in this chapter. Properties are calibrated such that simulated tests match the measured response of the specimens. It can be observed that the softening process of BK model matches up with the experimental results. The cohesive element approach provides an effective way to describe mechanical characteristics of cement interface and predict mechanical behavior of cement interfaces. Further sensitivity analysis revealed that Lavda's experiment results are sensitive to maximum shear strength, normal fracture energy and shear stiffness. Results show that specimen should reach maximum shear strength to start failure process; however, failure development is mainly a tensile fracture. The effect of normal toughness on loading curve is significant but no effect of shear toughness on loading curve. The force required to propagate the failure is dependent on the normal fracture energy while the load require to initiate the failure is not.

Then the cohesive element approach provides a tool to evaluate this process at the wellbore scale. Field scale sensitivity tests are also conducted for the selection of dominant factors on fracture containment. These two dominant parameters are cementing normal and shear strength. The proposed approach provides a tool to understand the competition between different interacting physical processes near the wellbore and an important methodology to examine the role of different properties. Moreover, the proposed approach can predict the influence on wellbore integrity of imperfect cement and excessive pore pressure near the wellbore. This provides an important insight on the role of cement mechanical integrity on wellbore isolation.

Additionally, our simulations show that due to the significance of overburden stress in comparison to changes in pore pressure, excessive pressure mainly facilitates shear failure. Imperfect cement bonding causes the variation and fluctuation of pore pressure, normal and shear stresses, fracture opening and slippage, which indicate the mechanism of crack initiation and propagation. The dimensionless crack length versus dimensionless time has been selected to demonstrate failure propagation or containment under different situations. Furthermore, the proposed approach can give enough evidences on the failure containment and integrity, which is also paramount for safe hydrofracturing and preventing environmental risk. All of these issues are highly valuable to the industry.

Nomenclature

B	Skempton's coefficient
C_t	Fluid leak-off coefficients on the top surfaces of the fracture
C_b	Fluid leak-off coefficients on the bottom surfaces of the fracture
D	Scalar stiffness degradation index
E	Rock Young's modulus, KPa
G	Shear modulus of rock, KPa
G_c	Critical fracture energies during deformation, J

G_n Work done by the tractions and their conjugate relative displacements in normal directions, J

G_s Work done by the tractions and their conjugate relative displacements in first shear directions, J

G_t Work done by tractions and their conjugate relative displacements in second shear directions, J

G_T Total energy in the mode-mix condition, J

G_s^C Critical fracture energies during deformation purely along the first shear directions, J

G_t^C Critical fracture energies during deformation purely along the second shear directions, J

G_T Total energy in the mode-mix condition, J

k Permeability tensor

K Fluid mobility, m^2/KPa.s

k_n Stiffness components in normal direction

K_{n0} Initial tensile stiffness

K_{s0} Initial value for shear stiffness

k_s Stiffness components in shear direction

L_f Crack length, m

p_b Pore pressures in the adjacent poroelastic material on the bottom surfaces of the fracture, KPa

∇p_f Fluid pressure gradient along the cohesive zone

P_p Pore pressure, KPa

P_p * Dimensionless pore pressure

p_t Pore pressures in the adjacent poroelastic material on the top surfaces of the fracture, KPa

q Fluid flux, m^3/s

r_w Wellbore radius, m

S * Dimensionless stress

S Effective stress, KPa

t^* Dimensionless time

t Real time, seconds

t_n Normal traction, KPa

t_{n0} Peak values of the nominal stress when the deformation is purely normal to the interface, KPa

t_{s0} Peak values of the nominal stress when the deformation is purely in shear direction, KPa

t_s Tangential traction, KPa

v Poisson's ratio

v_u Untrained Poisson's ratio

w Crack opening, m

Δw^* Dimensionless fracture delamination opening

α Biot-Willis coefficient

β Rock thermal expansions, 1/K

β_f Fluid thermal expansions, 1/K

$\Delta\delta^*$ Dimensionless slippage displacement

δ_m Effective relative displacements, m

δ_{m0} Effective relative displacements corresponding to δ_{n0} and δ_{s0}, m

δ_{mf} Effective relative displacements corresponding to δ_{nf} and δ_{sf}, m

δ_n Crack opening displacement, m

δ_{nf} Critical relative normal displacements when tractions diminish, m

δ_s Crack sliding displacement, m

δ_{sf} Critical relative shear displacements when tractions diminish, m

ς Change of fluid content, m^3

η Material parameter

References

Barenblatt, G. I., 1962, The Mathematical Theory of Equilibrium Cracks in Brittle Fracture, Journal of Applied Mechanics, 1962, pp: 7, 55-129.

Benzeggagh, M. L., and Kenane, M., 1996, Measurement of Mixed-Mode Delamination Fracture Toughness of Unidirectional Glass/Epoxy Composites with Mixed-Mode Bending Apparatus, Composites Science and Technology, 1996, Vol. 56, pp: 439–449.

Berger, A., Fleckenstein, W. W., Eustes, A. W., and Thonhauser, G., 2004, Effect of Eccentricity, Voids, Cement Channels, and Pore Pressure Decline on Collapse Resistance of Casing, SPE 90045, SPE Annual Technical Conference and Exhibition, Houston, Texas, 26-29, September 2004.

Bois, A. P., Garnier, A., and Laudet, J. B., 2012, Use of a Mechanistic Model To Forecast Cement-Sheath Integrity, SPE Drilling & Completion, Vol. 27(2), pp: 303-314.

Bois, A. P., Garnier A., Rodot, F., Saint-Marc, J., and Aimard N., 2011, How To Prevent Loss of Zonal Isolation Through a Comprehensive Analysis of Microannulus Formation, SPE 124719-PA. SPE Drilling and Completion, Vol. 26 (1), pp: 13-31.

Bosma, M., Ravi, K., van Driel, W. L., and Schreppers, G. J., 1999, Design Approach to Sealant Selection for the Life of the well, SPE 56536, SPE Annual Technical Conference and Exhibition, Houston, 3-6 October 1999.

Bour, D., 2005, Cyclic Steam Well Design: A New Approach to Solve an Old Problem of Cement Sheath Failure in Cyclic Steam Wells, SPE 93868-MS, SPE Western Regional Meeting, Irvine, California Mar 30 - Apr 01 2005.

Bourgoyne, A. T., Chenevert, M. E., Millheim, K. K., and Young, F.S., 1986, Applied Drilling Engineering, Society of Petroleum Engineering Vol. 2, pp: 312-324.

Boyd, D., Al-Kubti, S., Khedr, O. H., Khan, N., Al-Nayadi, K., Degouy, D., Elkadi, A., and Kindi, Z. A., 2006, Reliability of Cement Bond Log Interpretations Compared to Physical Communication Tests Between Formations, SPE 101420-MS, Abu Dhabi International Petroleum Exhibition and Conference, 5-8 November 2006, Abu Dhabi, UAE.

Camacho, G. T., and Ortiz, M., 1996, Computational Modeling of Impact Damage in Brittle Materials, International Journal of Solids and Structures, Vol. 33(20-22), pp: 2899-2938.

Carter, L. G., and Evans, G. W., 1964, A study of cement-pipe bonding. Journal of Petroleum Technology, 16(2), 157-160.

Davila, C. G., Camanho, P. P., and de Moura, M. F., 2001, Mixed-Mode Decohesion Elements for Analyses with Progressive Delamination, NASA Langley Technical Report Server.

Detournay, E., and Cheng, A. H. D., 1991, Plane Strain Analysis of a Stationary Hydraulic Fracture in a Poroelastic Medium, International Journal of Solids and Structures, Vol. 37, No. 13, pp. 1645-1662.

Dugdale, D. S., 1960, Yielding of Steel Sheets Containing Slits. Journal of the Mechanics and Physics of Solids, Vol. 8, pp: 100-104.

Evans, G. W., and Carter, L. G., 1962, Bounding Studies of Cementing Compositions to Pipe and Formations, Drilling and production Practice.

Fleckenstein, W. W., Eustes, A. W., and Miller, M. G., 2000, Burst Induced Stresses in Cemented Wellbores, SPE 62596-MS, SPE/AAPG Western Regional Meeting, Long Beach, California,19-22 June 2000.

Gerstle, W. H., and Xie, M., 1992, FEM Modeling of Fictitious Crack Propagation in Concrete, Journal of Engineering Mechnics, Vol. 118 (2), pp: 416-434.Garnier, A., Saint-Marc, J., Bois, A.-P., and Kermanac'h, Y., 2010, An Innovative Methodology for Designing Cement-Sheath Integrity Exposed to Steam Stimulation, SPE Drilling & Completion, Vol. 25(1):58-69.

Ghabezloo, S., Sulem, J., Guédon, S., Martineau, F., and Saint-Marc, J., 2008, Poromechanical behaviour of hardened cement paste under isotropic loading, Cement and Concrete research, 38(12), 1424-1437.

Goodwin, K. J., and Crook, R. J., 1992, Cement Sheath Stress Failure, SPE Drilling Engineering, Vol. 7(4):291-296.

Gray, K., Podnos, E., and Becker, E., 2009, Finite-Element Studies of Near-Wellbore Region During Cementing Operations: Part I. SPE Drilling & Completion, 24(1), 127-136.

Griffith, J. E., Ravi, K., Saasen, A., and Nødland, N. E., 2004, Foam Cement Engineering and Implementation for Cement Sheath Integrity at High Temperature and High Pressure, SPE 87194-MS, IADC/SPE Drilling Conference, Dallas, Texas, 2-4 March 2004.

He, M. Y., Evans, A. G. and Hutchinson, J. W., 1994, Crack deflection at an interface between dissimilar elastic materials: role of residual stresses, International Journal of Solids and Structures, Vol. 25 (9), pp: 3443-3455.

He, M. Y., and Hutchinson, J. W., 1989, Crack Deflection at an Interface between Dissimilar Elastic Materials. International Journal of Solids and Structures, Vol. 25(9), pp: 1053-1067.

Hillerborg, A., Modeer, M., and Petersson, P., 1976, Analysis of Crack Formation and Crack Growth in Concrete by Means of Fracture Mechanics and Finite Elements, Cement Concrete Res, Vol. 1976 (6), pp: 773–782.

Hutchinson, J. W., 1990, Mixed Mode Fracture Mechanics of Interfaces, Metal/Ceramic Interfaces, Vol. 4, pp: 295-306.

Jiang, L., Guillot, D., Meraji, M., Kumari, Pu, Vidick, B., Duncan,B., Gaafar, G. R., and Sansudin, S. B., 2012, Measuring Isolation Integrity In Depleted Reservoirs, SPE 2012-078, SPWLA 53rd Annual Logging Symposium, June 16 - 20, 2012 , Cartagena, Colombia.

Jutten, J. J., Gulllot, D., and Parcevaux, P. A., 1989, Relationship between Cement Slurry Composition, Mechanical Properties, and Cement-bond-log Output, SPE 16652-PA, SPE production Engineering, 1989, pp: 75-82.

Kanninen, M., and Popelar, C., 1985, Advanced Fracture Mechanics. Oxford University Press, Oxford.

Kutchko, B. G., Strazisar, B. R., Dzombak, D. A., Lowry, G. V., and N. Thaulow, 2007, Degradation of well cement by CO_2 under geologic sequestration conditions, Environmental science and technology, 41(13), 4787-4792.

Ladva, H. K. J., Craster, B., Jones, T. G. J., Goldsmith, G., and Scott, D., 2005, The Cement-to-formation Interface in Zonal Isolation, SPE 88016-PA, IADC/SPE Asia Pacific Drilling Technology Conference Exhibition, Kuala Lumpur, Malaysia, 13-15 September 2005.

Le Guen, Y., Le Gouevec, J., Chammas, R., Gerard, B., Poupard, O., Oxand S. A., Van Der Beken, A. and Jammes, L., 2009, CO_2 Storage: Managing the Risk Associated With Well Leakage Over Long Time Scales, SPE 116424-PA, SPE Projects, Facilities & Construction, Vol. 3, pp: 87-96.

Li, Y. N., and Liang, R. Y., 1994, Peak Load Determination in Linear Fictitious Crack Model, Journal of Energy Mechanics, ASCE, Vol. 120 (2), pp: 232-249.

Ma, Y., Cui, M. R., Guo, X. Y., Shi, Q., and Li, L., 2007, How to Evaluate the Effect of Mud Cake on Cement Bond Quality of Second Interface? SPE 108240-MS, SPE/IADC Middle East Drilling and Technology Conference, Cairo, Egypt, 22-24 October 2007.

Mei, H. X., Kenneth, S. G., Liechti, M., and Huang, R., 2010, Initiation and Propagation Interfacial Delamination in Integrated Thin-film Structures, Thermal and Thermomechanical Phenomena in Electronic Systems (ITherm), 12th IEEE Intersociety Conference, Las Vegas, NV, 2-5 June 2010, pp: 1-8.

Mueller, D. T., and Eid, R. N., 2006, Characterization of the Early Time Mechanical Behavior of Well Cements Employed in Surface Casing operations, SPE 98632, IADC/SPE Drilling Conference, Miami, Florida, 21-23 February 2006.

Nabipour, A., Joodi, B., and Sarmadivaleh, M., 2010, Finite Element Simulation of Downhole Stresses in Deep Gas Wells Cements, SPE 132156, SPE Deep Gas Conference and Exhibition, Manama, Bahrain, 24-26 January 2010.

Nagy, P. B., 1992, Ultrasonic Classification of Imperfect Interfaces, Journal of Nondestructive Evaluation, Vol. 11(3), pp: 127-139.

Needleman, A., 1990, An Analysis of Tensile Decohesion along an Interface, Journal of the Mechanics and Physics of Solids, Vol. 38(3), pp: 289–324.

Nelson, E. B., 1990, Well cementing, Vol. 28, Elsevier Science.

Nguyen, O., Repetto, E. A., Ortiz, M., and Radovitzky, R.A., 2011, A Cohesive Model of Fatigue Crack Growth, International Journal of Fracture, Vol. 110, pp: 351-369.

Pandolfi, A., and Ortiz, M., 2002, An Efficient Adaptive Procedure for Three-dimensional Fragmentation Simulations. Engineering with Computers, Vol. 18, pp: 148-159.

Parcevaux, P., 1984, Pore Size Distrigution of Portland Cement Slurries at Very Early Stage of Hydration, Journal of Cement and Concrete Research, 1984, Vol. 14 (3), pp: 419-430.

Parcevaux, P., and Sault, P., 1984, Cement Shrinkage and Elasticity: A New Approach for a Good Zonal Isolation, SPE 13176, Offshore Technology Conference, Houston, TX, 16-19 September 1984.

Petersson, P. E., 1981, Crack Growth and Development of Fracture Zone in Plain Concrete and Similar Materials, Report TVBM-1006, Lund Institute of Technology, Lund, Sweden.

Ravi. K., Mcmechan, D. E., Reddy, B. R., and Crook, R. A., 2007, Comparative Study of Mechanical Properties of Density-Reduced Cement Compositions, SPE 90068, Annual Technical Conference and Exhibition, Houston, 26-29 September 2007, and published in June 2007 SPE Drilling and Completion.

Saidin, S., Sonny, I., and Nuruddin, M. F., 2008, A New Approach for Optimizing Cement Design to Eliminate Microannulus in Steam Injection Wells, SPE 12407-MS, International Petroleum Technology Conference, Kuala Lumpur, Malaysia, 3-5 December 2008.

Salehi S., and Nygaard R., 2011, Numerical Study of Fracture Initiation, Propagation, Sealing to Enhance Wellbore Fracture Gradient, SPE 11-186, 45th U.S. Rock Mechanics / Geomechanics Symposium, San Francisco, California, 26 - 29 June, 2011.

Tahmourpour, F., Exner, M., and Khallad, M., 2008, Design and Operational Factors for the Life of the Well and Abandonment, SPE 114866, CIPC/SPE Gas Technology Symposium 2008 Joint Conference, Calgary, Alberta, Canada, 16-19 June 2008.

Thiercelin, M, J., Dargard, B., Baret, J. F., and Rodriquez, W. J., 1998, Cement Design Based on Cement Mechanical Response, SPE 52890-PA, SPE Drill & Completion, Vo., 13(4), pp: 266-273.

Tvergaard, V., and Hutchinson, J. W., 1996, Effect of strain-dependent cohesive zone model on predictions of crack growth resistance, International Journal of Solids and Structures, Vol. 33, pp: 3297-3308.

Ulm, F. J., Constantinides, G., and Heukamp, F. H., 2004, Is concrete a poromechanics materials?—A multiscale investigation of poroelastic properties. Materials and structures, 37(1), pp: 43-58.

van der Kuip, M. D. C., Benedictus, T., Wildgust, N., and Aiken, T., High-level integrity assessment of abandoned wells, Energy Procedia, Volume 4, 2011, Pages 5320-5326.

Xie, M., and Gerstle, W. H., 1995a, Energy-based Cohesive Crack Propagation Modelling, Journal of Engineering Mechanics, American Society of Civil Engineers, Vol. 121 (12), pp: 1349–1458.

Xie, M., Gerstle, W. H., and Rahulkumar, P., 1995b, Energy-Based Automatic Mixed-mode Crack Propagation modeling, Journal of Engineering Mechanics, Vol. 121(8), pp: 914-923.

Yang, A. J., and Deeks, Z. J., 2007, Modelling Cohesive Crack Growth Using a Two-step Finite Element-scaled Boundary Finite Element Coupled Method, International Journal of Fracture, Vol. 143, pp: 333–354.

Yang, Z., and Xu, X. F., 2008, A Heterogeneous Cohesive Model for Quasi-Brittle Materials Considering Spatially Varying Random Fracture Properties, Computer Methods in Applied Mechanics and Engineering, Vol. 197(45-48), pp: 4027-4039.

Yang, Z. J., and Chen, J. F., 2004, Fully automatic modelling of cohesive discrete crack propagation in concrete beams using local arc-length methods. International Journal of Solids and Structure, Vol. 41(3-4), pp: 801–826.

Yang, Z. J., Su, X. T., Chen, J. F., and Liu, G. H., 2009, Monte Carlo Simulation of Complex Cohesive Fracture in Random Heterogeneous Quasi-brittle Materials, International Journal of Solids and Structures, 2009, Vol. 46(17), pp: 3222-3234.

CHAPTER 3. THREE-DIMENSIONAL ANALYSIS OF CEMENT SHEATH INTEGRITY AROUND WELLBORES

Abstract

The broaching of fluid through cement sheath imposes serious challenges to the integrity of the wellbore. Wellbore integrity is highly dependent upon the integrity of the interfacial bonding of the cement to the formation and casing. We utilized a three-dimensional field-scale numerical model to simulate propagation of cement failures when fluid leakage occurs around the casing shoe. The excessive fluid pressure provided by the leakage is the driving force for the cement failure. The interfaces of the cement sheath with the formation and casing are potential paths for growth of delamination cracks. These paths are represented by pre-inserted cohesive elements. Existence of non-uniform failure pattern around the wellbore is shown even for the case of isotropic in situ stresses and uniform cement properties. These spatial failure patterns cannot be predicted by traditional two-dimensional models. The non-uniform failure pattern helps us to better interpret measurements provided by traditional failure detection tools like CBLs and ultrasonic bond logs. Our simulations show that radial and tangential stress take essential role on failure propagations, but shear stress has a significant effect on failure initiations. Furthermore, the possibility of fracture containment and broaching is investigated by sensitivity analysis of cement interface properties. From these sensitivity tests, the rigidness, normal (and shear) strength of the interface, cement Young's modulus, and in situ stresses have been considered as major factors for fracture containment. It is found that larger values of cohesive interface normal (shear) strength, or the rigidness of the cement can effectively reduce the likelihood of failure around the wellbore. The presented model provides a systematic approach to understand and assess wellbore integrity in design and production stages.

Introduction

The cement sheath placed between the casing and formation is expected to provide zonal isolation throughout the life of a well. Cement sheath failures have been recognized as the main cause responsible

for upward fluid migration from hydrocarbon containing formations to shallow aquifers or surface (Bois et al., 2012). Because of the extremely low permeability of intact cement sheaths, the fluid seeps around the casing mainly via cracks and micro-annulus channels in the cement (Saidin et al., 2008). The seeping fluid is accompanied by accumulation of excessive pore pressure, which may be charged by a deeper kick zone through a leak in the casing, casing shoe or simply fluid migration along the damaged formation. For illustration purposes, a number of leakage scenarios are shown on the left side of Figure 3.1. Endurance of cement sheath integrity is a key to successful long-term wellbore integrity. Loss of this integrity may cause continuous flow and in extreme cases may lead to adverse consequences (Nesheli, 2006) such as large financial loss, abandonment and remediation, polluting the environment by dangerous (flammable and potentially toxic) formation or drilling fluid. Therefore, it is of significant importance to understand the mechanisms of onset and propagation of cement mechanical degradation around the wellbore. Six general failures mode in the cement sheath are demonstrated in Figure 3.1: a) radial cracking, b) plastic deformation in cement, c) debonding between casing and cement, d) debonding between cement and formation, e) incomplete cementing including partially cemented and no cement sheaths, and f) channelization.

The risk of radial cracking and plastic deformations is most significantly influenced by cement stiffness which is a function of cement composition and curing process (Bearden and Lane, 1961), for instance the chance of radial cracking is increasing by utilizing cement stiffer than the surrounding rocks. Plastic deformations are easily formed when cement is softer than the rock (Bois et al. 2011). Incomplete cement sheaths are usually formed because of poor cementing operations or cement shrinkage due to poor cement properties like high cement permeability and porosity. Large wellbore eccentricity and inclination are also known as one of the reasons for presence of incomplete cement sheaths (Aadnoy, et al, 1987). Channel formation can be accelerated by invasion of mobile fluid (gas) and its upward percolation along empty spaces formed during shrinkage. The channelization phenomenon more frequently occurs during “cement setting” (Parcevaux, 1984). Debonding of cement from the casing (or formation) is controlled by

several factors originated from cement composition, then extended to cement curing process, compaction, and wellbore tubular, loading and thermal stresses, as well as poor mud removal, formation surface roughness, interface chemical interactions, hydration and chemical shrinkage, and the formation environment. Each of these aspects has received special attention in the literature (Jutten, et al. 1989, Ladva et al. 2005, Bour, 2005, for example); however, there is still a need for an integrated model to determine the mechanical properties, which determine initiation and propagation of these failures. Compared with drilling, cement sheath failures commonly occur in the production and completion processes due to the deterioration effects over time. Even in situations where the cement was properly

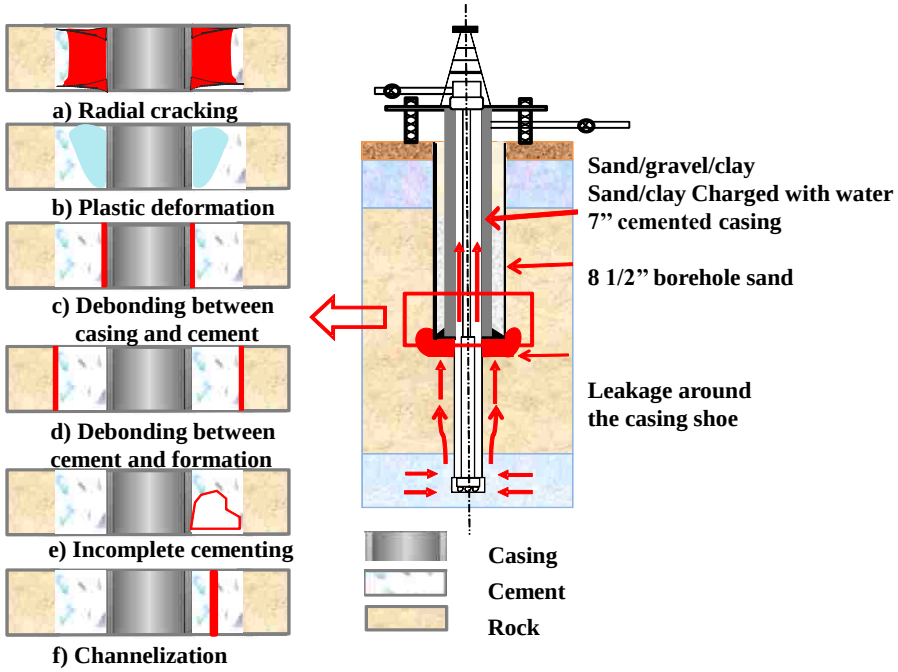

Figure 3.1 A schematic picture of fluid migration outside the casing is shown in the right picture. Left pictures show different mechanisms for failure initiation in small scale i.e. Radial cracking (a), plastic deformation of cement (b), debonding or delamination crack between cement and casing (c), delamination crack between casing and cement, (d) delamination crack between formation and cement, and channelization inside cement (f) . Flow path in each case is marked in red.

placed and initially provided a good hydraulic seal, the disappearance of zonal isolation with time is observed (Bois, et al., 2011 and 2012). Large stress variations during well life could be another important challenge to maintain cement sheath integrity, arising from sources such as casing leakage (Vignes and Aadnøy, B.S., 2010), sudden dynamic loading (Jackson and Murphey 1993), weight and temperature

variations of the mud (Savari and Kumar, 2012), perforation of the casing (Lecampion, et al, 2011), hydraulic fracturing (Lecampion and Prioul, 2013), acidization and finally production of the reservoir, variations of production rate, original flaws of cement sheath after setting (Bois, et al, 2011), pressure integrity tests (leakoff tests) (Lee, et al, 2004), and gas production (Pickle and Swan, 2012), as well as high pressure and temperature (Bour, 2005) in the wellbore. Although each failure category is discussed individually, it is important to know that various types of cement sheath failures might simultaneously exist in real cases. The unbalanced adhesion force and energy due to the interface heterogeneity could further increase the possibility of cement damage. Hence, the failure patterns and failure routes become more complex in real cases due to cement heterogeneity.

Several testing methods have been developed to indirectly measure cement normal and shear bond strength in the lab conditions (Bearden and Lane, 1961, Carter and Evans, 1964, and Ladva, 2005). In the literature, cement-interface bonding strengths, in general, are a function of cement slurry composition, formation properties, which could be roughly predicted with cement bond logs (CBL) by utilizing acoustic wave attenuation rate and acoustic impedance and some empirical correlations to estimate compressive strength and acoustic wave velocity behind the casing (Jutten et al. 1989). The advent of new ultrasonic technology (ULTs) in the past two decades partially satisfies these needs to provide quantitative integrity evaluation via a 360 ° scan of the casing-to-cement bond at a broadband frequency ranging from 250 to 700 kHz (Le Guen et al. 2009). Presence of gas and liquid behind the casing can be identified based on the thresholds set for acoustic impedance boundaries between different materials. The strength of cement bonding to casing and formation can be measured in the lab (Carter and Evans, 1964). For instance, Carter and Evans (1964) proposed an experimental setup to measure shear and normal bond strengths (they called it hydraulic bond and shear bond test, respectively) of cement to formation and casing; however, these tests were not done in pure shear or normal mode to measure tensile and shear strength of cement interfaces. Additionally, test results in the lab are much more complicated than being described by one-parameter so-called bond strength. Essentially, fracture energy and the failure damage

process are the missing pieces in the interpretation of Carter and Evans' tests. Lavda (2005) tried to adapt this test to measure shear bond strength between cement and shale by pulling out a shale core from a cement ring set in a piece of casing, although his interpretation was not basically different from that of Carter and Evans. Fracture initiation and its propagation along the cohesive interface also exist in other engineering applications such as debonding of thin films from their substrates in microchips, where a comprehensive review may be found in Freund and Suresh (2003). In spite of recent advances in describing the behavior of interfaces in engineering materials using more sophisticated constitutive equations, these techniques have not been introduced to this problem until recently. Dahi Taleghani and Wang (2013) suggested using cohesive interface models to cement integrity failure, which could use loading curves from regular cement strength tests to yield bond strength as well as fracture energy and allowable deformation at cement interfaces before complete failure. Dahi Taleghani and Wang (2013) showed how to use results from routine tests (e.g., Lavda, 2005 and Carter and Evans, 1964) and numerical simulation to derive required parameters for cohesive zone constitutive equations by inverse analyses. Here, we utilize cohesive interface model-to-model fracture initiation and propagation in 3D geometries under different situations using cohesive parameters estimated using the technique discussed in Dahi Taleghani and Wang (2013). For deriving cohesive parameters from lab tests due to simple conditions of the test, two-dimensional axisymmetric cohesive FEM models should be sufficient. However, issues like in situ stress anisotropy or wellbore inclination could potentially affect the geometry and onset of failure that requires three dimensional analyses.

In contrast to laboratory conditions, assessment of wellbore integrity and cement bond strength in the field is not possible by direct measurements. It is commonly evaluated by traditional cement evaluation (CBL) or Ultra-sonic logging techniques (ULT) (Lake, 2007, for example). CBL measurements rely on the amplitude attenuation of the acoustic signal to estimate the quality of cement placement in the annulus between metal casing and formation rock (Grosmangin et al., 1961). The attenuation rate can be calculated from signal amplitude to interpret the percentage of the casing cemented circumference, and

quantified as bond index (Longo, et al., 2012). The variable-density display tools (VBL) are usually combined with CBL for a better evaluation of the cement quality. The CBL-VBL combined system provides average measurements, which makes it difficult and sometimes impossible to detect small channels or localized failures. Also, it is difficult to distinguish between the cases of high-strength cement with channels versus even distribution of low-strength (foam) cements, which both generate similar overall response (Lake, 2007). This technique cannot be utilized in fast formations in which the formation arrival precedes the casing arrivals. In compared with the CBL-VBL combined system, ULT has been proved to be effective in identifying gas-contaminated cements from low-weight cement (foam cements) (Butsch, 1995). Ultrasonic tools normally require an impedance contrast in the materials behind the pipe to differentiate between cement and fluids (Havira, 1982). ULTs consist of the ultrasonic source and receivers together as a transducer to provide 360 ° azimuthal measurements around the borehole (Hayman et al, 1991). Color images of ULTs present a qualitative sense for identification of fluid types based on the impedance differences among gas, water and cement, as well as failure paths around the wellbore. Detectable failure patterns around the wellbore include circumferential delamination and partial delamination, as well as channelization, and randomly dispersed delamination. In order to give a general idea of possible failure patterns in the wellbore, two basic failure patterns, circumferential delamination and partial delamination are demonstrated in Figure 3.2. The likelihood of occurrence of different failure patterns from the mechanical point of view is investigated in this chapter.

Despite ULT advantages, there are some limitations for their applications (Boyd, et al., 2006, and Lake, 2007). The log quality can be influenced to some degree during the tool running process and during the cementing operations. Examples include 1) surface condition of casing, because ultrasonic pads require a smooth surface; 2) attenuation due to borehole fluid, an ultrasonic wave is attenuating faster at higher mud weights; 3) logging tool eccentricity, the eccentricity may lead to presenting exaggerated cement bonding on the ULTs; and 4) formation acoustic characteristics and hydrocarbon effects (Frisch, et al, 2000). More importantly, ULTs provide only post-failure assessment without

directly measuring strength of the intact cement. Finally, ULTs do not have the capacity to distinguish the failures incurred in the cement sheath from failures between interfaces of casing and cement (or formation), nor to provide the interface properties between these two interfaces. However, detecting failure geometry is important for fracture containment calculations, and interpreting ULT data. The ULTs like other logging tools, in the best-case scenario may provide a local measurement of interface quality, which is critical to investigate the likelihood of failure, but doesn't necessarily predict onset of failure and

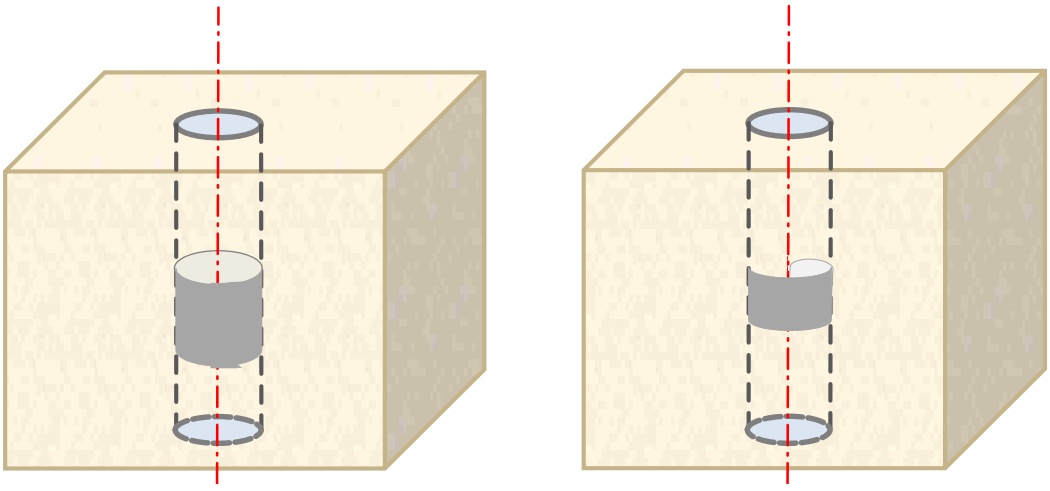

a) Circumferential delamination **b) Partial delamination**

Figure 3.2 Two selected idealized possible cement sheath failure patterns occur around the wellbore. These two basic failure patterns are (a) circumferential delamination and (b) partial delamination.

its containment. Therefore, having a sophisticated mechanical model will be a complement to logging and lab measurements to pursue an integrated assessment of the wellbore integrity under different conditions such as long-term production, drilling, fracturing, etc. This chapter conducts three-dimensional modeling with cohesive interface approach to predict how failures develop around the wellbore for given cement and formation conditions. The excessive pore pressure generated from the leakage around the casing shoe is considered as the main source for failure initiation and propagation. The heterogeneity of the cement interfaces, as well as wellbore inclination angle, eccentricity of the casing, and in situ stress anisotropy are different factors studied in this work to understand their possible influence on different stages of cement failures.

In the next section, the governing equations are introduced, and followed with the theory of the cohesive interface model for fracture initiation and propagation. Section 4 gives a description of the numerical model and dimensionless analysis for the problem. Sections 5 and 6 describe the results for the onset of delamination fractures and propagation of failure in cement sheaths under different conditions.

Governing Equations

To model phenomena occurring before, during, and after failure of the cement sheath, we considered the cement and the surrounding rock as a continuum with solid and fluid constituents. For the sake of simplicity, incompressible Newtonian fluid is used to represent formation fluid; however, incorporating compressible fluid in equations should be straightforward. The first governing equation is the fluid mass balance in the solid phase (Coussy, 2004)

$$\frac{\partial \varsigma}{\partial t} + q_{i,j} = 0 \ , \qquad \textbf{(3.1)}$$

where ς denotes the change of fluid content and q denotes the fluid flux. Upon formation of a delamination crack between cement and casing, fluid flow inside the fracture is considered as a laminar flow between two parallel plates i.e. Poiseuille's flow (Batchelor, 1967)

$$\frac{\partial w(s,t)}{\partial t} = \frac{1}{12\mu}\frac{\partial}{\partial s}(w^3(s,t)\frac{\partial P(x,t)}{\partial s}), \qquad \textbf{(3.2)}$$

where P is the pressure of the fluid inside the delamination crack and w is the width of the fracture. s is the coordinate along the fracture. In addition to this tangential flow, normal flow (i.e. leakoff) may cause further fluid exchange between the fracture and formation (Figure 3.3). The significance of this flow depends on the formation permeability, failure surface conditions and pressure difference between fluid inside the crack and pressure of fluid inside the formation. The normal flow, which is defined based on Darcy's Law, occurs in the fracture zone

$$q_b = c_b(p - p_f), \qquad \textbf{(3.3)}$$

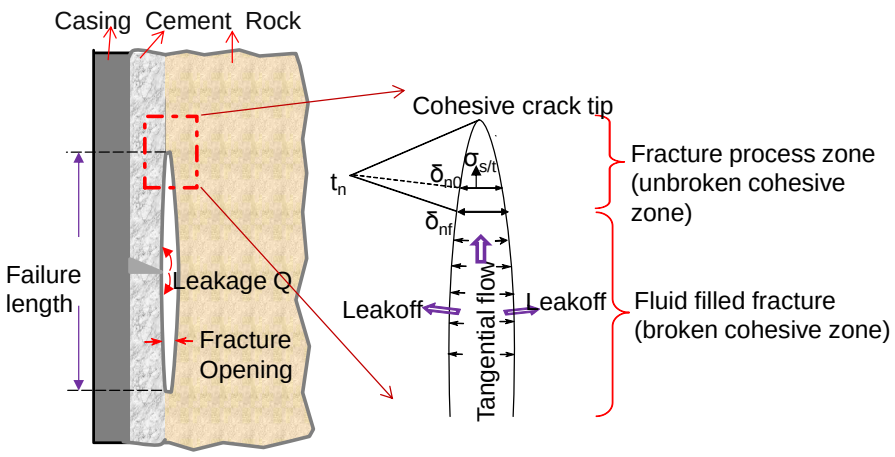

Figure 3.3 Schematic picture of normal and tangential fluid flow through opened fracture after cement failure.

where p_f is the fluid pore pressure in the formation adjacent to the fracture surface. The parameter c_b is the fluid leakoff coefficient, which is closely related to the effective permeability of the fracture surfaces.

We assumed that rock is fully saturated with the liquid. To incorporate pore elastic behavior of the rock, Biot's (1941) linear poroelasticity model is used to calculate stress and displacement distributions. Force equilibrium is the first equation to be satisfied

$$S_{ij,j} = 0, \qquad \textbf{(3.4)}$$

where S_{ij} are total stress components. Biot defined effective stress, S'_{ij}, as the part of the total stress that is applied to the solid skeleton of the rock that causes deformation and defined by the following relationship

$$S_{ij}' = S_{ij} - \alpha P \delta_{ij}, \qquad \textbf{(3.5)}$$

where P is the pore fluid pressure and α is the so-called Biot's constant. Here, we ignore any potential plastic deformation in the rock and cement. We also consider rock as a linear isotropic elastic material. Substituting Eq. (3.1), Eq. (3.4) and Eq. (3.5) into the constitutive equation, a relationship is derived to relate stresses, strains and pore fluid pressure. The resultant equations for rock and fluid interactions can be written as (Wang, 2000)

$$2Ge_{ij} = S_{ij} - v\sigma_{kk}\delta_{ij} + \alpha(1-2v)\delta_{ij}P + \beta\delta_{ij}T \quad , \quad \text{and} \tag{3.6}$$

$$2G\varsigma = \alpha(1-2v)S_{kk} + \frac{\alpha^2(1-2v)^2}{v_u - v}P - 2G\beta_f T \quad , \tag{3.7}$$

where G and v are the shear modulus and the Poisson's ratio of the rock, respectively. All the parameters used in the chapter are listed in the nomenclature at the end of the chapter.

The equations presented in this section describe displacement and stress distributions but these equations do not predict onset of fracture initiation and subsequent propagation of these fractures. Fractures may form whenever stress in any part of the material exceeds its strength, which could be shear stress, normal stress, or any combination of them. The most common method of modeling fracture propagation is the Griffith's criterion; however, this criterion can only predict propagation of pre-existing fractures, not their initiation. In this chapter, a cohesive interface approach is used to fill this gap. Description of this approach is provided in the next section.

Propagation of Fluid-Driven Fractures

The most challenging issue in modeling cement integrity is modeling initiation and propagation of interfacial cracks (delamination fractures), which are initiated by excessive fluid pressure inside the fractures. To overcome limitations of Griffith's criterion, cohesive crack theory has been used extensively for different engineering applications. Dugdale (1960) and Barenblatt (1962) originally proposed the cohesive zone approach to model the processing zone close to fracture tips in ductile materials. Further developments of this technique showed that this method can be used for problems with pre-defined fracture paths. This method can easily overcome complexities involved in common fracture propagation, by removing stress singularity at the fracture tips. As a consequence, this method can effectively reduce the computational burden raised by stress singularity at the fracture tips. Moreover, cohesive interfaces can be easily and dynamically incorporated into classic finite element frameworks as cohesive elements to update locations for crack initiation and propagation. These advantages make cohesive crack theory a suitable candidate for multiple crack growths in heterogeneous media (Yang, et al., 2009), as well as the

interface delamination along two dissimilar materials, such as an interface between ductile and elastic materials, or between two elastic-plastic materials (Hutchinson, 1990, Xie and Gerstle 1995, and Tvergaard, 2001). The cohesive zone framework has also been successfully applied to model fractures in cement-based materials (Hillerborg et al., 1976) and geomechanics problems like hydraulic fracturing (Sarris and Papanastasiou, 2011, Carrier and Granet, 2011). Successful applications in the past made the cohesive zone model a reliable and powerful tool to model interfacial delamination fractures among casing, cement and formation systems, and are a basis for the model examined in this chapter.

In the cohesive crack modeling approach, the cohesive zone is a predefined failure path with zero width and acts as an intact material before failure. In the failure zone, cohesive forces resist against the opening forces. The cohesive interface starts to open when the tractions applied to the interface are tensile. Once tractions reach a critical point, damage starts to appear, this is the basis for the traction separation law (Tvergaard and Hutchinson, 1996) shown in Figure 3.4. Meanwhile, the energy re-dissipates in the fracture processing zone; complete damage occurs when this energy is greater than the critical fracture energy, that's when cracks start to propagate (Xie, 1995). The traction separation law has been proposed in various types of relationships for different materials (for instance, see Shet and Chandra, 2002). Bilinear or triangular traction separation law has been adopted here following its successful applications in characterizing fracture processes in brittle materials, especially concrete structures (Hillerborg, et al. 1976, Davila, et al. 2001).

Typical bilinear softening curves for pure normal and shear loadings are illustrated in Figure 3.4a and b, respectively. When the traction in normal (or shear) direction, t_{n0} (or t_{s0}), reaches the critical strength, K_{n0} (or K_{s0}), or equivalently it reaches critical separation, δ_{n0} (or δ_{s0}), the fracture initiates in the previously assumed intact rock. Beyond this critical point, the process zone starts to undergo plastic deformations and micro-cracking under the tension (and or shear) tractions, which is the so-called softening transition zone between the complete failure zone and the undamaged material. The transition zone ends when tractions diminish, which is the complete failure point. When complete failure points are

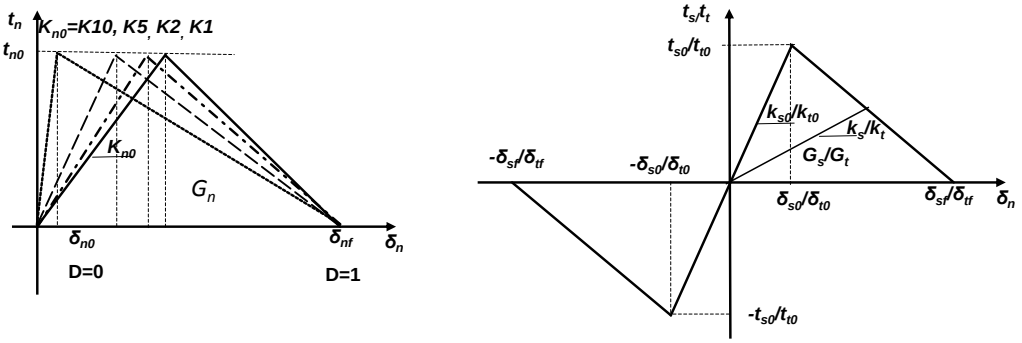

Figure 3.4 Linear Softening traction-separation law for the cohesive element under pure normal loading (left) and pure shear loading (right).

reached, the cohesive forces between the crack faces are gone, the relative displacement reaches the second critical value, δ_{nf} (δ_{sf} in shear) and the total fracture energy, G_c, is dissipated. For the bilinear traction separation law, the propagation critical energy, which is the minimum energy needed to propagate a crack can be described by

$$G_c = \frac{1}{2} t_0 \delta_f \,. \qquad \textbf{(3.8)}$$

Bilinear traction separation laws are defined for pure normal and shear loading modes, whereas general loading conditions could entail any arbitrary combination of normal and shear loading (mixed mode problem), therefore, it is necessary to consider the combinatory effect of normal and shear loadings. Moreover, damage onset and the corresponding softening behavior under mixed-mode loading may occur before any of the involved traction components reach their respective pure mode failure criteria (Camanho and Dávila, 2002b). The typical mixed mode failure characteristics can be represented by a quadratic failure criterion, which is more successful in prediction of the onset of delamination in previous investigations for mixed-mode problems (Cui et al., 1992, Camanho and Matthews, 1999). Damage initiates when a quadratic interaction function involving nominal stress ratios (Camacho and Ortiz, 1996) reaches one i.e.

$$\left\{\frac{\langle t_n \rangle}{t_{n0}}\right\}^2 + \left\{\frac{t_s}{t_{s0}}\right\}^2 + \left\{\frac{t_t}{t_{t0}}\right\}^2 = 1, \qquad \textbf{(3.9)}$$

where t_n , t_s and t_t represent the real values of normal and tangential (first and second shear) tractions across the interface, respectively. < > is the Macaulay bracket defined as

$$\langle t_n \rangle = \begin{cases} t_n, \ t_n \geq 0 & (tension) \\ 0, \ t_n < 0 & (compression) \end{cases} . \quad \textbf{(3.10)}$$

The metric for damage is a scalar stiffness degradation index, D , which represents the overall damage of the interface caused by all stress components. The stiffness degradation index is a function of the so-called effective relative displacements, δ_m by combining the tributes of δ_t , δ_s and δ_n ,

$$\delta_m = \sqrt{\langle \delta_n \rangle^2 + \delta_s{}^2 + \delta_t{}^2} . \quad \textbf{(3.11)}$$

For linear softening failures, the damage evolves with the index (Chen, et al., 1999)

$$D = \frac{\delta_{mf}\left(\delta_{m,\max} - \delta_{m0}\right)}{\delta_{m,\max}\left(\delta_{mf} - \delta_{m0}\right)}, \quad \textbf{(3.12)}$$

where $\delta_{m,\max}$ is the maximum effective relative displacement attained during loading history. δ_{m0} and δ_{mf} are the effective relative displacements corresponding to normal and shear deformations as shown in Figure 3.4.

Numerical Model

A coupled field-scale three dimensional poroelastic model shown in Figure 3.5 is used to investigate the cement integrity and failure patterns discussed in the previous section. The effects of cement heterogeneity, casing eccentricity, wellbore inclination, and in-situ stress anisotropy are investigated with this model. This model is consisted of casing, cement, rock and interfaces between cement with casing and formation. A cemented 7-in casing is located inside an 8-½ in borehole. The weight of the fluid inside the wellbore is assumed to be 9.3 lbm/gal. The leakage point around the casing shoe is located at the depth of 1923 m, which is in the middle of the finite element model. The leakage around the casing zone could have been originated from insufficient cement during placement, cement deterioration with time or

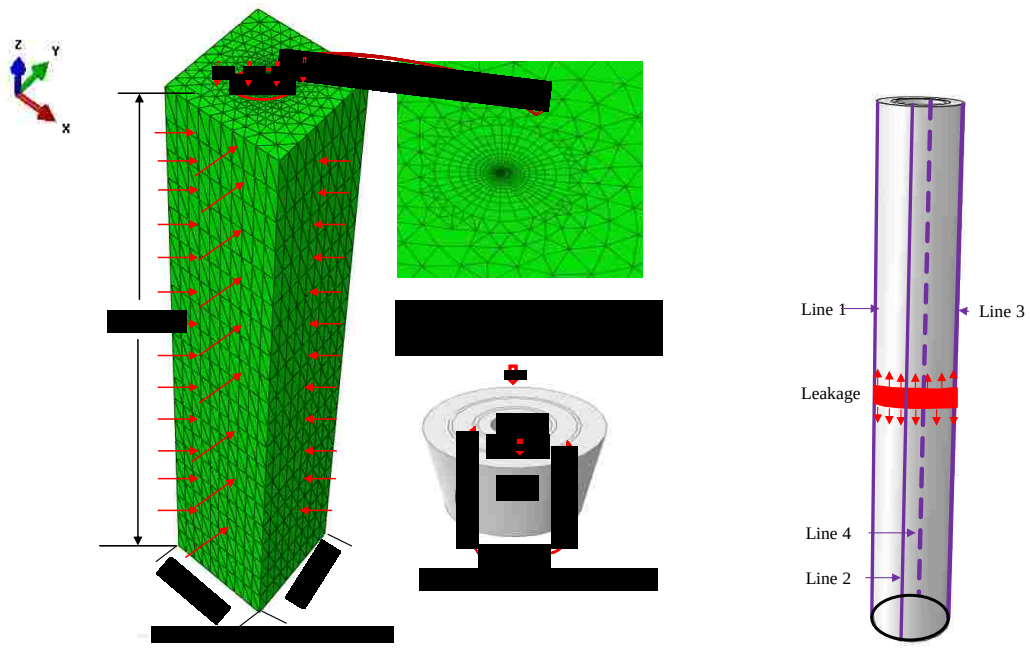

Figure 3.5 (a) A schematic picture of the numerical model with dimensions, boundary and loading conditions, and meshes for the three dimensional model. (b) this picture demonstrates the leakage position.

other issues. The leakage is driven by a pressure source charged by a deeper charging zone. Rock mechanical properties used in the model are borrowed from the rock physics handbook (Hall, et al., 2006) or from measurements reported in the literature (for instance Ballard, et al., 1994, Reeves, et al., 2006, Cosgrove, 2006, Mueller and Eid, 2006, and Lecampion, 2011). Values used for cement, casing, and rock interface properties are listed in the appendix. Casing, cement and formation, which are all homogeneous elastic materials with different properties, are bonded together along an interface as the potential failure path. Cohesive properties are introduced to layers of cohesive elements with zero thickness along cement interfaces. A fine mesh is placed near the wellbore to guarantee numerical convergence, and to properly capturing the details of stress redistribution within the cohesive zone during failure. Coarser elements are utilized far from the wellbore in order to reduce the computational costs. 1260, 2520, and 30,177 elements are used to mesh casing, cement, and the surrounding rock, respectively. A layer of eight- node three-dimensional cohesive elements with 1260 elements is used as the cohesive layer between casing and rock.

Pore pressure is coupled with cohesive elements by inserting four degrees of freedom in the middle layer of each cohesive element to improve continuity.

In order to make interpretation of the simulation results and comparison with analytical solutions easier, we assumed materials on either side of the interface are linearly elastic and isotropic. However using more complex material properties can be simply included in the model. The simulation is consisted of three steps. At the first step, initial equilibrium is achieved by assigning initial geostatic stress to each element, and assigning initial hydrostatic pore pressure to each node. No failure occurs during the equilibrium process because everything is at equilibrium and failure is assumed to be initiated by excessive pressure; then at the second step, excessive pore pressure (16,000 KPa) accumulates gradually following a linear buildup around the casing shoe. Finally, excessive energy added to the system by leakage source dissipates by fracture the rock and viscous dissipation of the fluid inside the fracture.

In order to eliminate the effects of parameters' dimensions and better understanding the physics of the problem, dimensionless parameters give a better insight into the problem. Dimensionless pressure, stress, crack length, time, crack opening and slippage are used to demonstrate initiation and propagation of the delamination cracks. First, let's define dimensionless time based on the wellbore radius and poroelastic diffusion coefficient (Detournay and Cheng, 1991) as

$$t^* = \frac{c \cdot t}{r_w^2}. \qquad \textbf{(3.13)}$$

The constant c in the above equation is the poroelastic diffusivity coefficient, which is different from the usual diffusivity and determined by

$$c = \frac{2KG(1-v)(v_u - v)}{\alpha^2 (1-2v)^2 (1-v_u)}, \qquad \textbf{(3.14)}$$

where K is the fluid mobility; ν is the drained Poisson's ratio; ν_u is undrained Poisson's ratio; t^* denotes dimensionless time; t denotes real time, in seconds; r_w denotes wellbore radius; α is the Biot-Willis coefficient.

Dimensionless length is simply defined by normalization with respect to the wellbore radius,

$$L^* = \frac{L_f}{r_w}, \tag{3.15}$$

where L^* denotes dimensionless crack length; L_f denotes the length of the failure zone. Similarly, dimensionless fracture width, Δw^*, is defined with respect to the wellbore radius. Dimensionless fracture opening and slippage are simply defined by normalization with respect to the wellbore radius, respectively

$$u_n{}^* = \frac{u_n E'}{P r_w}, \qquad u_s{}^* = \frac{u_s E'}{P r_w}, \tag{3.16}$$

where $u_n{}^*$ or $u_s{}^*$ denotes dimensionless fracture opening or slippage; u_n and u_s denote the fracture opening and slippage, respectively; $E' = E/(1-\nu^2)$, where E is the rock Young's modulus; and P is the pressure inside the rock. A similar definition has been used by Gordeliy et al. (2013) for a cylindrical crack embedded in an infinite domain. Dimensionless stress, S*, is defined as

$$S^* = \frac{S}{E}, \tag{3.17}$$

where S is stress, and E is the rock Young's modulus. Then, dimensionless pore pressure is defined as

$$P_P^* = \frac{P_P}{P_0}, \tag{3.18}$$

where P_0 is the initial pore pressure; P_p is the current pore pressure. The results and discussions presented in the following sections are based on the dimensionless parameters listed above. We first start with a

basic case: a vertical well with homogeneous and uniform cement properties exposed to a highly pressurized zone.

Vertical Well with Homogeneous Cement Properties

Wellbore system is considered as a cylinder embedded in an infinite formation. We are solving the problem of a cylindrical crack on the interface between the cement and an infinite elastic medium under pressurized fluid. We suppose that the two elastic bodies (cement and rock) are originally perfectly bonded. The driving force which is generated from the leaking at casing shoe tries to separate from each other. Cement failure is initiated by the pressurized fluid, and expanded from the leakage zone over time. The failure progress, represented by the dimensionless crack-length changes versus dimensionless time, shows that failure is not starting until the magnitude of the excessive pressure reaches a critical value (P_1* in Figure 3.6); upon reaching the critical threshold, failure advances rapidly. As soon as damage initiates in the system, the induced stresses at the fracture tips are large enough to propagate fractures. The critical

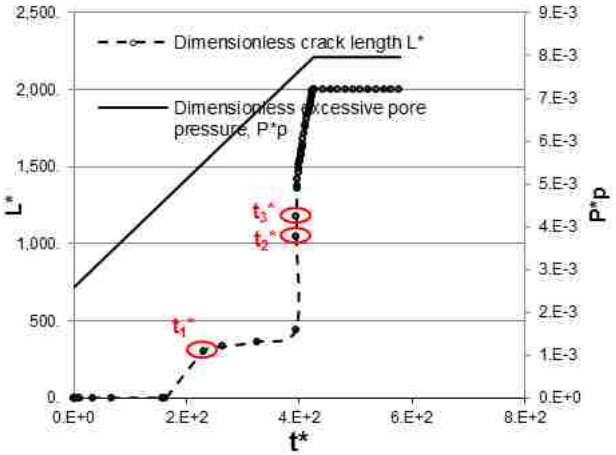

Figure 3.6 Buildup process of excessive fluid pressure in the leaking casing shoe and its inducing failure lengths around the wellbore is shown versus dimensionless time.

pressure is determined by the interfacial properties, cement and formation properties, rock in situ stresses, and the magnitude of excessive pressure. The induced damage changes local hydraulic conductivity and pore fluid pressure along the cement interface. Fluid pressure distribution during failure propagation from the leakage point is demonstrated in Figure 3.6. Excessive fluid pressure gradually builds up at the leakage zone without spreading much along the interface by leakoff, as a consequence, failure zone

expands. The leakage of fluid to the formation and cement is much less than the fluid flow in the interface, which is attributed to the higher fluid conductivity through the induced conduit in the interface in comparison with that of the low permeability cements.

Compressive in situ stresses in the rock resist against further propagation of delamination fractures, but excessive fluid pressure at the source, buoyancy forces and lower in situ stresses in shallower zones facilitate upward fracture propagation. Depending on the magnitude of these opposite drives and the strength of the cement interface, the delamination fracture may stop after propagation for a while or it may propagate uncontrollably to shallow aquifers or even to the surface. Figure 3.7 shows the fluid pressure profile at different stages of failure propagation (associated with t_1*, t_2*, and t_3* in Figure 3.6), and fluid pressure profile along the casing as shown in Figure 3.5b at Stage t_2*. We can observe that

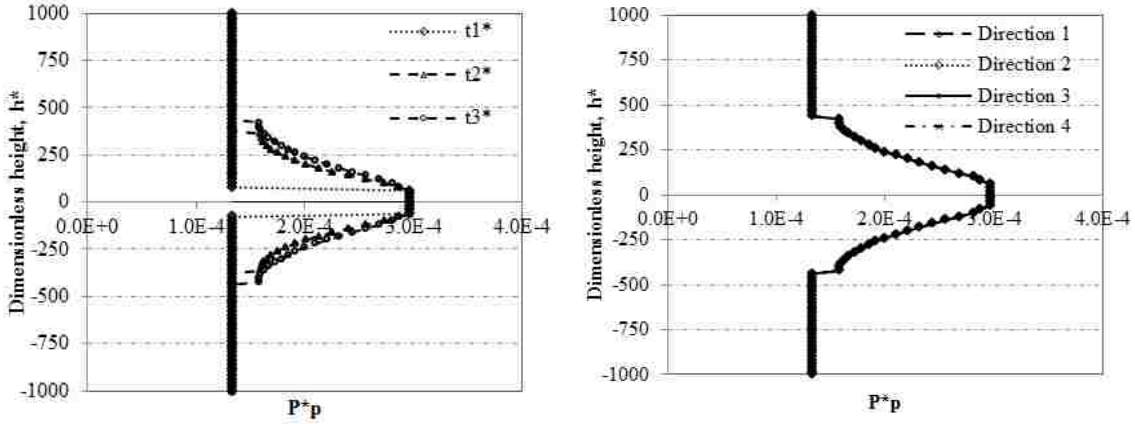

(a) Fluid pressure distribution at different time steps **(b) Fluid pressure along different directions at t_2***

Figure 3.7 Pore pressure buildup process along four directions of cement liner at different stages (t_3*>t_2*>t_1* shown in Figure 3.6).

excessive fluid pressure distributes along the wellbore with the accumulation of fluid pressure. Moreover, uniform fluid pressure distribution is observed around the wellbore in this case due to symmetry in loading and identical elastic properties across the interface.

Following changes in the fluid pressure, the distribution of normal and shear stresses along the cement liner undergoes changes to satisfy the equilibrium condition. The originally compressive stresses are disturbed by the fluid injection at the leakage zone. In order to simulate failure propagation process,

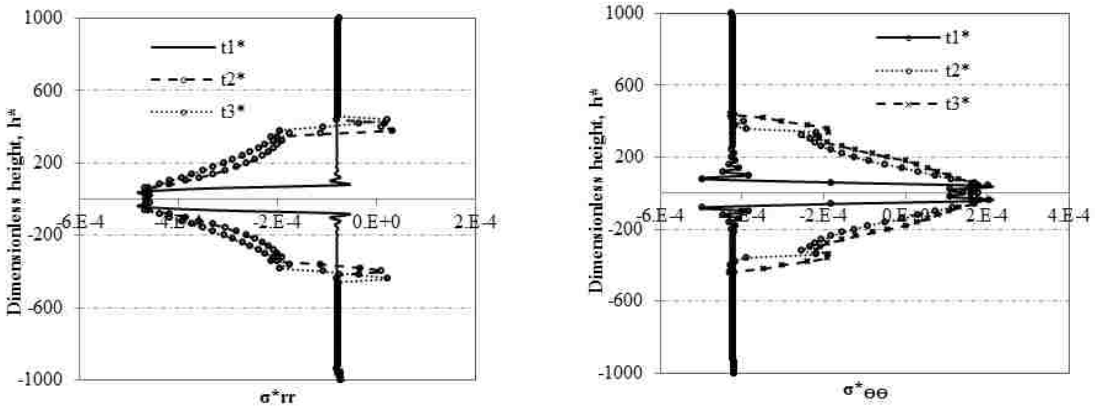

(a) Normal traction σ_{rr} **(b) Tangential traction $\sigma_{\theta\theta}$**

Figure 3.8 Normal and tangential stresses along the cement liner during the loading process at different dimensionless time $t_3^*>t_2^*>t_1^*$, where t_3^*, t_2^*, and t_1^* indicate dimensionless times shown in Figure 3.6.

normal and tangential tractions along the cement liner at three stages are shown in Figure 3.8. These three stages are designated by t_1^*, t_2^* and t_3^* in Figure 3.6. It can be observed that excessive fluid pressure induce tensile stress ahead of the fracture tip along the cement-rock interface. Due to the small length of the tensile zone, fine mesh is required to catch large stress gradient close to the fracture front. The fluid-pressure drops abruptly near the visual tip. The pressure ahead of the fracture tip decreases to values below the initial formation pressure and far away from the tips tends asymptotically to its initial undisturbed value. The results reveal that the tensile stress is contained in small region near the tip with its maximum value equal to the assumed tensile strength of the interface between cement and rock. During the fracturing process, there is a relief of the compressive stresses ahead of the fracture tip followed by a complete separation when the crack-opening reaches the critical value defined in the propagation criterion. This suggests that rigid-softening cohesive behavior provides higher constraint ability for fluid leaking prevention. It is worthwhile to mention that the maximum of shear stresses occurs close to the fracture tip, but its fluctuation is noticeably smaller, at least two orders of magnitudes, than normal and tangential stresses; therefore, shear stresses along the failure zones are not plotted here due to their less dominant effects on failure initiation and propagation. If the combination of stresses exceeds the failure initiation condition, the crack would be necessarily open at the crack tip, and mixed mode

conditions would pertain. This phenomenon is in agreement with previous discussions in the literature that pressurized fractures in cylindrical geometry are inherently mixed mode with Mode I as the dominant mode (Farris et al, 1989, and Dhaliwal et al, 1992).

Failure distributions at four directions along the cement liner are analyzed based on normal and tangential tractions distribution. The stress distributions are demonstrated in Figure 3.9 for directions

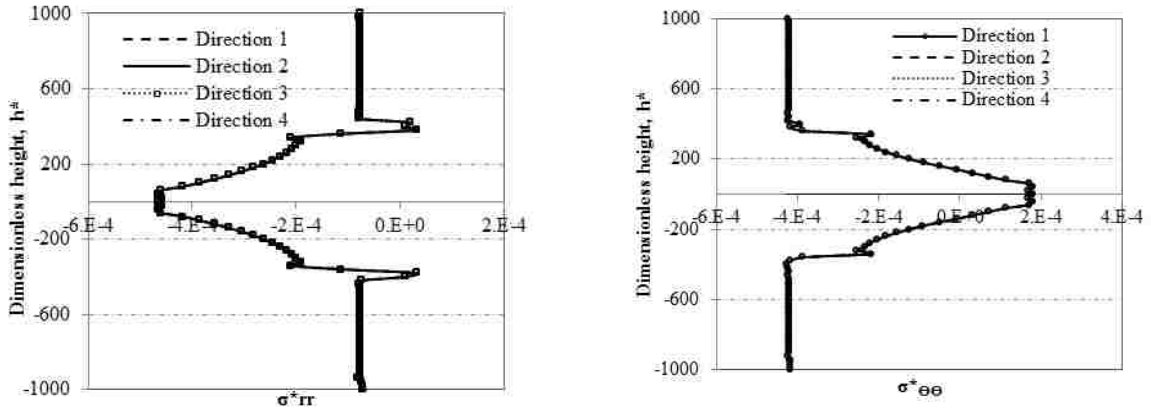

(a) Normal traction σ_{rr} **(b) Tangential traction $\sigma_{\theta\theta}$**

Figure 3.9 Normal and tangential stresses along the cement liner during the loading process at different directions. These four directions are illustrated in Figure 3.5.

shown in Figure 3.6. The uniform stress distributions can be seen around the wellbore, which is an indication of stable propagation of the fracture front in uniform order.

Additionally, the failure distributions at different directions for two stages (t_2* and t_3*) are shown in Figure 3.10. Failure propagation process is demonstrated based on damage index directly. It can be seen that damage initiates uniformly at the leakage zone and propagates uniformly around the wellbore at t_2*. However, this uniformity is only a transition process, which is quickly disrupted by further fluid migration. In this case, when excessive fluid pressure accumulates till time t_3*, the failure uniformity tends to fall apart, especially in the zones far from the leakage source. The non-uniform failure patterns are observed at four typical directions of the wellbore and obviously occur close to the crack tip. This failure non-uniformity exists even though the system with symmetric in situ stress, symmetric geometry, and uniform cement properties. The non-uniform phenomenon around the wellbore indicates complexity

of the failure propagation process due to the nonlinear nature of the equations governing cement mechanical behavior. Understanding this process could be beneficial for corrections of the average

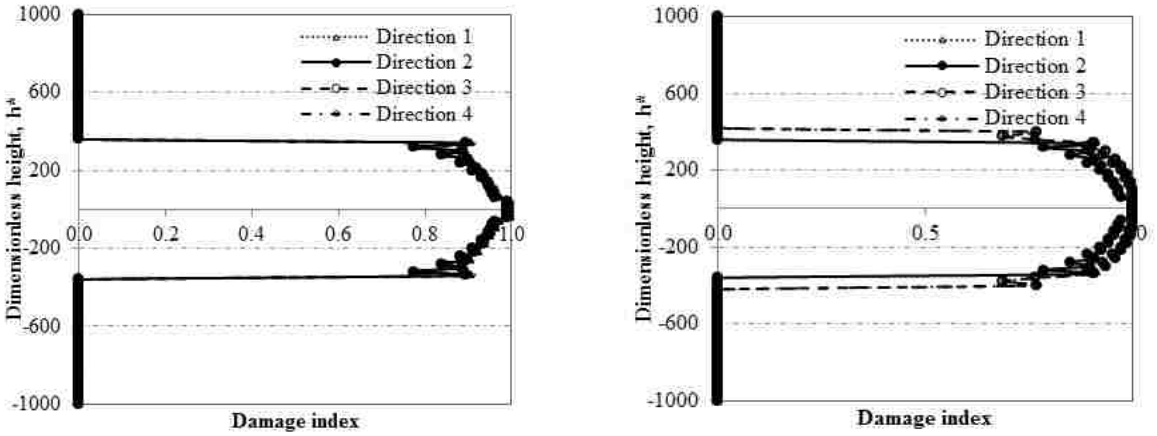

(a) Damage along four directions at t^*_2 **(b) Damage along four directions at t^*_3**

Figure 3.10 Damage in four directions of cement liner at specific stages (t^*_2 and t^*_3) shown in Figure 6 are demonstrated. These four directions are illustrated in Figure 3.5.

measurements provided by traditional failure detection tools such as cement bond logs and ultrasonic bond logs. The changes in the slop of fracture propagation length versus time in Figure 3.6 could be an indication of onset of instability at the fracture front.

Influence of Rock and Cement Properties on Failure

There are a multitude of parameters characterizing the cement and rock properties with a variety of failure behaviors, hence a synoptic discussion about the importance of different parameters on wellbore integrity is provided here. The parameters used for sensitivity analysis include cohesive properties of cement such as maximum normal strength (σ_{max}), maximum shear strength (τ_{max}), fracture energy (G_c), and cohesive interface stiffness (K_n). The effect of elastic properties of cement and formation rock, such as Young's modulus and Poisson's ratio, are considered as well. Despite the large number of parameters involved as listed in the appendix, the focus of this research is mainly on the effect of few essential parameters. To cause failure, an additional 16,000 KPa pressure is gradually and linearly accumulated around the leakage points as shown in Figure 3.6.

The onset of failure and its propagation is dependent on the adhesion ability of the cement to the formation and casing, hence cohesive interface parameters could be the determining parameters for fracture containment. We first conduct the sensitivity analysis on cement cohesive properties. To avoid interference with other properties, we assumed similar mechanical properties for rock and cement, similar Young's modulus (E) and Poisson's ratio (υ). We first conduct parametric analysis for cohesive constitutive equation to simulate the effect of transition from rigid-softening to elastic-softening behavior. Rigid-softening to elastic-softening transition can be represented by low to high cohesive stiffness, K_n, values (Figure 3.4) by keeping fracture energy constant. The rigid-softening behavior corresponds to stiff formation's rock (brittle behavior) whereas the elastic-softening behavior corresponds to soft formation's rock or ductile rocks (Sarris and Papanastasiou, 2011). In an attempt to investigate the influence of cohesive stiffness on the failure, five cases with K_n of 0.5, 1, 2, 5, and 10 times the slope of the traction separation curve are considered. The base case, K_n (×1) corresponds to elastic-softening behavior, and the K_n (×10) corresponds to rigid-softening behavior. Other properties including the maximum strength and fracture energy are the same for all cases similar to traction-separation curves shown in Figure 3.4. The crack lengths shown in Figure 3.11a demonstrate the failure developments for cases with different cohesive stiffness. The fracture lengths in the elastic-softening case, which corresponds to K_n (×1), shows longer fracture than those in rigid-softening case (K_n ×10). For a given excessive pressure, the elastic-softening cement undergoes a much longer failure zone compared to the rigid-softening cases, because fracture opening has the main rule for providing fluid conductivity and further fracture propagation is limited in situations with very large K_n.

Figure 3.11b shows the fluid pressure profile in the fracture during propagation. Results show that higher pressure is needed to propagate the fracture along the interface with higher cement stiffness. The pressure drop at the crack tip is more pronounced in the case with higher cement stiffness compared to the pressure drop in the case with lower cement stiffness. The pressure ahead of the fracture tip decreases to

values below the initial formation pressure, and the pressure in the undamaged zone that is far away from the tips tends asymptotically to its initial undisturbed value.

Normal and shear strength of the interface, which determine the elastic locking between bonded solid materials, may intuitively have significant effects on cement-rock interface integrity. Depending on

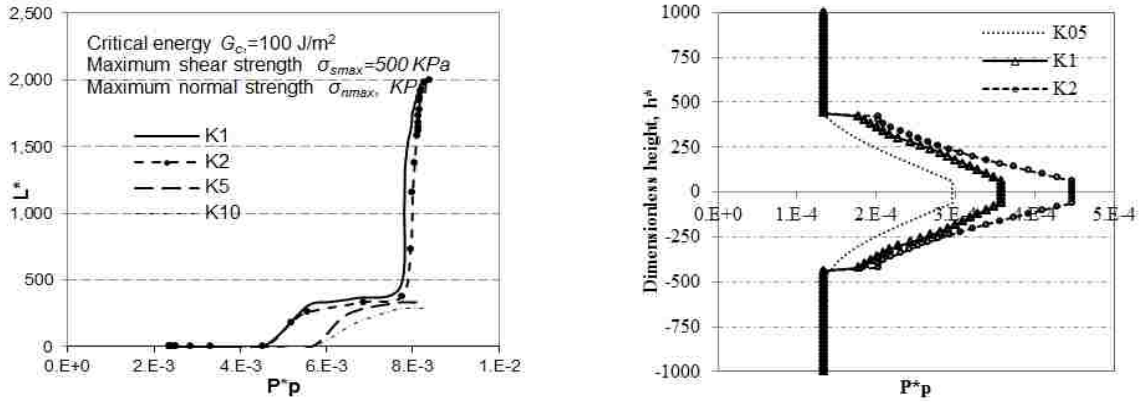

(a) Crack length **(b) Fluid pressure**

Figure 3.11 Crack lengths and fluid pressure profile along fracture for different cohesive stiffness are demonstrated.

presence of mudcake and its thickness, rock fabric and its permeability, water content of cement during setting time, the adhesive strength of cement to the formation rock could be very different (Parcevaux, 1984 Carter and Evans, 1964, and Carpenter et al, 1992). Hence, we consider a wide range of value for normal and shear strength of cement interface ranging from 200 KPa to 2000 KPa to check the wellbore integrity. We assume other properties like toughness to be constant. Fracture propagation versus excessive pressure is plotted in Figure 3.12a, the fracture opening versus dimensionless height is shown in Figure 3.12b as direct indicators of fracture development along the casing. It can be seen that it is difficult for the fracture to propagate in situations with high normal strength (2000 KPa) even with high excessive fluid pressure. However, the cement-rock interface is easier to be broken if maximum normal strength is smaller. This phenomenon indicates that maximum normal strength has a dominant effect on blocking fast failure propagation. Figure 3.12b shows that the fracture width profiles were almost doubled when the maximum normal strength is 1000 KPa relative to the case with low normal strength. Apparently, the

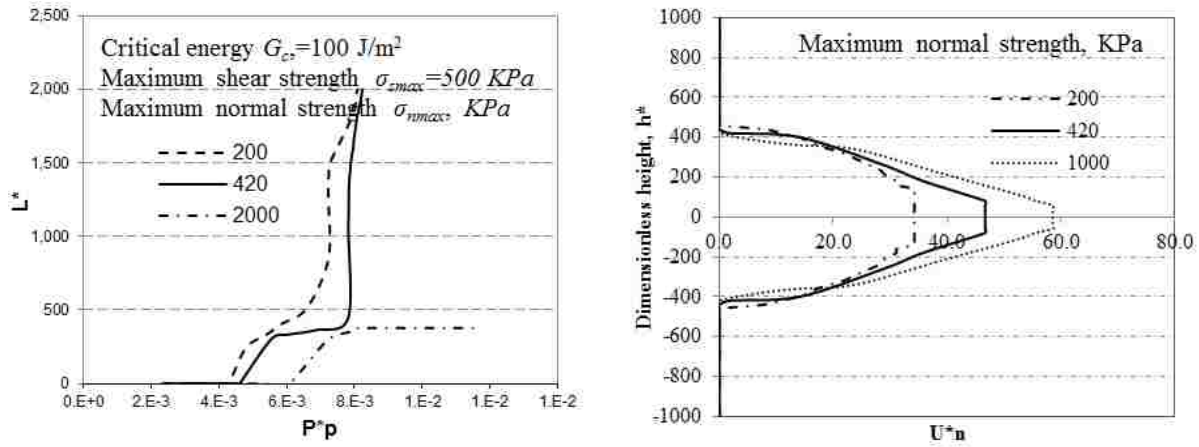

(a) Crack length **(b) Fracture width**

Figure 3.12 Comparison of crack lengths and fracture opening along the cement liner for different maximum normal stresses during pore pressure buildup and subsequent equilibrium process.

higher maximum normal strength of the interface is significant in constraining failure propagation around the wellbore, however, it is not practically possible to obtain a cement with such a high normal strength in the market.

A similar phenomenon occurs with the variation in maximum shear strength as maximum normal and

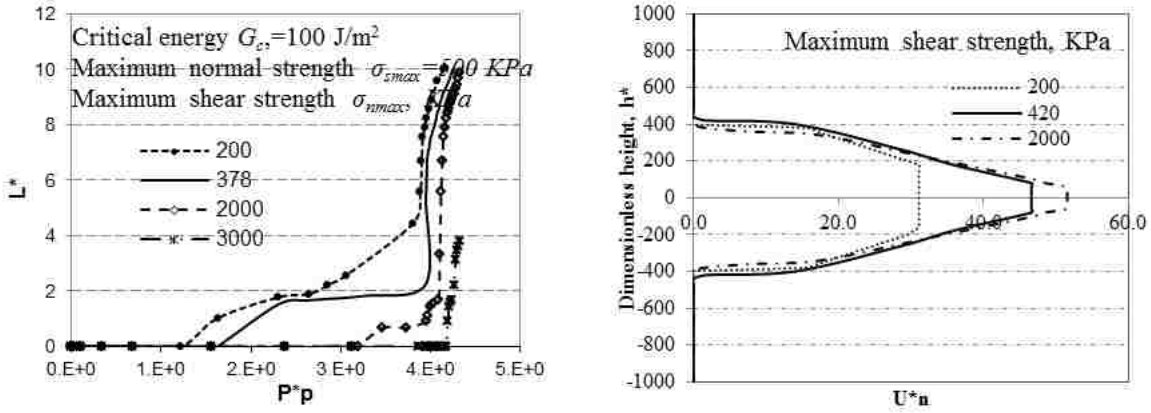

(a) Crack length **(b) Fracture width**

Figure 3.13 The comparisons of crack lengths for different maximum shear strength.

shear strength are both resisting factors against crack initiation. However, maximum normal and shear strength have different effects on failure initiation, which is governed by the complex nature of mixed mode failure. Comparing crack lengths and widths in Figure 3.12, the broaching around the wellbore as

shown in Figure 3.13 occurs even when the maximum shear strength reaches 2000 KPa, which is the blocking strength for maximum normal strength. In this case, when the maximum shear strength reaches 3000 KPa, there is enough strength for maintaining interface integrity, which indicates the less dominant effect that shear strength plays in the Mode I prevailing mixed mode system. The increase of shear strength at the interface can be achieved by better removal of mud remnant in the borehole and gratings on exterior surface of the casing.

The fracture propagation depends essentially on the flux of energy into the fracture process zone at the crack front, which can be compared with the critical energy for fracture growth. The toughness of the interface is the energy needed to create the two free surfaces along the interface. In an "ideally brittle" interface, the toughness is equal to critical energy. Hence, the energy flux is characteristic of the structure and is independent of the stress and strain distributions near the fracture front (Bazănt and Oh, 1983). However, energy is an important parameter because it largely determines the failure propagation ability. The roles that critical energy plays on the interface integrity are evaluated by fracture length and width as demonstrated in Figure 3.14. It can be observed that when critical energy is low (which are 50 J/m^2 and 100 J/m^2), similar uncontrolled crack broaching process occurred during the excessive pressure accumulation. On the other hand, when the critical energy is higher, broaching does not occur even in a

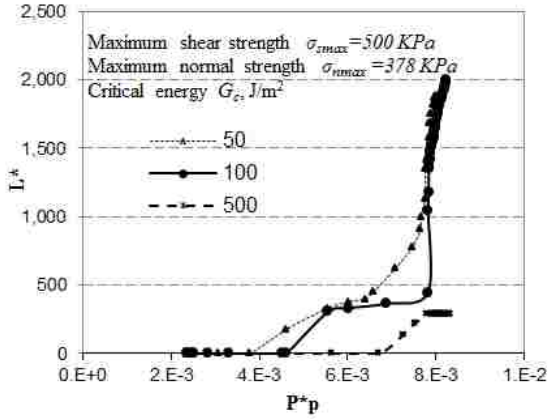

Figure 3.14 The comparisons of crack lengths with cohesive critical energy influenced by critical energy during fluid pressure buildup and subsequent equilibrium process.

larger pressure because the energy provided in the system is insufficient to push for progressive failure propagation.

Cylindrical interface crack propagation is also influenced by mechanical properties of cement and rock. When there is a significant mismatch in the elastic properties, which might be represented by large difference in Young's modulus, the cement-rock interface integrity could be different. In order to clarify this difference, three cases with different Young's modulus ratios of cement to rock, i.e. 0.8, 1.0 and 2.0, are presented to illustrate the influences of cement moduli on cement integrity during failure propagation process. Figure 3.15 (a) and (b) record the crack length and fracture opening during the process of

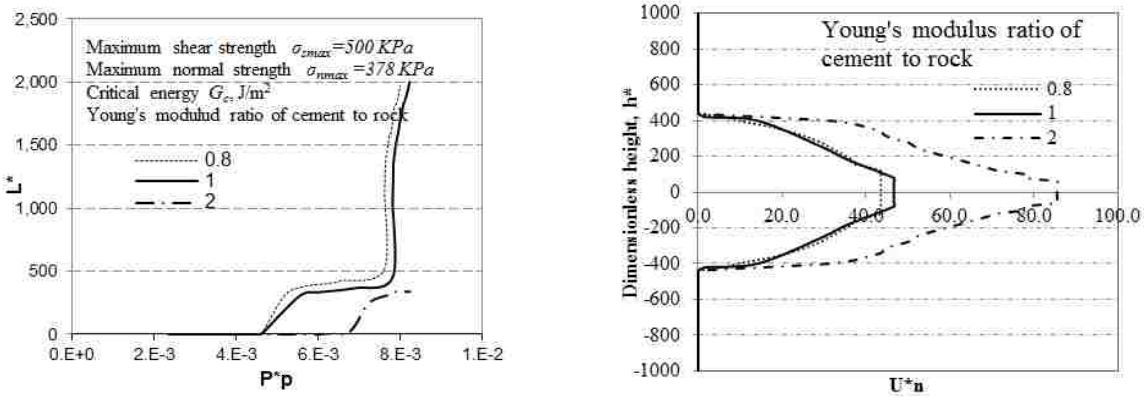

(b) Crack length **(b) Fracture width**

Figure 3.15 The comparisons of crack length and fracture opening along the cement liner influenced by Young's modulus during fluid pressure buildup and subsequent equilibrium process.

excessive fluid pressure buildup in the poroelastic solids for the cases with different Young's modulus ratios. The objective of these calculations was to investigate the containment capacity when adjusting the rigidness of cement, which is represented by cement Young's modulus. Results show that the higher excessive energy is needed to obtain the same crack length along the rigid cement interface (high Young's modulus in the cement). Moreover, the capacity of cement integrity is improved if increasing the Young's modulus of cement, because hard formations are stiff and generate large stresses, which increase the likelihood of debonding in the presence of high internal pressure.

To further investigate the effect of cement properties on wellbore integrity, cements with different Poisson's ratio have been modeled to understand the potential role of this parameter. As shown in Figure 3.16, expansion and contraction of cement defined by the variation of Poisson's ratio do not have a serious effect on the prevention of failure broaching.

Conclusions

A three-dimensional model is built using cohesive zone approach to predict wellbore integrity, and analyze the mechanism of failure propagation along the wellbore. A set of fully coupled models are simulated with the finite element methods with predefined potential failure paths without any assumption about the initial crack size and location. This 3D model has the capacity to predict spatial failure patterns

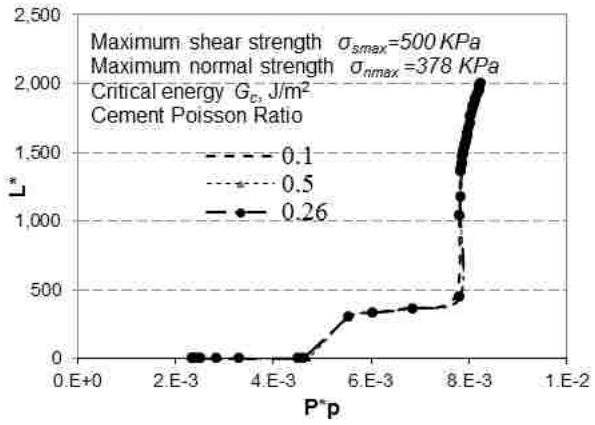

Figure 3.16 The comparisons of crack length along the cement liner for different values of Cement Poisson's ratio.

and their relative stress and fluid pressure distributions around the wellbore, which makes it more advanced than traditional two-dimensional models where failure paths are only limited to the direction parallel to the borehole axis. On one hand, this model can effectively characterize crack tip to track failure initiation mechanism, which can be demonstrated by the combination of tensile stress and shear stress based on quadratic traction separation law. On the other hand, the application of the cohesive zone approach can effectively avoid the complex calculation involved in stress singularity.

Our simulations investigated the mechanism of crack emergence and propagation near the wellbore by analyzing the variation of pore pressure, stresses, fracture opening, and damage around the wellbore. The

excessive fluid pressure induced due to leakage is the drive for the cement-formation interface failures. The non-uniformity failure exists even though the system with symmetric in situ stress, symmetric geometry, and uniform cement properties. The non-uniform phenomenon indicates the complexity of failure propagation process due to the nonlinear nature of the equations governing cement mechanical behavior. The non-uniformity around the failure front counteracts the limitations found in the average value of CBL, and provides a much deeper understanding of the failure distribution around the wellbore. Moreover, tensile residual stress and shear stresses observed at the crack tip of cement-rock interface gives important evidences for explaining the physical mechanism of the loss of wellbore integrity. The interface failure rate that is represented by the relationship between crack lengths and widths versus excessive fluid path is a combined function of the variation and fluctuation of pore pressure, normal and shear stresses, fracture opening, and energy distribution. Furthermore, interface failure and the hydraulic conductivity of the failure can further affect the pore pressure and stress distribution around the wellbore.

Additionally, we gave a synoptic discussion about the importance of different parameters on wellbore integrity. The possibility of fracture arrest or broaching is further investigated by field-scale sensitivity tests. From these sensitivity tests, the rigidness, normal (and shear) strength of the interface, and cement Young's modulus have been determined to be dominant parameters on fracture containment. It is found that larger values of cement stiffness, interface normal (or shear) strength, or the rigidness of cement can effectively reduce the possibility of failure broaching around the wellbore. It is noteworthy that sufficient non-linear behavior has been demonstrated in the calculated stress profiles from the bilinear behavior definition in cohesive models, giving confidence in the adequacy of simple softening relations in capturing the non-linear stress distribution ability along the failure zone, especially ahead of the crack tip.

Nomenclature

B Skempton's coefficient

C_t Fluid leak-off coefficients on the top surfaces of the fracture

c_b Fluid leak-off coefficients on the bottom surfaces of the fracture

D Scalar stiffness degradation index

E Rock Young's modulus, KPa

G Shear modulus of rock, KPa

G_c Critical fracture energies during deformation, J

G_n Work done by the tractions and their conjugate relative displacements in the normal directions, J

G_s Work done by the tractions and their conjugate relative displacements in first shear directions, J

G_t Work done by the tractions and their conjugate relative displacements in second shear directions, J

G_T Total energy in the mode-mix condition, J

k Permeability tensor

K Fluid mobility, m^2/KPa.s

k_n Stiffness components in normal direction

K_{n0} Initial tensile stiffness

K_{s0} Initial value for shear stiffness

k_s Stiffness components in shear direction

L_f Crack length, m

p_b Pore pressures in the adjacent poroelastic material on the bottom surfaces of the fracture, KPa

∇p_f Fluid pressure gradient along the cohesive zone

P_p Pore pressure, KPa

P_p * Dimensionless pore pressure

p_t Pore pressures in the adjacent poroelastic material on the top surfaces of the fracture, KPa

q Fluid flux, m^3/s

r_w Wellbore radius, m

$S*$ Dimensionless stress

S Effective stress, KPa

$t*$ Dimensionless time

t Real time, seconds

t_n Normal traction, KPa

t_{n0} Peak values of the nominal stress when the deformation is purely normal to the interface, KPa

t_{s0} Peak values of the nominal stress when the deformation is purely in shear direction, KPa

t_s Tangential traction, KPa

v Poisson's ratio

v_u Untrained Poisson's ratio

w Crack opening, m

$\Delta w*$ Dimensionless fracture delamination opening

α Biot-Willis coefficient

β Rock thermal expansions, 1/K

β_f Fluid thermal expansions, 1/K

$\Delta\delta*$ Dimensionless slippage displacement

δ_m Effective relative displacements, m

δ_{m0} Effective relative displacements corresponding to δ_{n0} and δ_{s0}, m

δ_{mf} Effective relative displacements corresponding to δ_{nf} and δ_{sf}, m

δ_n Crack opening displacement, m

δ_{nf} Critical relative normal displacements when tractions diminish, m

δ_s Crack sliding displacement, m

δ_{sf} Critical relative shear displacements when tractions diminish, m

ς Change of fluid content, m^3

η Material parameter

References

Aadnoy, B. S., Rogaland, R. C., and Chenevert, M. E., 1987, Stability of Highly Inclined Boreholes (includes associated papers 18596 and 18736), SPE Drilling Engineering, Vol. 2(4), pp: 364-374.

Ballard, T. J., Beare, S. P., and Lawless, T. A. 1994, Fundamentals of Shale Stabilization: Water Transport Through Shales, SPE 24974-PA, SPE Formation Evaluation, Vol. 9 (2), pp: 129-134.

Barenblatt, G. I., 1962, The Mathematical Theory of Equilibrium Cracks in Brittle Fracture, Journal of Applied Mechanics, 1962, pp: 7, 55-129.

Batchelor, G. K., 1967, An Introduction to Fluid Dynamics, Cambridge University Press, London, pp: 615-620.

Bazănt, Z. P., and Oh, B. H., 1983, Crack Band Theory for Fracture of Concrete, Materials and Structures, Vol. 16, pp. 155-177.

Bearden, W. G., and Lane, R. D., 1961, Engineered Cementing Operations to Eliminate WOC Time, SPE 61-017, Drilling and Production Practice.

Biot, M. A., 1941, General theory of three dimensional consolidation, J. Appl. Phys., 12(2), pp: 155–164.

Bois, A. P., Garnier, A., and Laudet, J. B., 2012, Use of a Mechanistic Model To Forecast Cement-Sheath Integrity, SPE Drilling & Completion, Vol. 27(2), pp: 303-314.

Bois, A. P., Garnier A., Rodot, F., Saint-Marc, J., and Aimard, N., 2011, How To Prevent Loss of Zonal Isolation Through a Comprehensive Analysis of Microannulus Formation, SPE 124719-PA, SPE Drilling & Completion, Vol. 26 (1), pp: 13-31.

Bour, D., 2005, Cyclic Steam Well Design: A New Approach to Solve an Old Problem of Cement Sheath Failure in Cyclic Steam Wells, SPE 93868-MS, SPE Western Regional Meeting, Irvine, California Mar 30 - Apr 01 2005.

Bourgoyne, A. T., Chenevert, M. E., Millheim, K. K., and Young, F. S., 1986, Applied Drilling Engineering, Society of Petroleum Engineering Vol. 2, pp: 312-324.

Camacho, G. T., and Ortiz, M., 1996, Computational modelling of impact damage in brittle materials, International Journal of Solids and Structures 1996, Vol.33, pp: 2899–2938.

Carpenter, R. B., Brady, J. L., and Blount, C. G., 1992, Effects of Temperature and Cement Admixes on Bond Strength, SPE 22063-PA, Journal of Petroleum Technology, Vol. 44(8).

Carrier, B., and Granet, S., 2011, Numerical modeling of hydraulic fracture problem in permeable medium using cohesive zone model, Engineering Fracture Mechanics 79 (2012), pp: 312–328.

Carter, L. G. and Evans, G. W., 1964, A Stufy of Cement-Pipe Bonding, JPT (Feb, 1964): 157-160.

Chen, J., M. A., Crisfield, A. J., Kinloch, E. P., Busso, F. L., and Qiu, Y., 1999, Predicting Progressive Delamination of Composite Material Specimens via Interface Elements, Mechanics of Composite Materials and Structures 6:301-17.

Coussy, O., 2004, Poromechanics, Number 3, John wiley &Sons, Ltd, West Sussex, England, 2004.

Dahi Taleghani, A., and Wang, W., 2013, Emergence of Delamination Fractures around the Casing and Its Stability, International Journal of Geomechanics, In review.

Davila, C. G., Camanho, P. P., and de Moura, M. F., 2001, Mixed-Mode Decohesion Elements for Analyses with Progressive Delamination, NASA Langley Technical Report Server.

Detournay, E., and Cheng, A. H. D., 1991, Plane Strain Analysis of a Stationary Hydraulic Fracture in a Poroelastic Medium, International Journal of Solids and Structures, Vol. 37, No. 13, pp: 1645-1662.

Dhaliwal, R. S., Saxena, H. S., and He, W. H., 1992, Stress intensity factor for the cylindrical interface crack between nonhomogeneous coaxial finite elastic cylinders. Eng. Fract. Mech., Vol. 43 (6), pp: 1039-1051.

Dugdale, D. S., 1960, Yielding of Steel Sheets Containing Slits. Journal of the Mechanics and Physics of Solids, Vol. 8, pp: 100-104.

Farris, T. N., Kokini, K., and Demir, I., 1989, The cylindrical crack, J. Appl. Mech. 56 (4), 981-983.

Freund, L. B., and Suresh, S., 2003, Thin Film Materials, Cambridge University Press, 2003.

Gordeliy, E., Piccinin, R., Napier, J. A. L., and Detournay, E., 2013, Axisymmetric benchmark solutions in fracture mechanics. Engineering Fracture Mechanics, in press.

Griffith, A. A., 1924, The Theory of Rupture, In Proc. First Internat. Congr. Appl. Mech.

Hall, J., Allanson, J., Gripp, K., and Slavotinek, A., 2006, Handbook of Physical Measurements. Oxford Publication**.**

Hillerborg, A., Modeer, M., and Petersson, P., 1976, Analysis of Crack Formation and Crack Growth in Concrete by Means of Fracture Mechanics and Finite Elements, Cement Concrete Res, Vol. 1976 (6), pp: 773–782.

Hutchinson, J. W., 1990, Mixed Mode Fracture Mechanics of Interfaces, Metal/Ceramic Interfaces, Vol. 4, pp: 295-306.

Jackson, P. B., and Murphey, C. E, 1993, Effect of Casing Pressure on Gas Flow through a Sheath of Set Cement, SPE/IADC 25698, SPE/IADC Drilling Conference, Amsterdam, 23-25 February 1993.

Jutten, J. J., Gulllot, D., and Parcevaux, P. A., 1989, Relationship between Cement Slurry Composition, Mechanical Properties, and Cement-bond-log Output, SPE 16652-PA, SPE production Engineering, 1989, pp: 75-82.

Ladva, H. K. J., Craster, B., Jones, T. G. J., Goldsmith, G., and Scott, D., 2005, The Cement-to-Formation Interface in Zonal Isolation, SPE 88016-PA, SPE Drilling & Completion, Vol.20, (3), pp: 186-197.

Lake, L. W., 2007, Petroleum Engineering Handbook (Vol.4): Reservoir Engineering and Petrophysics.

Lecampion, B., and Prioul, R., 2013, Competition Between Transverse And Axial Hydraulic Fractures In Horizontal Wells, SPE 163848-MS, 2013 SPE Hydraulic Fracturing Technology Conference, Feb 04 - 06, 2013 2013, The Woodlands, TX, USA.

Lecampion, B., Quesada, D., Loizzo, M., Bunger, A., Kear, J., Deremble, L., and Desroches, L., 2011, Interface debonding as a controlling mechanism for loss of well integrity: Importance for CO2 injector wells, Energy Procedia 4 (2011), pp: 5219-5226.

Lee, D., Bratton, T., and Birchwood, R., 2004, Leak-Off Test Interpretation And Modeling With Application To Geomechanics, SPE 04-547, Gulf Rocks 2004, the 6th North America Rock Mechanics Symposium (NARMS), June 5 - 9, 2004 , Houston, Texas.

Le Guen, Y., Le Gouevec, J., Chammas, R., Gerard, B., Poupard, O., Oxand, S. A., Van Der Beken, A., and Jammes, L., 2009, CO_2 Storage: Managing the Risk Associated With Well Leakage Over Long Time Scales, SPE 116424-PA, SPE Projects, Facilities & Construction, Vol. 3, pp: 87-96.

Mueller, D. T., and Eid, R. N., 2006, Characterization of the Early Time Mechanical Behavior of Well Cements Employed in Surface Casing operations, SPE 98632, IADC/SPE Drilling Conference, Miami, Florida, 21-23 February 2006.

Nesheli, B. A., and Schubert, J. J., 2006, Effect of Water Depth on Bridging Tendencies in Ultradeepwater Blowouts in Gulf of Mexico, SPE 103139-MS. SPE Annual Technical Conference and Exhibition, 24-27 September 2006, San Antonio, Texas, USA.

Parcevaux, P., and Sault, P., 1984, Cement Shrinkage and Elasticity: A New Approach for a Good Zonal Isolation, SPE 13176, Offshore Technology Conference, Houston, TX, 16-19 September 1984.

Pickle, B., and Swan, T., 2012, Slickline-Retrievable Wellhead Plugs and Downhole Plugging System Provides Wellbore Integrity for Extreme HPHT Environments, SPE 23630-MS, Offshore Technology Conference, 30 April-3 May 2012, Houston, Texas, USA.

Prince, N. J., and Cosgrove, J. W., 1990, Analysis of Geological Structures, Cambridge University Press.

Ravi, K., Mcmechan, D. E., Reddy, B. R., and Crook, R. A., 2007, Comparative Study of Mechanical Properties of Density-Reduced Cement Compositions, SPE 90068, SPE Drilling & Completion, Volume 22(2), pp: 119-126.

Reeves, G. M., Sims, I., and Cripps, J. C., 2006, Clay Materials Used in Construction: Engineering Geology Special Publication, Cromwell Press, Trowbridge, UK.

Saidin, S., Sonny, I., and Nuruddin, M. F., 2008, A New Approach for Optimizing Cement Design to Eliminate Microannulus in Steam Injection Wells, SPE 12407-MS, International Petroleum Technology Conference, Kuala Lumpur, Malaysia, 3-5 December 2008.

Sarris, E., and Papanastasiou, P., 2011, The influence of the cohesive process zone in hydraulic fracturing modelling. Int J Fract 2011; 167(1), pp: 33–45.

Savari, S., and Kumar, A., 2012, Wellbore Integrity Management: Dealing With Uncertainties, SPE 153359-MS, SPE Oil and Gas India Conference and Exhibition, 28-30 March 2012, Mumbai, India.

Shet, C., and Chandra, N., 2002, Analysis of Energy Balance When Using Cohesive Zone Models to Simulate Fracture Processes, Transaction of the ASME, Vol. 124, pp: 440-450.

Thiercelin, M, J., Dargard, B., Baret, J. F., and Rodriquez, W. J., 1998, Cement Design Based on Cement Mechanical Response, SPE 52890-PA, SPE Drill & Completion, Vol. 13(4), pp: 266-273.

Tvergaard, V., 2001, Resistance curves for mixed mode interface crack growth between dissimilar elastic-plastic solids. J. Mech. Phys. Solids 49, pp: 2689-2703.

Tvergaard, V., and Hutchinson, J. W., 1996, Effect of strain-dependent cohesive zone model on predictions of crack growth resistance, International Journal of Solids and Structures, Vol. 33, pp: 3297-3308.

Vignes, B., and Aadnøy, B. S., 2010, Well-Integrity Issues Offshore Norway, SPE 112535-PA, SPE Production & Operations, Vol. 25 (2), pp. 145-150.

Wang, H. F., 2000, Theory of Linear Poroelasticity with Applications to Goemechanics and Hydrogeology, Princeton University Press. Princeton and Oxford.

Xie, M., 1995, Finite element modeling of discrete crack propagation, PhD. thesis, University of New Mexico, USA.

Xie, M., Gerstle, W. H., and Rahulkumar, P., 1995, Energy-based automatic mixed-mode crack propagation modelling. Journal of Engineering Mechanics, Vol. 121, No. 8, August 1995, pp: 914-923.

Yang, Z. J., Su, X. T., Chen, J. F., and Liu, G. H., 2009, Monte Carlo Simulation of Complex Cohesive Fracture in Random Heterogeneous Quasi-brittle Materials, International Journal of Solids and Structures, 2009, Vol. 46(17), pp: 3222-3234.

CHAPTER 4. FAILURE PREDICTIONS AND MECHANISM ANALYSIS IN VARIOUS WELLBORE CONDITIONS

Abstract

Long-term wellbore integrity is seriously challenged by cement sheath failures and broaching. Porous heterogeneous microstructures of cement and formation make failures around the wellbore more complex. This complexity is further worsened by anisotropic in-situ stress field around the wellbore, as well as wellbore inclination and eccentricity. The spatial non-planar failure patterns caused in the system cannot be correctly predicted by traditional two dimensional models. Hence, a practical three dimensional model is required to reflect the real situation of wellbore integrity by considering the combined complexity.

A field-scale numerical model was developed to simulate spatial propagation of cement sheath failures when leakage occurs around the casing shoe. The interfaces between cement and formation (or casing) are potential failure paths, which are represented by pre-inserted cohesive elements with traction separation laws. This part provides a full range assessment of failure patterns and its dynamic propagation processes of micro-annulus cemented systems by considering various wellbore condition. It was found that the complexity of the failure patterns can be increased if interface heterogeneity exists. Moreover, fractures are prone to propagate along the borehole axis directions instead of cutting across the wellbore in stress anisotropic, inclined and eccentric wellbores. Furthermore, the analysis shows that the borehole becomes more sensitive toward failures with stress anisotropy, wellbore inclination, eccentricity, as well as interface strength heterogeneity. The mechanism of crack initiation and propagation near the wellbore is explored by analyzing the variations of pore pressure, stress, fracture opening, crack length as well as damage rates and patterns around the wellbore. Induced instantaneous flow rates and increased hydraulic conductivity of defects can further deteriorate integrity. The developed method provides a tool for a more accurate prediction of cement sheath integrity spatially and further investigates the containment conditions for wellbore integrity.

Introduction

The broaching of fluid through cement sheath imposes serious challenges to long-term wellbore integrity. These kinds of broaching are usually developed along weaker paths around the wellbore as a result of fluid pressurization, such as hydraulic fracturing (Lecampion and Prioul, 2013) and leakage around the casing shoe (Flak et al., 1995, Grace, 1994 and 2003). In order to understand the physical mechanism during the broaching and its influential parameters, it is significant to understand the liquid movements and failure paths around the wellbore. On one hand, liquid movement imposes significant influences on failure patterns and failure front stability (Saffman et al., 1958, Urhama, Y., 1989, and McKinley et al., 1995). Liquid movement does not usually occur around the wellbore uniformly due to rock and cement inherent heterogeneity and instability of flow in porous material (Mahadeva et al., 2010). However, fluid flow around the casing is restricted to a limited number of routes around the casing. The limited channel flow leads to a higher fluid flow velocity, which may further propagate the existing failure channels or grow to create small cracks. Consequently, the integrity of cement sheaths could be undermined due to the development of cracks and fissures in the annular cement (Fleckenstein et al., 2000, Berger et al., 2004, and Bour, 2005).

On the other hand, cement sheath failures have been recognized as the main factors and paths responsible for upward fluid migration. The fluid seeps around the casing due to the cracks and micro-annulus channels of the cement (Tarr and Flak, 2011). Cement sheath failures can be classified into six major categories: a) radial cracking, b) plastic deformation in cement, c) debonding between casing and cement, d) debonding between cement and formation, e) incomplete cement sheaths, including partially cemented and no cement sheaths, and f) channelization. The roles of these fractures is dictated by a number of factors, such as cement composition, cement curing process, thermal stresses, hydraulic stress, compaction, wellbore tubular, material heterogeneity, in situ stress anisotropy, wellbore inclination, eccentricity, as well as other down-hole environments. Some mechanisms may expedite the damage, such as high cement permeability and porosity, which can cause inner shrinkage and reduce significant empty

volume to form partially cemented casing or debonding. Both hydration and chemical shrinkage are important for the formation of debonding, partial cement sheaths or plastic deformation of cement. The invasion of highly mobile fluid (gas) in the cement matrix and percolation upward in the well can produce channels and possibly affect zone isolation. This phenomenon is especially common during the stage of "cement setting". High pressure and temperature cycles are another important factor that influences the cement sheath integrity. Moreover, weaker, heterogeneous and non-integrity interfacial bonds are more easily formed due to unsmooth wellbore formation surfaces, complex geology conditions, complex chemical components, complicated stress distributions, and weaker adhesion ability of cement. For example, clays are sensitive to the types and contents of salts in cements; however, the contents of clays in permeable sandstones and formations generally are different along formation interface profiles, which provide various cohesion forces in the interfaces between cement and formation. At the same time, other additives, like polymers and silicates, can serve several functions, including prevention of slurry dehydration and annular bridging during placement, enhanced bonding across permeable zones, rheology adjustment, and as an aid to gas migration control (Heathman, 2003). Furthermore, the failure patterns and failure routes become more complex under the effects of anisotropic in situ stresses, wellbore inclination and eccentricity due to stress variations and its induced complicated energy distributions (Chen et al., 1999, Silva et al., 1996, and Salehabadi et al., 2010).

The understanding of the potential liquid movement paths, cement sheath failures and their influential parameters gives the significant starting point for the design of successful drilling, production and completion operations to realize the long-term wellbore integrity (Wong et al., 2006, Bour, 2005, Jackson and Murphey, 1993, and Griffith et al., 2004). In order to decrease or eliminate the significantly adverse consequences on wellbore integrity induced by cement sheath failure, analysis and optimization research on cement-casing and cement-rock bonding has attracted researchers' attention in the past 20 years because of its weak characteristics (Parcevaux and Sault, 1984, Ladva et al., 2004 and 2005, and Bour, 2005). Lab, field and numerical tests are three significant aspects of long-term wellbore integrity research.

Since 1961, several lab testing methods have been established to measure cement normal and shear bond strength (Bearden and Lane, 1961, Carter and Evans, 1964, Carpenter et al., 1992, and Ladva, 2005). Carter and Evans (1964)'s lab test is selected as a typical example for detailed analysis. Carter and Evans (1964)'s proposed an experimental setup to measure shear and normal bond strengths (called "hydraulic bond and shear bond tests") of cement to formation and casing; however, shear and normal bond strengths of cement interfaces obtained from these tests are not accurate due to non-pure shear or normal modes provided in these lab tests. Moreover, the bond strength parameter acquired from these measurements is not enough to predict the complicated failure behavior. Essentially, fracture energy and the failure damage process are the missing pieces in the interpretation of Carter and Evans' tests. Lavda (2005) adjusted Carter and Evans's test to measure shear bond strength between cement and shale by pulling out a shale core from a cement ring set in a piece of casing, although his interpretation was basically not different from that of Carter and Evans. Shear bond strength and complicated failure behavior represented by the relationship of load and displacement were described in this test. However, this lab test was only conducted in isotropic confining conditions, which are more conservative than real wellbore conditions because more complicated failure behaviors of the interface should be obtained with consideration on material property heterogeneity, in-situ stress anisotropy, as well as wellbore locating conditions, such as wellbore eccentricity or inclination. Hence, assessment of wellbore integrity and cement bond strength in the field is not possible to be determined by direct methods.

In contrast to laboratory conditions, traditional cement evaluation (CBL) or Ultra-sonic logging (ULT) (Lake, 2007, for example) can be conducted in the field to evaluate cement bond integrity. CBLs and ULTs rely on the amplitude attenuation of the acoustic signal to estimate the quality of cement placement in the annulus between metal casing and formation rock (Grosmangin et al., 1961). The variable-density display tools (VBL) are usually combined with CBL for a better evaluation of cement quality. The CBL-VBL combined system provides average measurements, which makes it difficult and sometimes impossible to detect small channels or localized failures. Moreover, it is difficult to distinguish between

the cases of high-strength cement with channels versus even distribution of low-strength (foam) cements, which both generate similar overall responses. Compared to the CBL-VBL combined system, ULTs can present a qualitative sense for identification of fluid types based on the impedance differences among gas, water and cement (especially for gas-contaminated cements from low-weight foam cements), as well as failure paths around the wellbore (Butsch, 1995). Moreover, 360° azimuthal measurements provided by ULTs can give a circumferential measurement on failure patterns around the wellbore (Havira, 1982, and Hayman et al., 1991). However, ULTs are expensive to apply in the field, which makes its application limited at some stages. On the other hand, it is difficult for ULTs to predict failure initiation and failure front stability due to its average calculation, which limits its capacities on mechanism analysis and parameter sensitivity analysis.

Hence, a more sophisticated model is needed for correctly predicting failure behavior around the wellbore under real field conditions on the basis of lab test results. To address these needs, cohesive interface approaches have been verified to be suitable for fluid-driven fracture problems by effectively describing mechanical characteristics of cement interface during failure and predicting non-planar failure patterns. The cohesive interface approach was originally proposed by Dugdale (1960) and Barenblatt (1962) to model the processing zone of fracture tips in ductile material. In this approach, the cohesive zone is a pre-defined failure path without any presumptions of the initial crack size or location and traction separation law is the basic theory to describe failure behavior (Yang et al., 2009). Cohesive interface approach is more advanced and can be used to instead of Griffith's criterion (Griffith, 1924), because of: its prediction ability on fracture initiation that Griffith's criterion does not have; and its capacity to avoid calculating the singularity around crack tips involved in Griffith's brittle fracture theory. Hence, computational burden due to stress singularity at the tip of fractures can effectively be reduced in the cohesive interface approach. Moreover, the cohesive interface model has strong adaptability for the combination of other material and geometric nonlinearities (Xie and Gerstle, 1995, Needleman et al., 1990 and 1992). Moreover, it can realistically represent the energy dissipation during the fracture process

(Xie and Gerstle, 1995, and Xie et al., 1995). All these advantages give it a universal applicability on the non-linear fracture mechanics simulation (Petersson et al., 1981, Swenson and Ingraffea, 1991) with a higher accuracy (Petersson et al., 1981, Yang et al., 2008, and Deeks and Yang, 2007). These characteristics make cohesive crack theory apply in wide range, such as multiple crack growths in and indeterministic aspects of local failure (Corigliano and Ricci, 2001, Camacho and Ortiz, 1996, Yang and Xu, 2008, and Yang et al., 2009) by spreading embedded cohesive interface elements in the potential failure zone, which shows the flexibility of the cohesive interface model and can be widely applied in the heterogeneous modeling, as well as the interface delamination along two dissimilar materials, such as an interface between ductile and elastic materials, or between two elastic-plastic materials (Hutchinson, 1990, Xie and Gerstle, 1995, Tvergaard and Hutchinson, 1992, 1993, and Tvergaard, 2001). The cohesive zone framework has been successfully applied to model fractures in cement-based materials (Hillerborg et al., 1976) and geomaterials (Sarris and Papanastasiou, 2011(a) and 2001(b), and Carrier and Granet, 2011). The cohesive interface approach has been successfully applied in describing the behavior of cohesive zones in hydraulic fracturing (Lecampion, 2012) and wellbore integrity by predicting failure behavior of cement sheath systems by the axisymmetric model provided by Dahi Taleghani and Wang (2013). Successful applications in the past made the cohesive zone model a reliable and powerful tool to model interfacial delamination fractures between casing, cement and formation systems for this chapter.

In this research, a coupled three dimensional model with cohesive interface approach is conducted to reflect wellbore integrity under complex wellbore conditions. Potential delamination paths can be predefined by cohesive elements without any presumption of the initial crack size or location. In this system, the interfaces between cement and formation (or casing) are potential delamination paths, which are represented by pre-inserted cohesive elements with traction separation laws. These field-scale numerical models are aimed primarily at predicting the evolution of the fluid pressure, opening, size, and shape of the fracture when leakage occurs around the casing shoe. Moreover, this model provides a full range assessment of interface damage rates, failure patterns and dynamic failure propagation processes of

micro-annulus cemented systems by considering its heterogeneity, anisotropic in situ stresses, wellbore inclination and eccentricity. Furthermore, the mechanism involved in the system is explored. The developed method provides a tool for a better prediction of cement sheath integrity spatially under complicated wellbore conditions and gives more suggestions on cement property requirements to maintain wellbore containment.

Fluid Flow within Failure Zones

During the formation of failures between cement and rock, the normal and tangential fluid flow occurs through opened fracture. This process is well illustrated in Figure 4.1. To understand fluid flow behavior in the failure zone, a simple but appropriate model for fluid flow in a fracture, which is

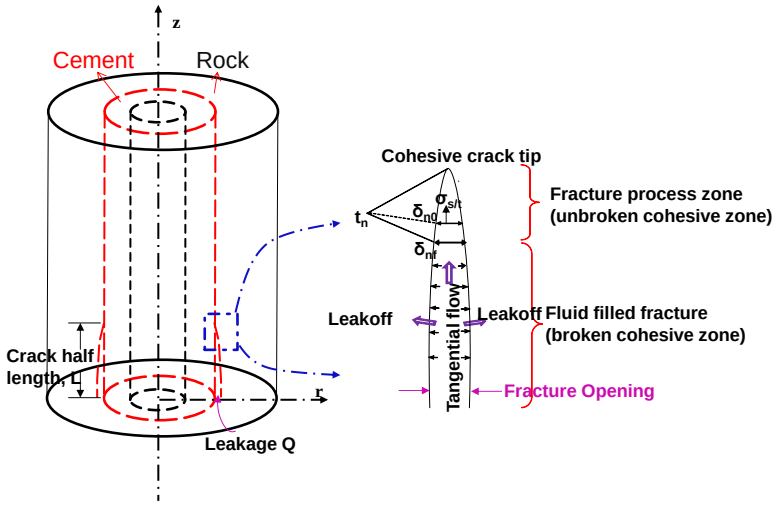

Figure 4.1 Schematic picture of normal and tangential fluid flow through opened fracture after cement failure.

surrounded by continuum rock and cement, is embodied in the lubrication theory. Laminar flow is presumed. Incompressible Newtonian fluid is used to represent formation fluid. Moreover, this model accounts for the time dependent rate of crack opening. The continuity equation which imposes the conservation of mass in the fracture between rock and cement (Peirce and Detournay, 2008) is shown below

$$\frac{\partial w}{\partial t} + \nabla \cdot q + (q_b + q_t) = Q(t)\delta(x, y) \ , \qquad \textbf{(4.1)}$$

where q is the fluid flux of the tangential flow, w is the crack opening. q, w, q_t, and q_b are all functions of x, y, and t. Moreover, $Q(t)$ indicates the injection rate. q_t and q_b, are the normal flow rates into the top and bottom surfaces of fractures, respectively, which reflect the leak-off through the fracture surfaces into the adjacent material. The normal flow shown in Figure 4.1 is defined based on Darcy's Law. The significance of this flow depends on the formation permeability, failure surface conditions and pressure difference between fluid inside the crack and pressure of fluid inside the formation.

$$\begin{cases} q_t = c_t(p - p_t) \\ q_b = c_b(p - p_b) \end{cases}, \tag{4.2}$$

where p is fluid pore pressure in the formation adjacent to the fracture surface. Moreover, c_t and c_b define the corresponding fluid leak-off coefficients, which can be explained to be the effective permeability of a finite layer of permeable material on the fracture surfaces.

Upon formation of delamination cracks between cement and formation, fluid flow inside the fracture will be considered laminar flow between two parallel fractures. This tangential flow is considered as Poiseuille's flow or the lubrication equation (Batchelor, 1967)

$$\frac{\partial w(s,t)}{\partial t} = \frac{1}{12\mu}\frac{\partial}{\partial s}(w^3(s,t)\frac{\partial P(x,t)}{\partial s}), \tag{4.3}$$

where *P* is the pressure of the fluid inside the delamination crack and *w* is the width of the fracture, *s* is the length coordinate along the fracture, and μ is the fluid viscosity.

By substituting Eqs. (4.1) and (4.2) into Eq. (4.3), Reynolds' lubrication equation (Peirce and Detournay, 2008, and Chen, 2012) is derived as

$$\frac{\partial w}{\partial t} + c_t(p - p_t) + c_b(p - p_b) = \frac{1}{12\mu}\frac{\partial}{\partial s}(w^3(s,t)\frac{\partial P(x,t)}{\partial s}) + Q(t)\delta(x,y) \tag{4.4}$$

Rock Deformation

In fluid saturated rocks, the basic theory of poroelasticity is derived by Biot (1941) to describe the relationship between the pore fluid and the elastic deformations. The theory is commonly applied to soil mechanics problems, especially for consolidation problems. The theory is described by fully coupled linear quasi-static field equations in terms of force equilibrium

$$S_{ij}' = S_{ij} - \alpha P \delta_{ij}, \quad \textbf{(4.5)}$$

where S_{ij} are total stress components exerted on solid and fluid components of saturated porous medium. S_{ij}' is effective stress defined by Biot as the part of the total stress that is applied to the solid skeleton of the rock. P is the pore fluid pressure and α is Biot's constant (Wang, 2000). The effective stress governs the deformation and failure of the rock.

Biot's poroelastic theory (Biot, 1941) includes a stress-strain constitutive equation and a fluid mass balance equation. It can be written in vector and tensor notations as

$$T = c : \varepsilon - \alpha I p \quad \textbf{(4.6)}$$

$$\zeta = \alpha \nabla \cdot u + \frac{\phi}{K_f} \quad \textbf{(4.7)}$$

where T is the total stress, c is the elasticity tensor of the solid matrix, ε is the strain tensor, p is the pore pressure, I is the identity matrix, and α is the Biot's constant representing the coupling between the stress and the pore pressure. In the second equation, ζ is the increment of fluid content, u is the displacement of the solid matrix, and 1/M is the specific storage coefficient at constant strain, which is related to the compressibilities of the fluid and solid phases. When both the solid and the fluid are assumed compressible, the coefficient 1/M is defined by

$$\frac{1}{M} = \frac{\alpha - \phi}{K_s} + \frac{\phi}{K_f} \quad \textbf{(4.8)}$$

Where ϕ is the material porosity, K_s is the bulk modulus of the solid grain material, and K_f is the bulk modulus of the fluid.

The isothermal equilibrium and negligible inertial forces are considered, which means that the equilibrium state is established at all times. Therefore, the force balance equation has the form

$$\nabla T + \rho g = 0 \quad \textbf{(4.9)}$$

Where ρ is the average density and g is the gravity. Combining it with Eq. (4.6) results in

$$\nabla \cdot (c : \varepsilon) - \alpha \nabla p + \rho g = 0 \quad \textbf{(4.10)}$$

For the slow transport of oil, water and gas, Darcy's law is assumed valid, which is

$$\mathrm{q} = -\rho_f \frac{1}{\mu} k \cdot (\nabla p - \rho_f g) = 0 \quad \textbf{(4.11)}$$

where q is the fluid flux, k is the permeability tensor, μ is the dynamic viscosity, and ρ_f is the density of fluid. The increment of fluid content ζ in Eq. (4.7) of Biot's theory is basically the fluid volume added into a control volume normalized by this control volume. By substituting it into Eq. (4.7), the mass balance equation for fluids becomes

$$\left(\frac{\alpha - \phi}{K_s}\mathrm{q} + \frac{\phi}{K_f}\right)\frac{\partial \mathrm{p}}{\partial \mathrm{t}} + \alpha \nabla \cdot \frac{\partial \mathrm{u}}{\partial \mathrm{t}} + \nabla \cdot \left[\frac{1}{\mu} k \cdot \left(\nabla p - \rho_f g\right)\right] = \quad \textbf{(4.12)}$$

The finite element formulation stems from Eqs. (4.9) and (4.12). The solid phase displacement u and the pore pressure p are chosen as the primary variables to be solved simultaneously in the finite element system.

In finite element method, the displacements and pore pressures are expressed using their values at a finite number of points in space (Lewis and Schrefler, 2000). In a discretized form, the unknown field parameter u and p for the whole space are calculated in terms of the values at the element nodes by substituting the known nodal values and choosing the interpolation functions. Their expressions with one element are

$$p = N_p \vec{p}, \qquad u = N_u \vec{u}, \qquad \varepsilon = \bar{B}\vec{u} \tag{4.13}$$

where $\vec{u}$ and $\vec{p}$ are the vectors of the values of the unknowns at the element nodes. The interpolation functions are matrices N_p and N_u for the displacements and the pore pressures, respectively. $\bar{B}$ is the matrix for the strain ε that contains the derivatives of the displacement interpolation functions.

Based on effective stress principle for porous media, the theory of poroelasticity can be approximated numerically using a standard Galerkin formulation as described in Zienkiewicz (1984) and Lewis and Schreffler (2000). Using the Galerkin method (Zienkiewicz and Taylor, 1984) to solve Eqs. (4.6) and (4.7), the finite element formulation becomes the following linear system for each element (Boone and Ingraffea, 1990). This method is only valid for the system with poroelasticity and low compressibility of fluid:

$$\begin{bmatrix} 0 & 0 \\ \bar{Q}^T & \bar{S} \end{bmatrix} \frac{d}{dt} \begin{Bmatrix} \vec{u} \\ \vec{p} \end{Bmatrix} + \begin{bmatrix} \bar{K} & -\bar{Q} \\ 0 & \bar{H} \end{bmatrix} \begin{Bmatrix} \vec{u} \\ \vec{p} \end{Bmatrix} = \begin{Bmatrix} F_u \\ F_p \end{Bmatrix} \tag{4.14}$$

where

$$\bar{K} = \int_\Omega \bar{B}^T D \bar{B} d\Omega; \qquad \bar{B} = L N_u; \qquad \bar{Q} = \int_\Omega \bar{B}^T \alpha m N_p d\Omega$$

$$\bar{S} = \int_\Omega N_p{}^T \left(\frac{1}{M}\right) N_p d\Omega \qquad \bar{H} = \int_\Omega (\nabla N_p)^T \frac{k}{\mu} (\nabla N_p) d\Omega \qquad F_u = \int_\Omega N_u{}^T \rho g d\Omega + \int_\Gamma N_u{}^T t d\Gamma$$

$$F_p = \int_\Omega (\nabla N_p)^T \frac{k}{\mu} \rho_f g d\Omega - \int_\Gamma N_p{}^T \frac{q}{\rho_f} d\Gamma \tag{4.15}$$

Here, $\bar{K}$ is the stiffness matrix of the solid phase, $\bar{Q}$ is the coupling matrix related to Biot's constant α, $\bar{S}$ is a compressibility matrix related to the bulk modulus of fluid and solid, and $\bar{H}$ is the permeability matrix. The two right-hand terms, F_u and F_p, are associated with the gravity and boundary conditions.

The external loading is represented by t, and q is the mass flow into or out of the element. The local element systems are assembled into a global system.

A symmetric system is usually preferred. Eq. (4.14) can be converted to a symmetric system by time differentiating the equation, so that it becomes

$$\begin{bmatrix} -\bar{K} & \bar{Q} \\ \bar{Q}^T & \bar{S} \end{bmatrix} \frac{d}{dt}\begin{Bmatrix} \vec{u} \\ \vec{p} \end{Bmatrix} + \begin{bmatrix} 0 & 0 \\ 0 & \bar{H} \end{bmatrix} \frac{d}{dt}\begin{Bmatrix} \vec{u} \\ \vec{p} \end{Bmatrix} = \begin{Bmatrix} \frac{d}{dt}F_u \\ F_p \end{Bmatrix} \quad \textbf{(4.16)}$$

To solve the dynamic problem, the central difference in time is applied to Eq. (4.16) to yield

$$\begin{bmatrix} -\bar{K} & \bar{Q} \\ \bar{Q}^T & \bar{S}+\bar{H}(\Delta t) \end{bmatrix} \begin{Bmatrix} \vec{u} \\ \vec{p} \end{Bmatrix}_{n+1} = \begin{bmatrix} -\bar{K} & \bar{Q} \\ \bar{Q}^T & \bar{S}-\bar{H}(\Delta t) \end{bmatrix} \begin{Bmatrix} \vec{u} \\ \vec{p} \end{Bmatrix}_{n} + \Delta t \begin{Bmatrix} -\frac{d}{dt}F_u \\ F_p \end{Bmatrix} \quad \textbf{(4.17)}$$

Equations presented above describe physical and numerical mechanisms involved in this work. However, these equations do not predict onset of fracture initiation and subsequent propagation of these fractures. For failure prediction and description, cohesive interface approach is used in this research. The detailed descriptions of this approach are introduced below.

Mechanics of Cohesive Zone Method

The mechanisms of material bonding, aggregate interlocking and surface friction involved in the fracture process zone can be described by traction separation law (softening laws). Bilinear or triangular traction separation law has been adopted here because of its successful application to characterize fracture processes in brittle materials especially concrete structures (Hillerborg et al., 1976, Gerstle and Xie, 1992, Li and Liang, 1994, and Davila et al., 2001). Typical bilinear softening curves for pure normal and shear loadings are illustrated in Figure 4.2a and b, respectively. In the failure zone, cohesive forces act against the opening forces and compensate the stress singularity at the tip. Cohesive interface starts to open when the tension or shear traction applied to the interface reach a critical point (Tvergaard and Hutchinson, 1996), t_{n0} (or t_{s0}), or equivalently it reaches critical separation, δ_{n0} (or δ_{s0}), the fracture initiates in the

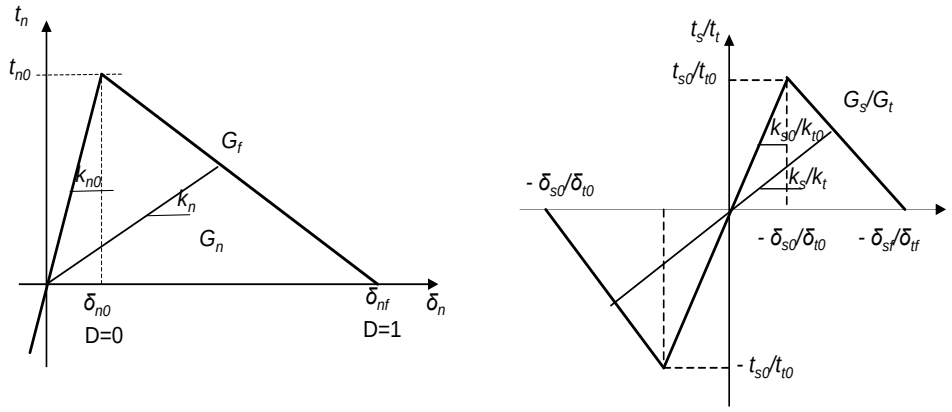

Figure 4.2 Linear Softening traction-separation law for the cohesive element under pure normal loading (left) and pure shear loading (right).

previous intact rock. Beyond this critical point, the process zone starts to undergo plastic deformation and micro-cracking under the tension (or shear) traction, which is the so-called softening transition zone between the complete failure zone and the undamaged material. The transition zone ends when tractions diminish, which is the complete failure point. When complete failure points are reached, cohesive forces between crack faces are gone, the relative displacement reaches the second critical value, δ_{nf} and δ_{sf}, and the total fracture energy, G_c, is dissipated. Meanwhile the energy re-dissipates in the fracture processing zone; complete damage occurs when the energy is greater than the critical energy. This is when cracks start to propagate (Xie, 1995). For the bilinear traction separation law, the propagation critical energy, which is the minimum energy needed to propagate the crack, can be described by

$$G_{i,c} = \frac{1}{2} t_{i,0} \delta_{i,f}, \qquad \text{with } i = n, s, t. \tag{4.18}$$

The complicated mixed mode condition is involved in the system. Damage is assumed to initiate when a quadratic interaction function involving the nominal stress ratios (as defined in the expression below) reaches a value of one.

$$\left\{\frac{\langle t_n \rangle}{t_{n0}}\right\}^2 + \left\{\frac{t_s}{t_{s0}}\right\}^2 + \left\{\frac{t_t}{t_{t0}}\right\}^2 = 1, \tag{4.19}$$

where t_n , t_s and t_t represent the real values of normal and tangential (first and second shear) tractions across the interface, respectively. < > is the Macaulay bracket and

$$\langle t_n \rangle = \begin{cases} t_n, \ t_n \geq 0 & (tension) \\ 0, \ t_n < 0 & (compression) \end{cases} , \quad \textbf{(4.20)}$$

The damage is characterized by a scalar stiffness degradation index D representing the overall damage of the crack caused by all physical mechanisms. It is a function of the so-called effective relative displacements δ_m combining the effects of δ_s and δ_n :

$$\delta_m = \sqrt{\langle \delta_n \rangle^2 + \delta_s^{\ 2} + \delta_t^{\ 2}} . \quad \textbf{(4.21)}$$

where < > is the Macaulay bracket and

$$\langle \delta_n \rangle = \begin{cases} \delta_n, \ \delta_n \geq 0 & (tension) \\ 0, \ \delta_n < 0 & (compression) \end{cases} \quad \textbf{(4.22)}$$

For linear softening, the damage evolves with the index (Chen et al., 1999), which is the damage variable that describes the nature of the evolution between initiation of damage and final failure. *D* monotonically evolves from 0 to 1 upon further loading after the initiation of damage.

$$D = \frac{\delta_{mf}\left(\delta_{m,\max} - \delta_{m0}\right)}{\delta_{m,\max}\left(\delta_{mf} - \delta_{m0}\right)}, \quad \textbf{(4.23)}$$

where $\delta_{m,\max}$ is the maximum effective relative displacement attained during the loading history. δ_{m0} and δ_{mf} are effective relative displacements corresponding to δ_{n0} and δ_{s0} , and δ_{nf} and δ_{sf} as shown in Figure 4.2, respectively.

Numerical Model

A coupled field-scale three dimensional poroelastic model shown in Figure 4.3 is used to investigate the cement integrity and failure patterns for different scenarios, such as interface strength heterogeneity,

anisotropic in-situ stresses environment, the inclined well or the wellbore with eccentricity. These

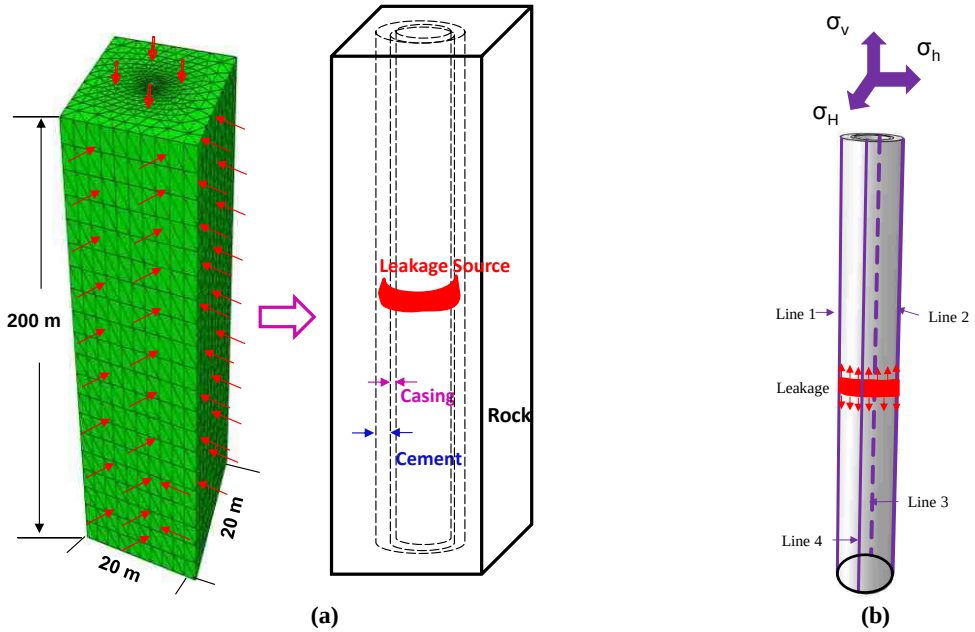

Figure 4.3 A schematic picture of the numerical model with dimensions, boundary and loading conditions, and meshes for the three dimensional model (shown in (a)). Also this picture demonstrates the leakage positions in (b).

scenarios more commonly exist in the real field. The model is cut from one part of the wellbore system around the surface leakage source. This model is located at the depth of 1923m of the rock with 0.535 psi/ft stress gradient and 0.465 psi/ft pore pressure gradient, respectively. Stresses and pore pressure are assigned to each element and each node of the system to avoid the failure formation during the equilibrium established process. The wellbore pressure is 1,3000 KPa, which is higher than average initial pore pressure 4000 KPa in the formation. The leakage around the casing shoe is considered as the drive for the loss of wellbore integrity. Rock mechanical properties used in the model are borrowed from Mueller and Eid (2006) and Lecampion (2011). Values used for cement, casing, and rock interfaces are listed in the appendix.

A cemented 7-in casing is located inside an 8-½ in borehole. The cement and formation (or casing) is bonded by cohesive interface. For the simplification, linearly elastic and isotropic bonded materials are assumed on both sides of the interface. The interfaces were considered as potential failure paths, which are represented by layers of cohesive elements with zero thickness. Aiming to guarantee solution

convergence and capture the details of stress re-distribution within the cohesive zone due to failure, fine mesh is placed near the wellbore. Moreover, coarser meshes were situated far from the wellbore in order to reduce the computational cost. There are 4,000, 4,000, and 53,903 elements used to mesh casing, cement and rock, respectively. One layer of eight node three dimensional cohesive elements with 4,000 elements is assigned as the cohesive layer between cement and rock (or casing). Pore pressure was coupled with cohesive elements by inserting four degrees of freedom in the middle layer of the cohesive element to improve continuity. Three steps are considered in the simulation, which include initial equilibrium establishment by assigning initial geostatic stress to each element and designating initial pore pressure to each node; excessive pore pressure (16,000 KPa) accumulation at the casing shoe; and excessive energy redistribution. Dimensionless parameters introduced in the previous chapters are used for result discussions.

Results and Discussions

Based on the discussions of the vertical wellbore located in isotropic in situ stress fields and with homogeneous interface strength, which has been discussed in the previous chapter, more realistic situations, such as the cases with interface strength heterogeneity, anisotropic in-situ stresses environments, the inclined well or the wellbore with eccentricity that usually happens in the field, are further considered and discussed. The failure propagation process with the gradual pressurized fluid buildups for the basic case with an isotropic in situ stress field and homogeneous interface strength has been shown in Figure 4.4 below to give the basic comparison for other cases. Similar excessive fluid pressure accumulation processes are applied in all models. It can be observed that cement failures are initiated and expanded with the aggregation by pressurized fluid and from the leakage zone over time. Failures retard until the magnitude of the excessive pressure has reached a critical level (t^*_1 shown in Figure 4.4), and upon reaching the critical threshold, failure starts to grow suddenly. At this point, the induced stresses at the fracture tips satisfy failure initiation and propagation criterions introduced above. Moreover, in order to investigate the ability of cement-rock interface blocking broaching, the fluid

channel is limited to the interface between cement and formation by assigning small leakage coefficient to the formation and cement that are bonded at both sides of interface. The broaching can be also expedited

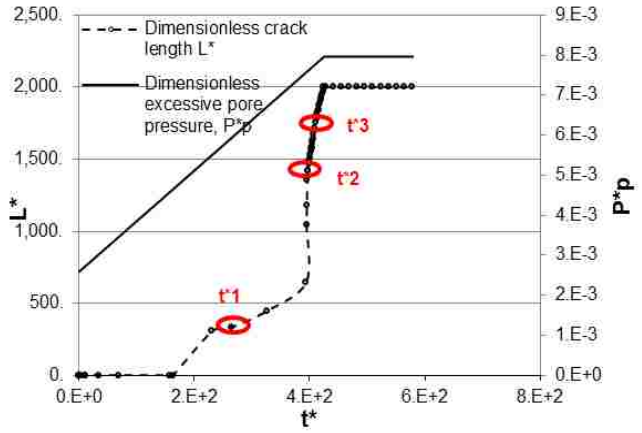

Figure 4.4 Buildup process of excessive pore pressure in the formation and its inducing failure lengths around the wellbore.

by the concomitant effects of local hydraulic conductivity and pressure along the damaged cement interface, which is ascribed to higher conductivity for transporting fluid in the induced conduit in the interfaces compared with the lower permeability cements. Two other typical dimensionless time variables t^*_2 and t^*_3 shown in Figure 4.4 are selected for further analysis.

Heterogeneity of the Cement Properties

Due to the heterogeneity of cement and formation, the material parameters usually have steep variations along the interface (Dhaliwal et al., 1992). In this work, imperfections that correspond to variation of interfacial strength, σ_{max}, are considered. Attention is focused on the variations in failure onset and its containment when the cement-rock interfacial strength, σ_{max}, is heterogeneous. The case with the homogeneous interface is considered as comparison basis, which has been introduced in the previous section. Two heterogeneous cases are compared here: Case-1 has 10% and Case-2 has 50% of cement surface composed of randomly distributed weak interfaces. The normal and shear strength of the weaker parts are 100 KPa, which are 320 KPa weaker than the other parts of cement liner. In this model, there is no preference in location of weak spots with respect to each other; in other words, there is no cross-correlation in the location of weak spots. However, the assumption of fully random distribution of cement

properties may not be completely consistent with situations where channelization may occur due to limited gas migration.

The failure patterns from these two cases introduced above are first investigated. The general ideas about the influences of interface strength heterogeneity on wellbore integrity can be obtained. The failure patterns along the cement liner involved in these two heterogeneous cases are stretched to interface contour maps with circumferential spread shown in Figure 4.5. The left chart (a) includes 10% weaker strength cohesive elements (Case-1), and the right chart (b) includes 50% weaker strength cohesive

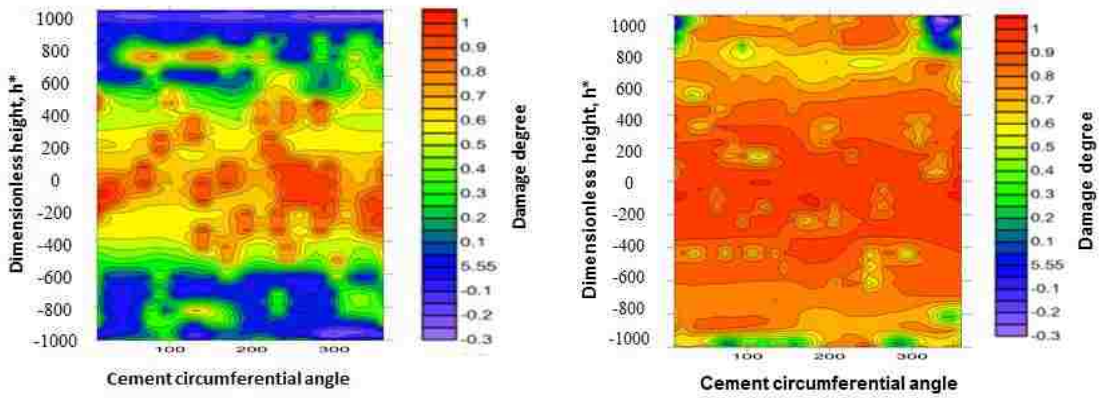

(a) The case with 10% weaker interface strength (b) The case with 50% weaker interface strength

Figure 4.5 Damage contour map for the cases with different property heterogeneities along the cement liner is demonstrated.

elements (Case-2). On one hand, it can be observed that non-uniform failure patterns have been formed in both cases. Compared to Case-1, the more serious but uniform failure patterns are formed in Case-2 as a consequence of more secondary partial channel reconnection existing in Case-2, which is caused by the 5-fold increment in the heterogeneity of the interface. The higher heterogeneity induces larger possibility for the interface damage and broaching under the effects of upward fluid flow. That is because that the energy is prone to flow in the zone with randomly distributed lower interface strength, and the failures are further worsened by fluid accumulation in failures with higher conductivity. Moreover, a myriad of patterns of cement sheath failures can be generated due to the diversification of interface property distribution.

On the other hand, the propagation rates are further analyzed depending on the relationship between imperfection percentages vs. dimensionless excessive pressure, which is demonstrated in Figure 4.6. The case with homogeneous interface strength (Weaker 0%) and the other two cases with heterogeneous interface strength (Weaker 10% and Weaker 50%) are compared in Figure 4.6. Similar failure propagation processes are observed in these three cases. Failure broaching is not started till the magnitude of the excessive pressure has reached a critical level, which is demonstrated by red, purple and orange circles in Figure 4.6. Once excessive pressure reaches a critical value, failure propagates suddenly, the failure broaching around the wellbore has been formed because the induced stresses at the fracture tips are large enough to propagate initiated fractures. The critical values are not the same in these three cases, the higher heterogeneous degree of cement-formation interface, the less energy (critical threshold) is required for the interface broaching. However, once the energy in the system reaches the critical threshold, the interface broaches very fast no matter what kinds of interface heterogeneity they have. Hence, the

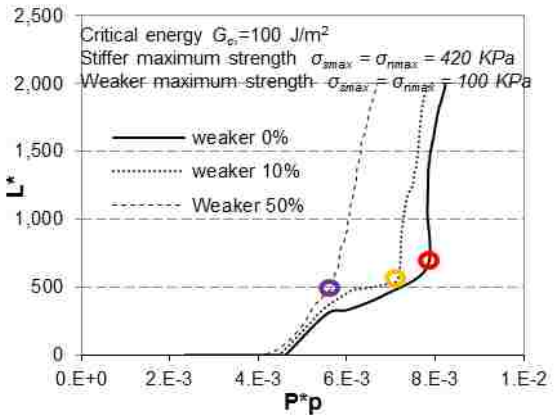

Figure 4.6 Buildup process of excessive pore pressure in the formation and its inducing failure lengths around the wellbore.

interface heterogeneity is one of paramount factors to determine critical threshold point and failure propagation rates.

To understand the deteriorated effects of interface strength heterogeneity on wellbore integrity, further analysis was conducted. For analysis convenience, four directions illustrated in Figure 4.3(b), which are parallel to vertical stress and have 90 ° equal angle distance from each other, are selected as comparison

basis. Case-2 with 10% weaker interface strength is selected for further analysis. Excessive fluid pressure acts as the main driving force to facilitate upward fracture propagation. Figure 4.7 shows fluid pressure profile along these four typical directions. The non-identical fluid pressure distributions are observed in the heterogeneous case, which is completely different from uniform fluid pressure in the case with isotropic horizontal in-situ stresses. The asymmetric development of the failure zone is ascribed to the heterogeneity of the interface strength. On the other hand, the failure non-uniformity can be further strengthened by the energy redistribution due to the complexity of failure patterns. On the contrary, the heterogeneity of interface is worsened due to energy redistribution during failure propagation process. Hence, the interface containment ability is greatly influenced by the heterogeneity of the interface.

Understanding of the subsequent events involved in cement-rock interface can be achieved by analyzing stresses of the debonded crack and the bonded interface, which is shown in Figure 4.8. It is found that tensile radial stress intensification occurs at the end of debond (crack tip). The tensile radial stress occurs at the crack tip if the stress intensification is large. Moreover, shear stress also has contribution on failure initiation and propagation. However, shear stresses are neglected in this part

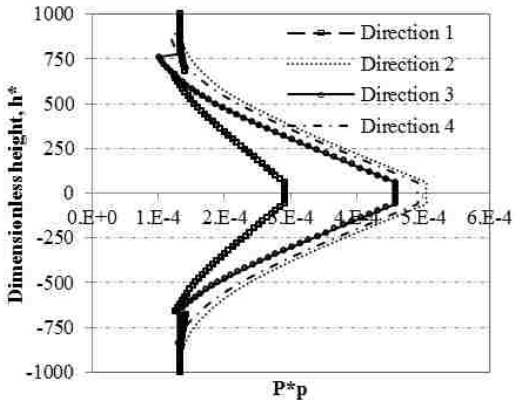

Figure 4.7 Fluid pressure along four typical directions of the wellbore is illustrated. These four directions are designated in Figure 6(b), which are parallel to hole axis and 90 °away from each other.

because they are at least two orders smaller than radial stress and tangential stresses. Failure initiates if the combination of the effects of radial, tangential and shear stress reaches the quadratic failure initiation criterion. On the other hand, the heterogeneous interface properties directly control the interface strength

and toughness. In practice, cements and rock are not smooth, which do not have uniformly straight and bonded interfaces. The opening and sliding resistance exist in different magnitude along the interface because the interface is governed by different frictional characteristics of the bonded interface. The characteristics of interface can be described by two independent parameters, which may be any two of the three parameters: namely cohesive energy, and either of cohesive strength or separation length, which have been introduced above. Hence, low fracture resistance interface exists in the interface zone with weaker interface strength, it facilitates for the occurrence of debonding when the interface is subjected to

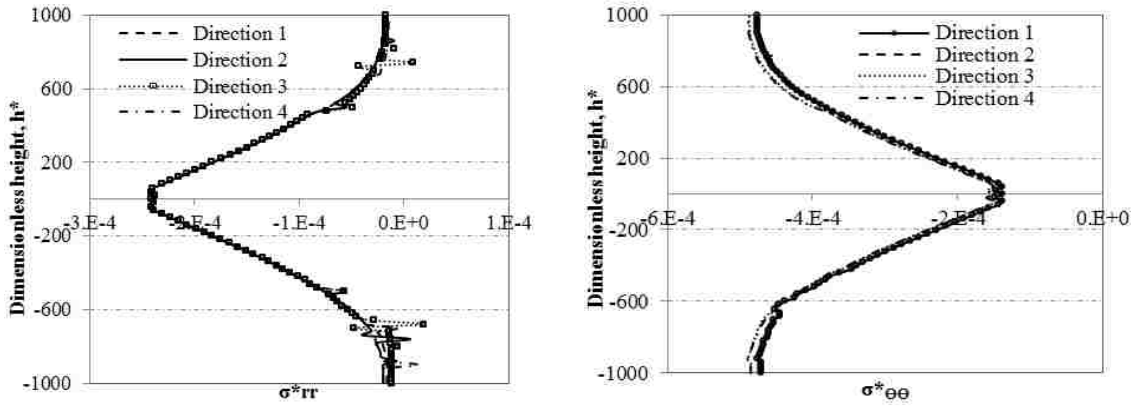

(a) Normal traction σ^*_{rr} **(b) Tangential traction $\sigma^*_{\theta\theta}$**

Figure 4.8 Normal and tangential tractions along four typical directions of the wellbore are illustrated. These four directions are designated in Figure 6(b), which are parallel to hole axis and 90 °away from each other.

the combined effects of residual radial tension, tangential stress and shear stresses. When fluid front approaches to some zones, it is easier for failure debonds extending along the interface and inhibiting at the harder interface zone because energy flows following the least energy paths. As a consequence of the heterogeneity of interface properties, the positions of crack tips are not always located at the same position as the end of the excessive fluid pressure. On the other hand, similar radial and tangential stresses are observed along different directions of the wellbore except stress intensification zones, which is ascribe to the homogeneity of in-situ stresses. Compared to the case with homogenous interface properties introduced above, the heterogeneity does not affect the stress distribution a lot except the crack tip zone.

However, it may influence the excessive energy distribution along the interface, which directly influences failure initiation, propagation, failure patterns and its containment.

The accompanied results of stress are fracture opening, which is demonstrated in Figure 4.9. The non-

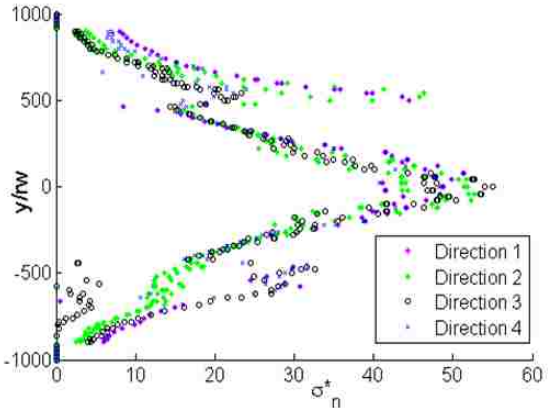

Figure 4.9 Fracture opening along four typical directions of the wellbore are illustrated. These four directions are designated in Figure 6(b), which are parallel to hole axis and 90 °away from each other.

smooth fracture opening at four typical directions further proves the determinant influences of interface heterogeneity on wellbore integrity. In the meanwhile, the incidence and extent of fracture opening is also greatly influenced by unbalanced energy, fluid conductivity in the damaged zone and stress distributions on the interface bonded materials. Rock heterogeneity and discontinuity may determine the position of fracture initiation as well as the stress level, especially shear stress at which a fracture occurs. Heterogeneities and discontinuities generally reduce the accuracy of fracture-pressure and fracture-position predictions.

Effects of Anisotropy in Stress Field

The consideration of in situ stress anisotropy in the model enables the engineer to make intelligent decisions on the design of cement sheath to maintain wellbore stability, which promotes the success of drilling, hydraulic fracturing, cementing and production process, as well as provides more effective assistance in recognizing possible causes of failures. In the anisotropic stress field, failure patterns generated are different from those in the isotropic stress field or the horizontal isotropic stress field, which are attributed to the effects of additional shear stress caused by the differences in in-situ stresses.

Generally, σ_H / σ_h ranges from 1 to 2 and σ_h / σ_v from 0.3 to 1.5 for typical depths of reservoirs (Tan et al., 1993, and Hill and Williams, 1993). In this part of research, a vertical well located in the anisotropic stress field is selected to investigate the effects of anisotropic in situ stresses on wellbore integrity. The case with the isotropic horizontal stress field is considered to be the comparison basis, which is Case-basis shown in Table 4.1. Only normal faulting stress regime ($\sigma_H > \sigma_v > \sigma_h$) is considered here, which are indicated as Case-1 in Table 4.1. In these three cases, minimum horizontal in situ stresses are the same, which are 37% of the overburden stress. The only difference between these three cases is the maximum horizontal in-situ stresses, which are 37%, and 55% of the overburden stress in Case-basis and Case-1, respectively.

Table 4.1 Wellbore integrity influenced by field in-situ stresses

Case No	In-situ stress combination relationship	σ_H, *KPa*	σ_h, *KPa*	σ_v, *KPa*	σ_H / σ_h	σ_h / σ_v
Case-basis	$\sigma_v > \sigma_H = \sigma_h$	6000	6000	16222	1.0	0.37
Case-1	$\sigma_v > \sigma_H > \sigma_h$	9000	6000	16222	1.5	0.37

Failure propagation patterns can provide direct information on wellbore integrity influenced by

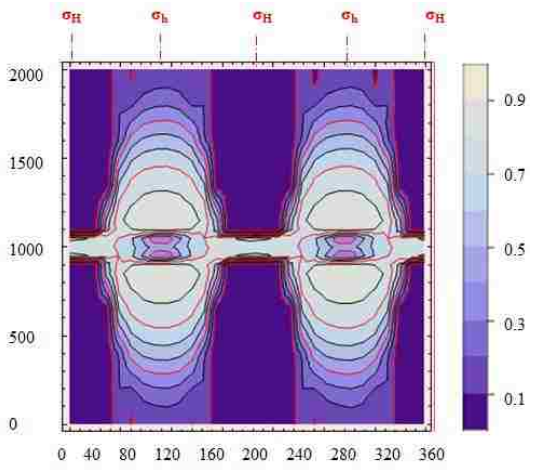

Figure 4.10 Failure contours along the stretching interface between cement and formation. Maximum damage obtained in two directions that are perpendicular to minimum horizontal stresses.

anisotropic stress field, which are illustrated in Figure 4.10. It can be observed that the least damage occurs along the directions that are perpendicular to maximum horizontal stress directions. On the contrary, the maximum damage occurs along the directions that are perpendicular to minimum horizontal stress directions because the least confining stresses is facilitate the occurrence of tensile failures. Moreover, failure front instability can also be observed at the crack tip. Failure front instability will be discussed in detail in a later section.

The deteriorated effects of field stress anisotropy on wellbore integrity are further discussed by analyzing stress and its subsequent fracture opening. Firstly, Figure 4.11 shows the pressure profile in the fractures at t_3* shown in Figure 4.4. The fluid pressure build ups around the leakage zone and then gradually decreases along the wellbore. The fluid front position is found to be at the point where the fluid pressure decreases to the initial undisturbed pore pressure. It was assumed in these computations that the formation domain is much less permeable than cement-rock interface, and fluid mainly flows along the cement-rock interface and the hydraulic conductivity greatly increases when failure occurs along the interface. With the leakage process, the fluid pressure gradually accumulates along the interface without

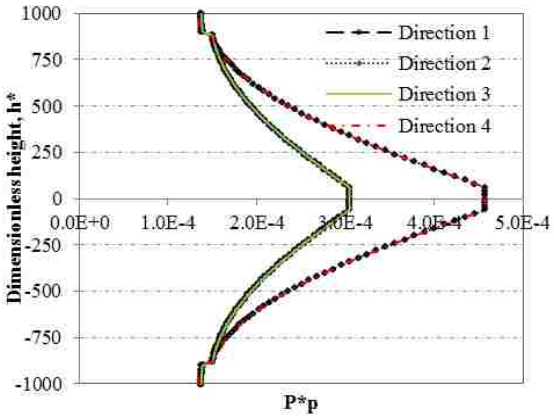

Figure 4.11 Fluid pressure along four typical directions of the anisotropic well are compared. Four selected directions have been indicated as Line 1, 2, 3 and 4 in Figure 4.5, respectively.

leaking into the formation. When the buildup pressure reaches to critical value, the excessive energy provided by fluid pressure exceeds to the critical strength of the interface, the interface is broken down abruptly near the crack tip.

Moreover, fluid pressure distribution is asymmetric along wellbore under the effects of anisotropic in situ stresses, which is shown in Figure 4.11. It is found that minimum fluid pressure occurs in Directions 1 and 3. The non-uniform excessive fluid pressure buildup process is mainly due to the fluid's tendency to flow along the least energy paths. The energy distribution is results of the combined effects of non-linear fluid flow and failure propagation influenced by the anisotropic in-situ stress environment. In this model, less compression occurs in Directions 2 and 4 because they are perpendicular to the minimum horizontal in situ stress (σ_h) relative to Directions 1 and 3 that are upright to maximum horizontal in situ stress (σ_H). Less compression facilitates fluid buildup. Hence, more fluid flow accumulates in Directions 2 and 4.

The analysis on normal and shear stresses at different directions shown in Figure 4.12 helps the further understanding on failure mechanism. The normal and shear stress on a debonded cement-rock interface caused by pressurized fluid results in a stress intensification at the end of the debond (crack tip) and cohesive stress relief at complete separation zone of the interface. During the fracturing process, there is a relief of the compressive stresses ahead of the fracture tip followed by a complete separation when the crack-opening reaches the critical value defined in the failure initiation criterion. The incidence and extent of such debonding has strong influences on the stress in the cement and rock and thus on interface

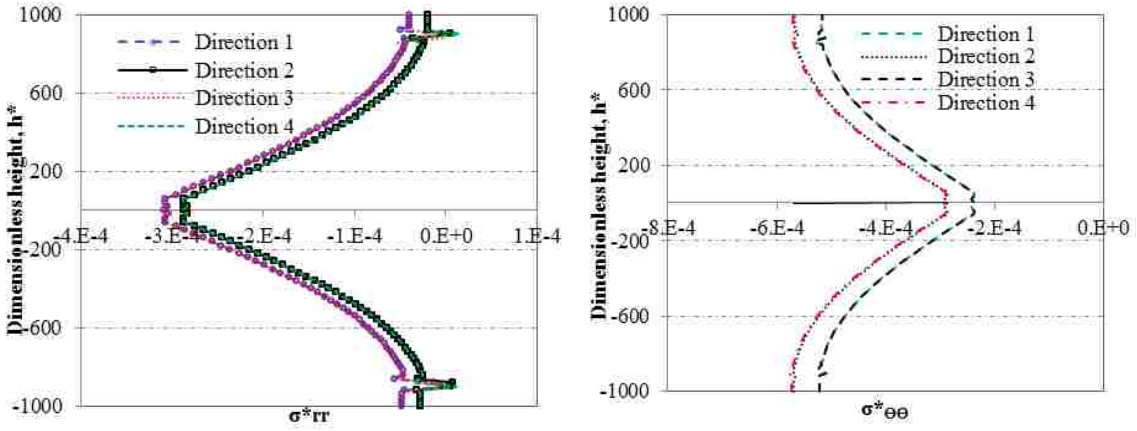

(a) Normal traction σ^*_{rr} (b) Normal traction σ^*_{rr}

Figure 4.12 Normal and tangential tractions along four typical directions of the anisotropic well are compared. Four selected directions have been indicated as Line 1, 2, 3 and 4 in Figure 4.5, respectively.

toughening. On the contrary, higher confining pressures in field conditions may increase the resistance of rock to fracturing, leading to an apparent increase of the fracture toughness. The anisotropic in situ stress distribution is inherent reason for the non-uniform stress distribution along the cement liner. At the same time, the normal and shear stresses at the bonded interface undergoes changes to satisfy equilibrium conditions with the fluid injection and failure propagation. Hence, comparing to normal and tangential stress distributed along Directions 2 and 4 that are perpendicular to the maximum horizontal in situ stress, less compression is exerted by minimum horizontal in situ stress along Direction 1 and Direction 3. Moreover, shear stresses, which are represented by $\sigma_{r\Theta}$, $\sigma_{\Theta z}$ and σ_{rz}, fluctuate at the failure tip zone. However, shear stress was at least two orders smaller than normal and tangential stresses, which lead to its relatively small but not negligible effects on wellbore integrity. In principal, by comparing the combination in situ stress and stress fluctuation caused by leakage and failure with the failure criterion introduced above, the wellbore integrity and the basic strength to prevent borehole failure can be assessed.

Inclination of the Wellbore

Stability of deviated boreholes is also an important subject in the petroleum industry because more mechanical instability problems can be caused in inclined and horizontal wells due to the alterations of the stress state and physical properties of the rock around the inclination hole (Aadnoy et al., 1987). These instability problems are commonly represented by borehole collapse, which often results in enlargement of the borehole and poor cement displacement in the drilling, producing phase and completion process. Research has been conducted on the management of the range of critical mud weights to maintain wellbore integrity of inclination wells (Aadnoy et al., 1987, and Jo and Gray, 2010). However, suitable mud weights cannot always counteract the risks of formation of cement sheath failures, especially in the inclination wells with original poor cement settings. Hence, continuous efforts are required to obtain failure containment in inclination wells.

To understand the integrity of inclined boreholes, the deviated wellbores, which oriented in the directions of 22 °, 45 °, 72 °, and 90 °(ϕ=22 °, 45 °, 72 °, and 90 °in Figure 4.13) from vertical in-situ stress, were designed. Before proceeding further, some presumptions must be clarified. The model investigated here is based on a linear elastic and isotropic model for stresses with $\sigma_v = 16222KPa$ and

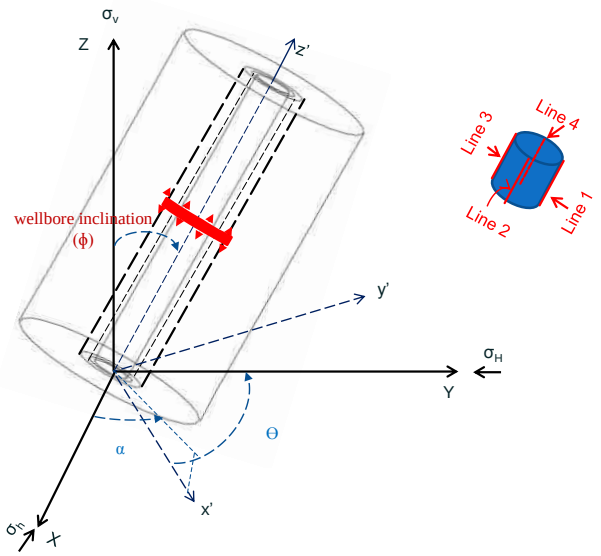

Figure 4.13 A schematic picture of the numerical model with dimensions, boundary and loading conditions, and meshes for inclined well is illustrated. The leakage position is colored in red.

$\sigma_H = \sigma_h = 6000KPa$. The directions of in situ principal stresses are assumed to coincide with the global coordinates formations (X, Y, and Z directions of Figure 4.13), directed horizontally and vertically, respectively. Moreover, the casing, cement and borehole are concentric. The uniform interface properties are also presumed. Figure 4.13 defines the inclination, ϕ, and azimuth, α, for borehole, and the drive provided by the pressurized fluid that arose from casing shoe leakage.

To assess sensitivity of wellbore stability with varying hole azimuth, which is represented by wellbore inclination, in the study field, critical fracture-initiation pressure (P_{cf}) is firstly investigated. P_{cf} is determined by the stress state in conjunction with a failure criterion. Figure 4.14 shows the sensitive influences of wellbore inclinations on P_{cf}. As the wellbore inclination increases, P_{cf} decreases by following three stages: slightly decrement stage, dramatically reduction stage and stable stage. The first

slightly decrement stage occurs when borehole inclination is small (less than 25°), P_{cf} is slightly less than that in vertical wells with isotropic horizontal in situ stress because the borehole axis is almost perpendicular to the plane of isotropy and the stress distributions are similar to the isotropic ones. P_{cf} decreases drastically at the second stage when borehole inclinations change from 20° to 70° due to the influences of in situ stress anisotropy. When wellbore inclination angle reaches and beyond 70°, the

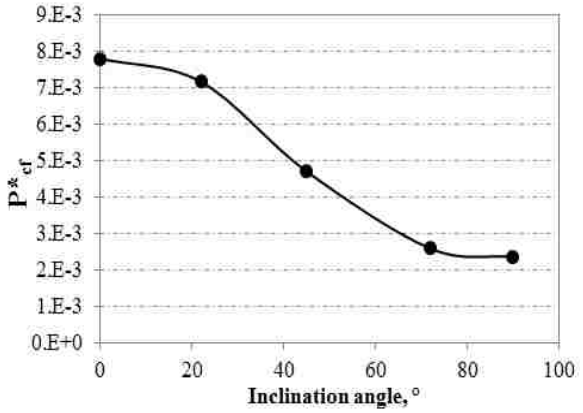

Figure 4.14 The variation of fracture initiation pressure (P_{fD}) with wellbore inclination angle ϕ.

broaching along cement interface can be formed easily regardless of wellbore pressurization. We can conclude that the in situ stress anisotropic effects can lead to a reduction in the fracture-initiation pressure in highly inclined wellbores. In other words, a larger possibility for loss of wellbore integrity exists in highly inclined wellbores. Physically, this implies that drilling the well beyond certain borehole inclinations without experiencing fracturing is not possible. Moreover, the magnitude of these critical angles is constrained by the in situ stress field and cement interface strength.

Failure propagation process is another important parameter that demonstrates the different failure processes of diverse inclined wells. Basic information about the inclination effects on failure rates are generated based on tracking the relationship of damage percentage vs. excessive energy provided around the casing shoe, which is illustrated in Figure 4.15. Five cases with inclinations of 0°, 20°, 45°, 70°, and 90° are compared. Our studies show that wellbore instability increases when the direction of the wellbore moves far away from the in-situ vertical stress. Note that this conclusion is obtained from wells in isotropic horizontal in situ stress environments, which is one typical case of normal faulting

environments. In these environments, breakout initiation is more likely to occur in wells that are highly deviated in the direction of horizontal stress (maximum horizontal stress, if anisotropic horizontal in situ stress exits) than for vertical wells. In less deviated cases with inclination angle 0 ° or 22 °, the failure initiates when excessive pore pressure reached P_{cf}. On the contrary, for higher inclination wells, such as 70 ° and 90 °, wellbore instability is lost even when the leakage around the casing shoe is very small. In

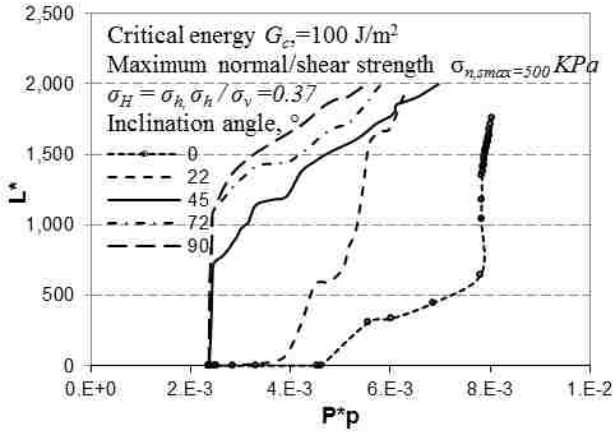

Figure 4.15 Fracture propagation process comparisons in different inclination wellbores with inclination angles stemming from 22 °, 45 °, 72 ° to 90 °.

other words, borehole becomes more sensitive toward instability with wellbore rotating from a vertical to a horizontal position. The loss of wellbore instability cannot be avoided in highly inclined cases. The

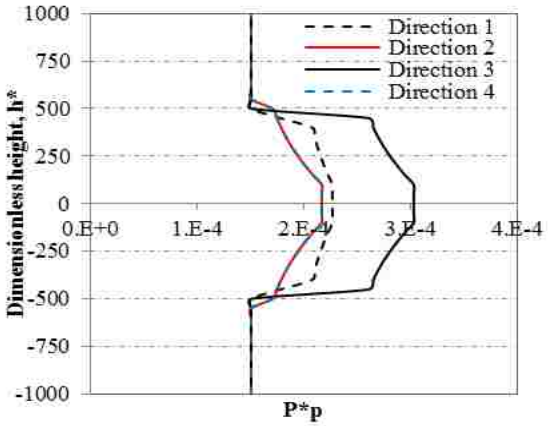

Figure 4.16 Fluid pressures along four typical directions of the 45 ° deviated well are compared. Four selected directions are indicated as Line 1, 2, 3 and 4 in Figure 4.18, respectively.

similar phenomenon has been observed in Aadnoy, et al. (1987) and Chen et al (1996). Therefore, the integrity of inclination wellbores is controlled not only by relative magnitudes of vertical, major and

minor horizontal stresses but also wellbore inclinations. Based on this investigation, good practice suggestions can be proposed on the inclination of the wells to guarantee successful process in well drilling, completion and its subsequent stability.

To understand the physical mechanism of wellbore stability involved in the inclination well, the case with the 45 ° inclination angle is selected for further analysis. Comparisons were also carried out for four typical directions: Line 1, Line 2, Line 3 and Line 4 shown in Figure 4.13. A specific time t^*_2 shown in Figure 4.4 is selected as the comparison basis. Figure 4.16 shows the pressure profile in the fracture and process zone during failure propagation. Similar fluid pressure distribution is observed along Dimension 2 and dimension 4 due to similar in-situ stress controlling effects. However, non-similar fluid pressure occurs along Directions 1 and 3 as a consequence of different effects that vertical in-situ stress takes, which is compressive effects along Direction 1 and tensile effects along Direction 3. The fluid pressure undergoes decrease from the leaking zone to the intact interface zone. The fluid front position is found to be the point where the fluid pressure reaches the initial undisturbed value. And this point is still called crack tip. Fluid pressure distributions demonstrate the energy redistribution around the wellbore.

Further understanding is obtained from fracture openings and stress distributions along the wellbore, which are demonstrated in Figures 4.17 and 4.18. Fracture opening can be considered as accompanying results of fluid pressure distribution. Figure 4.17 shows that the largest fracture opening exists along

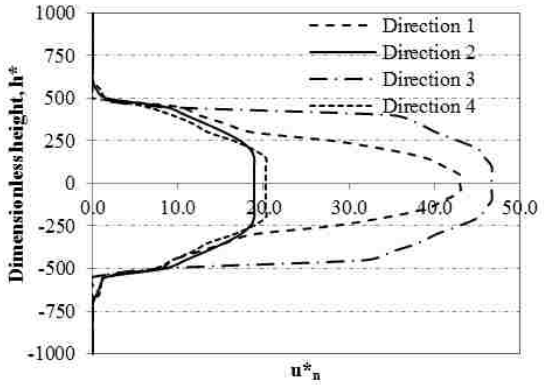

Figure 4.17 Fracture opening along four typical directions of the 45 ° deviated well are compared. Four selected directions are indicated as Line 1, 2, 3 and 4 in Figure 13, respectively.

Direction 3 and the least amount of fracture openings occur in Directions 2 and 4. To explain this

phenomenon, normal and tangential stresses at the cement-rock interface are analyzed. It can be observed that normal and tangential stresses are different even in the intact zone that is far away from the leaking source. That is because the in-situ stress is disturbed by well inclination. The vertical overburden stress is originally parallel to the axis of the well hole in vertical wells with non-direct influences on wellbore failures. However, the inclination of the well makes it possible that failures are inhibited in some directions and inspired in other directions due to different effects that in situ stress cause. This imbalance is further worsened as a consequence of the non-linear failure and energy distributions. In fact, the fracture opening is a consequence of the combination effects of stress distribution, excessive fluid energy and energy instability caused by unbalanced failure propagation. Moreover, the variations in magnitude of normal and tangential tractions are consistent with excessive fluid pressure that exerted, which emphasizes the dominant effects that fluid pressure takes on failure initiation and propagation.

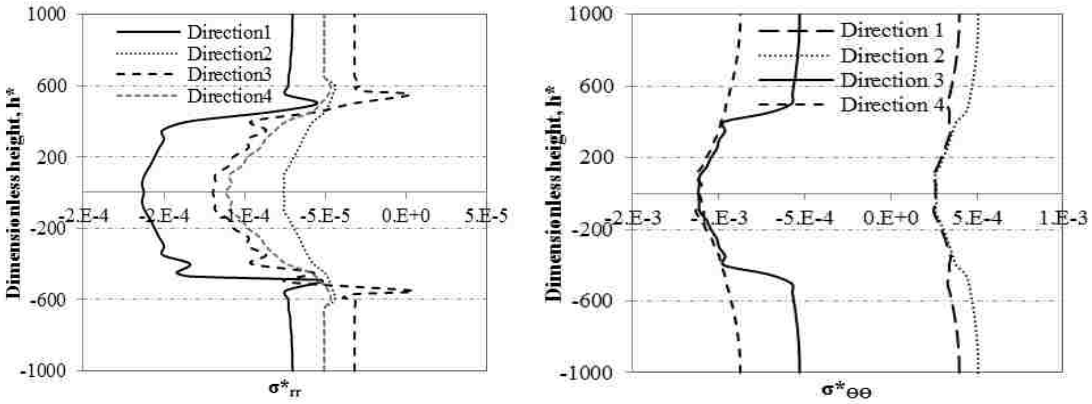

(a) Radial normal tractions σ^*_{rr} **(b) Tangential tractions $\sigma^*_{\theta\theta}$**

Figure 4.18 The comparisons of normal and tangential tractions along the cement liner of the 45° deviated well are demonstrated.

Furthermore, the failure patterns of 45° inclined well are demonstrated in Figure 4.19 in terms of failure contour, which is stretched from cylindrical interface between cement and rock. In order to limit the inclination to be the only influence variable in this case, uniform cohesive zone properties, formation properties and in situ stresses are considered as the priority. It can be observed that failures initiate from Line 1 and Line 3 and are prone to propagate along the axial directions rather than go around the

wellbore. With the propagation of failures along the axial direction, some of the energy promotes failures around the wellbore. Non-uniform failure patterns observed in this case demonstrate that wellbore

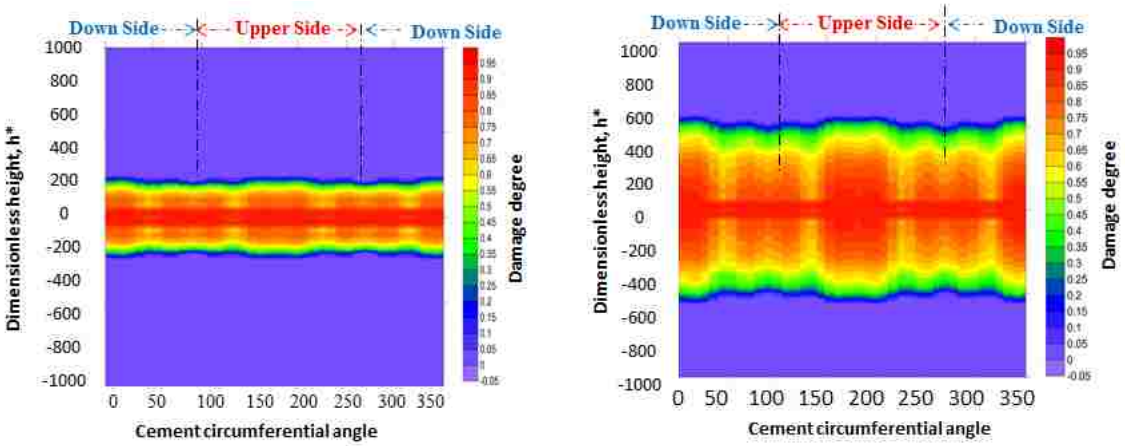

Figure 4.19 Failure propagation pattern along the cement liner of the 45° deviated well are demonstrated.

inclination is one of paramount parameters on controlling wellbore integrity. The borehole becomes more sensitive toward failures due to stress variation caused by wellbore inclination. In tectonically stressed areas, wellbore stability may be improved by choosing the proper geographic direction for the borehole.

Eccentricity of the Wellbore

Casing eccentricity also has governing influences on wellbore stability and is the main source of non-uniform loading of the casing (Salehabadi et al., 2009), especially from the cementing operation point of view and the long-term production process. Casing eccentricity is defined as the deviated degree of the casing from the center of the wellbore at the end of the casing running operation (Salehabadi et al., 2010). Casing eccentricity and cement channel usually happen simultaneously. When the casing is off-centered, the fluid tends to flow along the paths of least resistance, which induces non-uniform velocity distribution: faster on the wide side and slower on the narrow side of the geometry. The process of slurry displacement through wells is also governed by the viscosity and density ratio between fluids, flow rate, wellbore inclination angle besides annular eccentricity (Christopher, et al., 1990). Then the distorted fluids (cement slurry) may bypass the slowly moving drilling mud on the narrow side. The consequence is that the annulus may be left with a long strip of inefficient cementing displacement on the narrow part at

the end of the displacement process. This inefficient cementing tends to build up cement channeling, which usually accompanies the cavities that are filled with drilling mud, unset cement, or formation materials (Silva et al., 1996, and Salehabadi et al., 2010). Simultaneous cement channeling and casing eccentricity are the worst effects of deterioration in casing collapse resistance, wellbore integrity, as well as safety issues (Yuan et al., 2012, and Salehabadi et al., 2010). Hence, it is significant to know the effects of casing eccentricity and cement channeling on the wellbore integrity if cementing problems exist.

Prior to discussing numerical modeling, it is paramount to give a basic description of eccentricity. A casing that is cemented into the hole with non-uniform clearance is referred to as eccentric (Berger et al., 2004). The degree of eccentricity is described by the eccentricity of the annulus, *e*, which is expressed as a function of distance between pipe centers and borehole centers in Figure 4.20. The eccentricity is defined by

$$e = \frac{2D_{BC}}{(d_c - d_t)} \quad , \qquad \textbf{(4.24)}$$

where d_c and d_t are inner diameters of cement and outer diameters of the casing, respectively. The eccentricity, *e*, varies from 0 to 1. For two specific cases: e=0 is concentric and e=1 implies that the

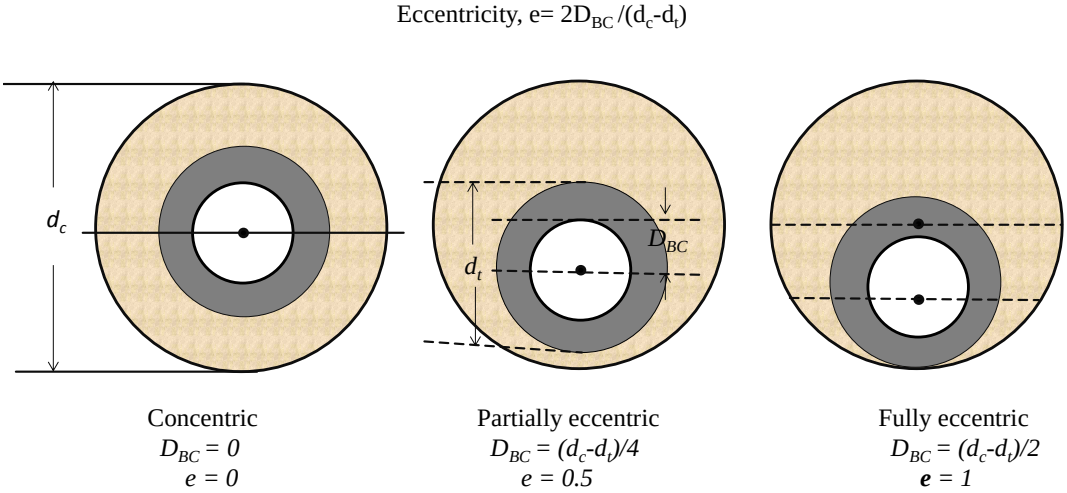

Figure 4.20 A schematic picture of the wellbore eccentricity is illustrated. Two typical eccentricity cases with e=0.5 or e=1.0 are compared with concentric case.

casing contacts the wellbore wall on the narrow side. A centric (e=0) and two eccentric casings (e=0.5 and e=1.0) shown in Figure 4.20 are analyzed here.

In order to simplify the model, horizontal isotropic stress fields are considered ($\sigma_v = 16222KPa$, $\sigma_h = \sigma_H = 6000KPa$). The vertical wells with e=0.5 and e=1.0, as well as the inclination well with a 45° orientation angle from the in-situ vertical stress, is analyzed and compared. The trapped fluid pressure existing around the wellbore is considered here to be the driving force for failure propagation. Moreover, these models also consider the variations of interface properties caused by eccentricity and inclination. Four cases are investigated here: Case-basis describes a concentric vertical well with uniform interface strength between cement and rock, which acts as the comparison basis; On the other hand, non-consistent interface strength is considered in Case-1, Case-2 and Case-3, where the narrow side of the wellbore has weaker strength ($\sigma_{n,max}$= $\sigma_{s,max}$= $\sigma_{t,max}$ =100 KPa) and the wider side of the wellbore has stronger interface strength ($\sigma_{n,max}$= $\sigma_{s,max}$= $\sigma_{t,max}$ =420 KPa). Case-1 and Case-2 are vertical wells at half (e=0.5) and full eccentricity (e=1), respectively. On the contrary, Case-3 is a 45° inclined well with half eccentricity (e=0.5). Therefore, its narrow side provides a higher potential fluid communication path between the formation and the borehole. These cases facilitate the analysis of the effects of eccentricity and inclination on wellbore integrity in eccentric wells. The requirements of failure containment are further defined based on eccentricity and the combination of eccentricity and inclination. Detailed information is listed in Table 4.2. Interface properties distributions for these three cases are demonstrated in Figure 4.21.

Table 4.2 Numerical analysis on the eccentricity and inclination of the wellbore

Case No	Eccentricity, °	Wellbore inclination angle, °	In-situ stress combination relationship, KPa	Interface strength, KPa	
				Wider side	Narrow side
Case-basis	0.0	0	$\sigma_v > \sigma_H = \sigma_h$ (16222>6000=6000)	420	
Case-1	0.5			420	100
Case-2	1.0			420	100
Case-3	0.5	45		420	100

The eccentricity effects on wellbore integrity are further investigated by comparing failure contours and failure processes. Case-1 with 0.5 eccentricities is selected as a typical example to understand the

physical process caused by the eccentricity. Failure contours that are generated from the stretching interface between cement and rock are investigated in Figure 4.22. It can be observed that damage initiates at the narrow side of the wellbore around the leakage source. Then failures are more prone to propagate parallel to the borehole axis at the narrow side instead of cutting around the wellbore, which is due to more stress concentration at the narrow side than those in the wider side caused by wellbore eccentricity, as well as weaker interface strength as a consequence of wellbore eccentricity. Moreover, failures also try to cut circumferentially across the borehole. Failures always propagate along the direction

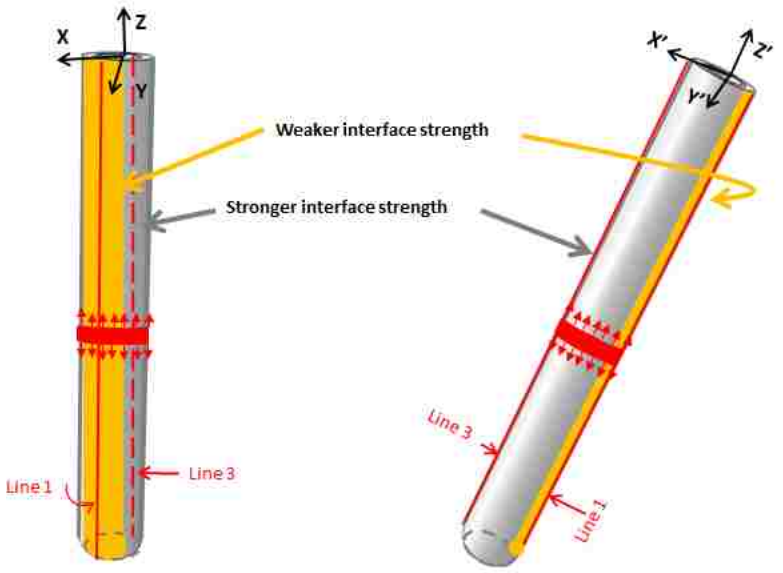

(a) Vertical well with eccentricity: e=0.5 (or 1.0) **(b) 45 °inclined well with eccentricity: e=0.5**

Figure 4.21 A schematic picture of the interface property distribution of numerical eccentricity model is demonstrated. The weaker interface caused by the eccentricity is colored in yellow. Eccentricity case: Vertical wells with e=0.5 and e=1.0 and 45 ° inclined well with e=0.5. Two lines are specified for further analysis. Line 1 and Line 3 represent weaker and strength part, respectively.

where the least energy is required. When failures propagate far away from the pressure source zone, non-uniform failure patterns tend to form, which is the consequence of non-uniform stress and energy distribution in the failure propagation process.

On the other hand, failure propagation process, which is represented by the relationship between dimensionless crack length changes versus dimensionless excessive fluid pressure, can directly indicate wellbore integrity for different inclination wells. Case-basis, Case-1 and Case-2 that are all vertical wells

with different eccentricities are compared in Figure 4.23. The vertical wellbore without eccentricity (Case-basis) shows that failure does not begin until the magnitude of the excessive pressure has reached a critical level, which is demonstrated by a red circle; failure starts to grow suddenly until excessive energy provided by leakage of fluid reaches the critical threshold. Beyond the critical threshold points, failure broaching forms because the induced stresses at the fracture tips are large enough to propagate initiated fractures. Moreover, the critical thresholds, which are illustrated by purple, orange and red circles in

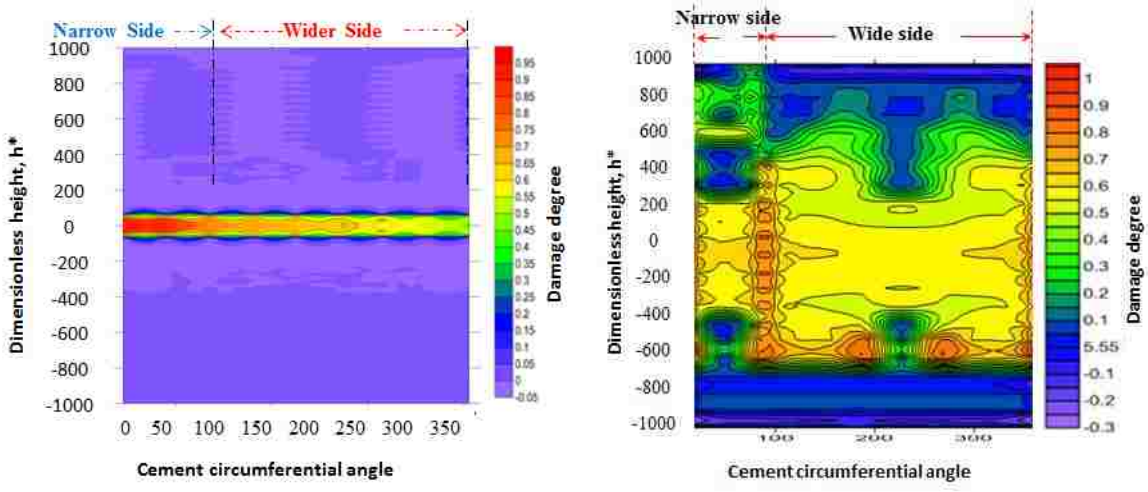

(a) t^*_1 **(b) t^*_3**

Figure 4.22 The Failure propagation patterns of vertical well with 0.5 eccentricity (Case-1 in Table 2) around the leakage zone are demonstrated.

Figure 4.23, decreases with the increment of the wellbore eccentricities. Case-1 and Case-2 have the cohesive interface strength and different eccentricity, which indicates significant effects of stress variations on wellbore integrity.

Further analysis is conducted by considering the wellbore inclination in the eccentricity wells. Case-3 in Table 4.3 describes a well with 45 °inclination and half eccentricity. Case-3 is compared to Case-1 with no inclination and half eccentricity. For simplicity, the interface strengths in these two cases are assumed to be the same to avoid the influences of properties. The concurrence of inclination and eccentricity is a common phenomenon in the oil industry because wellbore eccentricity is easily caused in inclined wells.

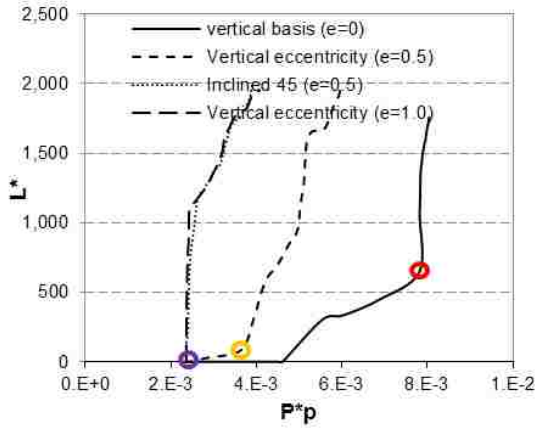

Figure 4.23 Fracture propagation process comparisons in different eccentricity wellbores with different eccentricities. Vertical basis has 0 eccentricity and uniform interfacial strength.

From Figure 4.23, we can observe that the critical threshold in Case-3 is smaller than that in Case-1, which demonstrates that the wellbore integrity could be further worsened when the wellbore is inclined. The combined effects of eccentricity and inclination increase the stress variations and concentration, which increases the possibility of the loss of wellbore integrity increases. This phenomenon is more obvious when an inclined wellbore is combined with the effects of a weaker interface. It can be concluded that critical pressure for failure broaching is determined not only by interfacial properties, cement and formation properties, rock in–situ stresses, as well as the magnitude of the excessive pressure, but also by the eccentricity and inclination of the wellbore.

Conclusion

We proposed a three dimensional model with a cohesive zone approach to reflect the real situations of wellbore integrity by considering its anisotropy, inclination, eccentricity, heterogeneity and complexity. This model predefined the potential failure paths by cohesive elements to track the sophisticated mechanical characteristics of cement interface during the leakage process. This model offers a full range of assessment on failure rates, failure propagation processes, and non-planar failure patterns. The spatial failure prediction ability of this model makes it more advance than traditional two dimensional models.

Our simulations explore the mechanism of crack initiation and propagation near the wellbore by analyzing the variation of fluid pressure, stresses, fracture opening and damage around the wellbore. The

excessive fluid pressure induced by the leakage is the drive for the cement-formation interface failures. The interface failure rate and propagation process can be influenced by the variation and fluctuation of fluid pressure and stresses. The combined effects of intensified tensile stress and shear stress occur at the crack tip, which initiates the failure if they satisfy with the failure initiation criterion. On the contrary, interface failure and the hydraulic conductivity of the interface can further affect fluid pressure and stress distribution around the wellbore.

Moreover, the interface containment ability is also influenced by the heterogeneity of the interface. The interface integrity can be deteriorated and the complexity of the failure patterns can be promoted if interface heterogeneity exists. Results show that higher heterogeneous degrees induce higher possibilities for interface broaching and faster evolution of channels under the effects of upward fluid flow induced by leakage. The heterogeneity of the interface more effectively represents real wellbore conditions because cement and formation have natural heterogeneous and unsmooth characteristics. Heterogeneity is usually formed during the complex consolidation process of the porous medium and subsequently strengthened due to its complex interactive effect with fluid flow.

Furthermore, wellbore stability is also influenced by the inclination of the wellbore, anisotropy in stress field, and wellbore eccentricity. Comprehensive analysis has been provided in these cases based on normal and shear stress, fracture opening, failure propagation rates and failure patterns. Accurate determination of the attributes of anisotropy in stress fields, wellbore inclination and eccentricity can provide more reliable predictions on wellbore integrity. It was concluded that wellbore integrity is greatly influenced by the confining stress and its distribution. The differences in in-situ stress can further inspire shear stress, which further worsen the wellbore integrity during the leakage process. Moreover, the influences of well inclination and eccentricity on wellbore integrity are also predominant. When the wellbore is rotated from a vertical to a horizontal position, the analysis shows that the borehole becomes more sensitive toward failures because degrees of in-situ anisotropy increase with the increment of

inclination. On the other hand, wellbore eccentricity can also deteriorate wellbore integrity due to non-uniform stress concentration around the wellbore and its concomitant channelization.

Additionally, simulations also show that the anisotropic, inclination and eccentricity wellbore fractures are prone to propagate along the borehole axis directions, instead of cutting across the wellbore. Non-uniform failure patterns and failure front instability can be obtained when cement-rock interface strength is heterogeneous, anisotropic in-situ stress environment, or wellbore inclination and eccentricity. The comprehensive consideration on heterogeneity, anisotropic in-situ stress field, wellbore inclination and eccentricity can effectively reduce the frequency or rate of wellbore instabilities.

Nomenclature

B Skempton's coefficient

$\bar{B}$ Matrix for the strain ε that contains the derivatives of the displacement interpolation functions

C Elasticity tensor of the solid matrix

c_b Fluid leak-off coefficients on the bottom surfaces of the fracture

c_t Fluid leak-off coefficients on the top surfaces of the fracture

D Scalar stiffness degradation index

F_p Force vector associated with boundary conditions

F_u Force vector associated with the gravity

g Gravity, m/s^2

G Shear modulus of rock, KPa

G_c Critical fracture energies during deformation, J

G_n Work done by the tractions and their conjugate relative displacements in the normal directions, J

G_s Work done by the tractions and their conjugate relative displacements in first shear directions, J

G_t Work done by tractions and their conjugate relative displacements in second shear directions, J

G_T Total energy in the mode-mix condition, J

$\bar{H}$ Permeability matrix

I Identity matrix

$\bar{K}$ Stiffness matrix of the solid phase

K Porous bulk modulus for the solid skeleton

k Permeability tensor

k_n Stiffness components in normal direction

K_{n0} Initial tensile stiffness

K_{s0} / K_{t0} Initial value for shear stiffness

k_s / k_t Stiffness components in shear direction

K_s Solid grain bulk modulus, KPa

K_f Bulk modulus of the fluid

$1/M$ Specific storage coefficient at constant strain

N_p Matrices for the displacements

N_u Matrices for pore pressures

$\vec{p}$ Pressure vector of the values of the unknowns at the element nodes

p Fluid pore pressure, KPa

p_t Pore pressures in the adjacent poroelastic material on the top surfaces of the fracture, KPa

p_b Pore pressures in the adjacent poroelastic material on the bottom surfaces of the fracture, KPa

q Fluid flux, m^3/s

$\bar{Q}$ Coupling matrix related to Biot's constant α,

$\bar{S}$ Compressibility matrix related to the bulk modulus of fluid and solid,

T	Total stress
t	Time, sec
t_n	Normal traction, KPa
t_{n0}	Peak values of the nominal stress when the deformation is purely normal to the interface, KPa
t_s / t_t	Tangential traction, KPa
t_{s0} / t_{t0}	Peak values of the nominal stress when the deformation is purely in shear direction, KPa
$\boldsymbol{u}$	Displacement of the solid matrix,
$\vec{u}$	Displacement vector of the values of the unknowns at the element nodes
ν	Poisson's ratio
ν_u	Undrained Poisson's ratio
w	Crack opening, m
α	Biot-Willis coefficient
δ_m	Effective relative displacements, m
δ_{m0}	Effective relative displacements corresponding to δ_{n0} and δ_{s0}, m
δ_{mf}	Effective relative displacements corresponding to δ_{nf} and δ_{sf}, m
δ_n	Crack opening displacement, m
δ_{nf}	Critical relative normal displacements when tractions diminish, m
δ_s / δ_t	Crack sliding displacement, m
$\delta_{sf} / \delta_{tf}$	Critical relative shear displacements when tractions diminish, m
$\boldsymbol{\varepsilon}$	Strain tensor
ς	Change of fluid content, m^3
μ	Viscosity, mPa.s

ρ Density of solid

ρ_f Density of fluid

References

Aadnoy, B. S., Rogaland, R. C., and Chenevert, M. E., 1987, Stability of Highly Inclined Boreholes (includes associated papers 18596 and 18736), SPE Drilling Engineering, Vol. 2(4), pp: 364-374.

Alfano, G., and Crisfield, M. A., 2001, Finite Element Interface Models for the Delamination Analysis of Laminated Composites: Mechanical and Computational Issues, International Journal for Numerical Methods in Engineering 50:1701-36.

Ballard, T. J., Beare, S. P., and Lawless, T. A., 1994, Fundamentals of Shale Stabilisation: Water Transport Through Shales, SPE 24974-PA, SPE Formation Evaluation, Vol. 9 (2), pp: 129-134.

Barenblatt, G. I., 1962, The Mathematical Theory of Equilibrium Cracks in Brittle Fracture, Journal of Applied Mechanics, 1962, pp: 7, 55-129.

Barrett, J. D., and Foschi, R. O., 1977, Mode II Stress Intensity Factors for Cracked Wood Beams, Engineering Fracture Mechanics, Vol.9, No.2, 1977, pp.371-378.

Batchelor, G. K., 1967, An Introduction to Fluid Dynamics, Cambridge University Press, London, pp: 615-620.

Bearden, W. G., and Lane, R. D., 1961, Engineered Cementing Operations to Eliminate WOC Time, SPE 61-017, Drilling and Production Practice.

Berger, A., Fleckenstein, W. W., Eustes, A. W., and Thonhauser, G., 2004, Effect of Eccentricity, Voids, Cement Channels, and Pore Pressure Decline on Collapse Resistance of Casing, SPE 90045-MS, SPE Annual Technical Conference and Exhibition, 26-29 September 2004, Houston, Texas.

Biot, M. A., 1941, General theory of three dimensional consolidation, J. Appl. Phys., Vol. 12(2), pp: 155–164.

Boone, J. T., and Ingraffea, A. R., 1990, A numerical procedure for simulation of hydraulically driven fracture propagation in poroelastic media. Int J Numer Anal Methods Geomech 14:27–47.

Bour, D., 2005, Cyclic Steam Well Design: A New Approach to Solve an Old Problem of Cement Sheath Failure in Cyclic Steam Wells, SPE 93868-MS, SPE Western Regional Meeting, Irvine, California Mar 30 - Apr 01 2005.

Bourgoyne, A. T., Chenevert, M. E., Millheim, K. K., and Young, F. S., 1986, Applied Drilling Engineering, Society of Petroleum Engineering Vol. 2, pp: 312-324.

Butsch, R. J., 1995, Overcoming Interpretation Problems of Gas-Contaminated Cement Using Ultrasonic Cement Logs, SPE 30509-MS, SPE Annual Technical Conference and Exhibition, 22-25 October 1995, Dallas, Texas.

Camacho, G. T., and Ortiz, M., 1996, Computational Modeling of Impact Damage in Brittle Materials. Int. J. Solids Structures 33, 2899–2938.

Camanho, P. P., and Dávila, C. G., 2002, Mixed-mode decohesion finite elements for the simulation of delamination in composite materials, NASA-Technical Paper, 211737(1), 33.

Camanho, P. P., and Matthews, F. L., 1999, Delamination Onset Prediction in Mechanically Fastened Joints in Composite Laminates, Journal of Composite Materials 33:906-27.

Carpenter, R. B., Brady, J. L., and Blount, C. G., 1992, Effects of Temperature and Cement Admixes on Bond Strength, SPE 22063-PA, Journal of Petroleum Technology, Vol. 44(8).

Carrier, B., and Granet, S., 2011, Numerical modeling of hydraulic fracture problem in permeable medium using cohesive zone model, Engineering Fracture Mechanics 79 (2012), pp: 312–328.

Carter, L. G. and Evans, G. W., 1964, A Stufy of Cement-Pipe Bonding, Journal of Petroleum Technology, (Feb, 1964): 157-160.

Charalambides, P. G., Lund, J., Evans, A. G., and McMeeking, R.M., 1989, A Test Specimen for Determining the Fracture Resistance of Bimaterial Interfaces, Journal of Applied Mechanics, 56, 77-82.

Chen, J., Crisfield, M. A., Kinloch, A. J., Busso, E. P., Matthews, F. L., and Qiu, Y., 1999, Predicting Progressive Delamination of Composite Material Specimens via Interface Elements, Mechanics of Composite Materials and Structures 6, pp: 301-17.

Chen, Z., 2012, Finite Element Modelling of Viscosity-dominated Hydraulic Fractures, Journal of Petroleum Science and Engineering, 88-89, 136–144.

Corigliano, A., and Ricci, M., 2001, Rate-dependent Interface Models: Formulation and Numerical Apllications, Int. J. Soilds Structures, Vol. 38, 547-576.

Cui, W., Wisnom, M. R., and Jones, M., 1992, A Comparison of Failure Criteria to Predict Delamination of Unidirectional Glass/Epoxy Specimens Waisted Through the Thickness, Composites 23(3):158-66.

Dahi Taleghani, A., and Wang, W., 2013, Emergence of Delamination Fractures around the Casing and Its Stability, International Journal of Geomechanics, In review.

Dávila, C. G., Camanho, P. P., and Moura, M. F., 2001, Mixed-Mode Decohesion Elements for Analyses With Progressive Delamination, 42nd AIAA/ASME/ASCE/AHS/ASC Structures, Structural Dynamics and Materials Conference (Seattle, Washington, U.S.A.).

Dávila, C. G., and Johnson, E. R., 1993, Analysis of Delamination Initiation in Postbuckled Dropped-Ply Laminates, AIAA Journal 31 (4): 721-727.

Deeks, Z. J., and Yang, A. J., 2007, Modelling cohesive crack growth using a two-step finite element-scaled boundary finite element coupled method, International Journal of Fracture, Vol. 143, pp: 333–354.

Dhaliwal, R. S., Saxena, H. S., and He, W. H., 1992, Stress intensity factor for the cylindrical interface crack between nonhomogeneous coaxial finite elastic cylinders, Eng. Fract. Mech. 43 (6), pp: 1039-1051.

Dugdale, D. S., 1960, Yielding of Steel Sheets Containing Slits. Journal of the Mechanics and Physics of Solids, Vol. 8, pp: 100-104.

Espinosa, H. D., Dwivedi, S., and Lu, H. C., 2000, Modeling impact induced delamination of woven fiber reinforced composites with contact/cohesive laws, Comput. Methods Appl. Mech. Engrg. 183 (3–4), 259–290.

Evans, 1962, Bounding Studies of Cementing Compositions to Pipe and Formations, SPE 62-072, Drilling and Production Practice, 1962.

Fjar, E., Holt, R. M., Raaen, A. M., Risnes, R., and Horsrud, P., 2008, Petroleum Related Rock Mechanics (2nd Edition), Printed or Bound in Hungary.

Flak P. E., Larry H., Muhanna, G. A., and Mohamed, A. Q., 1995, Case History: Relief Well Control of Underground Blowout In Bahrain, SPE 29859-MS, Middle East Oil Show, 11-14 March 1995, Bahrain.

Fleckenstein, W. W., Eustes, A. W., and Miller, M. G., 2000, Burst Induced Stresses in Cemented Wellbores, SPE 62596-MS, SPE/AAPG Western Regional Meeting, Long Beach, California,19-22 June 2000.

Gerstle, W. H., and Xie, M., 1992, FEM Modeling of Fictitious Crack Propagation in Concrete, Journal of Engineering Mechnics, Vol. 118 (2), pp: 416-434.

Griffith, A. A., 1924, The Theory of Rupture. In Proc. FirstInternat. Congr. Appl. Mech.

Griffith, J. E., Ravi, K., Saasen, A., and Nødland, N. E., 2004, Foam Cement Engineering and Implementation for Cement Sheath Integrity at High Temperature and High Pressure, SPE 87194-MS, IADC/SPE Drilling Conference, Dallas, Texas, 2-4 March 2004.

Grosmangin, M., 1961, A Sonic Method for Analyzing the Quality of Cementation of Borehole Casings, JPT (Feb, 1961) 165-175, Trans., AIME, 222.

Hall, J., Allanson, J., Gripp, K., and Slavotinek, A., 2006, Handbook of Physical Measurements, Oxford Publication.

Havira, R. M., 1982, Ultrasonic Cement Bond Evaluation, SPE 1982-N, SPWLA 23 Annual Logging Symposium, 1982.

Hayman, A. J., Hutin, R. and Wright, P. V., 1991, High Resolution Cementation and Corrosion Imaging by Ultrasound, paper KK, Transactions SPEWLA 32nd Annual Logging Symposium, Midland, Texas.

Heathman, J., and Beck, F., 2006, Finite element analysis couples casing and cement designs for HT/HP wells in East Texas, SPE 98869, IADC/SPE Drilling Conference Miami, Florida, 21-23 February 2006.

Hillerborg, A., Modeer, M., and Petersson, P., 1976, Analysis of Crack Formation and Crack Growth in Concrete by Means of Fracture Mechanics and Finite Elements, Cement Concrete Res, Vol. 1976 (6), pp: 773–782.

Hills, R., and Williams, A. F, 1993, The stress field of the North West Shelf and wellbore stability, APEA Journal. Vol. 33, pp: 373-385.

Hossain, M. M., Rahman, M. K., and Rahman, S. S., 2000, Hydraulic fracture initiation and propagation: roles of wellbore trajectory, perforation and stress regimes. J. Petrol. Sci. Eng. Vol. 27, pp: 129-149.

Hutchinson, J. W., 1990, Mixed Mode Fracture Mechanics of Interfaces, Metal/Ceramic Interfaces, Vol. 4, pp: 295-306.

Jackson, P. B., and Murphey, C. E, 1993, Effect of Casing Pressure on Gas Flow through a Sheath of Set Cement, SPE/IADC 25698, SPE/IADC Drilling Conference, Amsterdam, 23-25 February 1993.

Jo, H., and Gray, K. E., 2010, Mechanical Behavior of Concentric Casing, Cement, And Formation Using Analytical And Numerical Methods, SPE 10-142, 44th U.S. Rock Mechanics Symposium and 5th U.S.-Canada Rock Mechanics Symposium, June 27 - 30, 2010 , Salt Lake City, Utah.

Jutten, J. J., Gulllot, D., and Parcevaux, P. A., 1989, Relationship between Cement Slurry Composition, Mechanical Properties, and Cement-bond-log Output, SPE 16652-PA, SPE production Engineering, 1989, pp: 75-82.

Kårstad, E., and Aadnoy, B. S., 2005, Optimization of Borehole stability using 3D stress optimization. Proceedings of the SPE Annual Technical Conference.

Ladva, H. K. J., Craster, B., Jones, T. G. J., Goldsmith, G., and Scott, D., 2005, The Cement-to-Formation Interface in Zonal Isolation, SPE 88016-PA, SPE Drilling & Completion, Vol.20, (3), pp: 186-197.

Lake, L. W., 2007, Petroleum Engineering Handbook (Vol.4): Reservoir Engineering and Petrophysics.

Lecampion, B., 2012, Hydraulic Fracture Initiation From an Open-hole: Wellbore Size, Pressurization Rate And Fluid-solid Coupling Effects, SPE 2012-60146th U.S. Rock Mechanics/Geomechanics Symposium, June 24 - 27, 2012 , Chicago, Illinois.

Lecampion, B., and Prioul, R., 2013, Competition Between Transverse And Axial Hydraulic Fractures In Horizontal Wells, SPE 163848-MS, 2013 SPE Hydraulic Fracturing Technology Conference, Feb 04 - 06, 2013 2013, The Woodlands, TX, USA.

Lecampion, B., Quesada, D., Loizzo, M., Bunger, A., Kear, J., Deremble, L., and Desroches, L., 2011, Interface Debonding as a Controlling Mechanism for Loss of Well Integrity: Importance for CO2 injector wells, Energy Procedia 4 (2011), pp: 5219-5226.

Lewis, R. W., and Schreffler, B. A., 2000, The finite element method in the static and dynamic deformation and consolidation of porous media.Wiley, London.

Li, C. Y., Weng, G. J., and Duan, Z. P., 2001, Dynamic behavior of a cylindrical crack in a functionally graded interlayer under torsional loading.Int.J.SolidStruct, Vol. 36(42-43), 7473-7485.

Li, H., and Chandra, N., 2003, Analysis of crack growth and crack-tip plasticity in ductile materials using cohesive zone models, International Journal of Plasticity 19 (2003) 849–882.

Li, Y. N., and Liang, R. Y., 1994, Peak Load Determination in Linear Fictitious Crack Model, Journal of Energy Mechanics, ASCE, Vol. 120 (2), pp: 232-249.

Lockyear, C., Ryan, F., Daniel, F., and Gunningham, M. M., 1990, Cement Channeling: How To Predict and Prevent, SPE 19865-PA, SPE Drilling Engineering, Vol.5 (3), pp: 201-208.

Mahadevan, A., and Mahadevan, L., 2010, Flow-induced Channelization in a Porous Medium, EPL (Europhysics Letters) Vol. 98 (5), pp: 1-4.

Mueller, D. T., and Eid, R. N., 2006, Characterization of the Early Time Mechanical Behavior of Well Cements Employed in Surface Casing operations, SPE 98632, IADC/SPE Drilling Conference, Miami, Florida, 21-23 February 2006.

Needleman, A., 1987, A continuum model for void nucleation by inclusion debonding. J. Appl. Mech. 54, 525–531.

Needleman, A., 1990, An analysis of tensile decohesion along an interface. J. Mech. Phys. Solids 38, 289–324.

Oh, T. S., Rödel, J., Cannon, R. M., and Ritchie, R. O., 1988, Ceramic/Metal Interfacial Crack Growth, Toughening by Controlled Microcracks and Interfacial Goemetries, Acta Meterialia, 36, pp: 2083-2093.

Parcevaux, P., and Sault, P., 1984, Cement Shrinkage and Elasticity: A New Approach for a Good Zonal Isolation, SPE 13176, Offshore Technology Conference, Houston, TX, 16-19 September 1984.

Peirce, A., and Detournay, E., 2008, An implicit level set method for modeling hydraulically driven fractures, Comput. Meth. Appl. Mech. Eng. 197 (33–40), 2858–2885.

Petersson, P. E., 1981, Crack growth and development of fracture zone in plain concrete and similar materials, Report TVBM-1006, Lund Institute of Technology, Lund, Sweden.

Prince, N. J., and Cosgrove, J. W., 1990, Analysis of Geological Structures, Cambridge University Press.

Ravi. K., Mcmechan, D. E., Reddy, B. R., and Crook, R. A., 2007, Comparative Study of Mechanical Properties of Density-Reduced Cement Compositions, SPE 90068, SPE Drilling & Completion, Volume 22(2), pp: 119-126.

Reeder, J. R., and Crews, J. H., 1988, Mixed-Mode Bending Method for Delamination Testing, AIAA Journal, July, Vol. 28, No. 7, pp. 1270-1276.

Reeves, G. M., Sims, I., and Cripps, J. C., 2006, Clay Materials Used in Construction: Engineering Geology Special Publication, Cromwell Press, Trowbridge, UK.

Rice, J. R., 1968, A Path Independent Integral and the Approximate Analysis of Strain Concentration by Notches and Cracks, Journal of Applied Mechanics 31, pp: 379-86.

Russell, A. J., 1982, On the Measurement of Mode II Interlaminar Fracture Energies, Defence Research Establishment Pacific, Victoria, Canada, DREP Materials Rept. 82-0, Dec.1982.

Salehabadi, M., Jin, M.,, Yang, J., Haghighi, H., Ahmed, R., and Tohidi, B., 2010, Effect of Casing Eccentricity on Casing Stability Analysis in Wellbores Drilled in Gas Hydrate Bearing Sediments, SPE 131236-MS, SPE EUROPEC/EAGE Annual Conference and Exhibition, 14-17 June 2010, Barcelona, Spain.

Sarris, E, and Papanastasiou, P., 2001, Modelling of hydraulic fracturing in a poroelastic cohesive formation, Int J Geomech 2001, ASCE, GM., pp:1943-5622.

Sarris, E., and Papanastasiou, P., 2011 (a), The influence of the cohesive process zone in hydraulic fracturing modelling. Int J Fract 2011;167 (1), pp:33–45.

Sarris E, and Papanastasiou P., 2011 (b), Modelling of hydraulic fracturing in a poroelastic cohesive formation. Int J Geomech 2001. ASCE) GM., pp:1943-5622.

Schrefler, B. A., and Secchi, S, S., 2006, Onadaptive refinement techniques inmulti-field problems including cohesive frac- ture. Comput Methods Appl Mech Eng 195:444–461.

Siegmund, T., and Brocks, W., 2000, A numerical study on the correlation between the work of separation and the dissipation rate in ductile fracture. Engineering Fracture Mechanics 67, 139–154.

Silva, M. G. P., Martins, A. L., Barbosa, B. C., and Garcia, J. H., 1996, Designing Fluid Velocity Profiles for Optimal Primary Cementing, SPE 36136-MS, SPE Latin America/Caribbean Petroleum Engineering Conference, 23-26 April 1996, Port-of-Spain.

Swenson, D. V., and Ingraffea, A. R., 1991, The Collapse of the Schoharie Creek Bridge: A Case Study in Concrete Fracture, Mechanics. Int. J. Fracture, 51, 73-92, 1991. 43.

Tan, C. P., Willoughby, D. R., Zhou, S., and Hills, R. R., 1993, An Analytical Method for Determining Horizontal Stress Bounds Form Wellbore data, Int. J. Rock Mech. Min. Sci. & Geomech. Abstr. vol. 30, pp: 1103-1109.

Tarr, B.A., and Flak, L., 2011. Part 6 - Underground blowouts. Underground blowouts between subsurface intervals are common and can result in a significant escalation threat if not recognized quickly and controlled correctly.

Thiercelin, M. J., Dargard, B., Baret, J. F., and Rodriquez, W. J., 1998, Cement Design Based on Cement Mechanical Response, SPE 52890-PA, SPE Drill & Completion, Vol.13(4), pp: 266-273.

Tvergaard, V., 2001, Resistance curves for mixed mode interface crack growth between dissimilar elastic-plastic solids. J. Mech. Phys. Solids 49, pp: 2689-2703.

Tvergaard, V., 2006, Cohesive Models for Interface Debonding, Proceedings of the 28th Risø International Symposium on Materials Science: Interface Design of Polymer Matrix Composites – Mechanics, Chemistry, Modelling and Manufacturing.

Tvergaard, V., and Hutchinson, J. W., 1992, The relation between crack growth resistance and fracture process parameters in elastic-plastic solids. J. Mech. Phys. Solids 40, 1377-1397.

Tvergaard, V., and Hutchinson, J. W., 1993, The influence of plasticity on mixed mode interface toughness. J. Mech. Phys. Solids 41, 1119-1135.

Tvergaard, V., and Hutchinson, J. W., 1996, Effect of strain-dependent cohesive zone model on predictions of crack growth resistance, International Journal of Solids and Structures, Vol. 33, pp: 3297-3308.

Wang, H. F., 2000, Theory of Linear Poroelasticity with Applications to Goemechanics and Hydrogeology, Princeton University Press, Princeton and Oxford.

Wong, R. C. K., and Yeung, K. C., 2006, Structural Integrity of Casing and Cement Annulus in a Thermal Well Under Steam Stimulation, Journal of Canadian Petroleum Technology, Vol. 45 (12), pp: 6-9.

Xie, M., 1995, Finite element modeling of discrete crack propagation. PhD. thesis, University of New Mexico, USA.

Xie, M., and Gerstle, W. H., 1995, Energy-based cohesive crack propagation modeling, Journal of Engineering Mechanics, American Society of Civil Engineers, 121 (12), pp: 1349–1458.

Xie, M, Gerstle, W. H., and Rahulkumar, P., 1995, Energy-based automatic mixed-mode crack propagation modelling. Journal of Engineering Mechanics, Vol. 121, No. 8, August 1995, pp: 914-923.

Yang, Z., and Xu, X. F., 2008, A Heterogeneous Cohesive Model for Quasi-Brittle Materials Considering Spatially Varying Random Fracture Properties, Computer Methods in Applied Mechanics and Engineering, Vol. 197(45-48), pp: 4027-4039.

Yang, Z. J., Su, X. T., Chen, J. F., and Liu, G. H., 2009, Monte Carlo Simulation of Complex Cohesive Fracture in Random Heterogeneous Quasi-brittle Materials, International Journal of Solids and Structures, 2009, Vol. 46(17), pp: 3222-3234.

Yuan, Z. G., Schubert, J., and Teodoriu, C., 2012, HPHT Gas Well Cementing Complications and its Effect on Casing Collapse Resistance, SPE 153986-MS, SPE Oil and Gas India Conference and Exhibition, 28-30 March 2012, Mumbai, India.

Zienkiewicz, O. C., 1984, Coupled problems and their numerical solution, In: Lewis RW, Bettess P, Hinton E (eds) Numer- ical methods in coupled systems. Wiley, London.

CHAPTER 5. STIMULATION MULTI-ZONE FRACTURING IN VERTICAL WELLS

Abstract

Numerous multi-zone multistage hydraulic fracturing treatments are now being executed in low permeability oil and gas fields around the world. Due to the limited access to the subsurface, post-treatment assessments are mainly limited to few techniques such as tiltmeter, microseismic and tracer-logs. The first two techniques are mainly used to determine fracture extension; however, fracture height and fracture initiation at all perforation clusters could only be confirmed through radioactive tracer logs or detailed pressure analysis. In this chapter, we consider real examples from a field from Central America and investigate potential problems led to the limited generation of fractures in multi-zone treatments. For instance, some of the post-frac radioactive logs show very low concentration of tracers at some perforated zones in comparison with other zones. On the other hand in some cases, tracer logs indicate presence of tracers in deeper or shallower zones. Different reasons could cause fracture growth in non-perforated zones, including but not limited to: perforation design problems, casing/cement integrity problems, lack of containment, instability of fracture growth in one or some of the zones, and finally making a mistake in selecting lithology for fracturing. In this part, some of these issues have been examined for a few sample wells using treatment pressure data, petrophysical logs and post-frac tracer logs. Some recommendations in designing the length and arrangement of perforations to avoid these problems in future fracturing jobs are provided at the end of this part.

Introduction

Multi-zone multistage hydraulic fracturing treatments are extensively being executed nowadays in tight shale gas plays in North America. Historically because of limited pump rates and other technological shortcomings, each stage of stimulation jobs was mainly limited to a single high quality zone. The recent advances in logging tools and completion technology have generated more interests in pursuing novel techniques such as simultaneous multi-frac jobs, zip-fracs and multi-stage fracturing. Presence of multiple

fractures in a single stage may not be necessarily due to the multiple fracture initiation points. Interaction of hydraulic fracture with natural fractures may also lead to the formation of multi-stranded hydraulic fractures (Warpinski et al. 1993, Olson and Dahi Taleghani, 2009 and 2013) or a grid of propped fractures (Cipolla et al. 2010). In this article, we merely discuss multi-fracture problems generated due to the presence of multiple perforation intervals in each individual stage. Due to the geological nature of some formations, hydrocarbons may exist in multiple layers. From the economic point of view, production of all hydrocarbon containing layers is favorable to maximize production. Therefore, perforation at different intervals is performed in vertical wells to exploit more hydrocarbon bearing layers. The optimum design for perforation clusters requires fractures initiation at all clusters to obtain maximum drainage area in a given volume of rock. Although, it may not look to be a far reach goal, but in most hydraulic fracturing treatments, all perforation intervals will not open to fracturing fluids.

The basic assessment tool to investigate fracture initiation at different zones is post-frac radioactive tracers' logs. In this technique, particles of different radioactive elements such as Iridium, Scandium and Antimony are injected separately at different time during the treatment. The radioactive particles are moving with proppants and placed inside the fracture. Spectroscopy logging techniques are usually used to identify radioactive content changes after the treatment. Concentration of different radioactive tracers indicates the initiation of fractures as well as the approximate time of proppant placement at different locations (Gadeka and Smith, 1987). Among different tools, radioactive tracers are proved to be reliable and easier to interpret or at least to identify initiated fractures at the wellbore and measure their height and azimuth (Miller et al. 1994). Stricter environmental regulations and public awareness demand more environmental friendly substitutions like Boron Carbide instead of radioactive materials (Mulkern et al. 2012). Recently, distributed temperature logs as well as downhole acoustic devices have been used to assess the perforation effectiveness. The results of new developed technology might be used in the research presented here similar to the way radioactive tracer logs have been used.

This article will provide a short overview of different scenarios and issues that might occur during hydraulic fracturing in wells with multiple perforation clusters. We discuss principles that need to be considered in designing multi-cluster perforations in vertical and horizontal wells. In an ideal design, fractures are expected to be initiated and propagated through the entire perforated zone, and at the same

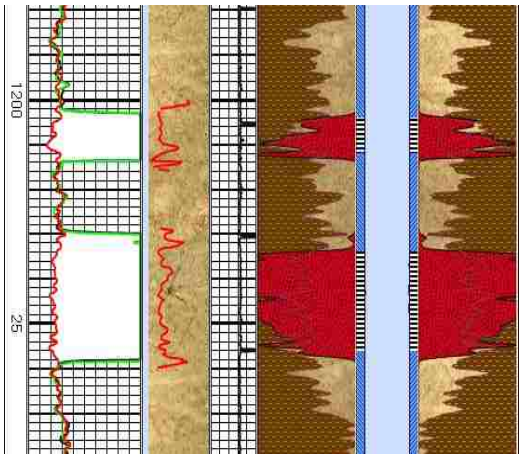

Figure 5.1 Tracer log of a tight oil vertical well in North America, fractures are initiated along the whole perforated zone and stayed contained in this zone after propagation. Horizontal tracer mark at 1207m looks to be the bedding plane artifact.

time remained almost fully contained in the perforated intervals (for instance look at Figure 5.1). Hence, the first step in designing treatments with multiple perforation clusters is choosing perforation size based on perforation spacing in order to reach breakdown pressure in all clusters, simultaneously. Post-frac radioactive logs (Gamma spectroscopy) run in different wells in various formations have revealed different situations in terms of fracture initiation and its propagation in treatment stages with multiple perforation clusters. In general, we can classify these issues into four major categories:

1. Fractures are initiated at all perforated zones and remain contained in the associated intervals. Treatment pressure data also confirm the continuous independent growth of fractures in all intervals. This is the best case scenario to maximize stimulated rock volume (SRV).

2. Fracture initiation and propagation are limited to one or several perforation zones due to the diversion of fracturing fluid to other clusters. When perforated zones are very close to each other, some of the initiated paths will not propagate farther inside the formation; therefore, SRV will be less than the

previous case. It is crucial to determine the critical spacing between the perforations based on fracturing fluid properties and rock mechanical properties to initiate fractures in all perforations.

3. Coalescence of fractures initiated at different perforation clusters inside the formation. In this case, extensive height growth could be identified from decreasing pressure. In general, a major part of the pumping horsepower might be spent in stimulating unfavorable zones (reduces SRV).

4. Post-frac radioactive logs show considerable concentrations of tracers outside the perforated zones or indicate tracers in deeper or shallower zones than the perforated zones, which mean uncontrolled fracture height growth beyond the perforated interval toward shallower or deeper part of the formation. Therefore, it is expected that the actual post-treatment fracture length is significantly below the design length. Different reasons could cause fracture growth in non-perforated zone including but not limited to: perforation design problems, casing/cement integrity problems, lack of containment, or making mistakes in selecting right lithology zone for fracturing. To avoid this issue, there have been some suggestions on perforation placement immediately below the base of the pay zone (for instance see Ahmed et al 1984).

Despite simplicity of running and interpreting post-frac tracer logs, they are suffering from a major deficiency as they provide data about the fracture geometry only at the borehole and nothing beyond that. Therefore in this chapter we tried to achieve a comprehensive assessment of the frac jobs by combining treatment pressure data with data acquired by other tools such as tracer logs, tiltmeter and microseismic data. Depending on the difference between principal in-situ stresses on one side and friction at perforations on the other side, fractures may not initiate at some clusters, or initiate at a different plane. The resulting tortuosity may cause further complications in the fracturing treatment and post-frac production. In this part, we try to review these challenges and give recommendations to avoid these issues in designing perforation at each fracture stage. Some field examples have been provided to support these analyses.

Pressure Analysis

From pump outlet on the surface to the tip of the fracture downhole, there are pressure drops all the way along this route. The overall pressure drop can be divided into four components: hydrostatic pressure drop, frictional pressure drop in casing, perforation friction pressure drop, and net pressure at the wellbore. Moreover, it is noteworthy that accurate information regarding formation and fracture parameters must be available to obtain accurate estimations. The overall pressure drop, therefore, can be combined with pressure at the tip of the fracture and a reference pressure to form a pressure equilibrium equation

$$p_{ref} = p_{c,i} + \Delta p_{w,i} + \Delta p_{pf,i} + \sum_{j=1}^{i} \Delta p_{h,j} + \sum_{j=1}^{i} \Delta p_{cf,j}\ , \quad \textbf{(5.1)}$$

where p_{ref} is the reference pressure at a certain depth of the well, p_c is the closure pressure of the fracture, which is generally equal to the formation minimum principal stress.

Fluid column inside the casing causes differences in hydrostatic pressure from surface to bottom. Hydrostatic pressure drop in casing intervals can be evaluated with

$$\Delta p_h = 0.052 \rho D, \quad \textbf{(5.2)}$$

where ρ is the density of the fracturing fluid, and D is the total vertical depth from the surface.

When fracturing fluid flows through pipes and casing, friction force all the way along the casing "drags" the fluid flow and causes a pressure drop for fluid flow in the casing. Frictional pressure drop in the casing interval can be estimated by

$$\Delta p_{cf} = c\,(Z_j - Z_{j-1}) \sum_{k=j}^{n} Q_k \left| \sum_{k=j}^{n} Q_k \right|^{d-1}, \quad \textbf{(5.3)}$$

where c and d are a constant and exponent calculated by fitting a power law model to tabulated friction pressure data. Q_k is the volumetric injection rate through k-th perforation cluster, and Z_j-Z_{j-1} represents the difference in measured depths (MD) between perforation clusters. There are also pressure drops across the perforations in casing, which must be taken into consideration in fracturing treatment design. This perforation frictional pressure drop, however, is usually negligible if the perforations are correctly sized

and phased; otherwise, it can be assumed to be constant for the duration of the treatment. The equation commonly used to estimate the frictional pressure drop across perforations implicitly assumes a short cylindrical shape of perforations

$$\Delta p_{pf} = 0.2369 \frac{q^2 \rho}{n^2 D_p^4 C^2}, \quad \textbf{(5.4)}$$

where ρ is the density of the fracturing fluid, q is the volumetric flow rate, n is the number of perforations, D_p is the diameter of perforations, and C is the discharge coefficient. In addition to these variables, erosion may occur when sand slurries are pumped across the perforations with large pressure difference, which subsequently result in a greater pressure drop across the perforations. Based on the experimental results of Crump and Conway (1988), the discharge coefficient can be approximated to 0.56 before erosion and 0.89 after erosion. Finally, the most complicated component of the overall pressure drop occurs inside the fracture, which should be calculated by fracture modeling.

In the presence of a single perforation cluster, these pressure drops can be calculated independently. However in case of multiple perforation clusters, slurry rate will be distributed between different fractures based on their hydraulic conductivity and pressure drops associated to each of these fractures. Hydraulic conductivity of fractures is a strong function of fracture's width $(\propto w^3)$, which is in general a function of fracture compliance. Depending on the fracture height, length and penetrated rock layers and shape of the fracture, its compliance could be determined.

Longitudinal Fractures or Transverse Fractures?

Longitudinal fractures are generally observed in vertical wellbores located in the regions with normal fault tectonic regime. Longitudinal fractures could cause many complications in terms of well integrity in horizontal wells. The main issue in the longitudinal fractures (or vertical fractures in vertical wells) is uncontrolled fracture growth and potential coalescence of fractures from different zones inside the formation. Uncontrolled height growth could cause major issues such as non-uniform distribution of proppants inside the fracture, fracture receding, and breaking the cap rock. The orientation of principal

far-field stresses determines fracture geometry; however, stress concentration around the wellbore may favor initiation of fractures in a different plane.

Hydraulic fractures in horizontal wells are intended and designed to be transverse. Transverse fractures allow having multiple fractures along the well. However in regions with low horizontal differential stress, initiation of longitudinal fractures is more likely. Small length of perforation clusters, deep perforation trajectory and slower injection rate would facilitate formation of transverse fractures (Abbas et al. 2013).

In vertical wells, fractures are intended to be longitudinal because transverse fractures will be stressed under the overburden load. Additionally since these fractures will change direction to align with far-field stresses, the generated tortuosity makes proppant placement very difficult. Figure 5.2 shows an example of short patch perforation zones practiced for fracturing jobs in several vertical wells in the basin studied

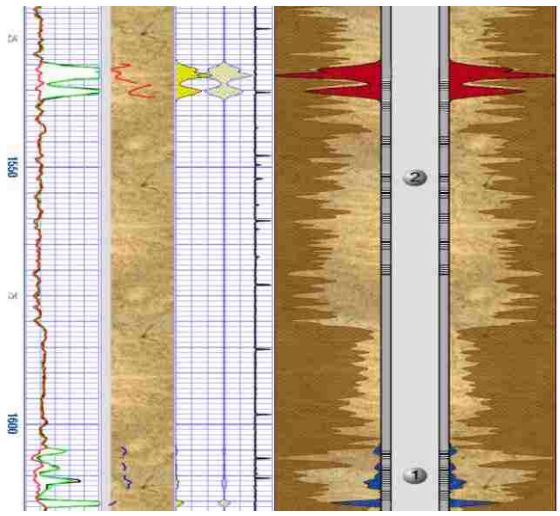

Figure 5.2 A two-stage fracturing job has been performed as shown above. The first stage shows limited fluid entry. In the second stage, tracers were only tracked in the shallower part of the zone.

by the authors. This basin is located in North America and is a low pressure low permeability very tight sand bearing mainly liquid hydrocarbons. This formation is naturally fractures and due to the extremely low permeability of the matrix, hydraulic fracturing plays a critical role for production. The depicted well has been stimulated in two stages. Each stage consists of several patches. Each patch has about a meter length and perforated with 4 shots per meter in 90 degrees phasing. However the size of the perforation

holes (0.5”) is larger than previous jobs in this basin (usually 0.32”), but due to the small number of holes (large spacing), a large portion of the pumping horse power is lost for breaking the formation at several points along each perforation interval with approximately low injection rate (25 bpm). Hence, treatment pressure is much higher than other jobs. Induced fracture in stage one is almost vertical and its height is about10m. On the other hand, fractures resulted in second stage are not vertical and formed about 8 meters apart although 35m of the well is perforated in this interval. Apparently, fracturing fluid pumped in the second stage has reached perforations with a pressure that was not large enough to initiate a large fracture, and most of the fluid is probably drained through the system of the natural fractures.

Simultaneous Growth of Multiple Fractures

To reach breakdown pressure at different perforation clusters, the injection flux should be divided between different intervals proportionally in order to induce fractures with equal lengths. Due to the geometry of fractures with respect to each other, fracture initiation at one depth does not hinder fracture initiation at other depths. The key to change the flux rate into each interval is changing the perforation sizes and their numbers in each interval. In the case of transverse fractures, injection rate distributed between fractures should be proportional to one-third power of their radius, which can be controlled mainly by friction loss at the perforation holes.

Propagation of multiple transverse fractures could be more complicated than longitudinal fractures. Depending on the size of transverse fractures and their spacing, they might develop stress shadows on each other. In other words, parallel pressurized fractures start to squeeze their neighbors to open their ways, and the size of their stress shadows depend on the fracture lengths. Due to the interacting stress shadows, the stress intensity factors at the tip of fracture-strands could decrease significantly in comparison to a single fracture, thus propagation of parallel strands is more likely to arrest.

The propagation of fractures is a problem of equilibrium and stability governed by the same laws as those for other dynamic systems. In the context of stability analysis, it makes more sense to use energy related terms, such as energy release rate instead of stress intensity factors. The most stable fracture

configuration for propagation is the configuration with maximum energy release. The coupled fluid flow-fracture mechanics analysis (Dahi-Taleghani 2011) demonstrates the importance of the interaction of hydraulic fracture branches on the resultant flow paths, as different types of critical states may arise: (1) some of the extending fractures are arrested; (2) some of the stationary fractures are activated; and/or (3) some of the stationary fractures begin to close. Following each possibility, different stimulated rock volume is expected. In these models, the fractures with the maximum intensity factors grow, however, in the case that several fracture tips have reached rock toughness (competing tips), a stability analysis will determine the fracture configuration path that leads to the maximum decrease in the total potential energy. The total potential energy, consisting of the strain energy and surface energy is considered for variational analysis. Following the second law of thermodynamics, we know that (Sumi et al. 1980): Among all admissible variations in the fracture lengths which correspond to a given variation in the pumped fluid and time, the ones which minimize the total potential energy produce the most stable state, and hence are the actual ones. The same issue may also occur in each stage of frac treatment in horizontal wells. The fracture opening displacements for parallel strands are smaller than that for a single fracture, which means higher fluid pressure gradient in parallel fractures. Trying different aspect ratios for fractures length and spacing, we concluded that when fractures (perforated zones) spacing is less than the fractures' length; fractures have a strong influence on each other and make stability analysis a requirement (Dahi-Taleghani, 2011). This phenomenon is also observed on regular stress driven fractures (Bazant and Cedolin, 1991).

Considering the fact that radioactive logs only provide information about the tracers' concentration at the wellbore, we should not expect to obtain much information about fracture geometry outside of the wellbore region by only using the post-frac logs. Consistent decline of treatment pressure while pumping the fracturing fluid at constant rate could be a sign of an uncontrolled height growth. In these cases, further pumping promotes fractures in the vertical direction (Figure 5.3). To avoid these issues, cement-rock and cement-casing integrity should be verified before starting fracturing jobs (More information

about current regulations may be found in API HF1 – Hydraulic Fracturing Operations – Well Construction and Integrity Guidelines, 1st Edition, October 2009).

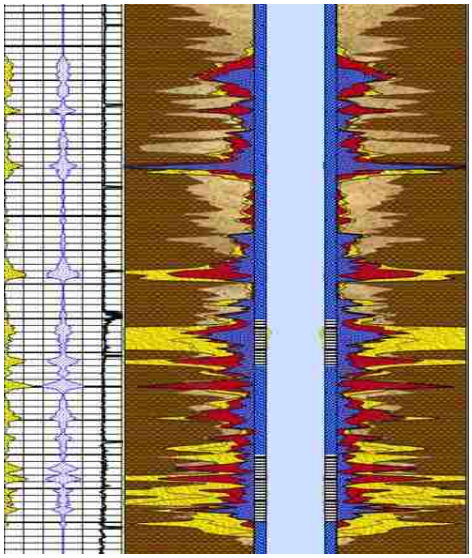

Figure 5.3 An example of fracture growth beyond the perforate intervals, in this case, pumping more fluid only adds to the fracture height not the fracture length.

Mechanics of Cohesive Zone

We use the cohesive zone approach to model fractures in this part. Cohesive zone approach is a good candidate to model fracture initiation and propagation in hydraulic fracturing (Sarris and Papanastasiou, 2011) and wellbore integrity (Dahi Taleghani and Wang, 2013). Cohesive constitutive equations were originally proposed by Dugdale (1960) and Barenblatt (1962) to describe ductile and interfacial cracks. Having cohesive forces acting against fracture opening removes stress singularity at the fracture tip. The cohesive interface starts to open when the tension or shear traction applied to the interface reaches a critical point (Tvergaard and Hutchinson, 1996). Further loading causes energy dissipation in the fracture processing zone, complete damage occurs when the energy becomes equal to the fracture toughness (Xie, 1995).

Typical bilinear softening curves for pure normal (Mode I) and shear loadings (Mode II or III) are illustrated in Figure 5.4a and b, respectively. A high initial stiffness (penalty stiffness, K) is used to hold

the top and bottom faces of the cohesive element together in the linear elastic range (point 1 in Figure 5.4). Linear behavior continues till stress has not reached the peak point. When normal (or shear) traction reaches maximum values, which are represented by t_{n0} and t_{s0} (t_{t0}) (Point 2 in Figure 5.4), or equivalent critical separations (δ_{n0}, δ_{s0} and δ_{t0}), the fracture initiates in the intact rock. Beyond this critical point,

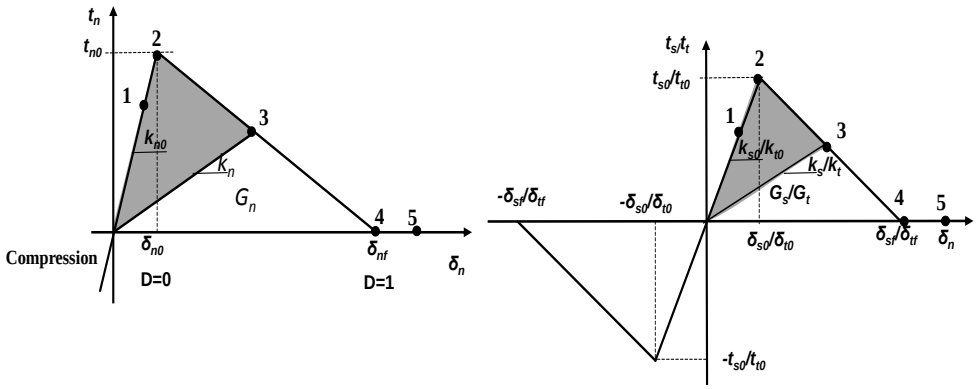

Figure 5.4 Linear Softening traction-separation law for the cohesive element under pure shear loading (left) and pure normal loading (right).

the process zone starts to undergo plastic deformation and micro-cracking, which define the so-called softening transition zone between the complete failure zone and the undamaged material and represented by Point 3 in Figure 5.4. The damage process completes at the complete failure point where cohesive forces between crack faces are gone, and the relative displacement between surfaces reaches the second critical value, δ_{nf} and δ_{sf} (or δ_{tf}), shown as point 4 in Figure 5.4. The area under the traction-relative displacement curves is the respective mode (Mode I, II or III) fracture toughness ($G_{n,C}$, $G_{s,C}$ and $G_{t,C}$ respectively).

In general, loading could be any arbitrary combination of normal and shear failures or a mixed mode problem, such as the casing-cement system involved in this study that requires considering the combinatory effect of normal and shear modes. Damage onset and the corresponding softening behavior under mixed-mode loading may occur before any of the traction components reaches its respective pure mode failure criteria. This is an issue that is usually neglected in the formulation of cohesive elements

(Camanho and Dávila, 2002a, and Cui et al, 1992). We can imagine that each loading mode has a contribution to provide enough energy for fracturing the rock. Hence, quadratic failure criterion could be a meaningful criterion for fracture propagation in mixed-mode problems in granular and cementous materials (Cui et al., 1992, Dávila and Johnson, 1993, Camanho and Matthews, 1999, Camanho and Dávila, 2002b), where compressive normal tractions are considered to have no effect on delamination onsets, which is listed below

$$\left\{\frac{\langle t_n \rangle}{t_{n0}}\right\}^2 + \left\{\frac{t_s}{t_{s0}}\right\}^2 + \left\{\frac{t_t}{t_{t0}}\right\}^2 = 1 \qquad \textbf{(5.5)}$$

The metric for damage is a scalar stiffness degradation index, *D*, which represents the overall damage of the interface caused by all stress components. The stiffness degradation index is a function of the so-called effective relative displacements, δ_m by combining the effects of displacement induced by different loadings i.e. δ_n, δ_s and δ_t. The total mixed-mode relative displacement δ_m is defined as

$$\delta_m = \sqrt{\langle \delta_n \rangle^2 + \delta_s{}^2 + \delta_t{}^2}\,. \qquad \textbf{(5.6)}$$

For linear softening, the damage evolves with the index (Chen, et al, 1999) is defined as

$$D = \frac{\delta_{mf}\left(\delta_{m,\max} - \delta_{m0}\right)}{\delta_{m,\max}\left(\delta_{mf} - \delta_{m0}\right)}. \qquad \textbf{(5.7)}$$

The propagation criterion for delamination crack is established in terms of the fracture toughness in different modes. The mixed-mode criterion proposed by Benzeggagh and Kenane (B-K criterion) (1996) is used here to accurately account for the variation of fracture toughness as a function of mode ratios. Although B-K criterion. This criterion is expressed as a function of the Mode I and Mode II fracture toughness and a parameter η obtained from MMB tests (Reeder and Crews, 1990) at different mode ratios

$$G_{nC} + \left(G_{sC} - G_{nC}\right)\left(\frac{G_s}{G_T}\right)^{\eta} = G_C, \text{ with } \; G_T = G_n + G_s \qquad \textbf{(5.8)}$$

If the Mode III loading occurs the criterion is

$$G_{nC} + (G_{sC} - G_{nC})\left(\frac{G_{shear}}{G_T}\right)^{\eta} = G_C, \text{ where } G_T = G_n + G_{shear} \quad \textbf{(5.9)}$$

where α and η are material properties.

Cohesive zone approach is more sophisticated than the Griffith's criterion due to lack of stress singularity at the crack tip and the capability for successful prediction of the fracture initiation, which are main limitations involved in Griffith's criterion (Griffith, 1924). Cohesive interfaces are considered as pre-defined fracture paths to overcome complexities involved in common fracture propagation. This approach can effectively reduce the computational cost by avoiding stress singularity calculation at the tip of fractures, especially in the presence of multiple fractures. Cohesive zone approach can be related to Griffith's theory as the area under the traction-relative displacement relation is equal to the corresponding fracture toughness (Rice, 1968). For example, in a bilinear cohesive interface softening model, the energy release related to pure mode one by

$$G = \frac{K_{Ic}^2}{\sigma_T E'} = \frac{\pi}{32}\frac{K'^2}{\sigma_T E'}, \quad \textbf{(5.10)}$$

where $K' = \sqrt{\pi/32}K_{Ic}$ is an equivalent fracture toughness.

Numerical Results

To further understand the mechanisms involved in multi-zone hydraulic fracture treatments, a coupled three-dimensional model using cohesive zones is built to simulate the initiation and propagation of multiple fractures. The verification tests are conducted by matching numerical results with radioactive log shown in Figure 5.1, Figure 5.2 or Figure 5.3.

This model consists of an 8-½ in borehole drilled through the block, which is demonstrated in Figure 5.5. The wellbore is protected by a 7-in cemented steel casing. For the sake of simplicity, materials on either side of the potential failure paths are linearly elastic and isotropic. The potential failure zones are

simulated by layers of cohesive elements with zero thickness. To verify simulation results, Case-1 is selected to match up the radioactive log results shown in Figure 5.1. In this case, two perforation clusters in different intervals are considered. The first upper perforation cluster has a short interval of about 3 m,

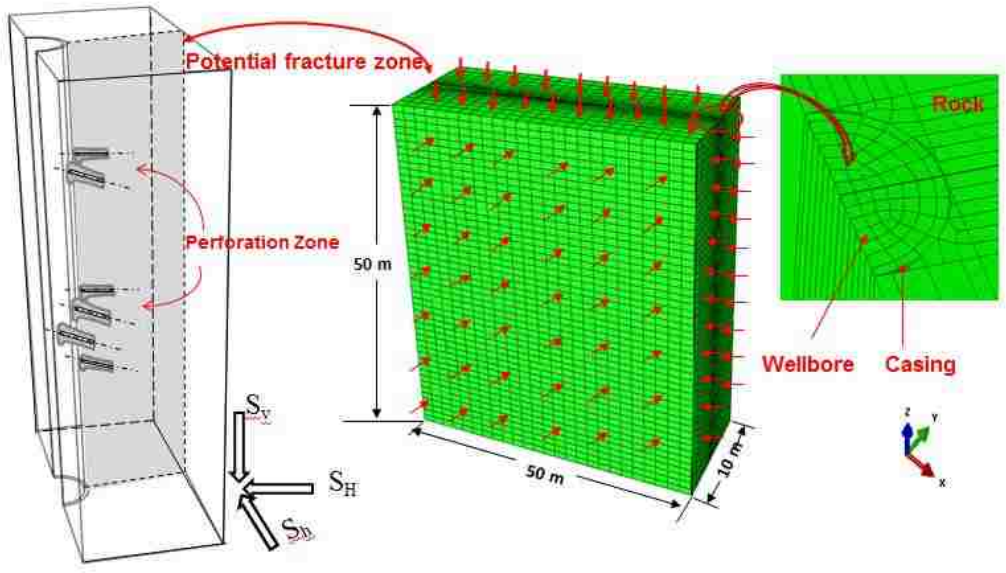

(a) (b)

Figure 5.5 A schematic picture of the numerical model with one potential hydraulic fracture zone and the interface between two planes are shown in (a). It also shows the model's dimensions, boundary and loading conditions, and meshes for the three dimensional model (shown in (b)).

which is located from 1203 m to 1206 m. The second cluster has a longer interval with a length of about 10 m located from 1218 m to 1228 m. The bottom of the upper interval is about 12 m above the top of the lower interval.

This model is meshed by commercial finite element package ABAQUS version 6.10. As illustrated in Figure 5.5b, fine meshes are placed close to potential failure zones to guarantee solution convergence, and to properly capture the details of failure propagation and energy re-distribution within the cohesive zone during failure propagation. On the other hand, coarse mesh is used far from the wellbore to reduce computational costs. Rock mechanical properties used in this model are borrowed from the rock physics handbook (Hall, J., et al, 2006) and from petrophysical logs. Values used for casing, rock and interface properties are listed in the appendix. The model is simulated in two steps. At the first step, initial

equilibrium by assigning initial geostatic stress and initial pore pressure; then at the second step,

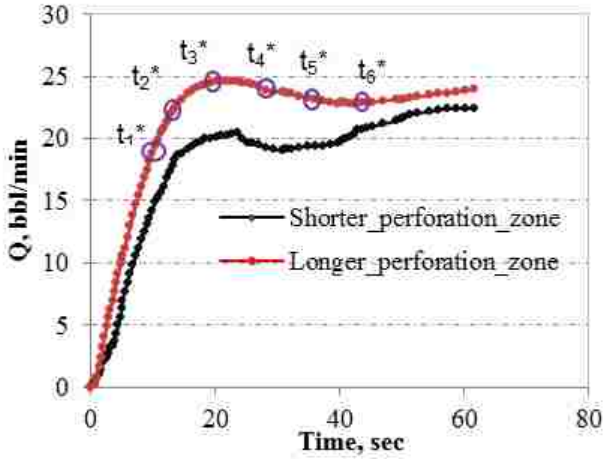

Figure 5.6 Injection rate variation at the perforation clusters.

perforation fluid with constant concentrated flow is injected in the wellbore. The constant injection rate Q_0 is 45 bbls/min. The hydraulic fracture is initiated by excessive fluid pressure induced by fluid injection.

In order to eliminate the effects of parameters dimensions, dimensionless time is used to demonstrate results, which provide a comparison basis for failure propagation, fracture opening of the homogeneous case and heterogeneous case. The dimensionless time is defined based on the wellbore radius and poroelastic diffusion coefficient (Detournay and Cheng, 1991),

$$t^* = \frac{c \cdot t}{r_w^2} \qquad \textbf{(5.11)}$$

The constant c is the poroelastic diffusivity coefficient, which is different from the usual diffusivity and determined by

$$c = \frac{2KG(1-v)(v_u - v)}{a^2(1-2v)^2(1-v_u)}. \qquad \textbf{(5.12)}$$

For the first numerical example, the rock is assumed to be homogeneous, which results in uniform interface properties. The high injection rate, Qo=45 bbls/min, is injected in the wellbore. The injected

fluid is diverted into two perforation clusters: the lower cluster with longer perforation length and the upper cluster with shorter length. The injected volume will be distributed between perforation in a fashion to maintain the fluid pressure between perforation to hydrostatic pressure and friction loss pressure. The pumping schedule or injection rate changes with time, which is illustrated in Figure 5.6. Fracture propagation pattern predicted by this model is demonstrated in Figure 5.7. It can be observed that formation breaks down almost simultaneously at these two perforation clusters due to similar perforation friction. However due to the different number of perforation holes, the height and consequently the compliance of induced fractures is different and although both fracture have been induced simultaneously but they propagate at different rates. In this vertical well, although both longitudinal and transverse fractures had chance to grow but only the longitudinal fractures propagate due to uniform rock properties and large difference between vertical and horizontal stresses. Since more fluid is injected into the lower

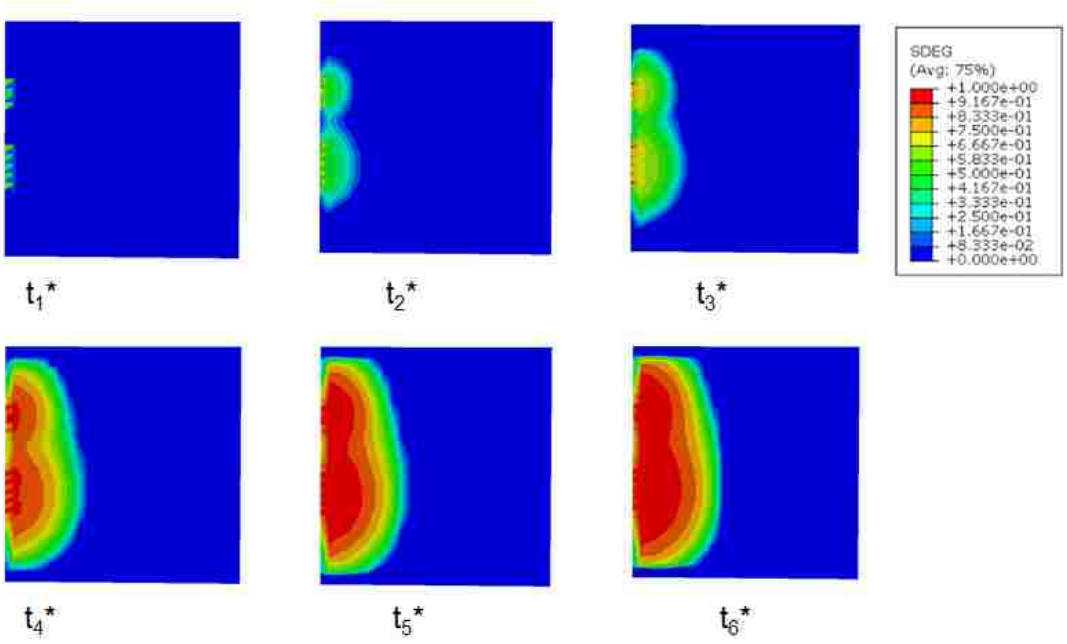

Figure 5.7 A schematic picture of fracture (shown in red) propagation in a model with two perforation clusters, where larger flow is diverted into the lower large perforation zone. The dimensionless time is as shown in Figure 5.6.

perforation cluster leads to the coalescence of fractures in the upper and lower perforation clusters. The coalescence of longitudinal fractures forms a larger fracture with lower compliance, which is less harmful

to the well integrity issues. In general, longitudinal fractures do not have limited hydraulic communication problems like transverse fractures, therefore it is less likely to buildup enough pressure at the wellbore to induce annulus fractures.

To consider the effect of heterogeneity, we consider a rock with heterogeneous properties, which induces the heterogeneity in the interface properties of the cohesive zone. Compared with homogeneous case, 10% fluctuations in normal and shear strength of the interface are considered. The rock strength in this 10% fluctuation zone is 80% less than those in other zones. Moreover, injection rates, Q_o=45 bbls/min is applied at the wellbore. It can be observed that failure initiates at two perforation clusters

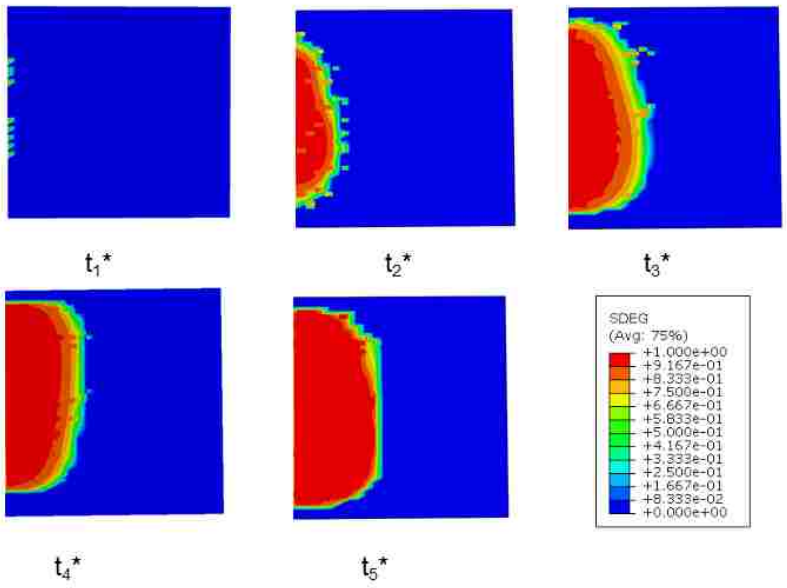

Figure 5.8 A schematic picture of fracture propagation through two perforation clusters, where larger volume of flow is diverted into the lower large perforation zone. In this example, the rock is considered to be heterogeneous case.

simultaneously. Compared with failure patterns in the case with homogeneous interface properties shown in Figure 5.8, larger fractured areas can be observed in this case with heterogeneous interface properties at the same dimensionless time, which is because the interface strength is worsened with the existence of randomly distributed weak interface.

Concluding Remarks

Based on discussions we had so far and findings through extra modeling and calculations, several important items in designing multiple-clusters for fracturing jobs should be considered. Stress field induced by parallel hydraulic fractures start to interact on each other when fractures' lengths become comparable with their spacing. Ignoring this fact will lead to the competition between fractures in horizontal wells as they try to squeeze their neighbors to open their growth path. In vertical wells, these fractures may merge into each other and result in stimulation of the layers, which are not favorable for production. This competition leads to increase in treatment pressure and the associated issues may increase the final cost significantly. In vertical wells located in formation with small differential stresses in vertical directions, there is likelihood of developing transverse fractures due to limited perforations. To avoid generating any near-wellbore tortuosity, hydraulic fractures should be done with attention to pressure drop at perforations and in vertical section of wellbores to maximize fracture length and minimize pumping pressure. The provided data shows that same perforation size and spacing has been used in stages with multiple perforation clusters, hence, breakdown pressure is not accomplished in all clusters at the same time. Apparently, most of the time, only one of the clusters reach to bearkdown pressure, upon fracture initiation in one of the clusters, fracturing fluid is lead to that specific cluster and other clusters remain intact. To dissolve this issue, different perforation size and spacing should be used to virtually provide same breakdown pressure in different clusters.

Using cohesive zone theory, we present a field-scale three-dimensional poroelastic model to match up the radioactive log results. The potential failure zones are represented by pre-inserted cohesive elements with the traction separation law as failure criterion. The matching results between failure patterns from numerical analysis and real field measurements using radioactive tracer-logs provide a benchmark for the model accuracy. On the contrary, the numerical results can effectively supplement the deficiency of failure initiation and propagation process involved in radioactive tracer-logs. Moreover, the numerical model can overcome the limitations that are inherent in the radioactive tracer-logs like limitation of the

data to the wellbore vicinity. The developed numerical method could be an effective tool for the assessment of simulating multi-zone fracturing.

References

Abbas, S., Lecampion, B., and Prioul, R., 2013, Competition Between Transverse And Axial Hydraulic Fractures In Horizontal Wells, 2013 SPE Hydraulic Fracturing Technology Conference. 2013.

Ahmed, U., Thompson, T. W., and Kelkar, S. M., 1984, Perforation Placement Optimization: A Modified Hydraulic Fracturing Technique, SPE/DOE/GRI paper 12841 presented at SPE/DOE/GRI Unconventional Gas Recovery Symposium, Pittsburgh, PA, 13-15 May.

Barenblatt, G. I., 1962, The Mathematical Theory of Equilibrium Cracks in Brittle Fracture, Journal of Applied Mechanics, 1962, pp: 7, 55-129.

Bazant, Z., Cedolin, L., 1991, Stability of structures, The Oxford engineering science series, Oxford University Press Inc, New York.

Benzeggagh, M. L., and Kenane, M., 1996, Measurement of Mixed-Mode Delamination Fracture Toughness of Unidirectional Glass/Epoxy Composites With Mixed-Mode Bending Apparatus, Composites Science and Technology 56:439-49.

Camanho, P. P., and Dávila, C. G., 2002, Mixed-mode decohesion finite elements for the simulation of delamination in composite materials, NASA-Technical Paper, 211737(1), 33.

Camanho, P. P., and Matthews, F. L., 1999, Delamination Onset Prediction in Mechanically Fastened Joints in Composite Laminates, Journal of Composite Materials 33:906-27.

Chen, Z. R., 2011a, Finite element modelling of viscosity-dominated hydraulic fractures, Journal of Petroleum Science and Engineering, 88-89 (2012): 136-144.

Chen, Z. R., 2011b, Modelling Simultaneous Growth of Multi-branch Hydraulic Fractures, ARMA 11-436, presented in ARMA annual meeting in San Francisco, CA.

Cipolla, C. L., Warpinski, N. R., and Mayerhofer, M. J., Lolon, E. P., and Vincent, M. C., 2010, The Relationship Between Fracture Complexity, Reservoir Properties, and Fracture-Treatment Design, SPE Production & Operations, Volume 25, Number 4.

Crump, J., and Conway, M., 1988, Effects of Perforation-Entry Friction on Bottomhole Treating Analysis, paper SPE 15474, Journal of Petroleum Technology (August 1988) 40, No. 8, 1041–1048.

Cui, W., Wisnom, M. R., and Jones, M., 1992, A Comparison of Failure Criteria to Predict Delamination of Unidirectional Glass/Epoxy Specimens Waisted Through the Thickness, Composites 23(3):158-66.

Dahi Taleghani, A., and Olson, J., 2009, Analysis of multi-stranded hydraulic fracture Propagation: an improved model for the interaction between induced and natural fractures, 2009, ATCE SPE 124884.

Dahi Taleghani, A., and Olson, J., 2013, How Natural Fractures Could Affect Hydraulic Fracture Geometry, Accepted for publication in SPE Journal.

Dahi Taleghani, A., and Wang, W., 2013, Emergence of Delamination Fractures around the Casing and Its Stability, International Journal of Geomechanics, In review.

Dandekar, A. Y., 2013, Petroleum Reservoir Rock and Fluid Properties, Second Edition, CRC press.

Dávila, C. G., and Johnson, E. R., 1993, Analysis of Delamination Initiation in Postbuckled Dropped-Ply Laminates, AIAA Journal 31 (4): 721-727.

Detournay, E., Cheng, A. H. D., 1991, Plane Strain Analysis of a Stationary Hydraulic Fracture in a Poroelastic Medium, International Journal of Solids and Structures, Vol. 37, No. 13, pp: 1645-1662.

Dugdale, D. S., 1960, Yielding of Steel Sheets Containing Slits. Journal of the Mechanics and Physics of Solids, Vol. 8, pp: 100-104.

Gadekea, L. L., and Smith, H. D., 1987, Trancerscan: A Spectroscopy Technique For Determining The Distribution Of Multiple Radioactive Tracers In Downhole Operations, The Log Analyst, Volume 28, Number 1.

Griffith, A. A., 1924, The Theory of Rupture, In Proc.FirstInternat. Congr. Appl. Mech.

Hall, J., Allanson, J., Gripp, K., and Slavotinek, A., 2006, Handbook of Physical Measurements, Oxford Publication**.**

Jutten, J. J., Gulllot, D., Parcevaux, P. A., 1989, Relationship between Cement Slurry Composition, Mechanical Properties, and Cement-bond-log Output, SPE 16652-PA, SPE production Engineering, 1989, pp: 75-82.

Lecampion, B., and Prioul, R., 2013, Competition Between Transverse And Axial Hydraulic Fractures In Horizontal Wells, SPE 163848-MS, 2013 SPE Hydraulic Fracturing Technology Conference, Feb 04 - 06, 2013 2013, The Woodlands, TX, USA.

Miller, W. K., Peterson, R. E., Stevens, J. E., Lackey, C. B., and Harrison, C. W., 1994, In-Situ Stress Profiling and Prediction of Hydraulic Fracture Azimuth for the West Texas Canyon Sands Formation, SPE Production & Facilities, Vol. 9, Number 3.

Mueller, D. T., and Eid, R. N., 2006, Characterization of the Early Time Mechanical Behavior of Well Cements Employed in Surface Casing operations, SPE 98632, IADC/SPE Drilling Conference, Miami, Florida, 21-23 February 2006.

Mulkern, M., Masnyk, B., Kramer, H., and Sites, J., 2012, A Green Alternative for Determination of Frac Height and Proppant Distribution, SPE 138500, Presented in SPE Eastern Regional Meeting, 12-14 October 2010.

Olson, J., and Dahi Taleghani, A., 2009, Modelling simultaneous growth of multiple hydraulic fractures and their interaction with natural fractures, 2009 SPE 119739, Hydraulic Fracturing Technology Conference.

Prince, N. J., and Cosgrove, J. W., 1990, Analysis of Geological Structures, Cambridge University Press.

Ravi. K., Mcmechan, D. E., Reddy, B. R., and Crook, R. A., 2007, Comparative Study of Mechanical Properties of Density-Reduced Cement Compositions, SPE 90068, SPE Drilling & Completion, Volume 22(2), pp: 119-126.

Reeder, J. R., and Crews, J. H., 1988, Mixed-Mode Bending Method for Delamination Testing, AIAA Journal, July, Vol. 28, No. 7: pp. 1270-1276.

Rice, J. R., 1968, A Path Independent Integral and the Approximate Analysis of Strain Concentration by Notches and Cracks, Journal of Applied Mechanics 31: 379-86.

Sarris, E., and Papanastasiou, P., 2011, The influence of the cohesive process zone in hydraulic fracturing modeling. International Journal of Fracture, Vol. 167(1), pp: 33-45.

Sumi, Y., Nemat-Nasser, S., and Keer, L. M., 1980, A new combined analytical and finite-element solution method for stability analysis of the growth of interacting tension cracks in brittle solids, International Journal of Engineering Science, Volume 18, Issue 1, Pages 211-224.

Thiercelin, M. J., Dargard, B., Baret, J. F., and Rodriquez, W. J., 1998, Cement Design Based on Cement Mechanical Response, SPE 52890-PA, SPE Drill & Completion, Vo., 13(4), pp: 266-273.

Tvergaard, V., and Hutchinson, J. W., 1996, Effect of strain-dependent cohesive zone model on predictions of crack growth resistance, International Journal of Solids and Structures, Vol. 33, pp: 3297-3308.

Warpinski, N.R., Lorenz, J.C., Branagan, P.T., Myal, F.R., and Gall, B.L., 1993, Examination of a Cored Hydraulic Fracture in a Deep Gas Well, SPE 22876.

Xie, M., 1995, Finite Element Modeling of Discrete Crack Propagation, PhD. thesis, University of New Mexico, USA.

CHAPTER 6. CEMENT SHEATH INTEGRITY DURING HYDRAULIC FRACTURING: AN INTEGRATED MODELING APPROACH

Abstract

Recent arguments about the possibility of underground water pollution in particular regions have raised significant concerns regarding wellbore integrity during hydraulic fracturing in shallow formations. In this paper, we take a look at the containment of annulus cracks that might develop during hydraulic fracturing treatments. Wellbore integrity is highly dependent on the integrity of the bonding between the cement and the formation as well as the bonding between casing and cement. Cement heterogeneity resulted from unsmooth borehole surfaces, complex geological conditions, mud cakes, and cement contamination. Excessive fluid pressure during hydraulic fracturing could provide the driving force not only for initiation and propagation of fractures in longitudinal and transverse directions, but also in cases of low confining pressure, it may lead to fracture propagation around the casing, i.e. annulus cracks. A coupled three-dimensional poroelastic model with embedded cohesive zones is used to simulate different fracture propagation scenarios that may occur in vertical and horizontal wells during hydraulic fracturing stimulations. The cohesive layer theory is utilized to model initiation and propagation of transverse, longitudinal and delamination fractures. Using the numerical analysis provided in this paper, few hydraulic fracturing cases were simulated by taking the advantage of the treatment pressure data and petrophysical logs, and the results were compared with the post-treatment radioactive tracer logs available for these wells.

Introduction

Wellbore integrity can be endangered during hydraulic fracturing treatment due to the occurrence of large fluid pressure and large fluid pressure fluctuation at the perforations. Hence, investigating the possibility of developing annulus fractures may have a significant importance on preventing any possible underground water pollution. Three kinds of fractures may develop in hydraulic fracturing treatments: annulus failures, transverse, and longitudinal fractures. Annulus fractures occur in cylindrical shapes

around the casing, which could be induced by a large treatment pressure or by large fluctuations in the treatment pressure, specially in cases of low confining stress or poor cement quality. Fracture propagation along the casing exterior not only breaks well integrity but it also dehydrates the fracturing fluid and in extreme cases it may cause near-wellbore screenout. The main focus in this research is investigating the likelihood of annulus fracture containment versus uncontrolled development. Similar cylindrical failure geometry exists in different engineering problems like fiber reinforced composite materials (Ozbek and Erdogan, 1969, and Close and Zbib, 1996). There have been efforts in calculating the stress intensity factor and the opening of the cylindrical fracture under uniform loading (Farris et al., 1989, and Zbib et al., 1995) or in the presence of inhomogeneities (Li et al., 2001) but the authors did not find any analytical or numerical solution for fluid-driven cylindrical fractures in the literature. The inherent cylindrical geometry of wellbores and weakness of cement sheath mechanical properties, due to heterogeneities, may assist the initiation of annulus fractures at the same time that fractures are growing in the formation. Historically, due to a major concentration of fracturing treatments in large depths, the confining in situ stresses were large enough to prevent any uncontrolled growth of fractures. Additionally, limiting fracturing jobs to single stage jobs reduced the likelihood of a large number of pressure fluctuations in a treatment well to cause progressive damage. Currently, utilization of hydraulic fracturing treatments in shallow formations and the popularity of multistage stimulation techniques make revisiting this problem beneficial to assure the safety of fracturing operations. Since the outcome of these integrity problems are most in the form of underground venting and it may not lead to any fluid flow to the surface, the integrity problem are hard to identify and may stay hidden for long periods of time without any implications unless it reaches the aquifers.

The common fracture geometries considered in hydraulic fracturing simulations are longitudinal and transverse fractures, which have failures planes reaching into the formations. Both types of fractures may concurrently develop delamination fractures between the casing and the formation due to excessive fluid pressure behind the casing. Transverse fractures are perpendicular to borehole axis while longitudinal

fractures are parallel to borehole axis. In general, fractures have a tendency to propagate along the direction that is perpendicular to the minimum principal stress, however, friction at the perforations, misaligned perforations and perforation at the inclined part of the wellbore may lead to the formation of fractures which are not normal to the minimum in–situ stress, at least close to the wellbore. Development of microannulus or annulus cracks may greatly facilitate fluid flow at the mouth of transverse fractures and, in some cases, help the transition of fracture geometry from transverse to longitudinal fractures and vice versa. Lecampion and Prioul (2013) showed the potential role of differential stresses caused at different injection rates on reorienting stresses around the wellbore and its consequent effect on the development of longitudinal fractures versus transverse fractures in horizontal wells. Minimizing the likelihood of annulus fracture formations would reduce the loss of fracturing fluid and divert it into the direction that facilitates further fracture penetration into the reservoir, which improves the effectiveness of stimulation treatments and maintains wellbore integrity after hydraulic fracturing.

To predict different modes of failure involved in hydraulic fracturing and its consequent effects on wellbore integrity, common fracture assessment tools like tiltmeter or microseismic tools cannot be employed. The main tools for monitoring annulus cracks are cement bond logs, tracer-logs, and distributed temperature logs, which all are post treatment assessment tools with limited capability to provide fracture geometry only at the wellbore. Hence, modelling may help us to predict these problems or more reliably interpret post-treatment assessments on the dimension of annulus cracks. The tracer log shown in Figure 6.1 is typical available data to investigate failure characteristics during hydraulic fracturing. The concentration of tracers confirms the opening of a fracture behind the casing but not the type of the failure. The “Yellow” and “Red” represent tracers pumped in the first and the second phase during the treatment, respectively. The reasons for fracture growth in non-perforated zones could be, but not limited to, fracture height growth or casing/cement integrity problems.

Although field evidence like tracer logs, gives us an important starting point to speculate about possible problems and build the simulation, but in general tracer-logs and other field measurements are

post-treatment failure assessments without any predictive capability. The high costs further limit their

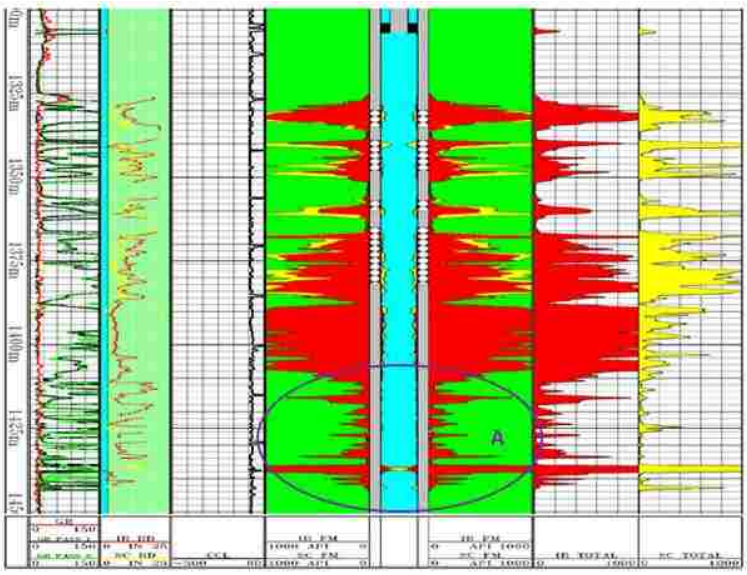

Figure 6.1 Tracer log of a stimulated well. Longitudinal (or axial) and transverse fractures are detected around an inclined well based on the tracers concentration. The tracers are presented by yellow color for the first phase and red color at the second phase.

wide application. Compared with field tests, the laboratory tests are easier to be conducted in the lab (Abass et al, 1996, van de Ketterij and Pater, 1999). However, the limited laboratory conditions cannot represent the real wellbore condition. To overcome these limitations, numerical simulations provide a way to investigate and predict wellbore integrity problems. The longitudinal and transverse fractures as well as their competition in terms of mechanical and geometrical aspects have been studied by using linear elastic strength criteria (Lecampion, et al, 2013) and cohesive zone method (Carrier and Granet, 2011). However, available models are capable of investigating the longitudinal and transverse fractures around the wellbore during hydraulic fracturing stimulation; the consideration of annulus failure and wellbore integrity involved in this process is missing.

In this paper, a coupled three-dimensional poroelastic model is developed which is capable of simultaneously modeling initiation and propagation of transverse, longitudinal and annulus failures. The potential failure zones are represented by pre-inserted cohesive elements with the bilinear traction separation law as the failure criterion. Excessive fluid pressure during hydraulic fracturing would provide

the driving force for fracture propagations. The comparison between failure patterns from numerical analysis and real field measurements, i.e. Radioactive tracer-logs, are used to provide a qualitative benchmark for the model. The developed method could be a predictive tool for the assessment of cement sheath integrity before starting hydraulic fracturing treatments. In this paper, we performed a comprehensive analysis on hydraulic fracturing and its concomitant wellbore integrity problems. Four different scenarios are selected for analysis: 1) delamination fracture in vertical wells stimulation; 2) delamination cracks in vertical section of the wellbore due to leakage at the casing shoe; 3) delamination cracks in the horizontal wells by taking into account the influences of formation and cement heterogeneity; and 4) delamination fractures in inclined wells. In the case of initiation of delamination cracks around the casing, the length of the debonded zone and its containment is discussed based on the results of the numerical model.

Governing Equations

Cement and the surrounding rocks are considered porous continuum with solid and fluid constituents in this model. For the sake of simplicity, incompressible Newtonian fluid is used to represent fracturing and formation fluid. We ignore any potential plastic deformation in rock or cement and consider rock as a linear isotropic elastic material. The force equilibrium equation are written in compact notation as

$$\sigma_{ij,j} = 0; \qquad (\mathbf{6.1})$$

where σ_{ij} are stress components. The governing equations to relate stresses, strains and pore fluid pressure, which are designated as coupled constitutive relationship for rock and fluid interactions (Wang, 2000), are represented below. The coupled constitutive relationship is used in mixed stiffness formulation, where stress is paired with the increment of fluid content as dependent variables in the constitutive equations (Biot, 1941):

$$\sigma_{ij} = 2G\varepsilon_{ij} + 2G\frac{\nu}{1-2\nu}\varepsilon_{kk}\delta_{ij} - \alpha\delta_{ij}P_P \qquad \mathbf{(6.2)}$$

$$\varsigma = \alpha \varepsilon_{kk} + \frac{\alpha}{K_u B} P_P \quad \textbf{(6.3)}$$

where G and v are shear modulus, rock and Poisson's ratio, respectively; P_P is the fluid pore pressure in the rock. The ς and B are the fluid content increment and Skempton's coefficient, respectively. The other parameters used in the above equations are defined in the nomenclature provided at the end of the paper. Fluid mass balance in the rock and cement can be described as

$$\frac{\partial \varsigma}{\partial t} + q_{i,j} = 0 \quad \textbf{(6.4)}$$

where q is the fluid injection rate. Upon the formation of a delamination crack between the cement and casing, fluid flow inside the fracture will be considered as laminar flow between two parallel fractures, i.e. Poiseuille's flow or lubrication equation (Batchelor, 1967), which is a tangential flow

$$\frac{\partial w(s,t)}{\partial t} = \frac{1}{12\mu} \frac{\partial}{\partial s} (w^3(s,t) \frac{\partial P(x,t)}{\partial s}) \quad \textbf{(6.5)}$$

where P is the fluid pressure inside the delamination crack, *w* is the fracture width, and *s* is the length coordinate along the fracture. Besides this tangential flow, normal flow (so-called leakoff) may cause further fluid exchange between the fracture and the formation, which flows in or out of the formation in the direction that is perpendicular to the fracture surface. The leakoff (also called normal flow) into the formation is defined, based on Darcy's law, as

$$q_{leakoff} = c_b (P - P_r) \quad \textbf{(6.6)}$$

where P_r is fluid pressure in the formation adjacent to the fracture surface. The parameter c_b defines the corresponding fluid leak-off coefficient, which can be described as a function of the formation effective permeability on the fracture surfaces and cake buildup due to fluid infiltration to the medium. The combined effects of tangential and normal flow determine the energy transportation between the fracture and the formation.

Equations presented above describe the physics of deformation and fluid flow around the wellbore and inside the delamination fractures; however, a model to predict fracture initiation and their subsequent propagation is not yet introduced here. Since the traditional failure criterion, Griffith's criterion, only predicts propagation of pre-existing fractures, not their initiation, a more general failure criterion is required. In this paper, we use the cohesive interface approach to address these needs. Description of this approach is given in the next section.

The Cohesive Zone Method

Failure initiation and development involved can be effectively described by cohesive zone method (CZM) due to its advantages. CZMs can easily overcome complexities involved in fracture propagation by avoiding singularity calculation at fracture tips. Moreover, CZMs can easily and dynamically implement crack paths into classic finite element frameworks (Li and Chandra, 2003) and incorporate multiple crack growths in heterogeneous media (Yang et al., 2009), which effectively release the computational burden from calculating singularity stress involved in conventional methods, such as Griffith's criterion. Moreover, CZMs have wide application scopes, such as metallic materials (Siegmund and Brocks, 2000), ceramic materials (Camacho and Ortiz, 1996), concrete structures (Hillerborg et al., 1976), composites (Espinosa et al., 2000), geomaterials (Carrier and Granet, 2011) and casing-cement interfaces (Dahi Taleghani and Wang, 2013). Needleman (1990) proposed that cohesive zone models are particularly attractive when interfacial strengths are relatively weak when compared with the adjoining material, such as an interface between ductile and elastic materials, or between two elastic-plastic materials (Xie and Gerstle 1995). Successful applications in the past guaranteed the cohesive zone model as a reliable and powerful tool to model interfacial delamination fractures between cement and formation systems for this chapter. This method has been successfully used for modelling hydraulic fracturing growth (Sarris and Poppantasie, 2001), microfractures reactivation during hydraulic fracturing (Dahi-Taleghani and Puyang, 2013), and interaction of hydraulic fractures and natural fractures (Dahi-Taleghani et al., 2013).

The traction separation law is used in CZM to predict failure initiation. In this approach, cohesive forces resist against the opening forces and compensate the stress singularity at the tip along the failure zone (Li and Chandra, 2003). A typical crack tip process zone is shown in Figure 6.2a. The processes occurring within the process zone are accounted for through the traction–displacement (T–δ) functional. T–δ relationship is essentially established to describe the physical behavior of the fracture process zone. The T–δ relationship can be described by two independent parameters, following three parameters, namely, cohesive critical energy, G_n, and either cohesive strength t_{n0} or separation length δ_{nf}. Bilinear traction separation law (Chen et al., 1999, and Dávila et al., 2001), which is also called Bilinear T–δ relationship, is selected for detailed analysis due to its successful application in characterizing fracture processes in brittle materials, especially in concrete structures (Hillerborg, et al. 1976, Gerstle and Xie, 1992). The Bilinear T–δ relationship is shown in Figure 6.2b. Points A, B and C of Figure 6.2b correspond to those in Figure 6.2a. Mathematically, crack tip can be assumed to be located at Point A, where the material separation has not yet taken place. Cohesive interface starts to open at point B when the tension or shear traction applied to the interface reaches a critical point (Tvergaard and Hutchinson, 1996), which is represented by t_{n0}. From the physics perspective, we assume that the crack tip should be located at the point B, where peak cohesive stress takes place. At point C, material has completely separated and the traction has vanished, which represents physical crack tip. The length of fracture process zone is defined by the distance between A and C. Cohesive traction acts all along this length of the fracture process zone. With the increment of interfacial separation, the traction across the interface reaches a maximum (point C), then decreases and eventually vanishes (point C), a complete decohesion is formed. Meanwhile, the energy dissipation in the fracture processing zone is represented by the area of $t_n - \delta_n$ triangle is the critical energy for failure propagation (Xie, 1995).

In the present work, failures induced by fluid pressure and in situ stresses may lead to mixed mode fracture in inclined wells, which requires considering the combinatory effect of normal and shear modes. Damage onset and the corresponding softening behavior under mixed-mode loading may occur before

any of the traction components involved reach their respective pure mode failure criteria (Camanho and Dávila, 2002). Hence, quadratic failure criterion is more realistic than maximum stress criterion (Camanho and Matthews, 1999, Camanho and Dávila, 2002) to describe the mixed mode failure behavior. The quadratic failure criterion is described as

$$\left\{\frac{\langle t_n \rangle}{t_{n0}}\right\}^2 + \left\{\frac{t_s}{t_{s0}}\right\}^2 + \left\{\frac{t_t}{t_{t0}}\right\}^2 = 1 \qquad \textbf{(6.7)}$$

where $\langle t_n \rangle$ demonstrates tensile tractions, which indicates that compressive normal tractions are considered to have no effect on delamination onsets.

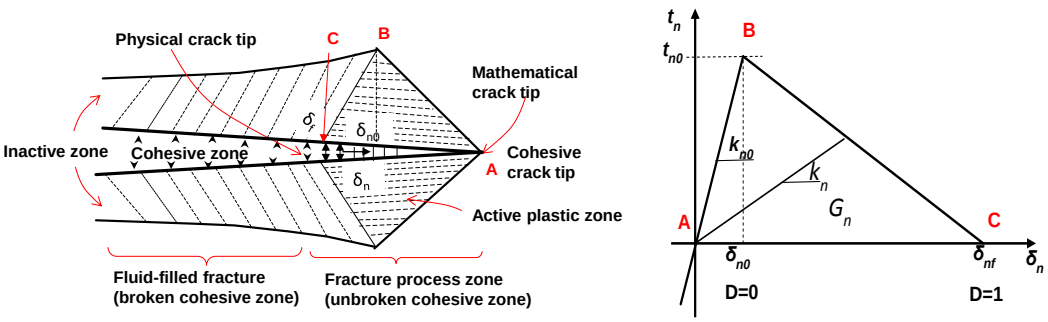

(a) Embedded cohesive process zone (b) Typical bilinear traction-separation curve

Figure 6.2 Embedded cohesive process zone is shown on the left and typical bilinear traction-separation curve of CZM is demonstrated on the right. Critical conditions for failure initiation and propagation, fracture process zone, as well as broken cohesive zone have been illustrated.

The metrics for damage is the stiffness degradation index, *D*, which represents the overall damage of the interface caused by all stress components. The stiffness degradation index is a function of effective relative displacements, δ_m, which combines the effects of δ_n, δ_s and δ_t. For linear softening, the damage evolves with the degradation index (Chen et al., 1999) as

$$D = \frac{\delta_{mf}(\delta_{m,\max} - \delta_{m0})}{\delta_{m,\max}(\delta_{mf} - \delta_{m0})} \qquad \textbf{(6.8)}$$

With the total mixed-mode relative displacement δ_m defined as

$$\delta_m = \sqrt{\langle \delta_n \rangle^2 + \delta_s{}^2 + \delta_t{}^2}\,. \qquad \textbf{(6.9)}$$

The delamination propagation criterion under mixed-mode loading conditions is established in terms of the energy release rates and fracture toughness, which are usually obtained from the following established tests: Mode I fracture toughness from the Double Cantilever Beam Specimen (DCB) (Oh et al, 1988); Mode II fracture toughness from the End Notched Flexure or the End Loaded Split tests (Russell, 1982). For mixed-mode I and II, fracture toughness from Mixed-Mode Bending test (Reeder and Crews, 1988) and Four-Point Flexure Specimen (Charalambides et al, 1989). Cohesive zone approach can be related to Griffith's theory of fracture because the area under the traction-relative displacement curve is equal to the corresponding fracture toughness regardless of its shape (Rice, 1968). For example, in a bilinear cohesive interface softening model the energy release rate can be simply given by

$$G' = \frac{K_{Ic}^2}{t_n E'} \qquad \textbf{(6.10)}$$

The effectiveness of the CZM is greatly dependent on the accuracy of input parameters. This part generalizes the work on how to use results from routine tests (e.g., Lavda, 2005 and Carter and Evans, 1964) and numerical simulation to derive required parameters for cohesive zone constitutive equations by inverse analyses. Routine pull-out tests have been widely applied to measure the shear bond strength and its deformability behavior between cement and shale. The pull-out test in Lavda (2005) showed that a shale core was pulled out from a cement ring set in a piece of casing. Then the shale core was dragged slowly by a brass rod with a diameter of 20mm when the cell walls and cement ring were supported. A schematic of push-out tester and a typical force versus displacement plot of this test are demonstrated in Figure 6.3a and 6.3b, respectively. The maximum observed load is considered as shear bond strength or yielding point of the interface. In order to characterize the failure damage mechanism between cement and formation, the cohesive interface model was made to estimate shear strength (peak and residual), and the deformability (shear stiffness) of the interface by matching up loading versus displacement

relationships from lab tests (Dahi Taleghani and Wang, 2013). Cement and formation (or casing) interfaces are considered as potential paths for failure, which could be represented by pre-inserted cohesive elements following bilinear traction separation behavior. Consequently, matching up loading-displacement curves from regular cement strength tests and numerical simulation tests are used to yield bond strength, fracture critical energy, this also shows allowable deformation at cement interfaces before complete failure. Moreover, the parameters generated have been approved to be effective in field-scale problems.

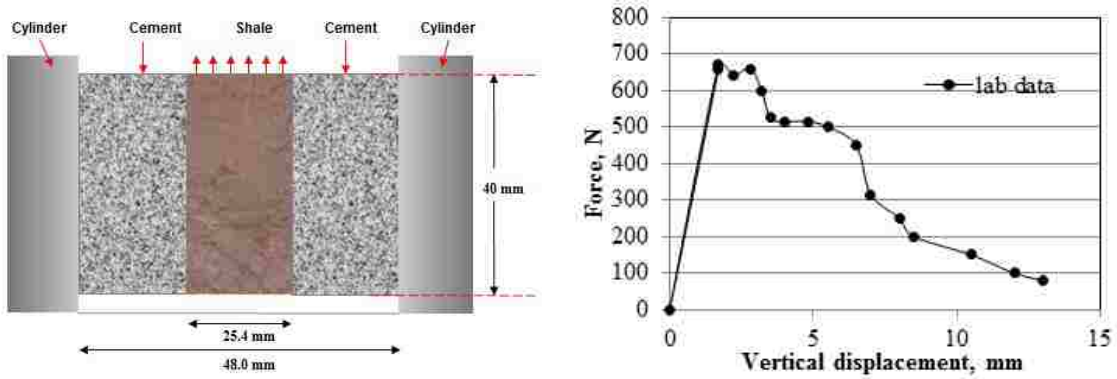

Figure 6.3 A schematic of the push-out test is shown on the left side. The loading curve measured in a push-out test for a sample of Oxford shale and cement is shown in the right picture (borrowed from Lavda, 2005). We use these loading curves to derive cohesive parameters by inverse analysis of the experimental configuration.

The cohesive zone model is a nonlinear constitutive equation that needs to be run with a coupled stress and fluid flow simulator to perform fracture and integrity analysis. Due to the inherent advantage of finite element analysis, such as flexibility in incorporating heterogeneity, anisotropy and nonlinear material properties, we chose to use finite element methods for modelling the problems discussed in this paper.

Numerical Model

The numerical solution of this problem can be obtained using standard Galerkin's formulation for the finite element methods used for poroelasticity problems (Lewis and Schreffler, 2000). The equation in matrix notation can be written as following

$$[K]\{u\}+[L]\{u\}=\{F\}$$
$$[S]\{\dot{p}\}+[L]^T\{\dot{u}\}+[H]\{p\}=\{q\} \quad \textbf{(6.11)}$$

where *u* is the nodal displacements, p are nodal pressures, F are nodal forces, q is nodal fluxes, [K] is the stiffness matrix, [L] is the coupling matrix, [H] is the flow matrix and [S] is the compressibility matrix. The first equation (1) is the stiffness equation and the second equation is flow equation. Unknown variables u and p are substituted by their nodal values and the interpolation functions (shape functions). The definition of matrices used in equation (1) are given below (Lewis and Schreffler, 2000)

$$[K]=\int_\Omega B^T D B\, d\Omega,\ [L]=a\int_\Omega N^u \begin{Bmatrix} d/dx \\ d/dy \end{Bmatrix} N^P\, d\Omega, \quad \textbf{(6.12)}$$

$$[S]=a\int_\Omega \left(N^P\right)^T \frac{1}{\tilde{Q}} N^P\, d\Omega,\ [H]=\kappa\int_\Omega N^u \begin{Bmatrix} d/dx \\ d/dy \end{Bmatrix} N^P \Bigg\}^T \begin{pmatrix} d/dx \\ d/dy \end{pmatrix} N^P \Bigg) d\Omega,$$

where D is the elasticity matrix, N^P and N^u are the shape functions for pressure and displacements, respectively. The parameter $\tilde{Q}$ is defined as

$$\tilde{Q}=\frac{BK}{\alpha(1-\alpha B)}. \quad \textbf{(6.13)}$$

To validate the numerical model, a two-dimensional finite element model is built in ABAQUS for a single fracture. The reservoir medium is assumed to be much larger than the hydraulic fracture dimension and is modeled with quadratic plane strain elements. The injection well is considered to be at the center of the model and a layer of cohesive interface passes through the injection well, which represents the possible paths for the hydraulic fracture and consists of 6-node cohesive elements. The maximum length of the hydraulic fracture in this model could be as large as 22 m, which is much smaller than the model size, to avoid any boundary effect. The boundaries of the model are constrained for normal deformations. The in-situ stresses are defined as initial stresses to avoid any excessive deformation in the initial equilibration process. The crack opening displacement profile and fluid pressure profile are demonstrated

in Figure 6.4, which are compared and are in agreement with the results reported previously by Sarris and Papanastasiou (2011).

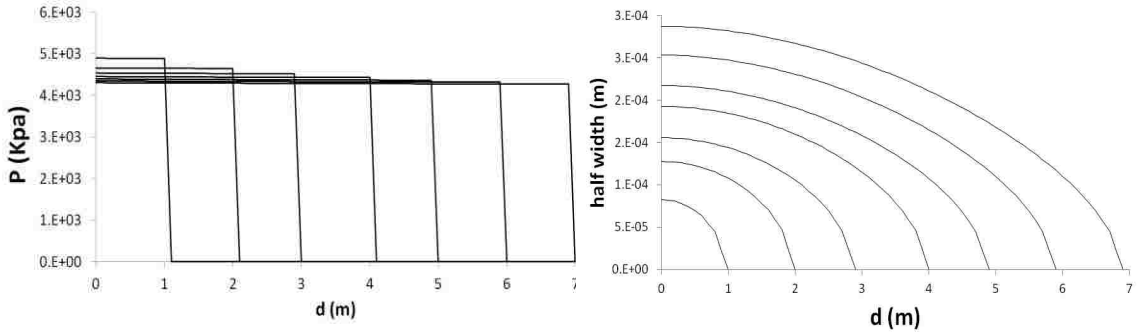

Figure 6.4 pressure profile along the half-length of the propagating fracture through cohesive path at different times. Fracture opening at the corresponding times is also demonstrated in the right graph.

Results and Discussions

In order to simulate wellbore integrity under different wellbore conditions, a coupled fluid-flow poroelastic finite element model is built to be able to consider different fracture geometries: annulus failures, longitudinal and transverse hydraulic fractures, and their mechanical characteristics. To consider the possibility of different fracture geometries growth, three dimensional analyses are inevitable. This model consists of an 8-½ in borehole drilled through the homogeneous block, as demonstrated in Figure 6.5a. The wellbore is protected by 7-in cemented steel casings. The fracturing fluid inside the wellbore has weights of 9.3 lbm/gal. We considered the propagation of annulus fractures at the perforations or around a leakage point, for instance, at a casing shoe. For the sake of simplicity, materials on either side of the interface are assumed to be linearly elastic and isotropic. The cement-casing and cement-formation will be considered as potential failure paths, which are simulated by pre-inserting cohesive layers with zero thickness (Ungsuwarungsri and Knauss, 1987). For fracture propagation inside the formation rock, cohesive elements have also been inserted in the rock in the direction of fracture propagation.

Figure 6.5b shows the numerical meshes used for finite element analysis. Solution convergence is improved by designating fine elements close to potential failure zones. A layer of coupled cohesive

elements with 1200 elements is assigned between cement and casing (or rock), in other words, a cohesive layer representing the cement layer. A layer with 1508 cohesive elements is considered as a potential failure path in the rock, which is perpendicular to the minimum horizontal stress. Moreover, there are 2400, 2400, and 30,177 elements used to model casing, cement and rock, respectively. Rock mechanical

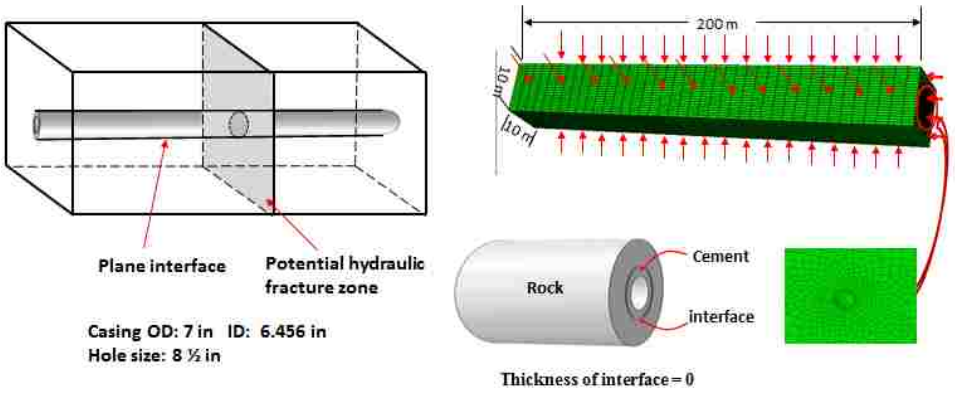

Figure 6.5 (a) A schematic picture of the numerical model with potential hydraulic fracture planes; (b) model's dimensions, boundary and loading conditions, and meshes for also demonstrate.

properties used in the model are extracted from measurements reported in the literature (Ballard et al., 1994). Values used for cement, casing, rock and interfaces are listed in the appendix. Cohesive interface properties between the cement and rock are generated from several lab experiments such as the shear bond test and the hydraulic bond test described in Dahi Taleghani and Wang (2013). Moreover, cohesive interface properties between rocks are borrowed from Chen's paper (2011). The simulation has been implemented in two steps. At the first step, initial equilibrium was achieved after assigning initial geostatic stresses and initial fluid pressure; then at the second step, a perforation fluid with constant concentrated flow is injected in the wellbore. Constant low injection rate, Q_o=25 bpm, is considered. The analysis of post-frac radioactive logs and numerical simulation has been conducted for different situations. The wellbore integrity and the competition between annulus fractures, transverse fractures and longitudinal fractures are investigated during hydraulic fracturing stimulation process.

Wellbore Integrity in Stimulation of Vertical Wells

Effective isolation of the stimulation zone is an important issue for practicing an environmental friendly hydraulic fracturing treatment. The loss of interval integrity may cause cross flow between different perforation zones or diversion of fracturing fluid to non-perforated zones. Similar situations may cause out of zone injection in water flooding treatments, however, temperature difference could play a critical role for water injectors but not in fracturing treatments as the net pressure is order of magnitudes larger than thermal stresses. To further elucidate this problem in vertical treatment wells, a post-frac radioactive log from a vertical well is selected for further analysis and discussion. This treatment is conducted in a basin with a very tight sand mainly bearing liquid hydrocarbons. A post-frac radioactive log, shown in Figure 6.6, demonstrates considerable concentrations of tracers located about ten meters away from the perforated zone. Treatment pressure analysis indicates much smaller fracture height; therefore the presence of a radioactive tracer could be an indication of the loss of cement integrity. The cement sheath failure forms an annulus that may act as a conduit for draining fracturing fluid (not proppants). Therefore, a portion of the pumping horsepower might be spent in stimulating unfavorable zones and in extreme conditions may cause near-wellbore screenout. However, underground contamination may cause more serious challenges for the operator. The absence of tracers in a part with high radioactive concentration is essentially an indication of lack of proppants in the extended zone, in other words, the annulus crack is so narrow that proppant may not pass through it easily. It is worthwhile to mention that the isolation of perforation zones highly depends on the combined effects of in situ stresses, cementing quality (e.g. eccentricity and inclination), and treatment pressure.

Although radioactive logs can effectively provide information about the tracers' concentration at the wellbore, it is difficult to obtain much information about the fracture geometry outside the wellbore region by only using post-frac logs (tracer or CBL logs). Additionally, radioactive logs do not have a predictive capability. Hence, more sophisticated techniques are required. To address these needs, we resort to modelling. A coupled three dimensional model is used to simulate failure development during

treatment. This numerical model is established to reproduce the failure pattern observed in Figure 6.6 in the wellbore and bottomhole pressure recorded in the field. Fracture propagation along the vertical section of the wellbore and into the formation is demonstrated in Figure 6.7a. It can be seen that three different fractures are generated in this case, which are, major longitudinal fractures at the perforations, annulus failures around the wellbore, and secondary longitudinal fractures in the lower weak layer. The annulus

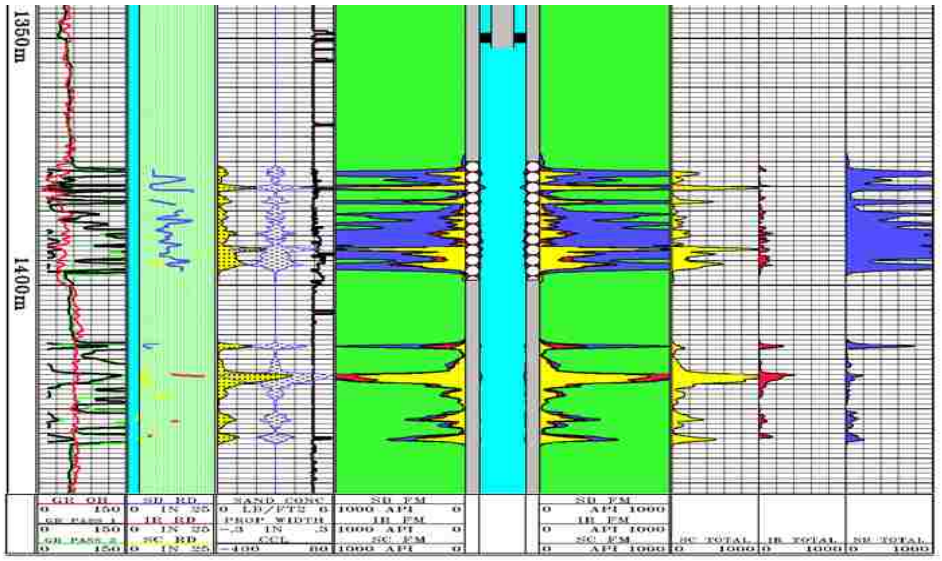

Figure 6.6 The post-frac radioactive log demonstrates out of zone fracture propagation during hydraulic fracturing. In this case, pumping more fluid lead the fractures to propagate in a lower weaker zone, which may contain a natural fracture.

opening around the wellbore provides important hydraulic conduit for hydraulic fluid transferring. The corresponding pressure response at the perforation zone is shown in Figure 6.7b. Pressure fluctuations during formation and growth of annulus crack are not unfortunately large enough to be capture in the pressure measruements. Zone A in the perforation zone of Figure 6.7a is selected for pressure analysis. The pressure magnitudes provide a diagnostic basis for fracture height and geometry. It can be observed that the relatively constant fluid pressure resulted during constant injection rate, which is a typical representative of the occurrence of longitudinal fractures (PKN fractures). Moreover, some energy is also lost during the formation of annulus failures. This failure behavior becomes more complicated when considering its induced premature screenout, fracture offset, enhanced fluid friction along the fracture

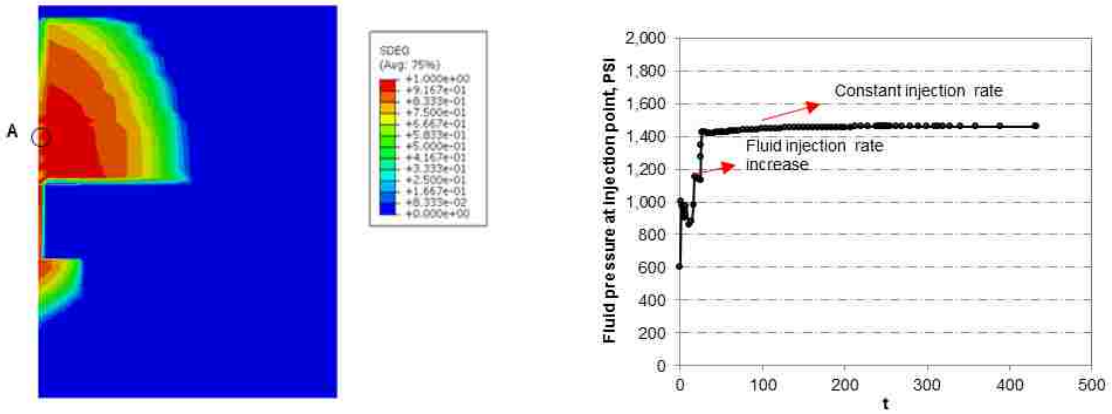

(a) Longitudinal fractures connected via a delamination fracture (b) Bottomhole pressure

Figure 6.7 Fracture propagation and its concomitant delamination crack propagation along the wellbore during hydraulic fracturing are demonstrated. Injected fluid is leaked to the formation in a depth much shallower than the perforation zone.

length and the creation of secondary fracture in weaker zones. In addition, the possible natural fractures located in the lower zone might be fed by the annulus and give the impression of the propagation of another fracture or larger fracture height.

Wellbore Integrity in the Vertical Section of the Well due to Leakage

In this part, we introduce another case: the wellbore integrity is challenged by a leakage at the casing shoe of the production casing. The leakage provides a driving source due to excessive fluid pressure (shown in Figure 6.8). Considering the extremely low permeability of the intact cement, the fluid seeps around the casing mainly via cracks and micro-annulus channels in the cement (Saidin et al., 2008). In this case, the casing shoe is mainly charged by leakage at casing shoe, or maybe charged by fluid migration from hydraulic fracturing in horizontal section of the wellbore.

A numerical experiment is conducted to study this scenario. The cylindrical interface between cement and formation, which is originally perfectly bonded, tries to separate from each other under the effects of pressurized fluid. The stimulation wellhead pressure and its fluctuation process in a field example from Woodford Shale is considered as shown in Figure 6.9. We assume that a virtual leakage exists at the casing shoe. The excessive energy, which is provided by pressurized fluid with large pressure and large pressure fluctuation, facilitates upward annulus fracture propagation, which can be shown in the form of

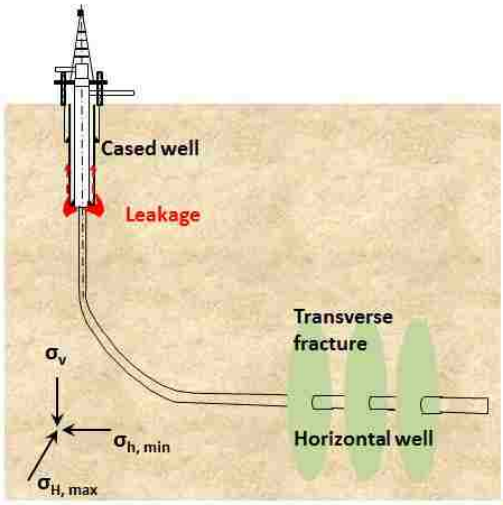

Figure 6.8 A schematic picture of excessive fluid leakage at the casing shoes during hydraulic fracturing stimulation process is illustrated. The pressurized fluid acts as the driving force to challenge the wellbore integrity.

crack length versus dimensionless time. When the magnitude of excessive pressure overcomes the magnitude of the opposition from rock in situ stresses and the strength of the cement, the delamination

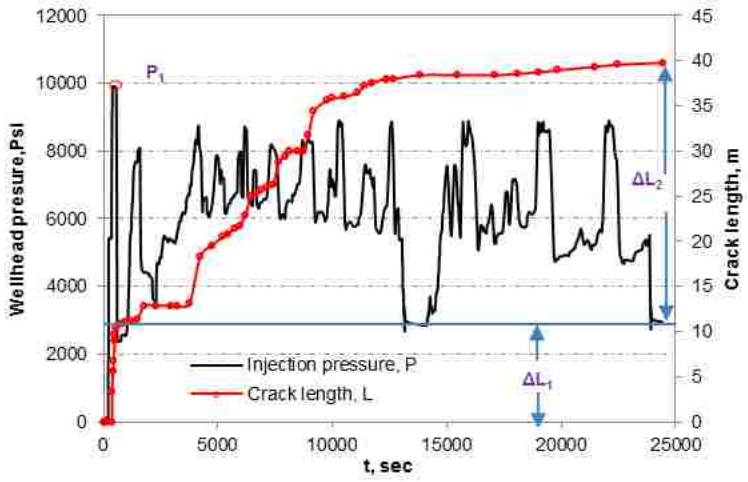

Figure 6.9 Buildup process of fluid pressure at the well head and its inducing failure lengths versus dimensionless time around the wellbore is demonstrated.

fracture starts to propagate. The pressure accumulation and fluctuation at the casing shoe is accompanied with wellbore pressure by considering another three important pressure items, which are hydrostatic pressure increment from surface to casing shoe, friction pressure drop all the way along the casing" drags" the fluid flow, as well as frictional pressure loss at the tip of the fracture. It is assumed that the

pressure accumulates at the leakage zone without leaking into the low permeability cements and formations, as a consequence, failure zone expands or broaches very fast because the enlarged energy is constrained along the interface. It can be observed from Figure 6.9, at the first stage, excessive pressure accumulates continuously until it reaches a critical pressure, P_1^*, then the fracture advances rapidly. Then at the second stage, the probability of occurrences of delamination failures increases with large pressure fluctuations because of complications in the fracture job or ball placement on the perforations. That is because the interface strength is degraded during the unloading process. However, the increasing trend of failure lengths at the second stage becomes smaller than that at the first stage due to smaller peak pressure. Simultaneously, the higher fluid conductivity through the induced conduit would promote further damage at the interface, which further facilitates the fluid to propagate uncontrollably to shallow aquifers or even to the surface with the accumulation of hydraulic fluid. Aiming at reducing the probability of occurrence of annulus failures around the wellbore, wellbore pressure and pressure stability could be a significant influential factor that needed to be considered and planed.

Wellbore Integrity in Horizontal Cemented Wells

In the case of executing multiple stage treatment along a horizontal wellbore, filling the completion requirements can be complicated. To ensure effective stimulations, these intervals must be isolated from each other via good cementing. A three-dimensional coupled model is used for the simulation. It is assumed that the well is drilled in the direction of the minimum horizontal stress.We can observe from Figure 6.10, hydraulic fractures in the horizontal well are tending to be transverse as it requires less energy to grow. Initiation of longitudinal fractures is likely due to large enough horizontal differential stress in this system. The main issue in the longitudinal fractures is uncontrolled fracture growth and potential coalescence of fractures from different zones inside the formation.

Moreover, it can be observed that the fracture initiation position and the shape of transverse fractures, as well as the completion quality may rely on stress anisotropy. Due to the different magnitude of horizontal and vertical in-situ stress, it is observed that fracture length, L, is almost twice of fracture

height, H. Longitudinal development of fracture length is confined by horizontal in-situ stress, while vertical development is confined by overburden in-situ stress. On the other hand, cement integrity is also controlled by interface quality and in-situ stress. In this case, cement deterioration is accompanied and worsened with the development of transverse fractures. The pressure magnitude provides a basis for the possibility of the occurrence of annulus failures during hydraulic fracturing. Two cases were considered:

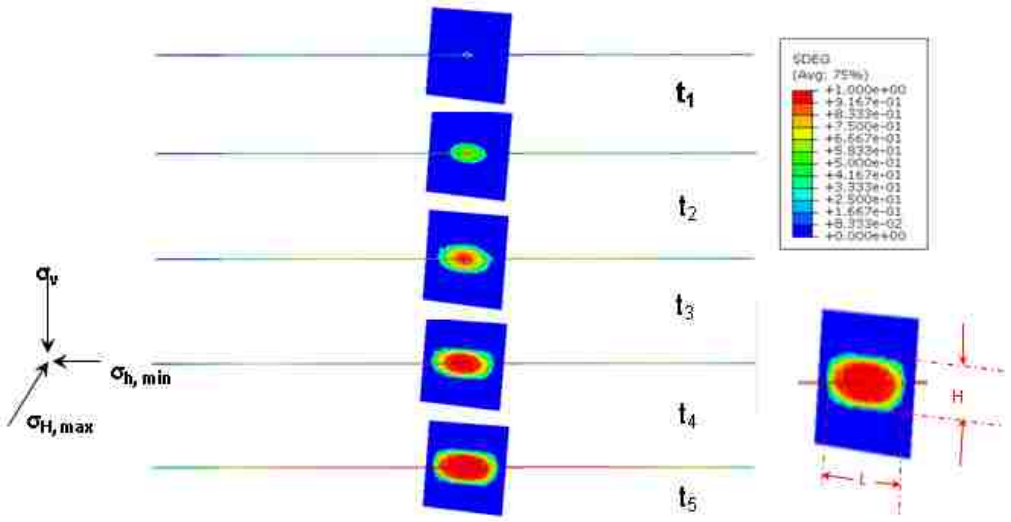

Figure 6.10 Fracture propagations along the wellbore and through the perforation zone located at horizontal wellbore are demonstrated. Transverse fractures and annulus fractures are observed. In this example, the rock, cement and interfaces are all considered to be homogeneous.

Case-1 cement liner is strong enough that no delamination occurs, while Case-2 weak cement interface leads to formation of annulus failures during fracturing. The bottom-hole pressure continuously increases until the fluid pressure is greater than the combined effects of stress resistance and the mechanical strength of rock. Once failures are initiated, the uncontrolled fracture growth is accompanied by a corresponding decrease in pressure. The pressure would not increase again until uncontrolled height growth ceases by other higher stress barriers. On the other hand, based on the comparisons of these two cases, the cement is easier to be broken than rock if there is weaker cement around the wellbore, such as Case-2. The weakness of annulus failures can be represented by lower bottom-hole pressure. The growth in annulus failures leads to additional pressure loss, which can partially limits fluid flow vertically into the lower stress zone.

In the real world, formation and cement are heterogeneous (Dhaliwal et al., 1992, and Prioul et al.,

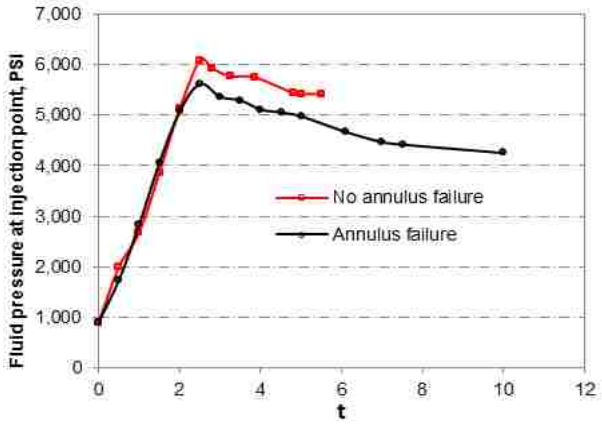

Pressure variation at one injection point

Figure 6.11 Pressure variation versus time at the injection point is shown for two cases: Case-1 is the case with no annulus failure and Case-2 has annulus failure developed around the wellbore.

2011). From numerical angle, the heterogeneity of interface properties may have significant effect on the geometry of the hydraulic fracture, stress concentration around the wellbore, as well as wellbore integrity. In this work, the effects of interface property heterogeneity on annulus fractures are investigated. The strength of cohesive interface is considered to be heterogeneous. The heterogeneity is increasing in terms of the variance of interface strength, which results in lower mean of peak loads. The heterogeneity exists along the interface between cement and rock, as well as the potential failure path in the rock. The heterogeneity occurs in the format of mingling 100 KPa with 320 KPa of interface strength. However, the assumption of fully random distribution of cement properties may not be consistent with the heterogeneity in the real situations due to its diversity. The failure propagations in the case with heterogeneous interface properties are demonstrated in Figure 6.12. Compared with failure patterns in the case with homogeneous interface properties shown in Figure 6.10, larger fractures are observed in the heterogeneous case at the same dimensionless time. That is because the interface strength is deteriorated with the existence of randomly distributed weak interface. On the other hand, it can be observed that non-uniform failure patterns exist along the failure envelope as a consequence of the deteriorated effects of randomly distributed weak interface. It is clear that weaker interface strength would significantly

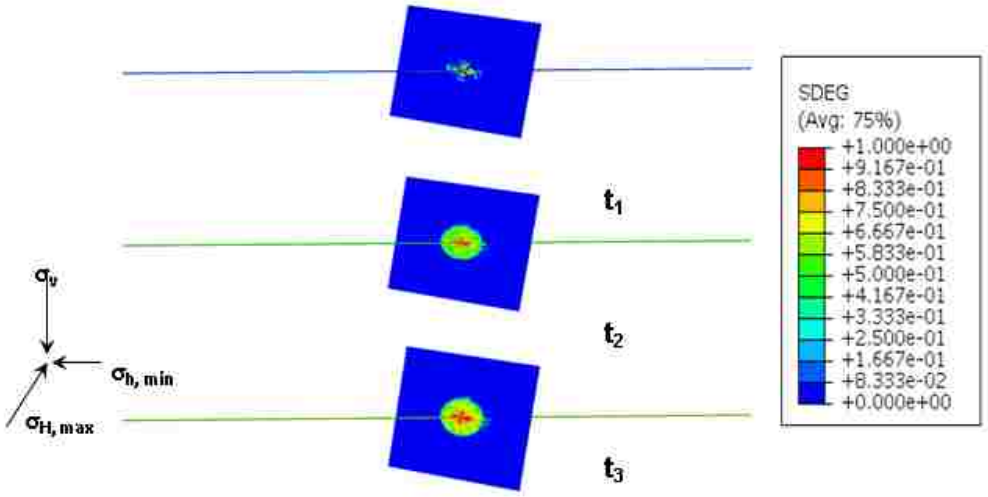

Figure 6.12 Fracture propagations along the wellbore and through the perforation zone located at horizontal wellbore are demonstrated. Transverse fractures and annulus fractures are observed around perforation zone. In this example, the rock is considered to be heterogeneous.

influence failure initiation and patterns, which further influences proppant placement inside the fracture, fluid flow touristy, excessive energy distribution, stress concentration and wellbore integrity. Hence, the heterogeneity in failure initiation and developments could cause the non-uniform distribution of proppants inside the fracture, fracture receding, and breaking the cap rock. Moreover, the possibility for uncontrolled failure broaching around the wellbore is increased due to the interface strength deterioration effects induced by interface property heterogeneity. In this case, transverse fractures and longitudinal fractures occur almost simultaneously. This analysis provides greater insight to the uncertain characteristics of wellbore integrity induced by material heterogeneity.

Wellbore Integrity in Inclined Cemented Wells during Hydraulic Fracturing

Zonal isolation is essential for successful fracture stimulation of high-angle wells and can be achieved by using good cementing practice and selective perforation (Economides and Nolte, 2000). In inclined wells, where wellbores are not aligned with principal stress directions, fractures grow in nonplanar geometries. The initiation, propagation, geometry, and consequently productivity of fractures are greatly influenced by misalignment with the principal stresses. Wellbore integrity problems are more likely to occur in these situations because of complex fracture geometry and stress distribution around the wellbore

as well as the higher treatment pressure induced by tortuosity. In this work, a simplified model with potential transverse and annulus fractures is demonstrated. The simulation is conducted for a 45 ºinclined wellbore. The developed patterns of transverse fractures and annulus failures are illustrated in Figure 6.13. Results show that compared with a vertical wellbore case, there is a large possibility for fracture extension in a direction dictated by local stress distribution around the wellbore. The reason for the transition toward more favorable transverse fractures with increments of wellbore inclination is intrinsically embedded in the stress field. The confining effects of vertical in-situ stresses on transverse

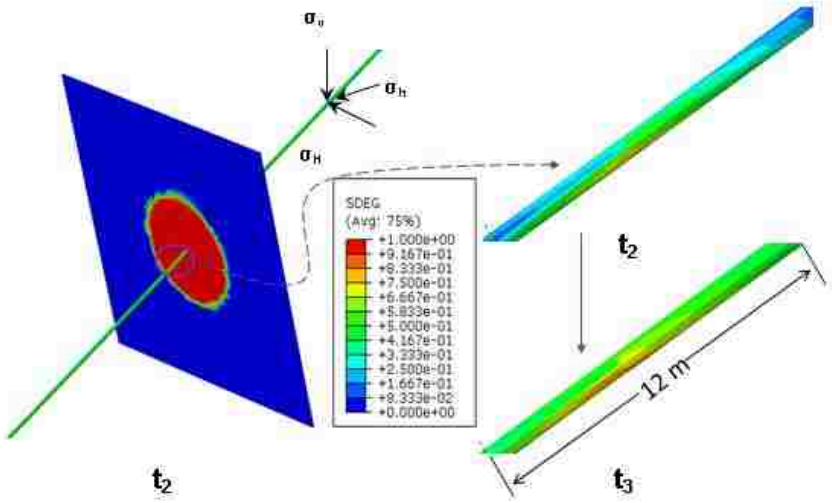

Figure 6.13 Fracture propagations along the wellbore and through the perforation zone in a 45 º inclined wellbore is demonstrated. Transverse fracture and annulus fractures are observed. In this example, the rock, cement and interfaces are considered as homogeneous poroelastic materials.

fracturing closing are partially released due to wellbore inclination. In this 45 ºinclined well, the stress normal to the delamination cracks is 30% less than the vertical well under the same conditions. Additionally, non-uniform annulus failure patterns are induced by the variation of in-situ stress confining effects caused by wellbore inclination. The largest failure zone occurs along the lower part of the inclined well. However, most of the extra energy provided by injected hydraulic fluid is released during transverse fracture propagation. In this case, it is also observed that annulus failures are concentrated around the perforation zone within 12 m at t_3. The annulus failures may be hindered at some lengths due to the

combined effects of flux flow into the cement sheath, stress distribution around the wellbore, interface properties, viscous dissipation and cement strength. In anticipation of preventing the loss of wellbore integrity, numerical models presented here can provide a tool to make contingency plans to control excessive pressure and establish a good communication between the wellbore and main fracture.

Conclusions

Based on discussions, we had a thorough comparison of post-treatment radioactive logs and numerical model results, cement sheath integrity takes an important role in practicing safe fracturing jobs in very shallow formations, however, the simulations do not show any uncontrolled fracture growth for deep enough stimulations. During hydraulic fracturing stimulation, pressurized fluid may cause annulus fractures around the wellbore, and fluid will start migrating through the cement sheath failure zones and in some rare cases out of zone fracturing. Moreover, we showed that the leakage around the casing shoe could cause failure broaching along the cement-formation interface and lead to integrity problems. All these phenomena could occur in the vertical, horizontal and inclined wells. In this research paper, numerical models are presented to provide a tool to assess challenges and make contingency plans to avoid these problems in designing perforation and completion at each fracture stage.

We used coupled three dimensional models to mimic the real wellbore situation during hydraulic fracturing stimulation. The potential failure zones are represented by pre-inserted cohesive elements with bilinear traction separation law as failure criterion. Matching results between numerical failure patterns and radioactive tracer-log's results provide a benchmark for model accuracy. Furthermore, numerical results can be extended for analyzing the mechanisms involved in these failures. The information obtained from numerical models, such as stress, fluid pressure, fracture opening and failure patterns, is beneficial for the understanding the mechanism involved in this system. Moreover, the numerical model can overcome the limitations that are inherent in the radioactive tracer-logs due to its characteristics of accuracy, economy and its predictive capability.

Nomenclature

B	Skempton's coefficient
c_b	Fluid leak-off coefficients of the fracture
c	Poroelastic diffusivity coefficient
D	Scalar stiffness degradation index
E	Rock Young's modulus, KPa
G	Shear modulus of rock, KPa
G'	Energy in pure mode fracture, J
G_n	Work done by the tractions and their conjugate relative displacements in the normal directions, J
k_{n0}	Initial tensile stiffness
k_n	Stiffness components in normal direction
K	Fluid mobility, m^2/KPa.s
K_u	Undrained bulk modulus, KPa
P	Pore pressure in the formation, KPa
P_0	Initial pore pressure in the formation, KPa
P_f	Fluid pressure inside the delamination fracture, KPa
P_r	Fluid pressure in the formation adjacent to the fracture surface, KPa
P^*	Dimensionless fluid pressure, KPa
q	Fluid injection rate, m^3/s
r_w	Wellbore radius, m
σ	Total stress, KPa
t	Real time, seconds
t_n	Normal traction, KPa

t_s / t_t Sheartraction, KPa

t_{n0} Peak values of the nominal stress when the deformation is purely normal to the interface, KPa

t_{s0} / t_{t0} Peak values of the nominal stress when the deformation is purely in shear direction, KPa

u_n Fracture opening, m

u_n^* Dimensionless fracture opening

v Poisson's ratio

v_u Undrained Poisson's ratio

w Crack opening, m

α Biot-Willis coefficient

β Rock thermal expansions, 1/K

β_f Fluid thermal expansions, 1/K

ε_{kk} Volumetric strain

ε_{ij} Strain components.

δ_n Crack opening displacement, m

δ_s / δ_t Crack sliding displacement, m

δ_{nf} Critical relative normal displacements when tractions diminish, m

δ_{sf} Critical relative shear displacements when tractions diminish, m

δ_m Effective relative displacements, m

δ_{m0} Effective relative displacements corresponding to δ_{n0} and δ_{s0}, m

δ_{mf} Effective relative displacements corresponding to δ_{nf} and δ_{sf}, m

ς Change of fluid content, m^3

η Material parameter

σ_{ij} Stress components

References

Abass, H. H., Hedayati, S., and Meadows, D. L., 1996, Nonplanar fracture propatation from a horizontal wellbore: Experimental study. SPE Production & Facilities, 11(3): 133-137.

Ballard, T. J., Beare, S. P., and Lawless, T. A., 1994, Fundamentals of Shale Stabilisation: Water Transport through Shales, SPE 24974-PA, SPE Formation Evaluation, Vol. 9 (2), pp: 129-134.

Batchelor, G. K., 1967, An Introduction to Fluid Dynamics, Cambridge University Press, London, pp: 615-620.

Biot, M. A., 1941, General theory of three dimensional consolidation, J. Appl. Phys., 12(2), pp: 155–164.

Bois, A. P., Garnier, A., and Laudet, J.B., 2012, Use of a Mechanistic Model To Forecast Cement-Sheath Integrity, SPE Drilling & Completion, Vol. 27(2), pp: 303-314.

Bourgoyne, A. T., Chenevert, M. E., Millheim, K. K., and Young, F. S., 1986, Applied Drilling Engineering, Society of Petroleum Engineering Vol. 2, pp: 312-324.

Camacho, G. T., and Ortiz, M., 1996, Computational modeling of impact damage in brittle materials, Int. J. Solids Structures 33, pp: 2899–2938.

Carrier, B., and Granet, S., 2011, Numerical modeling of hydraulic fracture problem in permeable medium using cohesive zone model, Engineering Fracture Mechanics 79 (2012), pp: 312–328.

Carter, L. G., and Evans, G. W., 1964, A study of cement-pipe bonding. Journal of Petroleum Technology, 16(2), 157-160.

Charalambides, P. G., Lund, J., Evans, A. G., and McMeeking, R. M., 1989, A Test Specimen for Determining the Fracture Resistance of Bimaterial Interfaces, Journal of Applied Mechanics, 56, pp: 77-82.

Chen, J., Crisfield, M. A., Kinloch, A. J., Busso, E. P., Matthews, F. L., and Qiu, Y., 1999, Predicting Progressive Delamination of Composite Material Specimens via Interface Elements, Mechanics of Composite Materials and Structures 6, pp: 301-17.

Chen, Z. R., 2011, Finite element modelling of viscosity-dominated hydraulic fractures, Journal of Petroleum Science and Engineering, 88-89 (2012), pp: 136-144.

Close, S., and Zbib, H. M., 1996, The stress intensity factors and interaction between cylindrical cracks in fiber-matrix composites. In: Voyiadjis, G. Z., Allen, D. H. (eds), Damage and interfacial Debonding in Composites. Elsevier Science B.V, pp: 3-27.

Dahi-Taleghani, A., Olson, J. E., and Wang, W., 2013, Thermal Reactivation of Microfractures and its potential impact on Hydraulic Fractures Efficiency, SPE-163872-PP, presented at 2013 SPE

Hydraulic Fracturing Technology Conference to be held 4 – 6 February, 2013 in The Woodlands, TX, USA.

Dahi-Taleghani, A., and Puyang, P., 2013, Post-Treatment Assessment of Induced Fracture Networks, SPE-166354-MS presented in SPE Annual Technical Conference & Exhibition in New Orleans, LA, USA.

Dahi Taleghani, A., and Wang, W., 2013, Emergence of Delamination Fractures around the Casing and Its Stability, International Journal of Geomechanics, Under review.

Dávila, C. G., Camanho, P. P., and Moura, M. F., 2001, Mixed-Mode Decohesion Elements for Analyses With Progressive Delamination, 42nd AIAA/ASME/ASCE/AHS/ASC Structures, Structural Dynamics and Materials Conference (Seattle, Washington, U.S.A.).

Detournay, E., and Cheng, A. H. D., 1991, Plane Strain Analysis of a Stationary Hydraulic Fracture in a Poroelastic Medium, International Journal of Solids and Structures, Vol. 37, No. 13, pp: 1645-1662.

Dhaliwal, R. S., Saxena, H. S., He, W. H., 1992, Stress Intensity Factor for the Cylindrical Interface Crack between Nonhomogeneous Coaxial Finite Elastic Cylinders, Eng.Fract. Mech. 43(6), pp: 1039-1051.

Economides, M. J., and Nolte, K. G., 2000, Reservoir Stimulation, John Wiley & Sons, LTD, Third Edition.

Farris, T. N., Kokini, K., and Demir, I., 1989, The Cylindrical Crack. J. Appl.Mech. 56(4), pp: 981-983.

Gerstle, W. H., and Xie, M., 1992, FEM Modeling of Fictitious Crack Propagation in Concrete, Journal of Engineering Mechnics, Vol. 118 (2), pp: 416-434.

Gordeliy, E., Piccinin, R., Napier, J. A. L., and Detournay, E., 2013, Axisymmetric benchmark solutions in fracture mechanics, Engineering Fracture Mechanics, in press.

Griffith, A. A., 1924, The Theory of Rupture, In Proc. FirstInternat. Congr. Appl. Mech.

Hillerborg, A., Modeer, M., Petersson, P., 1976, Analysis of Crack Formation and Crack Growth in Concrete by Means of Fracture Mechanics and Finite Elements, Cement Concrete Res, Vol. 1976 (6), pp: 773–782.

Ladva, H. K. J., Craster, B., Jones, T. G. J., Goldsmith, G., and Scott, D., 2005, The Cement-to-Formation Interface in Zonal Isolation, SPE 88016-PA, SPE Drilling & Completion, Vol.20, (3): 186-197.

Lecampion, B., 2012, Hydraulic Fracture Initiation From an Open-hole: Wellbore Size, Pressurization Rate And Fluid-solid Coupling Effects, SPE 2012-60146th U.S. Rock Mechanics/Geomechanics Symposium, June 24 - 27, 2012 , Chicago, Illinois.

Lecampion, B., and Prioul, R., 2013, Competition Between Transverse And Axial Hydraulic Fractures In Horizontal Wells, SPE 163848-MS, 2013 SPE Hydraulic Fracturing Technology Conference, Feb 04 - 06, 2013 2013, The Woodlands, TX, USA.

Li, C. Y., Weng, G. J., and Duan, Z. P., 2001, Dynamic behavior of a cylindrical crack in a functionally graded interlayer under torsional loading.Int.J.SolidStruct, 36(42-43), pp: 7473-7485.

Li, H., and Chandra, N., 2003, Analysis of crack growth and crack-tip plasticity in ductile materials using cohesive zone models, International Journal of Plasticity 19 (2003), pp: 849–882.

Mueller, D. T., and Eid, R. N., 2006, Characterization of the Early Time Mechanical Behavior of Well Cements Employed in Surface Casing operations, SPE 98632, IADC/SPE Drilling Conference, Miami, Florida, 21-23 February 2006.

Needleman, A., 1990, An Analysis of Decohesion along an Imperfect Interface, International Journal of Fracture 42, 21–40.

Oh, T. S., Rödel, J., Cannon, R. M., and Ritchie, R. O., 1988, Ceramic/Metal Interfacial Crack Growth, Toughening by Controlled Microcracks and Interfacial Goemetries, Acta Meterialia, 36, pp: 2083-2093.

Ozbek, T., and Erdogan, F., 1969, Some Elastic prohlems in fiber-reinforced composites with imperfect bonds, Int.J. Eng.Sci. 7(9), pp: 931-946.

Reeder, J. R., and Crews, J. H., 1988, Mixed-Mode Bending Method for Delamination Testing, AIAA Journal, July, Vol. 28, No. 7, pp: 1270-1276.

Reeves, G. M., Sims, I., and Cripps, J. C., 2006, Clay Materials Used in Construction: Engineering Geology Special Publication, Cromwell Press, Trowbridge, UK.

Rice, J. R., 1968, A Path Independent Integral and the Approximate Analysis of Strain Concentration by Notches and Cracks, Journal of Applied Mechanics 31, pp: 379-86.

Russell, A. J., 1982, On the Measurement of Mode II Interlaminar Fracture Energies, Defence Research Establishment Pacific, Victoria, Canada, DREP Materials Rept, Dec. 1982.

Saidin, S., Sonny, I., and Nuruddin, M. F., 2008, A New Approach for Optimizing Cement Design to Eliminate Microannulus in Steam Injection Wells, SPE 12407-MS, International Petroleum Technology Conference, Kuala Lumpur, Malaysia, 3-5 December 2008.

Sarris, E., Papanastasiou, P., 2011, The influence of the cohesive process zone in hydraulic fracturing modelling. Int J Fract 2011;167(1), pp:33–45.

Siegmund, T., and Brocks, W., 2000, A numerical study on the correlation between the work of separation and the dissipation rate in ductile fracture, Engineering Fracture Mechanics 67, pp: 139–154.

Tvergaard, V., 2001, Resistance curves for mixed mode interface crack growth between dissimilar elastic-plastic solids. J. Mech. Phys. Solids 49, pp: 2689-2703.

Van de Ketterij, R. G., and Pater, C. J., 1999, Impact of Perforations on hydraulic fracture tortuosity. SPE Production & Facilities, 14(2), pp: 131-138.

Wang, H. F., 2000, Theory of Linear Poroelasticity with Applications to Goemechanics and Hydrogeology, Princeton University Press, Princeton and Oxford.

Waters, G., Heinze, J., Jackson, R., Ketter, A., Daniels, J., and Bentley, D., 2006, Use of Horizontal Well Image Tools to Optimize Barnett Shale Reservoir Exploitation, SPE 103202-MS, SPE Annual Technical Conference and Exhibition, 24-27 September 2006, San Antonio, Texas, USA.

Weijers, L., and Pater, C. J., 1992, Fracture Reorientation in Model Tests, SPE 23790-MS, SPE Formation Damage Control Symposium, 26-27 February 1992, Lafayette, Louisiana.

Weijers, L., and Pater, C. J., 1994, Geometry of hydraulic fractures induced from horizontal wellbores, SPE Production & Facilities, 9(2), pp: 87-92.

Xie, M., 1995, Finite element modeling of discrete crack propagation, PhD thesis, University of New Mexico, USA.

Yang, Z. J., Su, X. T., Chen, J. F., and Liu, G. H., 2009, Monte Carlo Simulation of Complex Cohesive Fracture in Random Heterogeneous Quasi-brittle Materials, International Journal of Solids and Structures, 2009, Vol. 46(17), pp: 3222-3234.

Zbib, H. M., Hirth, J. P., and Demir, I.,1995, The stress intensity factor of cylindrical cracks, International Journal of Engineering Science, Volume 33, Issue 2, January 1995, pp: 247–253.

CHAPTER 7. CONCLUSIONS AND RECOMMENDATIONS

Wellbore integrity is a significant topic during the whole life of wells. In this dissertation, wellbore integrity was intensively investigated based on two major scenarios: wellbore integrity influenced by leakage at casing shoes and wellbore integrity during hydraulic fracturing stimulation.

Leakage Induced Delamination Cracks

Wellbore integrity strongly depends upon the integrity of the interfacial bonds between the cement and the formation (or the casing). Emergence of delamination fractures around casing and its stability due to leakage at casing shoes was investigated in this research. Leakage around the casing acts as driving force for failure development.

It has been shown here that Cohesive Zone Method (CZM) with Benzeggagh-Kenane (BK) formed bilinear traction separation law provide an effective method to describe the complicated mechanical characteristics of cement interface and predict failure behavior of cement interfaces. The robustness of the CZM is confirmed by establishing numerical models to reproduce the loading-displacement curves from laboratory. Moreover, fracture critical energy, cohesive strength or separation length, and the deformability (cohesive stiffness) are extracted for cohesive zone constitutive equations by inverse analyses. Then, these parameters are used to anticipate well-cement behavior for the field-scale problem.

Parameter sensitivity analysis on the role of each parameter in initiation and development of the failure zone is conducted in lab and field-scale numerical tests. Sensitivity results show that the rigidness, normal (and shear) strength of the interface, and cement Young's modulus have been determined to be dominant parameters on fracture containment. It is found that larger values of cement stiffness, interface normal (or shear) strength, or the rigidness of cement can effectively reduce the possibility of failure broaching around the wellbore.

Moreover, the understanding on crack emergence and propagation near the wellbore is analyzed by the variation of pore pressure, stresses, fracture opening, and damage around the wellbore. Moreover, these

models can effectively characterize crack tip to track failure initiation mechanism, which can be demonstrated by the combination of tensile stress and shear stress based on quadratic traction separation law. Results show that the excessive fluid pressure induced due to leakage is the drive for the cement-formation interface failures. The failures initiate if tensile stress and shear stresses at the crack tip of cement-rock interface satisfy with failure initiation criterion. The interface failure rate that is represented by the relationship between crack lengths and widths versus excessive fluid path is a combined function of the variation and fluctuation of pore pressure, normal and shear stresses, fracture opening, and energy distribution. Furthermore, interface failure and the hydraulic conductivity of the failure can further affect the pore pressure and stress distribution around the wellbore. On the contrary, interface failure and the hydraulic conductivity of the failure can further affect the pore pressure and stress distribution around the wellbore.

Additionally, three dimensional models are more sophisticated due to its capability to predict spatial non-planar failure patterns, which cannot be predicted by axisymmetric models. The non-uniform failure has been seen to exist even though in situations symmetric in situ stresses, and uniform cement properties. The non-uniformity of failure zone indicates the complexity of failure propagation process due to the nonlinear nature of the equations governing cement mechanical behavior. The non-uniformity around the failure front counteracts the limitations found in the average value of CBL, and provides a better understanding of the failure distribution around the wellbore. On the other hand, interface heterogeneity, wellbore inclination and eccentricity, and anisotropic in-situ stress wellbore conditions were studied in this work. Results show that higher heterogeneous degrees induce higher possibilities for interface broaching and faster evolution of channels under the effects of upward fluid flow induced by leakage. Moreover, the influences of well inclination and eccentricity on wellbore integrity are also predominant due to in situ stress has different contributions around the wellbore, which cause different stress concentration. The comprehensive researches on various wellbore condition is benefit for reducing the frequency or rate of wellbore instabilities. The proposed approach can give enough evidences on the

failure containment and integrity, which is also paramount for safe hydro-fracturing and preventing environmental risk. All of these issues are highly valuable to the industry.

Formation of Annulus Cracks during Hydraulic Fracturing

Wellbore integrity can also be challenged during hydraulic fracture stimulation due to the uncontrolled failures around the wellbore. Hence, it is significant to understand the main characteristics of fractures involved in this process to reduce the possibility of underground pollution.

The developed numerical method provides an effective tool for the assessment of simulating hydraulic fracturing and its wellbore integrity. Firstly, the developed numerical method was proved to be effective to predict failures around the wellbore by matching failure patterns with radioactive tracer-log's results, which gave the confidence for the model accuracy. On the other hand, the numerical results can effectively supplement the deficiency of failure initiation and propagation process involved in radioactive tracer-logs due to its characteristics of accuracy, economy and its predictive capability. The developed numerical method is also effective for the assessment of simulating multi-zone fracturing.

Then numerical results are extended to offer a full range of assessment on failure rates, failure propagation processes, and non-planar failure patterns. Numerical models are used to: 1) investigate wellbore integrity in stimulation of vertical wells; 2) considers wellbore integrity in vertical section of the wellbore due to leakage at the casing shoe; 3) simulate the wellbore integrity in the horizontal wells by taking into account the influences of formation and cement heterogeneity; 4) examine the wellbore integrity in inclined wells. Three types of possible failures near the wellbore were studied: longitudinal fractures, transverse fractures and annulus failures. It was proved that during hydraulic fracturing stimulation, it is possible for pressurized fluid to cause longitudinal fracture around the wellbore, and to migrate through the cement sheath failures to damage the weaker formation that is several meters away from the perforation zone. Moreover, the leakage around the casing shoe could also cause failure broaching along the cement-formation interface and finally leads to the loss of wellbore integrity. Moreover, stress field and wellbore inclination controls the orientation of failures and competitions

between annulus, longitudinal and transverse fractures. The heterogeneity of the interface makes failure development process becomes more complicated. Furthermore, the information obtained from numerical models, such as stress, fluid pressure, fracture opening and failure patterns, is benefit for the understanding on mechanism involved in this system. In this part, numerical models presented provide a tool to review these challenges and make contingency plans to avoid these problems in designing perforation and completion at each fracture stage.

Recommendations

Lab Measurements of Cohesive Properties: Interface parameters between cement and rock (or casing) obtained from traditional pull-out tests cannot represent the real interface properties in the field due to the lack of consideration of the real wellbore conditions, such as temperature and pressure. Hence, more sophisticated methods are required to measure tensile and shear cohesive parameters for effectively modelling wellbore integrity for different environmental conditions. Various laboratory tests are suggested to effectively evaluate cement-to-casing (or to-formation) interface bond strength at elevated temperature and pressures. These recommended tests for future study are listed as follow, such as 1) Confined pull-out test of cement bond interface; 2) Double cylindrical cantilever test; 3) Four-point flexure cylindrical beam test; and 4) Double cleavage drilled compression test.

Incorporating Ultra-sonic logging Tests (ULTs): The appearance of ULTs further improved the resolution in near-wellbore failure identification and bottom-hole condition prediction. ULTs are especially superior CBL-VBL combined system due to its capacity of detecting small channels or localized failures, which is impossible to be detected by average measurements provided by the combination of CBL and VBL. The advantages of ULTs are especially obvious in some cases, such as the interpretation of gas-contaminated cement and low weight cement (foam cement).

Field and lab, as well as numerical ULTs are recommended for future study. Field ULTs would provide an effective tool to verify the results in the BTH conditions. Lab study can further measure the cement bond strength, which can be implemented in numerical simulation for the prediction of wellbore

integrity. Moreover, cement bond logging and ultrasonic logging may be further used to determine cohesive properties in the in situ conditions by inverse stress analysis. Furthermore, ULTs can also be conducted analytically and numerically, such as semi-analytical methods, finite difference time-domain techniques and finite element methods, based on parameter extracted from field and lab ULTs. Cement sheath and near wellbore integrity can be further investigated by comprehensively considering laboratory and numerical ultrasonic logging tests.

APPENDIX

Material Information for Chapter 2

a. Cement mechanical properties in shear bond test of cement and shale

The mechanical properties of the cement G used for the calculations are summarized in Table 2.1.

Table 2.1 Mechanical Properties of Cement

(Note: "a" and "b" borrowed from Mueller and Eid (2006) and Lecampion (2011))

Mechanical Properties of cement [a]	
Types	Class G
Young's Modulus[a], KPa	3.043×10^6
Poisson's ratio[a]	0.26
Density[a], Kg/m^3	1893
Permeability[b], mD	0.001
Porosity[b]	0.20

b. Shale formation properties in shear bond test of cement and shale

Shale is consociated, fissured, silty, rarely sandy, intermediate to high and occasionally very high plasticity clay (Reeves, et al, 2006). The elastic and mechanical properties of the shale used in the model are introduced in Table 2.2.

Table 2.2 Mechanical Properties of Oxford Shale

(Note: "a", "b" and "c" borrowed from Prince and Cosgrove (2006), Ballard, et al (1994) and Reeves, et al (2006))

Types	Oxford shale
Young's Modulus[a], KPa	3.25×10^6
Poisson's ratio[a]	0.26
Density[c], Kg/m^3	2000
Permeability[b], mD	500
Porosity[b]	0.35

c. Cement mechanical properties in shear bond test of casing and cement

Detailed mechanical properties of the cement used for the calculations are summarized in Table 2.3.

Table 2.3 Mechanical Properties of Cement

(Note: "a" and "b" borrowed from Mueller and Eid (2006) and Lecampion (2011))

Mechanical Properties of cement [a]	
Types	Class A
Young's Modulus[a], KPa	2.77×10^6
Poisson's ratio[a]	0.26
Density[a], Kg/m^3	1869
Permeability[b], mD	0.001
Porosity	0.20

d. Casing Properties in shear bond test of casing and cement

Grade P-110 casing, with outside diameter 7 in, inside diameter 6.094 in, and 32 lbm/ft nominal weight and Grade C-75 casing, with outside diameter 5 in, inside diameter 4.276 in, and 28 lbm/ft nominal weight (Bourgoyne, et al. 1986), is chosen for this model. Mechanical Properties obtained from Haliburton Redbook (1999), which is shown in Table 2.4.

Table 2.4 Thermal Elastic and Mechanical Properties of Casing

Mechanical Properties	Inner Casing	Outter Casing
Casing Grade	C-75	P-110
Dimensions	5" × 4.276"	7" × 6.094"
Young's Modulus, KPa	2.1×10^8	1.95×10^8
Poisson's ratio	0.28	0.30
Density, kg/m^3	7850	7850

e. Casing Properties used in the real model test

Grade H-40 casing, with outside diameter 7 in, inside diameter 6.456 in, and 20 lbm/ft nominal weight (Bourgoyne, et al. 1986), is chosen for this model. Thermal Elastic and Mechanical Properties obtained from Haliburton Redbook (1999), which are shown in Table 2.5.

Table 2.5 Thermal Elastic and Mechanical Properties of Casing

(Note: "a", "b" and "c" borrowed from Jutten (1989), Thiercelin et al. (1997), and Ravi et al. (2007), respectively)

Thermal Elastic Properties of Casing [a, c]		Mechanical Properties of Casing [b]	
Specific heat, J $kg^{-1}K^{-1}$	500	Young's Modulus, KPa	2.0×10^{8}
Thermal expansion coefficient, K^{-1}	1.3×10^{-5}	Poisson's ratio	0.27
Thermal conductivity, W/mK	15.0	Density, kg/m^3	8000

f. Interface Properties

Cohesive interface properties used in this model are listed in Table 2.6. The maximum nominal stress criterion is considered to predict damage initiation. Then linear traction separation law (softening law) is used to describe the damage evolution based on the energy required for the separation of two sides of the interface.

Table 2.6 Properties of the cohesive interface between casing and cement

Shear bond strength, KPa	Hydraulic bond strength, KPa (Psi)	Cohesive stiffness, KPa	Critical Energy G_c, J/m^2	Fluid Leak off coefficient	Gap flow, Kpa.s
348	348	8.5 E7	50	2.5E-6	1e-6

Material Information for Chapter 3

a. Cement mechanical properties

The mechanical properties of the cement G used for the calculations are summarized in Table 3.1.

Table 3.1 Mechanical Properties of Cement

(Note: "a" and "b" borrowed from Mueller and Eid (2006) and Lecampion (2011))

Mechanical Properties of cement			
Types	Class G		
Young's Modulus, KPa	30.043×10^6	Density, Kg/m^3	1893
Poisson's ratio	0.26	Permeability, mD	0.001
Porosity	0.20		

b. Shale formation properties

The elastic and mechanical properties of the shale formation used in the model are introduced in Table 3.2.

Table 3.2 Mechanical Properties of Shale Formation

(Note: "a", "b" and "c" borrowed from Prince and Cosgrove (2006), Ballard, et al (1994) and Reeves, et al (2006))

Mechanical Properties of Shale Formation	
Young's Modulus[(a)], KPa	3.25×10^6
Poisson's ratio[(a)]	0.26
Density[(c)], Kg/m^3	2000
Permeability[(b)], mD	500
Porosity[(b)]	0.35

c. Casing Properties

Grade H-40 casing, with outside diameter 7 in, inside diameter 6.456 in, and 20 lbm/ft nominal weight (Bourgoyne, et al. 1986), is chosen for this model. Thermal Elastic and Mechanical Properties obtained from Haliburton Redbook (1999), which is shown in Table 3.3.

Table 3.3 Thermal Elastic and Mechanical Properties of Casing

(Note: "a", "b" and "c" borrowed from Jutten (1989), Thiercelin et al. (1998), and Ravi et al. (2007), respectively)

Mechanical Properties of Casing [b]	
Young's Modulus, KPa	2.0×10^{8}
Poisson's ratio	0.27
Density, kg/m^3	8000

d. Interface Properties

Cohesive interface properties used in this model are listed in Table 3.4. The quadratic nominal stress criterion is considered to predict damage initiation. Then linear traction separation law (softening law) is used to describe the damage evolution based on the energy required for the separation of two sides of the interface. Cohesive interface properties are generated from pull out test between cement and rock (or casing) provided by Carter-Evans (1964) and Ladva's (2005) and then are derived by its subsequent numerical tests by Dahi Taleghani and Wang (2013).

Table 3.4 Properties of the cohesive interface

Properties of the cohesive interface between casing and cement				
Shear bond strength, KPa	Hydraulic bond strength, KPa (Psi)	Cohesive stiffness, KPa	Critical Energy G_c, J/m^2	$\alpha=\frac{\delta_0}{\delta_f}$
Properties of the cohesive interface between cement and casing				
2000	500	30 E6	100	0.2
Properties of the cohesive interface between cement and formation				
420	420	30 E6	100	0.2

Material Information for Chapter 4

a. Cement mechanical properties

The mechanical properties of the cement G used for the calculations are summarized in Table 4.1.

Table 4.1 Mechanical Properties of Cement

(Note: "a" and "b" borrowed from Mueller and Eid (2006) and Lecampion (2011))

Mechanical Properties of cement [a]	
Types	Class G
Young's Modulus[a], KPa	30.043×10^6
Poisson's ratio[a]	0.26
Density[a], Kg/m^3	1893
Permeability[b], mD	0.001
Porosity[b]	0.20

b. Shale formation properties

Shale in this system is consociated, fissured, silty, and rarely sandy. It is intermediate to high and occasionally very high plasticity clay (Reeves et al., 2006). The elastic and mechanical properties of the shale formation used in the model are introduced in Table 4.2.

Table 4.2 Mechanical Properties of Shale Formation

(Note: "a", "b" and "c" borrowed from Prince and Cosgrove (2006), Ballard, et al (1994) and Reeves, et al (2006))

Mechanical Properties of Shale Formation	
Young's Modulus[a], KPa	3.25×10^6
Poisson's ratio[a]	0.26
Density[c], Kg/m^3	2000
Permeability[b], mD	500
Porosity[b]	0.35

c. Casing Properties

Grade H-40 casing, with outside diameter 7 in, inside diameter 6.456 in, and 20 lbm/ft nominal weight (Bourgoyne, et al. 1986), is chosen for this model. Thermal Elastic and Mechanical Properties obtained from Haliburton Redbook (1999), which is shown in Table 4.3.

Table 4.3 Thermal Elastic and Mechanical Properties of Casing

(Note: "a", "b" and "c" borrowed from Jutten (1989), Thiercelin et al. (1998), and Ravi et al. (2007), respectively)

Mechanical Properties of Casing [b]	
Young's Modulus, KPa	2.0×10^8
Poisson's ratio	0.27
Density, kg/m^3	8000

d. Interface Properties

Cohesive interface properties used in this model are listed in Table 4.6. The quadratic nominal stress criterion is considered to predict damage initiation. Then linear traction separation law (softening law) is used to describe the damage evolution based on the energy required for the separation of two sides of the interface. Cohesive interface properties are generated from pull out tests between cement and rock (or casing) provided by Carter-Evans (1964) and Ladva's (2005) and then are derived by its subsequent numerical tests by Dahi Taleghani and Wang (2013).

Table 4.4 Properties of the cohesive interface

Properties of the cohesive interface between casing and cement				
Shear bond strength, KPa	Hydraulic bond strength, KPa (Psi)	Cohesive stiffness, KPa	Critical Energy G_c, J/m^2	$\alpha=\frac{\delta_0}{\delta_f}$
Properties of the cohesive interface between cement and casing				
2000	500	3 E6	100	0.2
Properties of the cohesive interface between cement and formation				
420	420	3 E6	100	0.2

Material Information for Chapter 5

a. Shale formation properties

The elastic and mechanical properties of the shale formation used in the model are introduced in Table 5.1.

Table 5.1 Mechanical Properties of Shale Formation 1

Mechanical Properties of Shale Formation	
Young's Modulus, KPa	3.25×10^{6}
Poisson's ratio	0.26
Density, Kg/m^3	2000
Permeability, mD	500
Porosity	0.35

b. Casing Properties

Grade H-40 casing, with outside diameter 7 in, inside diameter 6.456 in, and 20 lbm/ft nominal weight (Bourgoyne, et al. 1986), is chosen for this model. Thermal Elastic and Mechanical Properties obtained from Haliburton Redbook (1999), which is shown in Table 5.2.

Table 5.2 Mechanical Properties of Casing

(Note: "a", "b" and "c" borrowed from Jutten (1989), Thiercelin et al. (1998), and Ravi et al. (2007), respectively)

Mechanical Properties of Casing [(b)]	
Young's Modulus, KPa	2.0×10^{8}
Poisson's ratio	0.27
Density, kg/m^3	8000

c. Interface Properties

Cohesive interface properties used in this model are listed in Table 5.3. The quadratic nominal stress criterion is considered to predict damage initiation. Then linear traction separation law (softening law) is used to describe the damage evolution based on the energy required for the separation of two sides of the interface. Cohesive interface properties are provided by Chen (2009).

Table 5.3 Properties of the Cohesive Interface

Properties of the cohesive interface			
Hydraulic bond strength, KPa	2000	Cohesive stiffness, KPa	30 E6
Shear bond strength, KPa	500	Critical Energy G_c, J/m^2	100

Material Information for Chapter 6

a. Cement mechanical properties

The mechanical properties of the cement G used for the calculations are borrowed from Mueller and Eid (2006) and summarized in Table 6.1.

Table 6.1 Mechanical Properties of Cement

Mechanical Properties of cement			
Types	Class G		
Young's Modulus, KPa	30.043×10^6	Density, Kg/m^3	1893
Poisson's ratio	0.26	Permeability, mD	0.001
Porosity	0.20		

b. Shale formation properties

Shale in this system is consociated, fissured, silty, and rarely sandy. It is intermediate to high and occasionally very high plasticity clay (Reeves et al., 2006). The elastic and mechanical properties of the shaleformationused in the model are introduced in Table 6.2.

Table 6.2 Mechanical Properties of Shale Formation

Mechanical Properties of Shale Formation			
Young's Modulus, KPa	3.25×10^6	Permeability, mD	500
Poisson's ratio	0.26	Porosity	0.35
Density, Kg/m^3	2000		

c. Casing Properties

Grade H-40 casing, with outside diameter 7 in, inside diameter 6.456 in, and 20 lbm/ft nominal weight (Bourgoyne, et al. 1986), is chosen for this model. Thermal Elastic and Mechanical Properties obtained from Haliburton Redbook (1999), which is shown in Table 6.3.

Table 6.3 Thermal Elastic and Mechanical Properties of Casing

Mechanical Properties of Casing	
Young's Modulus, KPa	2.0×10^{8}
Poisson's ratio	0.27
Density, kg/m^3	8000

d. Interface Properties

Cohesive interface properties used in this model are listed in Table 6.4. The quadratic nominal stress criterion is considered to predict damage initiation. Then linear traction separation law (softening law) is used to describe the damage evolution based on the energy required for the separation of two sides of the interface. The properties of cement-formation interface and rock interface are provided by Dahi Taleghani and Wang (2013) and Chen (2011), respectively.

Table 6.4 Properties of the cohesive interface

Properties of the cohesive interface between casing and cement				
Shear bond strength, KPa	Hydraulic bond strength, KPa (Psi)	Cohesive stiffness,KPa	Critical Energy G_c, J/m^2	$\alpha=\frac{\delta_0}{\delta_f}$
Properties of the cohesive interface between cement and formation				
420	420	420	420	0.2
Properties of the cohesive interface in the rock				
1800	800	30 E6	100	0.2

VITA

Wei Wang was born in Zhuanghe City, Liaoning Province, China, in 1980. She attended Northeast Petroleum University in China in September 2000, where she received her Bachelor and Master in Petroleum Engineering in 2004 and 2007. Then she came to University of Wyoming in 2007 and got a Master in Petroleum Engineering in 2009. Then she was admitted to the Graduate School of Louisiana State University in Spring of 2010 for the doctoral program in the Craft & Hawkins Department of Petroleum Engineering. She specializes in Geomechanics simulation, Underground venting, and Wellbore integrity.